New Physics Hunt at the Large Hadron Collider with the ATLAS Detector: Search for Heavy Exotic Resonances and Upgrade of the Transition Radiation Tracker DAQ System

by

Vincent Wai Sum Wong

B.A.Sc., The University of British Columbia, 2014

A THESIS SUBMITTED IN PARTIAL FULFILLMENT

OF THE REQUIREMENTS FOR THE DEGREE OF

DOCTOR OF PHILOSOPHY

in

The Faculty of Graduate and Postdoctoral Studies

(Physics)

THE UNIVERSITY OF BRITISH COLUMBIA

(Vancouver)

July 2021

The following individuals certify that they have read, and recommend to the Faculty of Graduate and Postdoctoral Studies for acceptance, the dissertation entitled:

New Physics Hunt at the Large Hadron Collider with the ATLAS Detector: Search for Heavy Exotic Resonances and Upgrade of the Transition Radiation Tracker DAQ System

submitted by **Vincent Wai Sum Wong** in partial fulfillment of the requirements for the degree of **Doctor of Philosophy** in **Physics**.

Examining Committee:

Colin Gay, Professor and Head, Physics & Astronomy, UBC
Supervisor

Scott Oser, Professor, Physics & Astronomy, UBC
Supervisory Committee Member

Jeremy Heyl, Professor, Physics & Astronomy, UBC
University Examiner

Takamasa Momose, Professor, Chemistry, UBC
University Examiner

Additional Supervisory Committee Members:

Gary Hinshaw, Professor, Physics & Astronomy, UBC
Supervisory Committee Member

Gordon Semenoff, Professor, Physics & Astronomy, UBC
Supervisory Committee Member

Abstract

Many theories beyond the Standard Model suggest new particles at the TeV energy scale, that could be produced in proton-proton collisions delivered by the CERN Large Hadron Collider and collected by the ATLAS experiment. Since 2016, the accelerator has surpassed its expected value of luminosity by up to a factor of two. The data acquisition system of the ATLAS Transition Radiation Tracker had to be upgraded to meet the demand from the challenging beam conditions and the higher trigger rate in Run II beyond the original design of the tracking detector. The improvements developed in the hardware and firmware of the DAQ system are documented in this dissertation, with a study to evaluate the performance of the system.

This dissertation also presents two searches for new massive bosons at the TeV scale. The first analysis searches for heavy resonances decaying into a hadronic Z/W/Higgs boson and a photon. The boosted Z/W/Higgs boson is identified using large-radius jet mass and substructure informations. The analysis is based on 36 fb^{-1} of $\sqrt{s} = 13$ TeV proton–proton collision data, collected with the ATLAS detector in Run II of the Large Hadron Collider. No significant deviations from the Standard Model prediction is observed. Upper limits are set on the signal cross section multiplied by the branching fraction of resonance for the three different diboson final states at 95% confidence level, excluding those productions at 10–0.2 fb in the resonance mass range of 1–6.8 TeV.

The second analysis searches for scalar leptoquark pair productions, where each leptoquark decays into a top quark and an electron or a muon. The search sensitivity is optimized for high leptoquark masses, at which the hadronic decay products of each top quark are contained within a large-radius jet. The analysis exploits the full Run II dataset that corresponds to an integrated luminosity of 139 fb^{-1}. No significant excess of events is found. Lower mass limits on leptoquarks decaying into electron–top-quark or muon–top-quark pair are set to 1.48 TeV and 1.47 TeV at 95% confidence level.

Lay Summary

The Standard Model of particle physics is currently the best theory that encapsulates the fundamental building blocks of nature and their interactions. Its consistency with nature has been proven unflinching in numerous experimental tests; however, the theory contains unresolved shortcomings that require theories beyond the Standard Model, many of which predict new massive fundamental particles. This dissertation presents searches for new forces of nature at the highest energy ever reached by physicists, using the ATLAS detector at the Large Hadron Collider. Contributions to the upgrade of the data acquisition of the tracking sub-detector, called the Transition Radiation Tracker, are also presented. Although no new particles were found, the possible territories where new physics could lie are narrowed down.

Preface

This dissertation presents my contributions to the ATLAS experiment from 2014 to 2020, under the supervision of C. Gay. The work is ultimately based on the successful operation of the Large Hadron Collider and the experimental apparatus of the ATLAS experiment, which are both subjects of a large international collaboration. The entire process from the data acquisition to the reconstruction of physics objects is a shared effort among the entire ATLAS Collaboration, that is comprised of over thousands of scientists from 182 institutions in 38 countries. Every qualified ATLAS member is listed on each external publication or public result, in purely alphabetical order. The work of Chapter 9, 11 and 12 are my primary work, which in many cases relies on the work of numerous individuals. The acknowledgment of their contributions will be given below, along with my original contributions as part of the effort.

None of the text in the dissertation is not written by me, and no text is taken directly from previously published articles or internal documentations. All figures documented in this dissertation represent my own work unless explicitly indicated in this preface or credited with a reference in the caption. Figures with the label **ATLAS** are results officially approved by the ATLAS Collaboration for peer-reviewed journals. Figures labeled with **ATLAS** *Preliminary* are preliminary public results approved typically for releases in the form of conference notes or public documents. Figures labeled with **ATLAS** *Internal* are results that have not gone through the official ATLAS approval but have been presented in internal ATLAS talks or included in internal supporting documents. Figures labeled with **ATLAS** *Work In Progress* are results not approved by the collaboration, yet depend on the ATLAS data or simulated samples produced using the ATLAS simulation infrastructure. The suffix *Simulation* is added to a figure label if the results rely on ATLAS simulated samples only.

I started my contributions to the Transition Radiation Tracker as my service task, which granted me my ATLAS authorship and right to analyze the data. I continued to work as part of the Transition Radiation Tracker DAQ team for my whole life of doctoral studies. As a DAQ expert, I was responsible for ensuring that this sub-detector system was functioning properly and recording data of good quality, while I conducted electronic maintenance in the ATLAS detector. In my 24/7 7-day on-call shifts, my role was to provide support to monitor shifters in the ATLAS Control Room for any problem during data taking. In addition, I acted as the main engineer of the off-detector field-

programmable-gate-array-based readout electronics, in collaboration with C. Gay and Z. Gecse. My expertise in the processing and compression of data in the DAQ system led me to the following contributions:

- Upgraded the firmware and hardware of the readout electronics to cope with the Large Hadron Collider Run II beam conditions, as described in Section 9.4. The development in the firmware related to the reduced readout mode and the output bandwidth was performed by Z. Gecse. The hardware upgrade of the S-LINK interface card was performed by the DAQ team as a collaborative effort.
- Performed studies to assess the data compression performance of the DAQ system, as documented in Section 9.5.
- Implemented in situ monitoring registers in the firmware of the readout electronics for real-time monitoring of crucial bottlenecks in the data processing system and any occurrence of data corruption.
- Developed web-based monitoring tools for remote surveillance of the status of the readout electronics.
- Repairs and maintenance of the readout electronics.
- Provided support in the DAQ team by troubleshooting issues in the readout system during the ATLAS operation.

I presented the upgrade work in the following conference talk:

> *ATLAS Transition Radiation Tracker Firmware Upgrade for LHC Run 2*, The Winter Nuclear and Particle Physics Conference 2016, February 11 – 14, 2016; Banff, Canada

The work was also presented in the following poster, by K. Mistry, on behalf of the ATLAS Collaboration, in which I reviewed the part I contributed:

> *ATLAS Transition Radiation Tracker (TRT) Electronics Operation Experience at High Rates*, Topical Workshop on Electronics for Particle Physics 2015, September 28 – October 2, 2015; Lisbon, Portugal

Additionally, the upgrade work was documented in internal supporting documentations, in which I took part as an editor.

Inspired by the 750 GeV diphoton excess observed in 2015, I joined an analysis team to search for new heavy resonances decaying into $Z\gamma$ / $W\gamma$ / $H\gamma$, even though the excess did not last when more data was collected. The analysis is presented in Chapter 11. In this analysis, I was the lead analyzer in a group of 15 members, and made contributions to the design and coding of the analysis strategy, including the following:

- Developed general code for event selections.
- Performed the optimization of the signal region selection criteria, and devised the use of b-tagging techniques to further optimize signal sensitivity by categorization.
- Designed the background modeling methodology, and developed various tests to validate the background fit.
- Developed configuration file that implements the analysis strategy into the statistical framework HFITTER.
- Documented the background fitting method and the relevant test in internal ATLAS documentation.
- Presented the analysis to the ATLAS Collaboration for approval, and addressed comments during the review process.

The preparation of the data and simulated samples was performed by E. Khramov and S. Li. The development of the analysis framework and the optimization of event selection were performed individually and cross-checked between M. Feng and me. The signal modeling was developed by M. Feng. While the general statistical framework HFITTER was developed by N. Berger, A. Hoecker, and B. Lenzi, the analysis-specific configuration file was prepared by B. Liu and me. The evaluation of systematic uncertainties was performed by E. Khramov. The publication of the analysis was written by W. Fedorko and A. Goshaw, and was published in Physical Review D:

> ATLAS Collaboration, *Search for heavy resonances decaying to a photon and a hadronically decaying Z/W/H boson in pp collisions at* $\sqrt{s} = 13$ *TeV with the ATLAS detector*, Phys. Rev. D 98 (2018) 032015.

Due to my involvement in the analysis, I also had the opportunity to co-chair the Diboson VV session with A. Picazio in the ATLAS DBL-HBSM Joint Workshop (2017) for discussion and future planning of this analysis and other similar analyses.

Intrigued by the potential of a hypothetical particle, called leptoquark, in explaining the recent experimental hints of lepton flavor universality violation in B decay, I decided to start a new analysis to search for leptoquarks, as presented in Chapter 12. I had the opportunity to work on the analysis individually, which is rare in a huge collaboration like ATLAS. I developed all of the analysis-specific work, with dependence on common tools used by the collaboration. While the simulated background samples were centrally provided by the collaboration like the previous analysis, I produced the signal samples with the ATLAS simulation infrastructure. I developed the analysis framework based on a code skeleton with primary contributions from Y. H. Chen and E. Khoda. The general statistical framework TREXFITTER employed in the analysis was primarily developed

by L. Valéry and M. Pinamonti. As the analysis contact, I was responsible for a detailed internal supporting documentation, internal ATLAS talks for status update and approval, and addressing comments during the review process. The publication of the results was primarily written by me, with editing by A. Lister, and was submitted to European Physical Journal C:

> ATLAS Collaboration, *Search for scalar leptoquark pair production decaying into top-quarks and leptons at* $\sqrt{s} = 13$ *TeV with ATLAS detector*, arXiv:2010.02098 [hep-ex]

A superseded preliminary version of the publication in the form of conference notes was also presented:

> ATLAS Collaboration, *Search for pair production of scalar leptoquarks decaying to first or second generation leptons and boosted hadronically decaying top quarks in pp collisions at* $\sqrt{s} = 13$ *TeV with the ATLAS detector*, ATLAS-CONF-2020-033

In addition, I presented, on behalf of the ATLAS Collaboration, the analysis and various related analyses in the following conference talks, and written proceedings for the talks:

> *Search for scalar leptoquark pair production decaying into top-quarks and leptons at* $\sqrt{s} =$ 13 *TeV with ATLAS detector*, 40th International Conference on High Energy Physics, July 28 – August 6, 2020; Prague, Czech Republic

> *Searches for new phenomena in final states involving leptons and jets using the ATLAS detector*, 9th International Conference on New Frontiers in Physics, September 4 – 12, 2020; Crete, Greece

Finally, Figure 13.2 in the Chapter 13 was produced by A. Mann to show the combined effort of various analysis teams targeting the different but relevant decay modes of leptoquarks.

Table of Contents

List of Tables

List of Figures

Glossary

ASDBLR Amplifier/Shaper/Discriminator/Baseline-Restoration Integrated Circuit

ASIC application-specific integrated circuit

BCMS Batch Compression, Merging and Splitting

BDT boosted decision tree

BSM beyond the Standard Model

CKM Cabibbo–Kobayashi–Maskawa

CMB cosmic microwave background

CP Charge-Parity

CR control region

CRC cyclic redundancy check

CSC Cathode Strip Chamber

CTP Central Trigger Processor

DAQ data acquisition

DTMROC Digital Time Measurment ReadOut Chip

EM electromagnetic

FCCC flavor-changing charged current

FCNC flavor-changing neutral current

FE front-end electronics

FPGA field-programmable gate array

GIM Glashow-Iliopoulos-Maiani

GUT Grand Unified Theory

HEC hadronic endcap

HLT high-level trigger

HOLA High-speed Optical Link for ATLAS

HT high-level threshold

IBL Insertable B-Layer

ID Inner Detector

LFU lepton flavor universality

LHC Large Hadron Collider

LO leading order

LQ leptoquark

LT low-level threshold

MDT Monitored Drift Tube

MLE maximum likelihood estimate

MS Muon Spectrometer

NLO next-to-leading order

NNLL next-to-next-to-leading-log

NNLO next-to-next-to-leading order

NSE Network Search Engine

PDF parton distribution function

PS Proton Synchrotron

QED Quantum Electrodynamics

QFT Quantum Field Theory

QCD Quantum Chromodynamics

RF radiofrequency

ROD ReadOut Driver

ROS ReadOut System

RPC Resistive Plate Chamber

SCT Semiconductor Tracker

SM Standard Model

SPS Super Proton Synchrotron

SR signal region

SUSY supersymmetry

TDAQ Trigger and Data Acquisition

TGC Thin Gap Chamber

TRT Transition Radiation Tracker

TTC Timing and Trigger Control

VEV vacuum expectation value

WIMP weakly-interacting massive particle

Acknowledgments

First, I want to start by thanking my supervisor, Colin Gay, for his guidance and expertise, in both physics and electronics, throughout my entire PhD, as well as the amazing opportunity to be based at CERN for a full year and the great flexibility in all of the short trips to CERN and conferences. I am also grateful for the help I received from Zoltan Gecse, who gave me a lot of inspirations in the upgrade work of the Transition Radiation Tracker. I am also thankful to Wojtek Fedorko for always sharing his invaluable knowledge to guide me. Special thanks must also go to Alison Lister for all the fruitful discussions. And many thanks to everyone else in the UBC-ATLAS group. It has been a stimulating environment to work in. The feedbacks provided both during and outside of group meetings brought immeasurable improvement to the work in this thesis.

Thank you my awesome TRT colleagues for all the fun memories crawling through the ATLAS detector and fixing things, in particular: Chris, Sarah, Bijan, Khilesh, Daniil, Elodie, Keisuke, Ian, Shion and Joe. It is hard to quantify how much the TRT would have not been running so smoothly without the impressive teamwork. It has been my great pleasure to be part of the fantastic team.

I must also thank all collaborators from the $V\gamma/H\gamma$ analysis group for having been such a supportive and motivated team. Special thanks to Shu Li and Zhijun Liang for your leadership and friendship during my first-ever analysis work in particle physics.

Next, I must say my research would have definitely not been possible without the contribution of each individual in the ATLAS collaboration, regarding areas from the operation of the many sub-systems of the detector, to the relentless support of combined performance groups. The selfless dedication by everyone in the collaboration has taught me a lot what the word 'collaboration' means on both scientific and social level.

I want to also thank all my friends, both inside and outside the world of physics, including the ones that I have made along my journey. It would not have been as unforgettable without you. To my parents, thank you for your love over the years, always supporting me to do what I want. To my siblings, Vivien and May, thank you for always being supportive and believing in me. You two have always been my role model, motivating me to pursue my dream. Last but not least, thank you Cherry for your love and everything all these years, especially the time I spent traveling around. Your month-long visit during my stay at CERN made the long-distance separation an enjoyable

memory. Thank you for making the stressful time endurable. I'm excited about the many more years we spend together in the future. I love you more than ever.

Chapter 1

Introduction

The Standard Model of particle physics is the best mathematical description of the fundamental particles and their interactions through the electromagnetic, the weak and the strong forces. The Brout-Englert-Higgs mechanism described in the Standard Model provides an explanation to the origin of subatomic particle masses and was confirmed through the discovery of the Higgs boson in 2012 by the ATLAS and CMS experiments at CERN's Large Hadron Collider. Even though the Standard Model has demonstrated tremendous predictive power in almost all experimental measurements of the subatomic world over the past century, the theory is known to be incomplete. It omits the fourth known fundamental force in the universe – gravity; it does not accommodate dark matter, dark energy nor neutrino masses; and it raises theoretical problems such as the origin of the hierarchy between the electroweak scale and the Planck scale. These shortcomings have convinced many physicists that there must be new physics beyond the Standard Model. Many extensions of the Standard Model predict the existence of new massive particles possibly in the TeV energy scale.

With the start of Run II for the Large Hadron Collider in 2015, a doorway to the discovery of unknown particles with masses at the order of TeV has been opened, thanks to the highest-ever collision energy level with the center-of-mass energy of 13 TeV. This dissertation presents two searches for new bosons as part of the broad exotic physics search program in ATLAS using proton–proton collisions recorded during Run II. The first analysis focuses on the search for heavy resonances decaying into final states consisting of a Z/W/Higgs boson and a photon, wherein the Z/W/Higgs boson decays into hadrons. While the leptonic final state could suffer from a lower cross section of background processes, this final state has the advantage of having a larger branching ratio compared with the leptonic final state. In scenarios where the resonance mass is at the order of 1 TeV, the background processes become less considerable. The hadronic final state thus offers higher sensitivity. The Z/W/Higgs boson is also expected to have a significant Lorentz boost; the decay products of the boson are identified as one wide-angle cluster of energy deposits in the calorimeter, referred to as a large-radius jet. Jet substructure and b-tagging techniques are employed to enhance

sensitivity to the hadronic boson decay. This search uses the proton–proton collisions recorded in 2015–2016, with an integrated luminosity of 36.1 fb^{-1}.

The second analysis searches for a new kind of gauge bosons that couple to quark-lepton pairs, called leptoquarks. They have recently attracted particular attention because they could address the deviations from the Standard Model observed in B-meson decays. Many leptoquark searches have been performed in ATLAS assuming leptoquarks couple to quarks and leptons of the same generation; the choice, however, is a priori arbitrary. Leptoquarks coupling to third-generation quarks have been proposed as promising solution to the B-anomalies. This motivates the pioneering search for pair productions of top-philic cross-generational scalar leptoquarks decaying into pairs of top quarks and electrons, or top quarks and muons. In particular, the presented search explores the fully hadronic final state in the boosted regime, in which the decay products of each top quark are contained within a large-radius jet. This search uses proton–proton collisions recorded over the full Run II, corresponding to an integrated luminosity of 139 fb^{-1}.

Since 2017, the Large Hadron Collider has been upgraded to further increase the intensity of the proton beams, reaching twice the initial design goal. The increased luminosity has opened up even larger opportunities to explore territories of new physics, but also posed challenges to the data acquisition system of the ATLAS Transition Radiation Tracker to compress and read out the interesting proton-proton collision data fast enough. The new luminosity record leads to an overall hit occupancy of around 80% and a readout rate of 100 kHz, which exceeds the maximum occupancy of 50% and maximum readout rate of 80 kHz that the Transition Radiation Tracker was initially designed for. The hardware and firmware of the readout system have been upgraded to cope with the unprecedented luminosity, as part of the work documented in this dissertation.

This dissertation is structured as follows: the theoretical foundation and motivation are laid down in Part I, beginning with Chapter 2 to 3 that describe a summary of the Standard Model and its shortcomings. Various theories beyond the Standard Model relevant to the presented searches are then introduced in Chapter 4. Chapter 5 presents the basics of proton-proton collisions. The first half of Part II introduces the experimental facilities that are used to deliver the data analyzed in this dissertation, whereas the second half describes how raw detector measurements are reconstructed and identified as meaningful physics objects with a focus on those utilized in the presented analyses. In Part III, the data acquisition system of the Transition Radiation Tracker, as well as the upgrade for the preparation of Run II, is described. A study of the data compression performance is also discussed alongside. In Part IV, the two performed searches for exotic signatures are presented. Firstly, Chapter 10 introduces the general statistical methodology employed to interpret the search results. Then, Chapter 11 presents the search for heavy resonances decaying into Z/W/Higgs boson and a photon. Finally, Chapter 12 presents the search for pair-produced scalar leptoquarks decaying into electron–top-quark or muon–top-quark pair. The dissertation concludes in Chapter 13 with suggestions for future work on the analyses.

Part I

Theoretical Motivation

Chapter 2

Standard Model

The Standard Model (SM) of particle physics [1–4] is our best mathematical description that encapsulates how the tiniest components of matter interact with each other. It was established in the mid-1970s, and since then, over half a century, numerous experimental measurements have proven its accurate prediction and description of the interactions among fundamental particles across a wide range of phenomena. After the discovery of the long-sought Higgs boson at the Large Hadron Collider (LHC) [5, 6], particle physicists can crown this elegant model in triumph — *the Absolutely Amazing Theory of Almost Everything*.

This chapter will give an overview of the particle content in the SM and the interactions between them in Section 2.1. Section 2.2 reviews the major features of the electroweak sector, followed by the Brout-Englert-Higgs mechanism that gives masses to the fundamental particles via spontaneous symmetry breaking. Section 2.3 gives a brief overview of the strong interaction.

Throughout this dissertation, the natural unit system will be used, with the speed of light in vacuum c, the Planck constant $\hbar$ and the vacuum permittivity ε_0 rescaled to unity.

2.1 Elementary Particles and Forces

Elementary particles are fundamental in the sense that no substructures have yet been found in these particles. The elementary particles, as shown in Figure 2.1 could be divided into two distinct classes: fermions and bosons. Fermions have spins that come in half-integer multiple, and they are the building blocks of matter. Bosons carry integer spin and act as force carriers that mediate the fundamental interactions between fermions and themselves. In the SM, there are three generations (or families) of fermions. Each generation consists of two kinds of fermions called leptons and quarks. There are six leptons, carrying either unit electric charge (electron e, muon μ, tau τ) or zero charge (electron neutrino ν_e, muon neutrino ν_μ, tau neutrino ν_τ). Furthermore, leptons are split into different generations by their flavors, (e, ν_e), (μ, ν_μ), (τ, ν_τ). The masses of charged leptons increase as one goes from the first to the third generation, starting from m_e of 511 keV to m_μ of

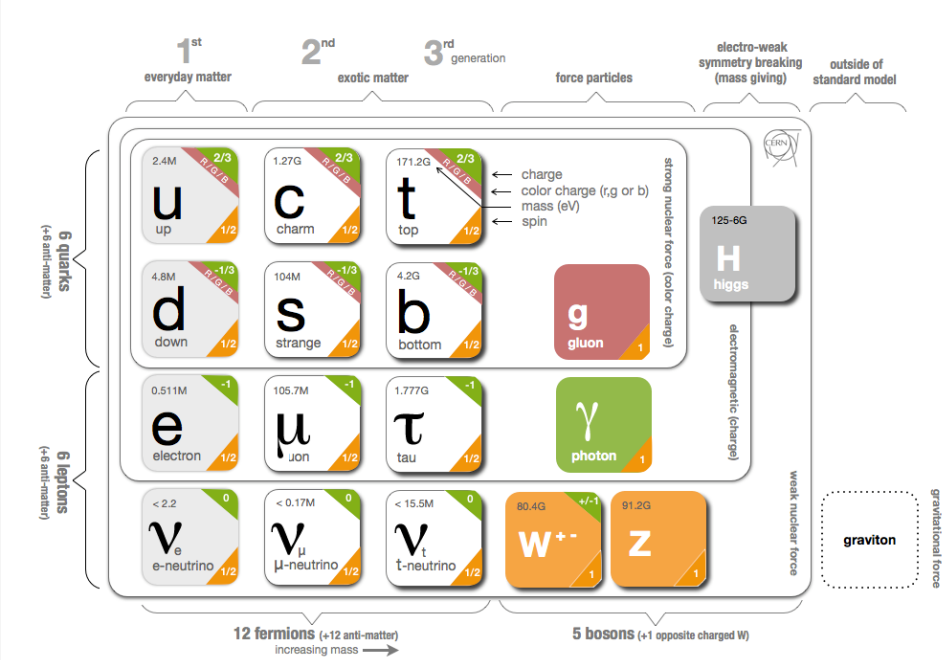

Figure 2.1: This Standard Model infographic lists the name and properties (mass, charge, spin) of all known particles in the SM, adapted from Ref. [9], using information from Ref. [7].

105.7 MeV and then m_τ of 1.777 GeV [7]. Neutrinos are assumed to be massless in the SM; however, the phenomenon of neutrino oscillations implies that neutrinos have tiny but non-zero masses. The current experimental upper limit set on the sum of neutrino masses is $0.06\,\text{eV} < \sum m_\nu < 0.152\,\text{eV}$ [7, 8]. On the other hand, there are six quarks which are divided into two groups: up-type (up u, charm c, top t) and down-type (down d, strange s, bottom b) quarks. The up-type (down-type) quarks possess an electric charge of $\frac{2}{3}|q_e|$ ($-\frac{1}{3}|q_e|$). Similarly to leptons, quarks also form a mass hierarchy in the three generations, (u, d), (c, s), (t, b), where top quarks have the heaviest mass of 173 GeV [7]. For each fermion, there exists an anti-fermion that has the exact same mass but oppositely-signed charge. Stable, ordinary matter on earth is essentially made of fermions from the first generation with u- and d-quarks in a nucleon surrounded by electrons in the electron shell.

While fermions make up the building blocks of nature, gauge bosons play a vital role in mediating the fermions' interaction. If there were no gauge boson to stick lepton and quarks together, there would be no atoms and consequently no stars and lives. Three fundamental forces, namely strong nuclear force, weak force and electromagnetic force, are described in the SM by the inclusion of four kinds of spin-1 gauge bosons: photon γ, gluon g, Z^0 boson and $W^\pm$ boson. Firstly, the photon is responsible for electromagnetism and is massless. All fermions except neutrinos carry

electric charge and hence take part in electromagnetism. Secondly, the gluon is the force carrier of the strong force. In strong interaction, color charge is used to describe a related property possessed only by quarks and gluons in analogous to electric charge in electromagnetism. It comes in three manifestations for quarks, red, blue and green, and the corresponding anti-colors for anti-quarks. However, unlike the slowly diminishing strength of electromagnetism over distance, strong force remains constant no matter how much further two quarks are apart. Due to this unique property of strong force, quarks have never been observed individually as a free particle. Instead, they are confined within white (or colorless) composite particles that are called hadrons; nevertheless top quarks have short lifetime and would decay before they can hadronize with other quarks. There exists two kinds of hadrons, mesons and baryons. Mesons are made of a quark–anti-quark pair with opposite color charge, while baryons are made of three quarks carrying a color combination of red, blue and green (or anti-red, anti-blue and anti-green for an anti-baryon). More descriptions of the strong interaction mechanism is described in Section 2.3. Lastly, the Z^0 boson and $W^{\pm}$ boson are the mediators of weak force, which is responsible for radioactive decays. All (left-handed) fermions carry the charge of weak interaction, known as weak isospin, and hence interact with Z boson and W boson. Weak interaction is the only interaction that allows the changing of quark flavor or the transformation between a charged lepton and a neutrino of the same flavor. It is short-ranged because the Z and W bosons are massive and short-lived, where their masses are found to be roughly 91 GeV and 80 GeV respectively [7]. In addition to the gauge bosons, there is one remaining particle in the SM table, the Brout-Englert-Higgs boson (or in short the Higgs boson). It is the only known spin-0 elementary particle, and is responsible for giving rise to the masses of all the aforementioned particles via spontaneous electroweak symmetry breaking (see Section 2.2).

The fundamental interactions between particles are mathematically formulated upon Quantum Field Theory (QFT), a framework that successfully reconciles quantum mechanics and special relativity. All the dynamics and kinematics of the elementary particles are specified in a single Lagrangian density formula. Particles are represented by quantum fields in certain gauge theories, where the Lagrangian density is invariant under local transformations from the corresponding symmetry groups. Thinking in terms of symmetries ease the construction of Lagrangian candidates as they strictly constrain the set of possible particles and interactions. This was first illustrated in the relativistic quantum mechanics of electrons, Quantum Electrodynamics (QED). In QED, the Lagrangian is:

$$\mathscr{L}_{\text{QED}} = \bar{\psi} i\gamma^{\mu}(\partial_{\mu} + ieQA_{\mu})\psi - m\bar{\psi}\psi - \frac{1}{4}F_{\mu\nu}F^{\mu\nu} \tag{2.1}$$

for a spinor field ψ with mass m, and a vector field A_{μ} representing a photon described by a field-strength tensor $F_{\mu\nu} = \partial_{\mu}A_{\nu} - \partial_{\nu}A_{\mu}$. The constant e in the Lagrangian denotes the coupling strength of the vector field to fermions, known as the fine structure constant $\alpha = e^2/4\pi \approx 1/137$. Consider a local U(1) phase transformation $\psi \to e^{iQw(x)}\psi$, it can be shown that the free-field Lagrangian

for a Dirac spinor of mass m is not invariant for a varying parameter $w(x)$. Particularly, an extra term $\bar{\psi} i\gamma^{\mu}(iQ\partial_{\mu}w)\psi$ appears. To keep the Lagrangian invariant under the local phase transformation, a vector field is necessary and has to undergo transformation:

$$\begin{cases} \psi \to e^{iQw(x)}\psi \\ A_{\mu} \to A_{\mu} - \frac{1}{e}\partial_{\mu}w \end{cases} . \tag{2.2}$$

This implies that $\partial_{\mu} + ieQA_{\mu} := D_{\mu} \to e^{iQw(x)}D_{\mu}$, where the differential operator D_{μ} is sometimes called a covariant derivative. The photon field-strength tensor and thus the vector kinetic term would remain unchanged. However, no mass term for the photon field may appear in the Lagrangian, as the theory would then no longer be gauge invariant. In brief, the QED Lagrangian in Eq. 2.1 is invariant under the combined transformations of Eq. 2.2 for any arbitrary function $w(x)$. In the language of group theory, the gauge symmetry of QED is under the $U(1)$ group. According to Noether's theorem, theories with gauge symmetries contain redundancy, i.e. some degrees of freedom are not physical. In the case of QED, the vector field A_{μ} has four independent components but there are only two independent physical transverse polarization states. One degree of freedom is already reduced due to the lack of $\partial_0 A_0$ term in the form of the photon kinetic term, meaning that A_0 is not dynamical, while another degree of freedom is effectively removed by the invariance under gauge transformations, resulting in only two polarization states.

By extending the Lagrangian construction principle to the other fundamental particles, the SM is formalized to an $SU(3)_C \times SU(2)_L \times U(1)_Y$ gauge group. $SU(3)_C$ is the gauge symmetry of the strong interaction, while $SU(2)_L \times U(1)_Y$ combine to describe the weak and electromagnetic forces. The $SU(3)$ group has eight generators, or equivalently, eight gluons in Quantum Chromodynamics (QCD). Gluons are massless as expected from local gauge invariance, similarly to photons in QED. The $SU(2) \times U(1)$ group has four generators, but the corresponding gauge bosons, except photon, are observed to be massive. The indication of broken gauge symmetry in nature leads to the need of an additional fundamental spin-0 boson. The theory was confirmed by the discovery of the Higgs boson by the ATLAS [5] and CMS [6] collaborations in 2012. The symmetry breaking mechanism will be discussed in more details in the following section.

2.2 Electroweak and Spontaneous Symmetry Breaking

The Glashow-Weinberg-Salam theory [1–3] is a unified theory of two of the four fundamental interactions: the electromagnetic and weak interactions. Although Yang–Mills developed the non-Abelian gauge theory that has become the cornerstone of QFT [10] in the 1950s, unifying the electromagnetic and weak charged interactions seemed implausible at the time due to the awfully different behaviors between them. One major problem is that electromagnetism is parity-conserving

but weak interactions were discovered to violate mirror symmetry at β decay experiments[1]. It was learned that charged current interactions couple only to left-handed fermions. Mathematically, this implies the left- and right-handed components of a fermion field

$$\psi_{L/R} = \frac{1 \mp \gamma^5}{2} \psi \tag{2.3}$$

transform differently under the $SU(2)_L$ symmetry group, with the former (latter) one being a doublet (singlet). The interaction term of the weak interaction takes the form of $\gamma^\mu(1-\gamma^5)$, meaning that the weak charged force couples only to the left-handed component. This is understood as the vector minus axial vector $(V-A)$ coupling structure of weak interaction [13, 14]. In the electroweak theory, this problem was solved by proposing an extended model of a larger symmetry group $SU(2)_L \times U(1)_Y$ [1–3] when the gauge boson Z^0 was not known until weak neutral current was discovered in the Gargamelle experiment [15]. The $SU(2)_L \times U(1)_Y$ group is generated by the isospin operators $I_1,\ I_2,\ I_3$ and the hypercharge Y. The hypercharge and the third component of weak isospin are related to the electric charge by the Gell-Mann–Nishijima formula [16, 17]:

$$Q = I_3 + \frac{1}{2}Y. \tag{2.4}$$

To preserve the local gauge invariance, a triplet of vector fields W_μ^j (where $j = 1,2,3$) associated to the isospins and an isosinglet field B_μ associated to the hypercharge are introduced. The covariant derivatives for the left- and right-handed fermions now reads

$$\begin{aligned} D_\mu^L &= \partial_\mu + ig\frac{\sigma_j}{2}W_\mu^j + ig'\frac{Y_L}{2}B_\mu \\ D_\mu^R &= \partial_\mu + ig'\frac{Y_R}{2}B_\mu \end{aligned}, \tag{2.5}$$

where g and g' denote the coupling constant for $SU(2)_L$ and $U(1)_Y$ respectively, and σ_j the Pauli matrices. For the isotriplet W_μ^j, the field strength tensors are expressed as:

$$W_{\mu\nu}^a = \partial_\mu W_\nu^a - \partial_\nu W_\mu^a + g f_{abc} W_\mu^b W_\nu^c, \tag{2.6}$$

[1] In 1957, the Wu experiment found that the number of electrons emitted from a Cobalt^{60} nuclei opposite to the nuclear spin was more than that along the spin [11]. Two years later, Goldhaber, Grodzins and Sunyar found that neutrinos emitted in β decay were all polarized in the opposite direction to their momentum [12].

where f is the totally anti-symmetric structure constant that defines the commutation relation of the $SU(2)_L$ generators $[\frac{\sigma^a}{2}, \frac{\sigma^b}{2}] = if^{abc}\frac{\sigma^c}{2}$. Hence, the electroweak kinematics Lagrangian becomes:

$$\begin{aligned}\mathscr{L}_{\text{EW}} = &\sum_L \bar{\psi}_L \gamma^\mu (\partial_\mu + ig\frac{\sigma_j}{2}W_\mu^j + ig'\frac{Y_L}{2}B_\mu)\psi_L + \sum_R \bar{\psi}_R \gamma^\mu (\partial_\mu + ig'\frac{Y_R}{2}B_\mu)\psi_R \\ &- \frac{1}{4}B_{\mu\nu}B^{\mu\nu} - \frac{1}{4}W_{\mu\nu}^j W_j^{\mu\nu}.\end{aligned} \tag{2.7}$$

Although the electroweak theory cleared the hurdle of parity violation and succeeded in predicting the existence of Z boson, it was not able to break the curse of local gauge symmetry that forbids mass terms for gauge bosons; meanwhile, the short-rangeness of the weak interaction suggests massive intermediate vector bosons. Furthermore, fermions are forced to be massless as well. This can be realized by trying to add a mass term $m\bar{\psi}\psi$ for the fermions. When rewritten using helicity projections, $m\bar{\psi}_R\psi_L$ and $m\bar{\psi}_L\psi_R$ terms remain. Since the left- and right-handed fermions transform differently under $SU(2)_L \times U(1)_Y$, the Lagrangian would not be invariant unless fermions are massless. The problem of forbidden gauge boson and fermion mass terms was later solved by incorporating the Brout-Englert-Higgs mechanism (proposed in 1964) into the electroweak theory [18–21]. The mechanism relies on the concept of spontaneous symmetry breaking which occurs when the vacuum state of a field does not respect the symmetry of the underlying action of the system, thus giving rise to symmetry breaking terms. The Higgs field is introduced into the SM to play such a role. It is an isospin doublet, with weak isospin of $\frac{1}{2}$, formed by two complex scalar fields,

$$\Phi = \begin{pmatrix} \phi_1 + i\phi_2 \\ \phi_3 + i\phi_4 \end{pmatrix}. \tag{2.8}$$

The Lagrangian regarding the Higgs field is defined as:

$$\mathscr{L}_{\text{Higgs}} = (D_\mu \Phi)^\dagger (D^\mu \Phi) - V(\Phi) \tag{2.9}$$

with potential

$$V(\Phi) = \mu^2 \Phi^\dagger \Phi + \lambda(\Phi^\dagger \Phi)^2, \tag{2.10}$$

where λ is assumed to be positive to ensure vacuum stability. The vacuum state could behave differently in two situations depending on the sign of μ^2. When $\mu^2 \geq 0$, the potential has a single minimum at $\Phi = 0$. Otherwise, it has a circular valley of degenerate minima at a radius of $|\Phi|^2 = v^2/2$, where $v = \sqrt{-\mu^2/\lambda}$ is called the vacuum expectation value (VEV). At the beginning of the Universe, as the Universe expanded and cooled down, the Higgs field underwent a phase transition from a minimum of 0 to the VEV. The electroweak symmetry is said to be broken spontaneously when $\mu^2 < 0$. The Higgs field perturbing around the VEV could be re-parameterized in the form of:

$$\Phi(x) = \frac{1}{\sqrt{2}} \exp\left(i\frac{\zeta_j(x)\sigma^j}{2v}\right) \begin{pmatrix} 0 \\ v+h(x) \end{pmatrix}, \tag{2.11}$$

where σ_j are the Pauli matrices, and $\zeta_j(x)$ and $h(x)$ are four real scalar fields. According to the Goldstone theorem, these $\zeta_j(x)$ fields are the massless Nambu-Goldstone bosons that appear when the vacuum breaks $SU(2)_L$. Since field configurations related by gauge transformations are physically equivalent, the choice of gauge should not affect the predictions of physical observables. Thus, one could choose the unitary gauge in which the Higgs field becomes

$$\Phi(x) = \frac{1}{\sqrt{2}} \begin{pmatrix} 0 \\ v+h(x) \end{pmatrix}, \tag{2.12}$$

where the degrees of freedom along the circle of minima is removed, or in other words, the Nambu-Goldstone bosons are removed by setting $\zeta_j(x) = 0$.

The Higgs potential now takes the form:

$$V(\Phi) = \lambda \frac{1}{2} m_H^2 h^2 + \frac{m_H^2}{2v} h^3 + \frac{m_H^2}{8v^2} h^4 - \frac{\lambda v^4}{4}, \tag{2.13}$$

where $m_H = v\sqrt{2\lambda}$ is the mass of the excitation field $h(x)$, known as the Higgs boson H. The second and third term describe the structure of the self-interaction of the Higgs boson.

To keep the vacuum invariant under $U(1)_{em}$, the Higgs field should have no electric charge. According to Eq. 2.4, the hypercharge Y_H should be set to 1. As a consequence, the $(D_\mu\Phi)^\dagger(D^\mu\Phi)$ term yields:

$$(D_\mu\Phi)^\dagger(D^\mu\Phi) = \frac{1}{2}\partial_\mu h \partial^\mu h + \frac{1}{8}g^2(v+h)^2|W_\mu^1 + iW_\mu^2|^2 + \frac{1}{8}(v+h)^2|gW_\mu^3 - g'B_\mu|^2. \tag{2.14}$$

By diagonalizing the mass basis of W_μ^j and B_μ, a new orthonormal basis becomes:

$$\begin{aligned} W_\mu^\pm &= \frac{1}{\sqrt{2}}(W_\mu^1 \mp iW_\mu^2) \\ Z_\mu &= \frac{1}{\sqrt{g^2+g'^2}}(gW_\mu^3 - g'B_\mu) \\ A_\mu &= \frac{1}{\sqrt{g^2+g'^2}}(g'W_\mu^3 + gB_\mu), \end{aligned} \tag{2.15}$$

and now the four mass terms for $W^\pm$, Z^0 and γ can be seen by changing Eq. 2.14 into the new basis:

$$
\begin{aligned}
(D_\mu\Phi)^\dagger(D^\mu\Phi) =& \frac{1}{2}\partial_\mu h\partial^\mu h + \frac{1}{2}m_{W^\pm}^2(|W_\mu^+|^2+|W_\mu^-|^2) + \frac{1}{2}m_Z^2|Z_\mu|^2 + 0|A_\mu|^2 \\
&+ \sum_{V=W^+,W^-,Z}\left(\frac{m_V^2}{v}|V_\mu|^2 h + \frac{m_V^2}{2v^2}|V_\mu|^2 h^2\right)
\end{aligned}
\tag{2.16}
$$

with

$$
\begin{aligned}
m_{W^\pm} &= \frac{vg}{2} \\
m_Z &= \frac{v\sqrt{g^2+g'^2}}{2},
\end{aligned}
\tag{2.17}
$$

where the masses of $W^\pm$ and Z bosons are proportional to the electroweak gauge coupling while the photon is massless. The last term in Eq. 2.16 describes the interactions of gauge bosons with the Higgs boson. The Weinberg angle θ_W, or weak mixing angle, can be expressed in terms of the $W^\pm$ and Z boson masses:

$$
\frac{m_{W^\pm}}{m_Z} = \frac{g}{\sqrt{g^2+g'^2}} = \cos\theta_W. \tag{2.18}
$$

The above process of three would-be Nambu-Goldstone bosons providing each vector gauge field a longitudinal polarization and hence allowing the fields to become massive is essentially the Higgs Mechanism.

Moreover, the introduction of the Higgs field fixes the problem of forbidden fermion masses. Fermions could acquire mass by interacting with the Higgs field in the VEV, as constructed in the Yukawa Lagrangian:

$$
\begin{aligned}
\mathscr{L}_{\text{Yukawa}} =& -y_d^{ij}\bar{Q}_{iL}\Phi d_{jR} - y_u^{ij}\bar{Q}_{iL}\Phi^c u_{jR} - y_l^{ij}\bar{L}_{iL}\Phi e_{jR} + (h.c.) \\
\overset{\Phi\to\text{VEV}}{=}& -y_d^{ij}\frac{v+h}{\sqrt{2}}\bar{d}_{iL}d_{jR} - y_u^{ij}\frac{v+h}{\sqrt{2}}\bar{u}_{iL}u_{jR} - y_l^{ij}\frac{v+h}{\sqrt{2}}\bar{e}_{iL}e_{jR} + (h.c.),
\end{aligned}
\tag{2.19}
$$

where $\Phi^c = i\sigma_2\Phi^*$, and Q_L (u_R, d_R) and L_L (e_R) are the quark and lepton left-handed doublets (right-handed singlets). The terms involving v and h are, respectively, the mass terms of fermions and the Higgs-coupling terms to fermions. In general the Yukawa interaction matrices could be non-diagonal, but they could always be bi-diagonalized using a pair of unitary matrices $V_f^{L,R}$ such that:

$$
\begin{aligned}
V_d^{L\dagger}y_d V_d^R &= \frac{\sqrt{2}}{v}\text{diag}(m_d, m_s, m_b) \\
V_u^{L\dagger}y_u V_u^R &= \frac{\sqrt{2}}{v}\text{diag}(m_u, m_c, m_t) \\
V_e^{L\dagger}y_e V_e^R &= \frac{\sqrt{2}}{v}\text{diag}(m_e, m_\mu, m_\tau)
\end{aligned}
\tag{2.20}
$$

Consider the interaction of fermions to massive $W^{\pm}$ bosons in the mass eigenbasis, the relevant terms could be rewritten as:

$$\begin{aligned}\mathscr{L}_{\mathrm{EW}} \supset & \frac{g}{\sqrt{2}}\bar{u}_L\gamma^\mu W_\mu^+ d_L + \frac{g}{\sqrt{2}}\bar{\nu}_L\gamma^\mu W_\mu^+ e_L + (h.c.) \\ = & \frac{g}{\sqrt{2}}\bar{u}'_L(V_u^{L\dagger}V_d^L)\gamma^\mu W_\mu^+ d'_L + \frac{g}{\sqrt{2}}\bar{\nu}'_L(V_\nu^{L\dagger}V_e^L)\gamma^\mu W_\mu^+ e'_L + (h.c.).\end{aligned} \tag{2.21}$$

The $V_u^{L\dagger}V_d^L$ term is defined as the Cabibbo–Kobayashi–Maskawa (CKM) matrix [22, 23], which can be parameterized by three mixing angles θ_{ij} and the Charge-Parity (CP)-violating KM phase δ [23]:

$$\begin{aligned}V_{\mathrm{CKM}} \equiv & V_u^{L\dagger}V_d^L \\ = & \begin{pmatrix} V_{ud} & V_{us} & V_{ub} \\ V_{cd} & V_{cs} & V_{cb} \\ V_{td} & V_{ts} & V_{tb} \end{pmatrix} \\ = & \begin{pmatrix} c_{12}c_{13} & s_{12}c_{13} & s_{13}e^{-i\delta} \\ -s_{12}c_{23} - c_{12}s_{23}s_{13}e^{i\delta} & c_{12}c_{23} - s_{12}s_{23}s_{13}e^{i\delta} & s_{23}c_{13} \\ s_{12}s_{23} - c_{12}c_{23}s_{13}e^{i\delta} & c_{12}s_{23} - s_{12}c_{23}s_{13}e^{i\delta} & c_{23}c_{13} \end{pmatrix} \\ |V_{\mathrm{CKM}}| \simeq & \begin{pmatrix} 0.974 & 0.225 & 0.004 \\ 0.224 & 0.974 & 0.042 \\ 0.009 & 0.041 & 0.999 \end{pmatrix},\end{aligned} \tag{2.22}$$

where $s_{ij} = \sin\theta_{ij}$ and $c_{ij} = \cos\theta_{ij}$. The values of the entries in the CKM matrix are constrained by numerous experiments that study the very rich content of flavor physics with precise measurements. Since quark mixing has been observed, the electroweak eigenstates of quarks are not truly the physical mass eigenstates.

2.3 Quantum Chromodynamics

Quantum Chromodynamics (QCD) is a non-Abelian gauge theory that describes the strong interaction of quarks and gluons. The Lagrangian of QCD takes the form

$$\mathscr{L}_{\mathrm{QCD}} = \sum_q \bar{q} i\gamma^\mu D_\mu q - \frac{1}{4}G^a_{\mu\nu}G_a^{\mu\nu}, \tag{2.23}$$

where the covariant derivative reads

$$D_\mu = \partial_\mu + ig_s\frac{t_a}{2}G^a_\mu. \tag{2.24}$$

The whole hadron spectrum that we observe today can be classified according to the $SU(3)_C$ symmetry, assuming that the wide variety of hadrons is constructed from fundamental constituents as quarks. The introduction of the color charge provides an explanation to the existence of some hadrons. If the color hypothesis is not put forward in a quark model, then for instance, the Δ^{++} baryon that is composed of three up quarks with their spin aligned would not be possible according to the Pauli principle. The hypothesis naturally explains the existence of mesons and baryons as color singlets. Color charge was shown to be three-valued based on the determined R_{had}-ratio

$$R_{\text{had}} = \frac{\sigma(e^+e^- \to \text{hadrons})}{\sigma(e^+e^- \to \mu^+\mu^-)} = N_{\text{color}} \sum_f q_f^2 \tag{2.25}$$

in electron–positron annihilation experiments. The first direct proof of the existence of gluon was also provided using electron–positron collisions by detecting three-jet events, in which one of the jets is generated by hard gluon radiation. To confirm the existence of quarks, the internal quark structure of hadrons is studied by performing deep inelastic scattering experiments. For example, a proton is found to be composed of two u quarks and one d quark, which define the macroscopic quantum number of a proton. These point-like constitutes of a hadron are known as valence quarks. The valence quarks are bound together by the exchange of gluons, while the gluons could split into gluons or form a sea of quarks by fluctuating into pairs of quark and anti-quark. Valence quarks, sea quarks and gluons are understood as the parton content of a hadron. Another realization from deep inelastic scattering experiments is that the strength of strong force decreases as the energy scale increases, and thus quarks are quasi-free at high energies. Such phenomenon is called asymptotic freedom. It is a consequence of the anti-screening effect from gluon self-interaction overcompensating the color charge screening of quarks. On the other side of the coin, QCD coupling strength grows with distances, resulting in confinement of quarks in the form of colorless bound states. The running coupling constant of QCD, α_S, is measured as a function of momentum transfer scale Q^2, as shown in Figure 2.2.

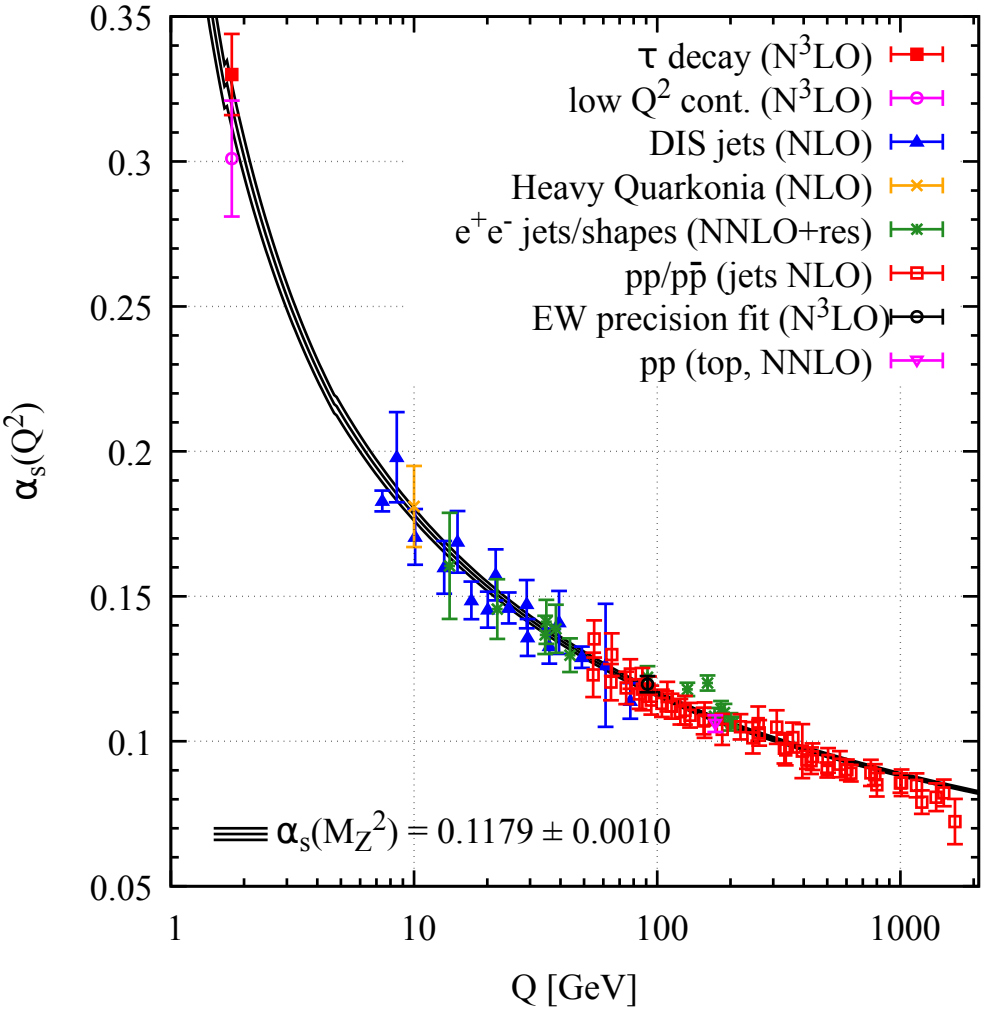

Figure 2.2: Historical measurements of α_S as a function of Q, from a variety of different experiments and physical processes. [7]

Chapter 3

Success and Limitations of SM

The success of the SM is built from the contributions of a very large number of physicists and engineers over decades. It involves the interplay between experiment and theory, where experimental discoveries are explained conjointly by a coherent theoretical model, and then the model is put into test and serves as an exploration guide to experiments. The SM has been probed extensively in numerous precision measurements, and yet no significant deviation from the SM has been found. For instance, the emission of a Higgs boson by a top–anti-top quark pair was observed for the first time at the LHC in 2018 [24, 25], leading to a direct measurement of the top–Higgs coupling that once again verifies the validity of the SM. Figure 3.1 shows the total and fiducial cross section measurements for a range of representative SM production at $\sqrt{s} = 7$, 8, and 13 TeV performed with the ATLAS detector. Despite that the SM is working so well, there are phenomenological problems that cannot be explained within the SM and likely require the introduction of new physics beyond the Standard Model (BSM). In this chapter, main motivators for BSM physics are outlined in several aspects.

3.1 Quantum Gravity

One obvious shortcoming of the SM is that it does not include the gravitational force, but only the other three fundamental forces. Due to the weakness of gravity[1], gravitational effects never contribute significantly in particle physics experiments. Although one could consider quantum disturbances around a fixed background metric, and obtain a QFT for a spin-2 particle-like excitation field that corresponds to a graviton, such a theory is non-renormalizable and it could only be trusted as an effective field theory at energy scale $E \ll M_{\mathrm{Pl}}$. There are ongoing efforts to come up with a quantum theory of gravity that could describe the microscopic structure of spacetime near the Planck

[1]The size of gravitational constant $G_N \sim \mathcal{O}(10^{-39}\ \mathrm{GeV}^{-2})$ is negligible, compared with the Fermi constant $G_F \sim \mathcal{O}(10^{-5}\ \mathrm{GeV}^{-2})$, the fine-structure constant $\alpha \sim \mathcal{O}(10^{-2})$ and the strong coupling constant $\alpha_{\mathrm{S}} \sim \mathcal{O}(1)$ at low energies.

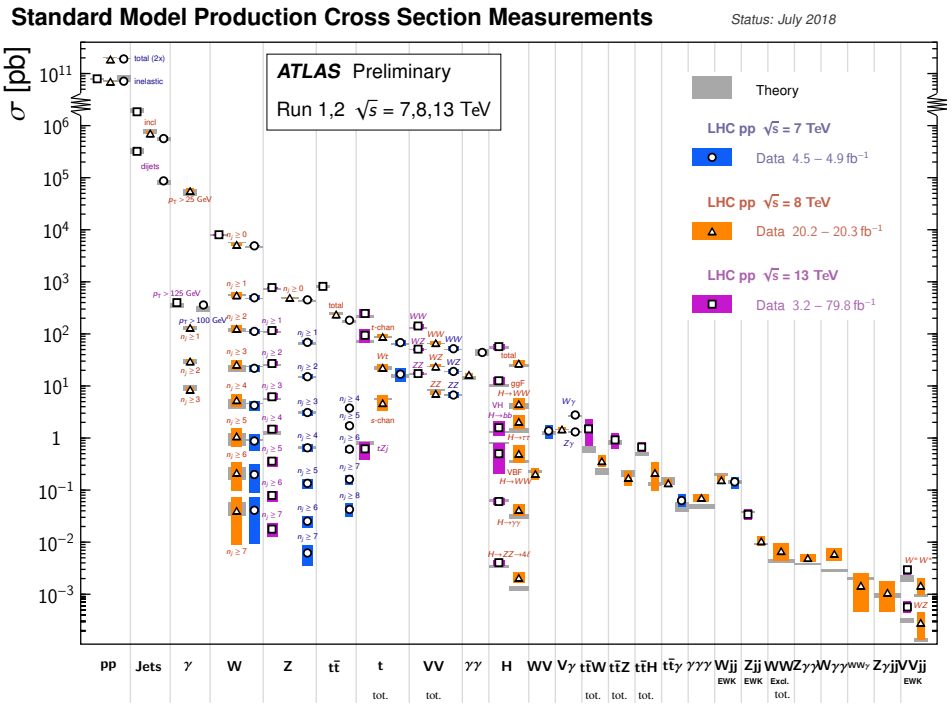

Figure 3.1: Summary of representative total and fiducial production cross section measurements, compared with the corresponding theory expectations at $\sqrt{s} = 7$, 8, and 13 TeV. [26]

scale. Popular proposals could be grouped into two classes of theories: a perturbative approach that requires reference to a fixed background metric, like superstring theory [27], and a non-perturbative one that is background independent, lke loop quantum gravity [28, 29]. In either case, a successful theory should reduce to a low-energy effective field theory with leading terms in the action matching up with those in the classical limit.

3.2 Cosmology

Modern cosmology aims to understand the origin and structure of the Universe. The most popular idea in the community is the Λ-CDM theoretical framework which successfully explains, with an expanding hot-Big-Bang model, the formation and evolution of the large scale structure in the Universe [30]. From the cosmological observables there arise three main puzzles that suggest new physics beyond the SM: the uniformity of the Universe, the existence of dark matter and dark energy, and the dominance of matter over anti-matter.

The Universe was found to be extremely uniform over very large distances based on the measurement of cosmic microwave background (CMB) radiation. The CMB is a residual photon background leftover from an early stage of the Universe, which was found to have a mean temperature T

of about 2.73 K with anisotropies of the order of $\Delta T/T \sim 10^{-5}$ [31]. In the beginning of the Universe, the subatomic particles (mostly protons, electrons and photons) were in thermal equilibrium. As the Universe expanded and cooled down to a temperature below the ionization energy of ground-state hydrogen ($T \lesssim 13.6$ eV), the charged particles combined to form the first neutral atoms. This process is known as recombination. As the Universe continued to expand and the Compton scattering started to become ineffective, photons decoupled from the matter and propagated freely, becoming what we see today as the CMB. However, by back tracking in time, many different regions of the CMB were casually disconnected. It would have been a miracle that those regions have the same temperature by coincidence. Hence, the idea of inflation was introduced to suggest that there was a period of exponential expansion of the spacetime, allowing a small casually connected region to expand drastically to cover the entire sky today. The inflation mechanism could be realized in QFT and string theory [32], explaining how microscopic quantum fluctuations could transform into the seeds of the inhomogeneous structure observed in the Universe today. The simplest example of models introduces a scalar field as the inflaton field that is slowly rolling down its nearly-flat potential, which gives its name slow-roll inflation [33].

In cosmology, CMB is also a powerful tool to determine what the Universe is made of. By measuring the temperature fluctuation of CMB with a series of experiments, including the Cosmic Background Explorer, the Wilkinson Microwave Anisotropy Probe, and the Planck satellite [34–36], it was realized that SM matter only contributes to a small fraction of the total matter in the Universe, and the vast majority is made of what is called dark matter. The presence of dark matter is also observed via gravitational lensing effects and unexpectedly flat galactic rotation curves. Furthermore, the Universe today is found to be mostly made of an unknown form of energy, which is responsible for the accelerating expansion of the Universe. According to the most recent measurement results from Planck, the Universe is made of 68.3% dark energy, 26.8% dark matter and 4.9% baryonic SM matter [37]. Clearly, the SM cannot be the complete theory that describes our Universe. To satisfy the cosmological observation of dark matter, the minimal extension to the SM includes an introduction of a new massive stable particle as the dark matter candidate. It must be weakly interacting but carries no electric nor color charge. It is also not hot because it would otherwise be excluded by the large-scale structure formation. Many BSM theories are proposed to incorporate a weakly-interacting massive particle (WIMP) as a dark matter candidate, while different search methods are underway to cover a wide range of possible dark matter masses. Search methods include direct detection with deep underground dark matter detectors, indirect detection by identifying excesses in fluxes of cosmic rays, and search for dark matter production in high-energy colliders. Unfortunately, no experiment has discovered any dark matter candidate yet.

The last puzzling cosmological observation is the baryon asymmetry observed in the Universe today. The difference between the amount of matter and anti-matter is expressed in terms of baryon–to–photon number density ratio $\eta \equiv \frac{n_B - n_{\bar{B}}}{n_\gamma}\big|_{\text{today}} = (6.13 \pm 0.04) \times 10^{-10}$. As one would typically

assume that equal amount of matter and anti-matter was produced in the Big Bang, some post-inflationary mechanism must be at work in the early Universe to create such asymmetry [38]. The broken baryon symmetry implies that there must be CP violation, in addition to departure from thermal equilibrium and baryon number violation [39]; the complex phase in the CKM matrix, however, is the only source of CP violation within the SM and its value has been stringently bounded by neutron electric dipole moment measurements [40]. The allowed complex phase ($|\Theta_3| \lesssim 10^{-10}$) is too small to explain the observed baryon asymmetry [7], indicating the need of BSM physics to provide viable mechanism.

3.3 Neutrino Masses and Oscillation

In the SM, neutrinos are massless and their flavor is conserved, unlike the quarks mixing in the CKM matrix. However, neutrinos are observed to transform from one type to another over long distances. This phenomenon is called neutrino oscillation [41]. It implies that neutrinos have non-degenerate mass eigenstates. When the mass eigenstates of an initial flavor state travel over a distance with different phases, it results in a change of flavor in the final state. One popular SM extension is to add three gauge singlets $N_R = (1,1,0)$ as the right-handed neutrinos, via the Lagrangian

$$\mathscr{L}_{\rm N} = -y_N^{ij}\bar{L}_{iL}\widetilde{\Phi}N_{jR} - \frac{1}{2}m_N^{ij}N_{iR}^T C N_{jR} + (h.c.), \tag{3.1}$$

where y_N is the Yukawa coupling constant, L_L is the SM lepton left-handed doublet, $\widetilde{\Phi} = i\sigma_2\Phi^*$ is the Higgs field, C is the charge conjugation matrix and m_N is the mass of the right-handed neutrino. After electroweak symmetry breaking, the mass matrix for the left-handed and right-hand neutrinos takes the form of

$$M_N = \begin{pmatrix} 0 & \frac{1}{\sqrt{2}}y_N v \\ \frac{1}{\sqrt{2}}y_N v & m_N \end{pmatrix}. \tag{3.2}$$

In the limit of $m_N \gg y_N v$, the neutrino mass eigenvalues become m_N and $(y_N v)^2/2m_N$, where the three light ones[2] are identified as the SM neutrinos, and the heavy Majorana ones as dark matter candidates. The inverse relationship between the SM and Majorana neutrinos gives the theory its name Seesaw (Type-I) model [42–46].

3.4 Hierarchy Problem and Naturalness

The huge difference between the electroweak scale ($\sim 10^2$ GeV) and the Planck scale ($\sim 10^{19}$ GeV) brings about a very large fine tuning of the SM, which is thought to be unnatural and is commonly referred to as the hierarchy problem. The problem starts from the Higgs mass not being protected by any symmetry from divergent corrections, unlike the fermions and gauge bosons being protected

[2]The negative mass value of the SM neutrino ν_{SM} is made positive by taking the chirality, i.e. redefining ν_{SM} as $\gamma_5\nu_{SM}$

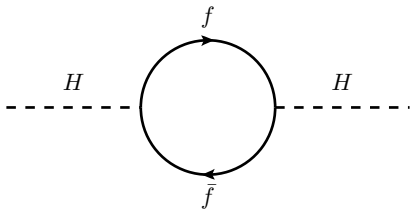

Figure 3.2: Feynman diagram of fermionic radiative loop correction to the scalar Higgs mass at one-loop level.

by chiral symmetry and gauge symmetry respectively. A radiative correction is applied to the Higgs mass due to the coupling of Higgs with all massive particles. The Higgs mass squared is expressed as:

$$m_H^2(\Lambda) = m_H^2 + \Delta m_H^2, \tag{3.3}$$

where $m_H^2 = 2v^2\lambda$ corresponds to the bare Higgs mass and Δm_H^2 indicates the radiative correction. For instance, the one-loop correction from fermion, with Feynman diagram as shown in Figure 3.2, is given by:

$$\Delta m_H^2 = -\frac{y_f^2}{16\pi^2}\left[2\Lambda^2 + \mathcal{O}\left(m_f^2 \ln(\frac{\Lambda}{m_f})\right)\right], \tag{3.4}$$

where Λ is the energy cutoff scale. If Λ is at the order of Planck scale, then some high fine-tuning would be required to accommodate the observed Higgs mass of 125 GeV. This suggests the need of new physics to introduce particles that would naturally cancel the quantum corrections. In the SM, the dominant contributions to the quantum corrections are brought by top quark, W/Z bosons and Higgs boson. If the fine-tuning is required to be at the order of a few percent, then the cutoff energy would be expected to be at $\Lambda \sim 10$ TeV. Hence, it is motivated to search for new particles at this scale, which is possibly within the reach of the LHC.

3.5 Tension in Flavor Anomalies and Muon Anomalous Magnetic Moment

Apart from the above phenomenological problems that highlight the incompleteness of the SM, precision measurements are performed to probe the SM directly and persistently. If experimental results are deviating from SM predictions, it would shed some light on where new physics lies. A recent example that has caught a huge attention is the B meson decay measurements, which shows some deviations but not statistically significant enough to declare the discovery of new physics.

One group of discrepancy is the R_K and R_{K^*} anomalies, where the observables $R_{K^{(*)}}$ is defined as:

$$R_{K^{(*)}} \equiv \frac{\Gamma(B \to K^{(*)}\mu^+\mu^-)}{\Gamma(B \to K^{(*)}e^+e^-)}, \tag{3.5}$$

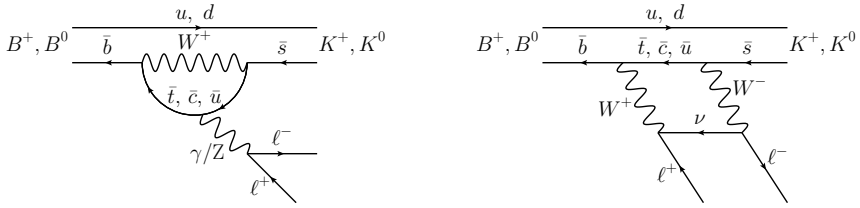

Figure 3.3: Feynman diagram of Flavour Changing Neutral Current $b \to s\ell^+\ell^-$ decays at one-loop level in the SM.

The Feynman diagram for the measured flavor-changing neutral current (FCNC) process with $b \to s$ transition is shown in Figure 3.3. In the SM, these FCNC processes of B-meson decay are induced only at loop level and strongly suppressed by the Glashow-Iliopoulos-Maiani (GIM) mechanism [47]. The rareness of their occurrence makes them an excellent probe for new physics searches. To be clean from theoretical limitations, the ratio measurement of the branching fractions for $B \to K^{(*)}\mu^+\mu^-$ and $B \to K^{(*)}e^+e^-$ decays is commonly taken to cancel out the CKM-matrix dependence and most of the hadronic uncertainties. In addition, it is essential to understand the experimental uncertainties emerging from the differences between the electron and muon reconstructions, due to trigger response and bremsstrahlung radiation. As an auxiliary measurement, the ratio of the branching fractions for $B \to K^{(*)}J/\Psi(\to \mu^+\mu^-)$ and $B \to K^{(*)}J/\Psi(\to e^+e^-)$ resonant decays is typically employed to reduce the systematic uncertainties related to the differences in electron and muon reconstructions.

While $R_{K^{(*)}}$ is expected to be around one due to lepton flavor universality (LFU), an evidence for the breaking of the universality with a significance of 3.1σ has been announced by the LHCb experiment [48], in addition to a persisting deviation of $2.1-2.6\sigma$ observed in previous measurements at the LHCb and Belle experiments [49–51]. Moreover, a 3.3σ deviation is observed in an angular analysis of the $b \to s\mu\mu$ process with the LHCb experiment [52]. A global combination shows that the best fit for the single-coefficient scenario $C_9^{bs\mu\mu} \simeq -C_{10}^{bs\mu\mu}$ against the SM has a pull of 6.5σ, where $C_9^{bs\mu\mu}$ and $C_{10}^{bs\mu\mu}$ are the Wilson coefficients associated with the effective semi-leptonic dimension-six operators[3] describing $b \to s\mu\mu$ transitions [53].

Another discrepancy is measured in a flavor-changing charged current (FCCC) process that involves $b \to c$ transition. The anomalies are observed in $R_{D^{(*)}}$ measurements, which is defined in Eq. 3.6.

$$R_{D^{(*)}} \equiv \frac{\Gamma(\bar{B} \to D^{(*)}\tau^-\bar{\nu})}{\Gamma(\bar{B} \to D^{(*)}\ell^-\bar{\nu})}, \quad \text{for } \ell = \mu, e. \tag{3.6}$$

The relevant Feynman diagram is shown in Figure 3.4. After combining the most recent measurements taken by the Belle experiment [54] with the other previous experimental results from the

[3] $\mathcal{O}_{9,V} = (\bar{s}_L\gamma^\mu b_L)(\bar{\ell}\gamma_\mu\ell)$ and $\mathcal{O}_{10,A} = (\bar{s}_L\gamma^\mu b_L)(\bar{\ell}\gamma_\mu\gamma_5\ell)$

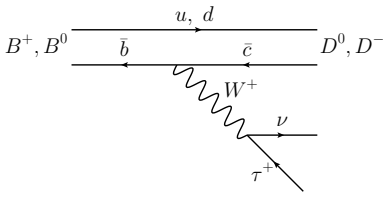

Figure 3.4: Feynman diagram of Flavour Changing Charged Current $b \to c\tau^-\nu$ decays at tree level in the SM.

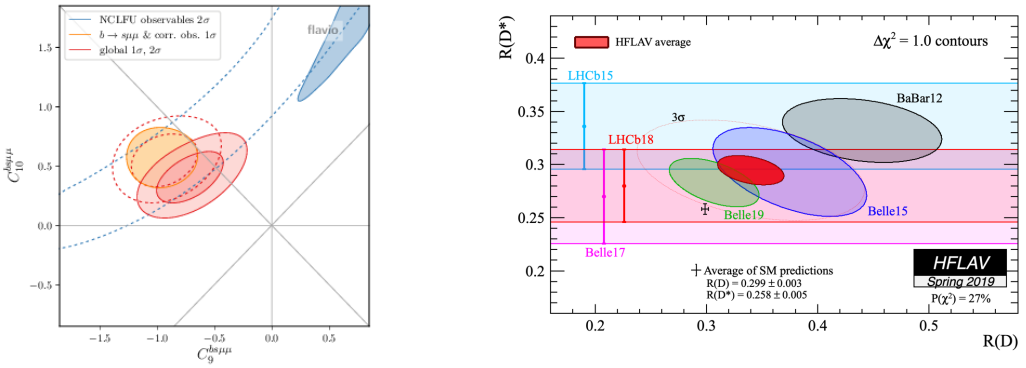

Figure 3.5: Left panel shows the confidence regions from a global combined fit of $b \to s\ell\ell$ measurements in the $\left(C_9^{bs\mu\mu}, C_{10}^{bs\mu\mu}\right)$ plane [53]. Right panel shows the averages of the $R_{D^{(*)}}$ ratios as computed in Spring 2019 by the Heavy Flavor Averaging Group [60].

BaBar, Belle and LHCb experiments [55–59], the present world average in the R_D–R_{D^*} phase space is about 3.1σ from the SM prediction [60], as shown in Figure 3.5.

At the same time, there is a long-standing deviation from the SM in the measurement of muon anomalous magnetic moment by the E821 experiment at Brookhaven National Laboratory [61], followed by a confirmation by the Fermilab Muon g-2 experiment [62]. A muon with spin $\overrightarrow{S}$ has a magnetic moment of

$$\overrightarrow{M} = g_\mu \frac{q_e}{2m_\mu} \overrightarrow{S}; \quad g_\mu \equiv 2(1+a_\mu) \tag{3.7}$$

The g-factor g_μ is exactly equal to two at tree level, but taking into account quantum loop effects would lead to a small nonzero offset a_μ, called the anomalous magnetic moment of muon. The Feynman diagrams of the representative SM contributions for the lowest loop order are shown in Figure 3.6. With the latest improvement on the calculation of the hadronic contributions, the discrepancy between the Brookhaven result and the theoretical expectation is found to be 3.7σ greater than the SM prediction [63]. In addition, the Fermilab Muon g-2 experiment has recently announced its first results following up the muon anomalous magnetic moment. A consistent deviation of 3.3σ is observed, leading to a 4.2σ tension after combining with the previous Brookhaven results [62].

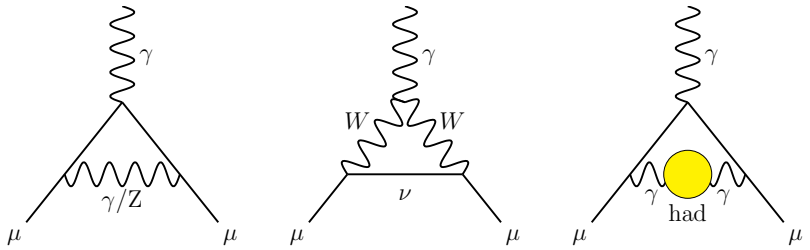

Figure 3.6: Feynman diagrams of the representative SM contributions to a_μ at the lowest loop order: first order QED (left), lowest-order weak (middle), lowest-order hadronic (right).

Because of the anomalies mentioned above, BSM models involving leptoquark have gained a lot of interest for its promising ability to solve the variety of discrepancies. This provides a motivation for the leptoquark searches performed, as part of the dissertation, in Chapter 12. A summary of Leptoquark models is described in Section 4.2 of the following chapter.

Chapter 4

Beyond Standard Model

The SM, as explained in the previous chapter, leaves several fundamental questions unanswered, but theorists have proposed many extensions of the SM that might bring us to a more complete and unified theory. This chapter aims at introducing a handful of them to motivate the searches presented in this dissertation. In Section 4.1, several BSM scenarios are particularly reviewed because of their naturalness that resolves the hierarchy problem. These BSM theories typically predict new heavy particle at the TeV scale with short lifetime, that results in a resonant structure in the invariant mass spectrum as reconstructed from the decay particles, like the $Z\gamma$ / $W\gamma$ / $H\gamma$ resonances sought in Chapter 11. The other hypothetical particle, leptoquark, that is targeted in the second search analysis (Chapter 12) naturally emerges in the context of many Grand Unified Theory (GUT) models, where the strong, weak and electromagnetic forces are unified. The existence of leptoquarks could provide an explanation to observed deviation from the SM in b-physics and muon anomalous magnetic moment measurements, as discussed in the previous chapter. Possible leptoquark (LQ) candidates are discussed in Section 4.2.

4.1 Physics Beyond the Standard Model Predicting New Heavy Resonance

Three concepts of BSM theories, supersymmetry, new strong dynamics and extra dimensions, are discussed here as a solution to the hierarchy problem. These theories are particularly popular as they predict the existence of new particles in the energy regime that LHC can reach.

4.1.1 Supersymmetry

Supersymmetry (SUSY) is a spacetime symmetry by which every particle in the SM has a superpartner with a spin that differs by one half [64]. These superpartners are collectively called sparticles. For each particle contributing loop correction to the Higgs mass, there would be a corresponding sparticle giving loop correction with the opposite sign that cancels it. The cancellation would be

exact if the particle-sparticle pair has the exact same mass. However, no sparticle has ever been observed, indicating that SUSY needs to be broken but softly. This motivates searches for sparticles with mass in the TeV range at the LHC. If sparticle masses are in the TeV range, then the running gauge couplings would unify remarkably well at a high energy scale. Particularly, in R-parity[1] conserving SUSY models, the lightest sparticle would be stable and usually neutral, making it a good candidate for dark matter. In a low scale supersymmetry (SUSY) breaking scenario, scalar sparticle, sgoldstino, could contribute to $H \to Z\gamma$ due to Higgs–sgoldstino mixing [65, 66]. Nevertheless, squarks in R-parity violating SUSY models couple to a lepton–quark pair effectively as leptoquarks.

4.1.2 New Strong Dynamics

In the SM, the Higgs boson is treated as a fundamental particle. However, to explain the masses of the electroweak gauge bosons without encountering the hierarchy problem, one could include a new strong dynamics called technicolor [67] to induce electroweak symmetry breaking, instead of introducing the Higgs mechanism. Although the simplest technicolor does not necessarily have a Higgs-like fundamental particle, such a particle could be accommodated as a bound state of fermions by a variation of the technicolor theory, and hence given the name composite Higgs models [68]. In these models, a Higgs-like doublet arises as a pseudo-Nambu-Goldstone boson when an enlarged global symmetry of the strong dynamics spontaneously and explicitly breaks down. The Higgs-like doublet then triggers the breaking of electroweak symmetry.

4.1.3 Extra Dimensions

While the SM is embedded in a 3+1 dimensional space-time, i.e. three space-like and one time-like, it is possible that there are extra dimensions hidden from our perception. Since the first attempt in 1921 by Kaluza and Klein to unify gravity and electromagnetism with an extra spatial dimension [69–71], many extra-dimensions theories have been proposed. A class of them is called Large Extra Dimensions, in which only gravity is allowed to propagate in the extra dimensions. The strength of gravity gets diluted across the extra dimensions and thus appears much weaker than what it truly is, with the true scale of quantum gravity in the full $(4+N)$-dimensional theory $M_{4+N} \ll M_{\text{Pl}}$ [72–74]. Another popular class is called Warped Extra Dimensions. Randall and Sundrum suggested that gravity appears to be extremely weak because it is localized away from the SM particles in a fifth dimension, that is warped on itself and orthogonal to the other 3+1 dimensions. If the Higgs is localized at the weak brane and the warp factor is large enough, then the effective electroweak symmetry breaking scale could be warped down to the TeV scale whereas the Higgs mass m_H would stay at the Planck scale as suggested by naturalness [75].

[1] R-parity is defined as $P_R = (-1)^{3B-L+2s}$, where B is baryon number, L is lepton number and s is spin.

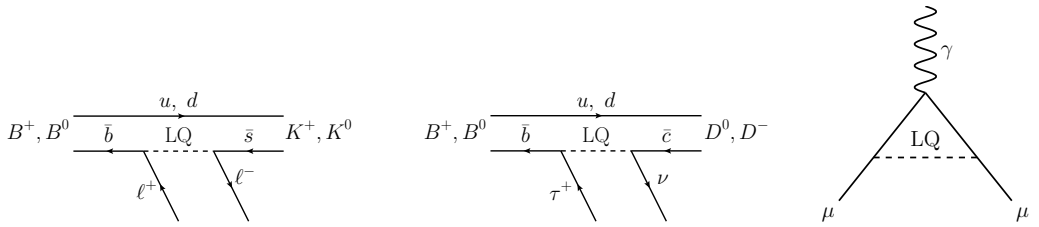

Figure 4.1: Feynman diagrams contributing to Flavour Changing Neutral Current $b \to s\ell^+\ell^-$ decays (left), Flavour Changing Charged Current $b \to c\tau^-\nu$ decays (middle) and muon magnetic moment (right) via a leptoquark, respectively.

4.1.4 Resonance Signatures for New Physics

Searches for resonances decaying to a pair of fermions or bosons is a direct way to discover new particles in collider physics. Fermionic decay channels have a glorious history of discovering particles, such as the J/Ψ meson and the Z boson, that have made better understanding of the SM. On the other hand, bosonic decay channels are interesting to probe when the couplings of a new particle to fermions are suppressed. For example, the discovery of the Higgs boson was announced in three diboson channels, $H \to ZZ \to 4\ell$, $H \to WW \to \ell\nu\ell\nu$ and $H \to \gamma\gamma$. Although the discovery of Higgs boson has made an important milestone, BSM theories discussed above suggest that new physics is expected and may involve (spin-0, 1 or 2) heavy bosons at the TeV scale. These particles could be sought in the $W\gamma$, $Z\gamma$ and $H\gamma$ channels as proposed in Ref. [76–80], relevant searches are thus performed in the analysis presented in Chapter 11.

4.2 Leptoquark Phenomenology

The quark and lepton sectors of the SM are intriguingly similar, motivating one to hypothesize a fundamental symmetry between the two sectors. Such a symmetry can be found in many GUTs, such as Georgi–Glashow models which are based on $SU(5)$ gauge symmetry [81], Pati-Salam models which are based on $SU(4)$ color symmetry [82], and R-parity violating SUSY models. These models commonly predict a new class of color triplet bosons coupled to quarks and leptons simultaneously called Leptoquarks. There are 14 species of leptoquarks, characterized by their spin, fermion number $F = 3B + L$, weak isospin, and chirality of the coupling. They are either singlet, doublet or triplet under $SU(2)$, and carry absolute fractional electric charge of $\frac{1}{3}$, $\frac{2}{3}$, $\frac{4}{3}$ or $\frac{5}{3}$. Table 4.1 summarizes the properties of the various species. Recently, LQs have gained more attention as they could account for the recent anomalies in the $R_{K^{(*)}}$ and $R_{D^{(*)}}$ measurements by contributing at tree-level diagrams. Besides the B decay anomalies, leptoquarks can also contribute to the muon anomalous magnetic moment at one-loop level to address the long-standing deviation from the SM. The relevant Feynman diagrams contributions via LQ are illustrated in Figure 4.1.

Table 4.1: Summary of various scale and vector leptoquarks, and their quantum numbers. The notation uses the field $Q \equiv (u_L,\ d_L)$ to denote the left-handed quark doublet, $L \equiv (\nu_L,\ e_L)$ as the left-handed lepton doublet, U and D as the up- and down-type right-handed quark singlets, and E as the right-handed charged lepton singlet.

Spin-0 LQ	$(SU(3)_C, SU(2)_L)_{U(1)_Y}$	$\lvert q_e \rvert$	$F = 3B + L$	Symbol
QL triplet	$(3,3)_{-1/3}$	$(2/3, -1/3, -4/3)$	2	S_3
QL singlet	$(3,1)_{-1/3}$	$-1/3$	2	S_1
U^cL	$(\bar{3},2)_{-7/6}$	$(-2/3, -5/3)$	0	R_2
D^cL	$(\bar{3},2)_{-1/6}$	$(1/3, -2/3)$	0	$\tilde{R}_2$
QE^c	$(3,2)_{7/6}$	$(2/3, 5/3)$	2	R_2
U^cE^c	$(\bar{3},1)_{1/3}$	$1/3$	0	S_1
D^cE^c	$(\bar{3},1)_{4/3}$	$4/3$	0	$\tilde{S}_1$

Spin-1 LQ	$(SU(3)_C, SU(2)_L)_{U(1)_Y}$	$\lvert q_e \rvert$	$F = 3B + L$	Symbol
$Q^\dagger L$ triplet	$(\bar{3},3)_{-2/3}$	$(1/3, -2/3, -5/3)$	0	U_3
$Q^\dagger L$ singlet	$(\bar{3},1)_{-2/3}$	$-2/3$	0	U_1
$U^{c\dagger}L$	$(3,2)_{1/6}$	$(-1/3, 2/3)$	2	$\tilde{V}_2$
$D^{c\dagger}L$	$(3,2)_{-5/6}$	$(-4/3, -1/3)$	2	V_2
$Q^\dagger E^c$	$(\bar{3},2)_{5/6}$	$(1/3, 4/3)$	0	V_2
$U^{c\dagger}E^c$	$(3,1)_{5/3}$	$5/3$	2	$\tilde{U}_1$
$D^{c\dagger}E^c$	$(3,1)_{2/3}$	$2/3$	2	U_1

4.2.1 Leptoquark Production in pp Collisions

To directly search for LQs at the LHC, there are two principal production mechanism of LQ in pp collisions: single and pair productions. Since LQs are colored particles, the dominant pair production processes are gluon–gluon fusion and quark–anti-quark annihilation. The t-channel lepton exchange process contributes to the total cross section at the 10% level, and thus not considered for the interpretation of the presented results. For leptoquarks coupling with higher generations of quarks, the contribution from the t-channel lepton exchange process would be even smaller due to the relative suppression of the parton constituent within the proton. While the pair production is largely insensitive to the Yukawa coupling $\lambda_{\ell q}$ at a LQ–lepton–quark vertex, LQs could also be singly produced with an associated lepton by quark–gluon scattering, of which the production cross section is proportional to the square of the LQ–lepton–quark coupling. The leading-order Feynman diagrams of single and pair production are illustrated in Figure 4.2 & 4.3 respectively. Additionally, LQs could mediate Drell-Yan-like dilepton production in the t- or u-channel with $\mathcal{O}(\lambda_{\ell q}^4)$ cross section. Figure 4.4 sketches the potential exclusion limits on the processes of LQ pair production, LQ single production and LQ-mediated dilepton production in the $\lambda_{\ell q}$–m_{LQ} plane. As mentioned above, LQs can be of either scalar or vector nature; the production cross section of vector LQs could be

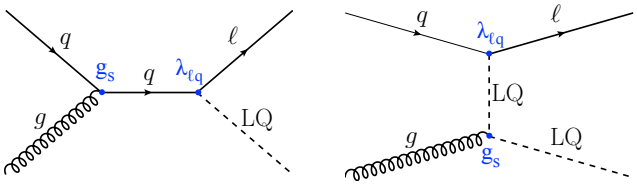

Figure 4.2: The lowest-order Feynman diagrams contributing to LQ single production: s-channel (left) and t-channel (right).

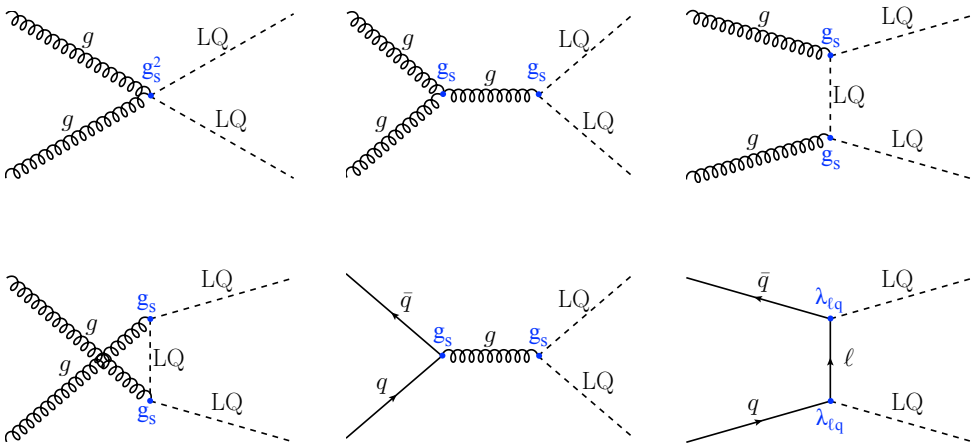

Figure 4.3: The lowest-order Feynman diagrams contributing to LQ pair production. In this paper, the t-channel lepton exchange diagram is not considered.

boosted relative to that of scalar LQs via an extra coupling to a massive gluon partner in the minimal set of vector companions [83]. Since the production of scalar LQ is less model dependent and the dependence of event topology on the LQ spin is fairly small as shown in Ref. [84], only scalar LQ production is considered in the presented analysis (Chapter 12).

While more than one Yukawa coupling is needed to explain the B-anomalies, LQs are typically assumed to couple to quarks and leptons via a single Yukawa interaction in a search for simplicity. The LQ–lepton–quark coupling is determined by two parameters: a model parameter β and the coupling parameter λ. The coupling to charged lepton is given by $\sqrt{\beta}\lambda$, and the coupling to neutrino by $\sqrt{1-\beta}\lambda$. In general, the branching fraction $\mathcal{B}$ of a LQ is largely reflected by β alone; however, it could also be sensitive to the mass of the decay products in low LQ mass scenarios. If β is not zero nor one, the pair production could have an asymmetric final state $(\ell^{\pm}q)(\bar{\nu}'\bar{q}')$, while the single production could have charge lepton and neutrino at the same time in the final state. The search phase space could be effectively explored by designing dedicated analyses for $\mathcal{B} = 0$, 0.5, 1.

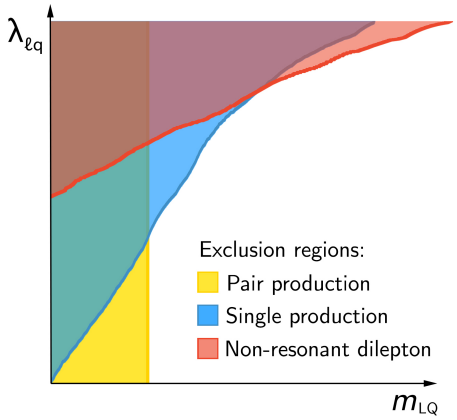

Figure 4.4: A cartoon illustration of the potential exclusion limits for the processes of LQ pair production, LQ single production and LQ-mediated dilepton production on the LQ–lepton–quark coupling $\lambda_{\ell q}$ as a function of LQ mass m_{LQ}.

4.2.2 Current Status of Leptoquark Searches at the LHC

To cover all the various possible LQ–lepton–quark couplings and final states in single and pair production, one could search for LQ systematically based on the distinctive signatures of the final states. The signatures could be formulated in two matrices, one for pair production and one for single production as shown in Figure 4.5. Light quarks and anti-quarks u, d, s, $\bar{u}$, $\bar{d}$, $\bar{s}$ from leptoquark decays are all reconstructed as light-flavored jets, whereas final states involving c quarks and anti-quarks are sometimes targeted using c-tagging technique. Separate grids are dedicated to heavy flavor quarks (b, t, $\bar{b}$, $\bar{t}$) for their dissimilar signatures from the light-jets, as B hadrons are relatively long-lived, and top quarks mainly decay into a b-quark and an on-shell W boson. For pair production, 'j' refers to final states containing a pair of light-jets, 'c' refers to a pair of c-jets or a c-jet–light-jet pair, and 'b' ('t') refers to a pair of b-jets (top quarks) or a b-jet–top-quark pair. For each class of quarks, the final states are further divided into more specific classes according to the number of charged leptons and neutrinos. Electrons and muons are collectively denoted as 'ℓ' in the matrices because the relevant analyses essentially exploited common strategies, whereas the identification of tau leptons is complicated by its further leptonic or hadronic decays.

Many searches for leptoquarks have been performed during Run 1 and 2, but no evidence for the existence of leptoquarks is observed so far. Figure 4.6 summarizes the up-to-date best exclusion limits of LQ mass from the published ATLAS and CMS results during Run 1 and 2 [86–98]. The corresponding object selections to the various final states are described in the second to fourth columns. The presented search in this dissertation is the only searches performed in the LQ$\to \mu t$ and LQ$\to et$ channel by ATLAS up to now, placing an exclusion limit at the LQ mass of almost 1.5 TeV [97]. On the other hand, CMS has performed a search in the LQ$\to \mu t$ channel with partial Run

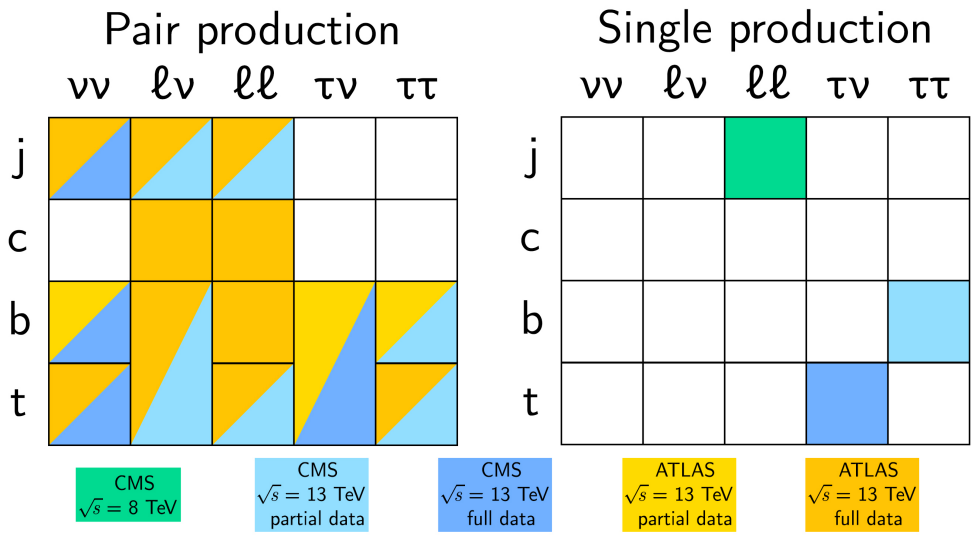

Figure 4.5: Summary of all possible final states in leptoquark pair (left) and single (right) productions. The matrices are filled if the final states have been covered by ATLAS or CMS analyses. This figure is adapted and extended from reference [84, 85].

2 data, setting a mass limit of 1.42 TeV [90].

4.2.3 Indirect Constraints and Viable Leptoquark Explanations

Given strong experimental constraints on proton decay lifetime from baryon number violating process like $p \to \pi^0 e^+$ [100], one common concern in GUTs is the trigger of fast proton decay. Leptoquarks generally could also possess diquark couplings that lead to proton instability at tree level, and hence, leptoquarks are considered only if they conserve baryon and lepton numbers by possessing fermion number $F = 0$ [101].

As rare lepton-flavor-violating processes are precisely measured, stringent constraints are imposed on simultaneous leptoquark couplings to more than one generation of leptons [102]. For instance, the most stringent limit of $\mathrm{BR}(\mu \to e\gamma) < 4.2 \times 10^{-13}$ on radiative $\mu \to e\gamma$ decays established by the MEG experiment [103] would lead to bounds on simultaneous leptoquark couplings to electron and muon. Rare decay processes $\ell \to \ell'\ell'\ell''$ could also be invoked by LQs at one-loop level and thus impose constraints on simultaneous LQ couplings, but in a weaker degree.

Nevertheless, the observed b-anomalies, as discussed in Section 3.5, hint at the type of LQs that would still be viable without violating the constraints. For example, it is suggested in Ref. [104] that flavorful models with single scalar (S_3) or vector (U_3) LQ triplet are capable of explaining the hints of lepton universality violation in R_K, $R_{K^{(*)}}$ measurements. In these models, the LQ–lepton–quark couplings follow the hierarchal structure and quark mixing in the SM with larger couplings to heavy flavor quarks. Mixed models of LQ could also address the anomalies, like the one with a doublet

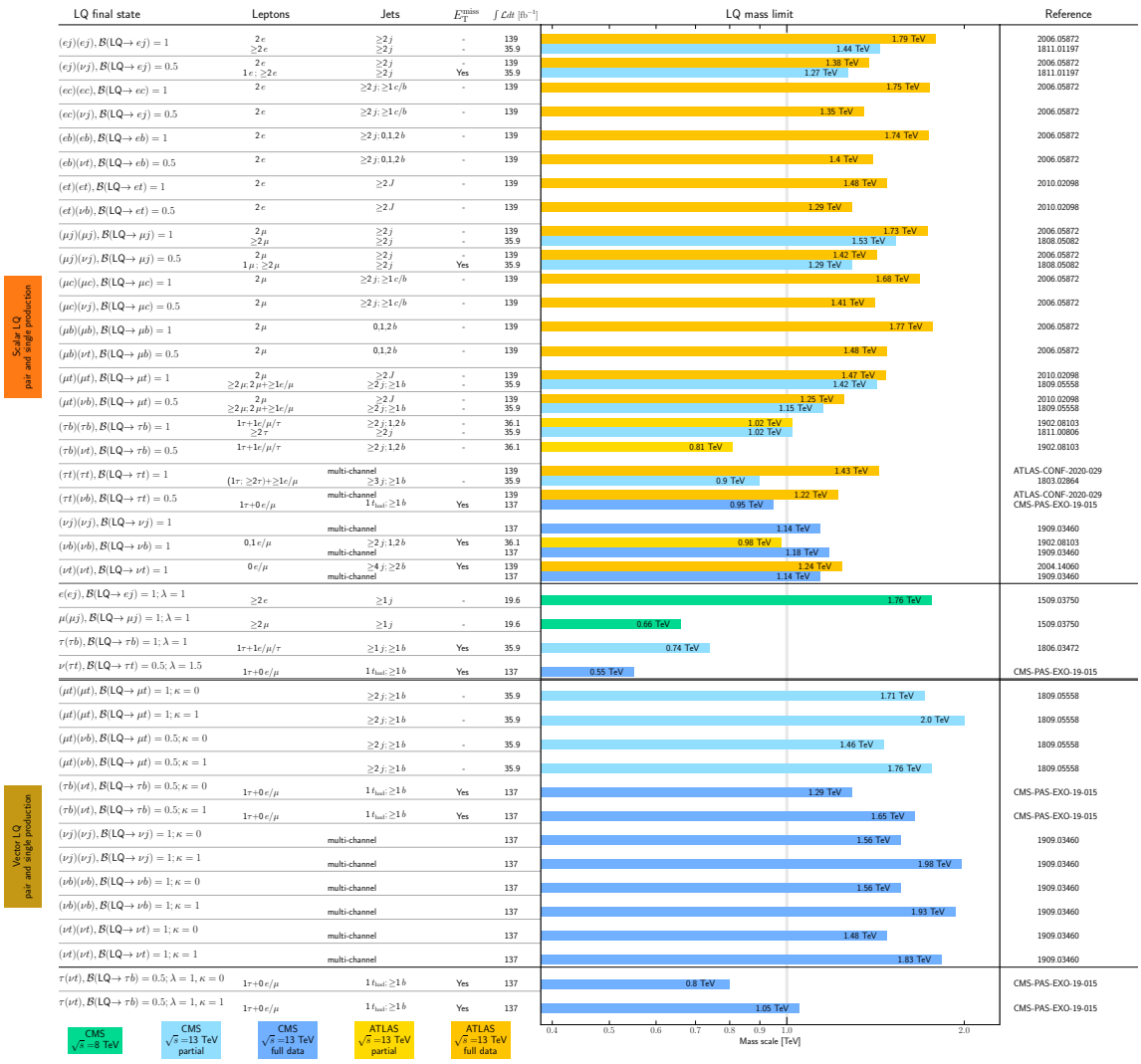

Figure 4.6: Summary of reach of ATLAS and CMS searches for single and pair production of scalar and vector leptoquarks. Only a representative selection of the available results is shown [86–99]. Green bands indicate 8 TeV CMS data results; ice blue (azure) bands indicate 13 TeV CMS data results with partial (full dataset); yellow (orange) bands indicate 13 TeV data results with partial (full) dataset.

and a singlet LQ ($R_2 + \tilde{U}_1$) in Ref. [105], which also proposes predominant coupling to top quarks and muons.

Chapter 5

Physics of Proton-Proton Collisions

In hadron-hadron collisions at high energies like the LHC, the fundamental scattering process is between the parton constituents of the hadrons. Although the hard scattering between partons is calculable with perturbative QCD, the full solution to hadron-hadron collisions must account for the compositeness of hadrons, in which the strong coupling is large and perturbative physics breaks down. However, since the hard scattering takes place with large momentum transfers between the colliding partons, the partons could be approximated as a set of free particles, and the cross section of the high-energy-scale parton interaction could be factorized from the non-perturbative proton structure at the low scale. Given the difficulty of non-perturbative QCD calculations, the proton structure is instead determined from deep inelastic scattering experiments, as described in Section 5.1. Section 5.2 then gives an overview of how the cross section of proton–proton collisions is calculated from the measured parton density structure of a proton and the cross section for partonic processes.

5.1 Parton Distribution Functions

To describe the parton density of the colliding protons, the distribution of quarks and gluons within a proton is modeled and measured from a series of deep inelastic scattering experiments. The number density of a parton type p with a certain momentum fraction x of the longitudinal proton momentum at some squared momentum transfer Q^2 is given by the parton distribution function $f_p(x_p, Q^2)$. These parton distribution functions (PDFs) are extracted by fitting a parametric model in flexible form to experimental data. Since the dependency of PDFs on Q^2 is calculable using the DGLAP QCD evolution equations [106–108], one could measure the PDFs at a starting energy scale Q_0^2 to predict physics at higher Q^2. The data initially included in the fit are obtained from lepton-nucleon scattering experiments and the HERA electron-proton collider. As LHC data become available, they are also included in the fit to apply tighter constraints, particularly using precision measurements of Drell-Yan, jets and $t\bar{t}$ productions [7], improving the accuracy of the PDFs. The CT [109–111],

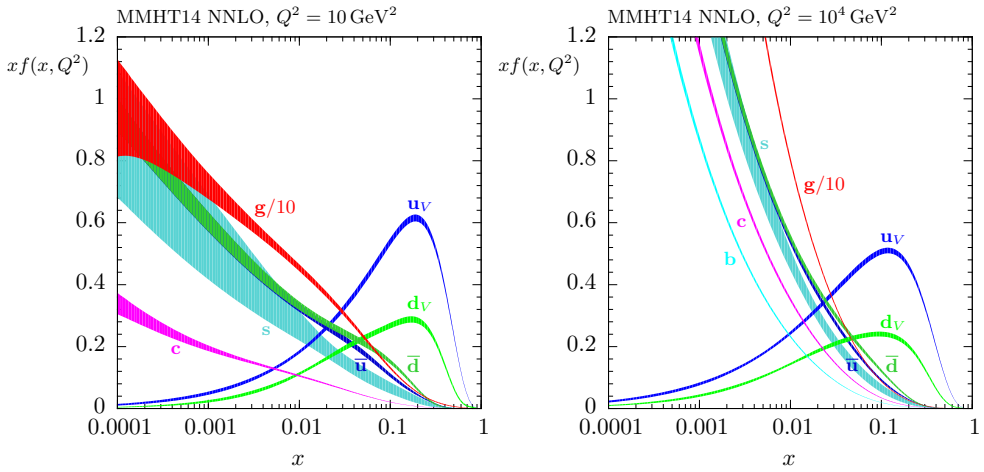

Figure 5.1: The parton distribution functions of a proton for invariant momentum transfers $Q^2 = 10\,\mathrm{GeV}^2$ (left) and $10^4\,\mathrm{GeV}^2$ (right), as a function of the longitudinal momentum fraction x that a parton carries relative to the proton momentum. Figures are taken from Ref. [113].

MSTW/MMHT [112, 113] and NNPDF [114, 115] sets are the harmonized choice of PDF sets used in ATLAS, as they include substantial Tevatron and LHC data, as well as information from fixed target experiments and HERA. As an example, Figure 5.1 illustrates the MMHT2014 PDF set [113] with $Q^2 = 10$ GeV^2 and 10^4 GeV^2. As shown in the figure, the valence quarks of proton carry significant momentum fraction, whereas the sea quarks and gluons dominate at the low-x range as they are created by gluon splitting. As the momentum transfer increases, quarks and gluons are depleted at high-x while the probability of finding them at low-x grows.

5.2 Scattering Rates at High Energy Proton Colliders

The cross section in particle physics is a measure for the probability of a specific process to take place when two particles collide. According to factorization theorem [116], due to the huge difference in the scales at which the hard scattering of partons and the dynamics of proton occur, the cross-section for proton-proton collisions with final state X can be calculated by convoluting short-distance partonic cross section $\sum_{n=0}^{\infty} \alpha_s^n \hat{\sigma}_{ij\to X}^{(n)}$ with the PDFs $f_{i/j}$ of the two interacting partons i and j:

$$\sigma_{pp\to X} = \sum_{n=0}^{\infty} \alpha_s^n(\mu_R^2) \sum_{i,j} \int dx_1 dx_2 f_i(x_1,\mu_F^2) f_j(x_2,\mu_F^2) \times \hat{\sigma}_{ij\to X}^{(n)}(x_1 x_2 s, \mu_R^2, \mu_F^2) + \mathcal{O}(\frac{\Lambda_{\mathrm{QCD}}^2}{Q^2}), \quad (5.1)$$

where s is the center-of-mass energy of the two protons, μ_R^2 and μ_F^2 are the renormalization and factorization scale respectively, and the last term $\mathcal{O}(\frac{\Lambda_{\mathrm{QCD}}^2}{Q^2})$ accounts for additional corrections from

non-perturbative effects. The renormalization scale is an arbitrary parameter introduced to absorb ultraviolet singularity into a renormalized coupling. The factorization scale is a parameter that factorizes the collinear divergence into a renormalized PDF. In other words, it defines the boundary that separates the physics of particle interaction at the long and short distances. In principal, physical observables do not depend on the choice of these scales when all higher order contributions are taken into account; it is, however, not practical to compute all of them, as the number of Feynman diagrams grows exponentially. Processes are typically calculated up to next-to-leading order (NLO) or next-to-next-to-leading order (NNLO) precision in most Monte Carlo event generators, and the scale dependences are taken into account as theoretical uncertainties by varying these two scale parameters by a factor of 2 and 0.5.

Part II

Experimental Facilities

Chapter 6

The Large Hadron Collider

The Large Hadron Collider (LHC) is the world's most powerful particle accelerator located at CERN, the European Organization for Nuclear Research near Geneva, Switzerland. It is a 27-kilometer-long ring that sits in a tunnel 100 meters beneath the ground, spanning the border between Switzerland and France. To recreate and investigate the conditions of the early Universe just after the Big Bang, extremely high-energy collisions of particles are carried out in the collider. The collider is designed to perform primarily proton–proton (pp) collisions with a center-of-mass energy up to 14 TeV, and lead–lead ($PbPb$) collisions up to 5.52 TeV for the study of quark-gluon-plasma [117]. These collisions take place at four interaction points, where four distinctive particle detectors are individually located at each point. Two of the detectors, ATLAS [118] and CMS [119], are so-called general-purpose detectors, whereas the other two, ALICE [120] and LHCb [121], are dedicated detectors to study QCD under extreme conditions and b-physics respectively. Besides, there are four smaller experiments at the LHC ring, namely LHCf [122] (near ATLAS), TOTEM [123] (near CMS), MoEDAL [124] (near LHCb) and FASER [125] (near ATLAS), which target particles that are produced in the forward direction along the collision axis near the interaction points.

With a focus on pp collisions in the preparation of this dissertation, Section 6.1 gives an overview of the accelerator infrastructure. Then, Section 6.2 describes how protons are accelerated bunch by bunch in a train structure. Finally, Section 6.3 reviews the performance of LHC.

6.1 The Complex of Accelerator Rings

Protons are accelerated in a chain of accelerator rings before approaching almost the speed of light in the LHC. The complex of the accelerators is illustrated in Figure 6.1. Protons are first extracted by ionizing hydrogen, and fed into a linear accelerator, LINAC 2, that accelerates them to 50 MeV. The protons are then injected into the first accelerator ring called the BOOSTER, followed by larger and larger rings, the Proton Synchrotron (PS), the Super Proton Synchrotron (SPS), and finally the LHC. The proton energy is boosted at each stage, starting from the BOOSTER, to an energy of

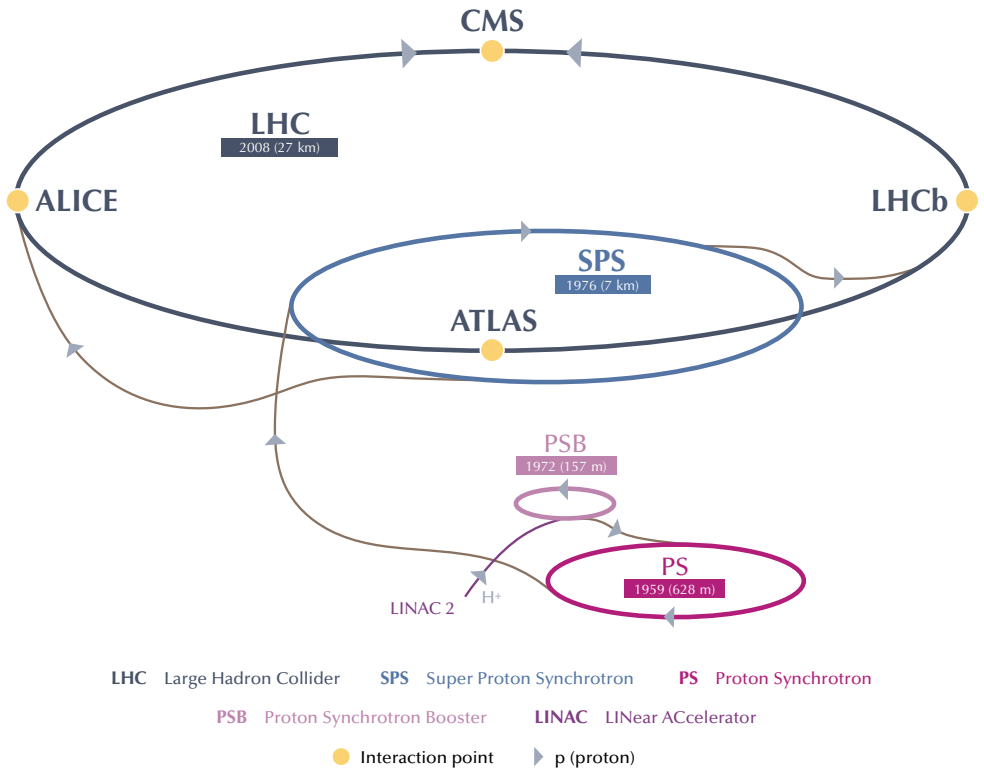

Figure 6.1: CERN's accelerator complex for proton–proton collisions, starting from the injection chain to the LHC machine. This figure is adapted from Ref. [126].

1.4 GeV, 25 GeV, 450 GeV, and finally up to 7 TeV in the LHC. Protons are filled in bunches into the LHC in both clockwise and anti-clockwise directions via two transfer lines, where the opposing proton bunches cross at the interaction points.

The LHC is not perfectly circular; in fact it consists of eight roughly-three-kilometer-long arcs interleaved with straight sections. In each arc, 154 superconducting niobium-titanium (NbTi) dipole magnets are installed to produce a magnetic field of 8.3 T for bending the proton beam, where the magnets are cooled by superfluid helium to a temperature below 2 K. In addition, 49 main quadrupole magnets are employed to focus the beam. In the straight sections, radiofrequency (RF) cavities are used to deliver an accelerating field of 5 MV/m by powering each cavity with an oscillating voltage of 2 MV at 400 MHz. These cavities keep the protons tightly bunched, as well as accelerating them to the desired momentum. The compactness of proton bunches is crucial to maintaining a high chance of collisions at the four collisions points.

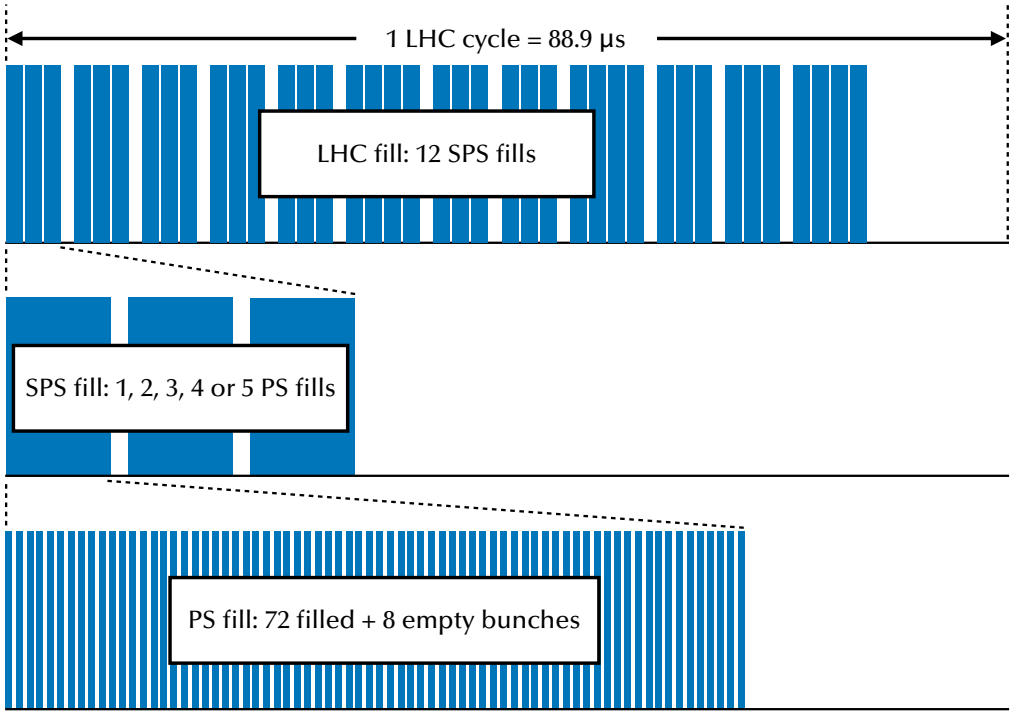

Figure 6.2: Bunch structure of the standard 25 ns filling scheme. This figure is adapted from Ref. [127].

6.2 LHC Bunch Structure

Rather than containing a continuous stream of protons, an LHC proton beam is a series of proton bunches regularly spaced along the accelerator ring. Each bunch is a bundle of roughly 100 billion protons squeezed into a tiny size that is a few micron wide and a few centimeters long. The proton bunches are separated from each other by a minimum distance of 7.5 meters or 25 nanoseconds. In other words, the two opposing bunches of protons cross each other at 40 MHz, resulting in about a billion collisions per second. These bunches of protons in the LHC ring, as well as the small rings, are filled by several fillings of the previous ring. To fill up the LHC, there are a total of 12 SPS fills. Each SPS fill can be of variable length, consisting of 1–5 PS fills. While the PS can accommodate 84 25-ns spacings, the PS fills are produced with certain pattern of bunch train, which are defined with three filling schemes in Run II: the standard scheme [127], the Batch Compression, Merging and Splitting (BCMS) scheme [128, 129], and the 8b4e scheme [130]. Figure 6.2 describes the standard 25 ns scheme as an example to illustrate the beam structure.

The standard scheme is the starting scheme employed in 2015 and early 2016. The bunch structure of each PS fill has 72 consecutive proton-filled bunches. In July 2016, a new beam production scheme, namely the BCMS scheme, was introduced to increase the luminosity of the LHC by reduc-

ing the transverse emittance. It has 48 consecutive proton-filled bunches per PS fill instead. The 8b4e production scheme was introduced during the 2017 Run to mitigate the so-called 16L2 vacuum issue, in which air was accidentally inserted into the LHC beam vacuum. The scheme produces 7 cycles of 8 filled bunches, interleaved by 4 empty bunches, in each PS fill. Due to its *e*-cloud suppression capability, the scheme is mixed with the BCMS scheme to provide similar beam brightness.

6.3 Luminosity and Performance

The rate of event yield for a specific process $pp \to X$ with a cross section of $\sigma_{pp\to X}$ is given by

$$\frac{\mathrm{d}N_{pp\to X}}{\mathrm{d}t} = \sigma_{pp\to X}\mathcal{L}, \tag{6.1}$$

where $\mathcal{L}$ is the instantaneous luminosity. While the collision energy needs to be high enough to possibly create any heavy new particles, the collision rate is also important to the occurrence of rare new physics events. The luminosity determines the collision rate, and is thus a key figure of merit to measure the ability of a collider.

The instantaneous luminosity delivered by a collider is given by the rate of proton crossings per intersection area of the two colliding beams, according to the following formula [131]:

$$\mathcal{L} = \frac{n_b N_p^2 f_{\mathrm{rev}}}{4\pi\sigma_x\sigma_y} F \ , \tag{6.2}$$

where n_b is the number of bunches, N_p is the number of protons per bunch, f_{rev} is the revolution frequency, $\sigma_{x/y}$ is the effective convoluted transverse beam size assuming a Gaussian charge distribution, and F is a geometric factor to account for the crossing angle of the beams at the interaction point. Since a stable particle in an accelerator follows an evolving ellipse with constant area in the transverse plane, the beam dimension is conventionally modeled as $2\sqrt{\varepsilon\beta}$, where ε is the transverse emittance that describes the effective transverse dimension of the beam based on the initial beam conditions, and β is the amplitude modulation that takes into account the correlation between the beam sizes in the transverse plane and longitudinal direction. The transverse beam width β increases as the beam moves further away in the longitudinal direction from the point of minimum transverse area like $\beta(z) = \beta^* + z^2/\beta^*$, where β^* is the minimum transverse width. This gives its name the hourglass effect due to the shape of the beam size. The beam size at the interaction point in the transverse plane can be expressed as

$$\sigma_x\sigma_y = \frac{\varepsilon_n\beta^*}{\pi\gamma} \ , \tag{6.3}$$

where $\varepsilon_n = \varepsilon\gamma$ is the normalized emittance after factorizing out the relativistic effect. Finally, the

Parameter	Design	Run I		Run II				Run III target
		2010-11	2012	2015	2016	2017	2018	2021-23
Center-of-mass energy [TeV]	14	7	8	13				13/13.5
Bunch spacing [ns]	25	50		25				25
Max. no. of bunches	2808	1380		2244	2220	2556	2556	2736
Bunch population [$10^{11}p$]	1.15	1.3	1.5	1.2	1.25	1.25	1.1	1.8
Peak luminosity [10^{34} cm^{-2}s^{-1}]	1.0	0.35	0.77	0.50	1.38	2.09	2.10	2
Delivered integrated luminosity [fb^{-1}]	-	5.5	22.8	4.2	38.5	50.2	63.3	235
Mean pileup	-	9.1	20.7	13.4	25.1	37.8	36.1	<60
Peak mean pileup	-	32.1	35.9	23.7	51.2	78.5	63.0	-

Table 6.1: The operation performance of proton–proton collision at the LHC during Run I and Run II, with luminosity and pileup as recorded by the ATLAS detector. Run III targets are taken from the presentations at 9th LHC Operations Evian Workshop [133].

geometric factor F is determined as

$$F = \left(1 + \left(\frac{\theta_c \sigma_z}{2\sigma_{xy}}\right)^2\right)^{-1/2} , \tag{6.4}$$

where θ_c is the full crossing angle at the interaction point, σ_z is the bunch length, and σ_{xy} is the transverse beam size at the interaction point, assuming the beams are round and identical in the transverse plane.

In a bunch crossing with high luminosity like the LHC, it is likely to have more than one proton–proton collision. The average number of interactions per bunch crossing is defined as (in-time) pileup [1]

$$\mu = \frac{\mathcal{L}\sigma_{\text{tot}}}{n_b f_{\text{rev}}} , \tag{6.5}$$

where σ_{tot} is the total cross-section of an inelastic proton–proton collision. While the pileup is directly proportional to the instantaneous luminosity, the maximum acceptable pileup is limited by the capabilities of experimental detectors, such as the capacity of the data acquisition systems and the reconstruction efficiency in a crowded environment full of particles. ATLAS was initially designed for a mean pileup of $\mu \approx 20$ and a luminosity of 1×10^{34} cm^{-2}s^{-1}. By the end of Run II, the mean pileup has reached a peak value of 78.5[2] and a peak luminosity of 2.1×10^{34} cm^{-2}s^{-1}. Figure 6.3 shows the distribution of pileup year by year during Run II as recorded by the ATLAS detector. The performance of the LHC over Run I and Run II is summarized in Table 6.1.

The data analyzed in preparation for this dissertation is collected at $\sqrt{s} = 13$ TeV during Run II of the LHC, which adds up to an integrated luminosity of 156.2 fb^{-1}. Figure 6.4 shows the integrated luminosity delivered by the LHC and recorded by the ATLAS detector during 2015–

[1] Bunch crossings can also be accompanied by out-of-time pileup which is contributed by proton–proton collisions in neighboring bunch crossings.

[2] Stable beam with peak mean pileup of 88.6 was tested during the last day of Run II

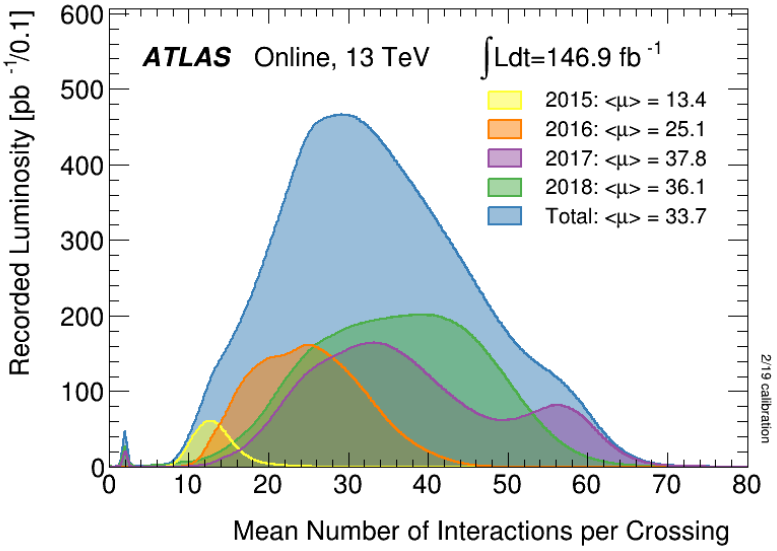

Figure 6.3: The number of proton–proton interactions per bunch crossing for the $\sqrt{s} = 13$ TeV data during stable beams from 2015–2018. [132]

2018. One of the presented analysis that searches for heavy resonances decaying to a photon and a $Z/W/$Higgs boson is based on the dataset collected during 2015–2016 as an early Run II result, whereas the other analysis that searches for leptoquark pair productions uses the full Run II dataset.

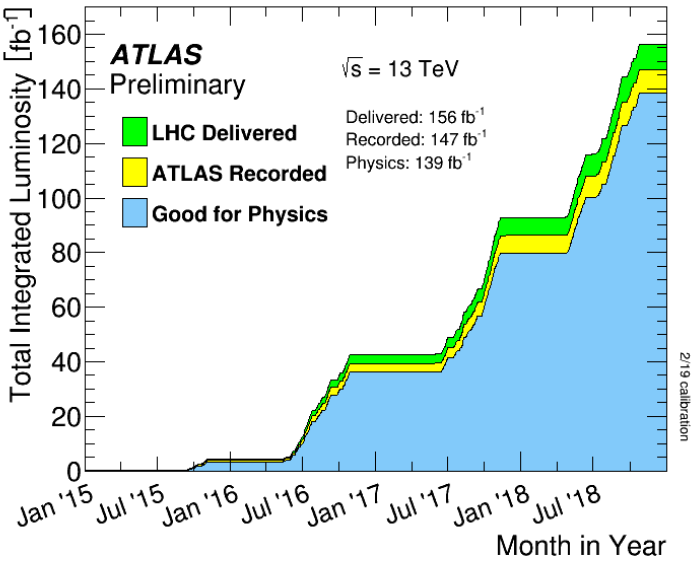

Figure 6.4: The cumulative integrated luminosity delivered to ATLAS (green), recorded by ATLAS (yellow), and certified as good quality data (blue) over 2015–2018 for proton–proton collisions at $\sqrt{s} = 13$ TeV. [132]

Chapter 7

ATLAS detector

The ATLAS experiment [118] is a general purpose detector designed to cover a wide range of physics programs, including the search for BSM physics, at the unprecedentedly high energy scales in the LHC. The detector is situated in an underground experiment cavern at LHC access point 1. As hinted by its name that comes from a titan in Greek mythology, ATLAS is the largest of the LHC detectors with a diameter of 24 meters and a length of 46 meters in the shape of a cylinder. It weighs about 7000 tonnes which is as heavy as the Eiffel Tower. While Figure 7.1 illustrates the structure of the ATLAS detector, an overview of the detector design is given in Section 7.1, followed by more details on three main sub-detector systems: the Inner Detector tracking system (Section 7.2), calorimeter system (Section 7.3) and the Muon Spectrometer (Section 7.4). Section 7.5 outlines the trigger and data acquisition system.

7.1 Detector Overview

The ATLAS detector is centered at the interaction point at LHC access point 1 and built around the LHC beam pipe with forward-backward symmetry, covering almost the full solid angle of 4π. It is composed of a series of concentric subsystems, each of which interacts differently to different kinds of particles, making the identification of different physical objects possible. The sub-detectors closest to the interaction point are the Inner Detector tracking system, which measures the trajectories of charged particles. The Inner Detector is surrounded by a calorimeter system that is designed to absorb and measure the energies of electromagnetically interacting particles and hadrons. The Muon Spectrometer is then installed at the outermost layer to measure the trajectories of escaping muons, as muons cannot be stopped by the calorimeter system. Each of the sub-detectors is divided into three regions: the central part called barrel region where the detector layers are parallel to the beam pipe, and the two ends called endcap regions where the detector layers are circular disks perpendicular to the beam pipe.

In the ATLAS experiment, a right-handed coordinate system is employed with its origin defined

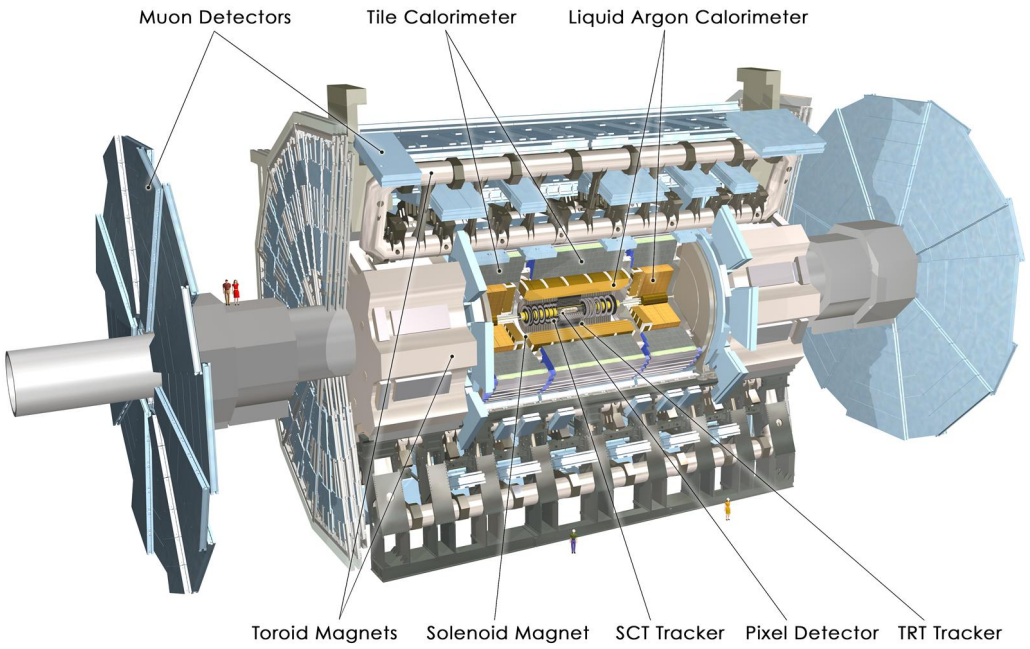

Figure 7.1: Cutaway view of the ATLAS detector and its sub-systems (with humans on the beam pipe as a reference scale) [134].

at the interaction point. The x-axis is defined in the direction pointing towards the center of the LHC ring, the y-axis points upwards towards the sky, and the z-axis extends along the beam pipe. The half of the detector located in the positive z-space is referred to as the A-side, and the other half in the negative z-space as the C-side. In the x–y plane, the azimuthal angle ϕ is measured in the counter-clockwise direction from the positive x-axis. The polar angle θ is measured relative to the positive z-axis, however, the pseudorapidity $\eta \equiv -\ln(\tan(\theta/2))$ is commonly used in practice instead of the polar angle, as differences in pseudorapidity are invariant under Lorentz boosts. Moreover, pseudorapidity provides an easier alternative to estimate rapidity, which is a measure for the relativistic velocity in the beam axis defined as $\mathsf{y} \equiv \frac{1}{2}\ln\left[(E+p_z)/(E-p_z)\right]$, in the limit of relativistic regime. Distances in the angular η–ϕ plane are commonly measured in units of $\Delta R \equiv \sqrt{(\Delta\eta)^2+(\Delta\phi)^2}$.

In the context of hadronic collisions, measurements in the transverse x–y plane play an important role in the reconstruction of particles that are invisible to the detector, like the SM neutrinos or any other weakly interacting neutral BSM particle. As the initial momentum in the x–y plane is negligible, the vector sum of transverse momentum of the invisible particles could be determined from the measurements of the visible objects by the law of conservation of momentum. The negative of vector sum of transverse momentum for the visible objects in a collision event is called the missing transverse momentum $E_{\mathrm{T}}^{\mathrm{miss}}$.

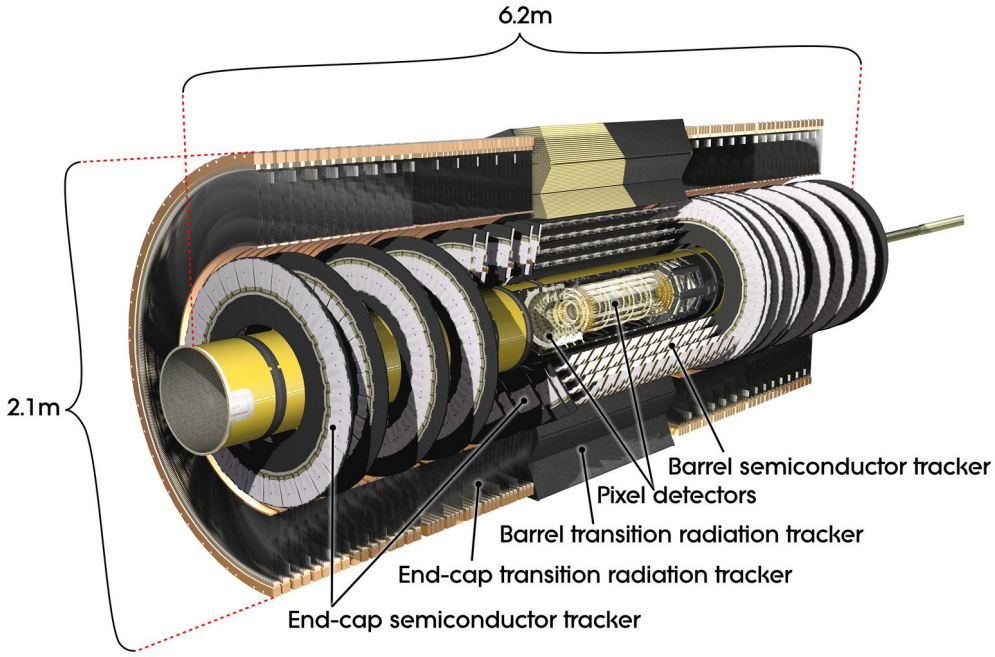

Figure 7.2: Cutaway view of the ATLAS Inner Detector tracking system and its subsystems [135].

7.2 The Inner Detector

Being the innermost system of the ATLAS detector, the Inner Detector (ID) is situated at only a few centimeters away from the beam line. It is designed to measure precisely the momentum of charged particles over a wide coverage of $|\eta| < 2.5$. Layers of sensors are employed to trace the path of any passing charged particle as hits in the sensors. The momentum and charge of the charged particle can be determined from how the trajectory bends in a homogeneous magnetic field of 2 T provided by a solenoid magnet surrounding the ID. As illustrated in Figures 7.2 and 7.3, the ID is composed of three independent subsystems, from the innermost to the outermost: the Pixel Detector, the Semiconductor Tracker (SCT) and the Transition Radiation Tracker (TRT).

7.2.1 Pixel Detector

The Pixel Detector is a tracker system based on silicon semiconductor technology. It has a high granularity for precise tracking and vertexing of where the tracks merge. This does not only allow efficient reconstruction of the primary interaction vertexes, but also secondary decay vertexes for tagging heavy-flavor quarks and τ-leptons. The pixel sensors are distributed in four layers in the barrel region and three disks in each of the endcap regions with a total coverage of $|\eta| < 2.5$. The

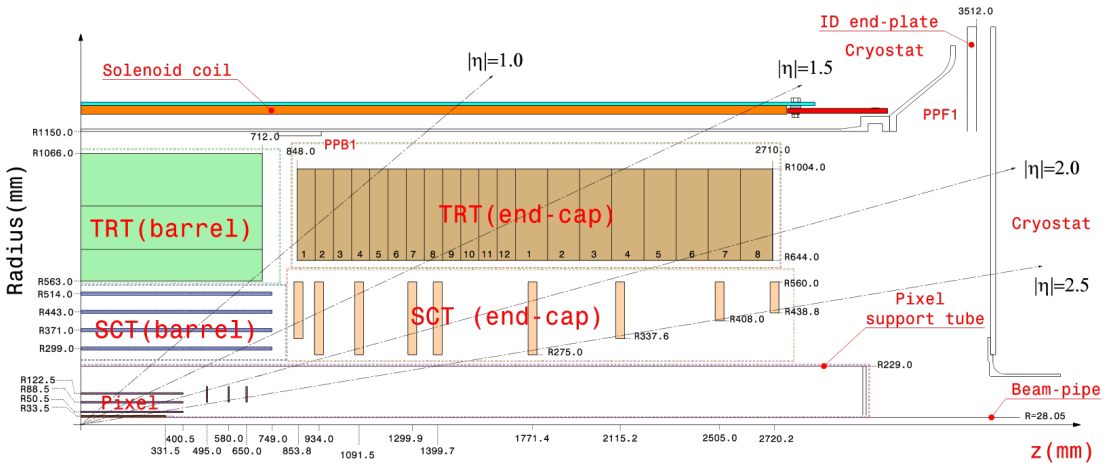

Figure 7.3: Plan view of a quarter-section of the ATLAS Inner Detector tracking system and its sub-systems. This figure is adapted from Ref. [136].

closest layer to the beam line, named the Insertable B-Layer (IBL) [137, 138], was added in 2014 before the beginning of Run II at a radius of 33.5 mm to handle higher radiation and pileup. This is achieved by using a mixture of 3D silicon sensors and traditional planar sensors, both of which are radiation-tolerant and are of nominal size 50 μm $\times$ 250 μm in R–ϕ $\times$ z, providing a resolution of 8 μm in R–ϕ and 40 μm in z. The original three layers and disks of planar sensors at radii 50.5, 88.5 and 122.5 mm have the same transverse dimension but a larger longitudinal dimension of 400 μm, giving a resolution of 14 μm in R–ϕ and 115 μm in z. The three outer layers of pixel sensors are grouped into 1744 modules, with a total number of 80 millions readout channels; the IBL sensors are grouped into 280 modules, summing up to a total number of 8 millions readout channels.

7.2.2 Semiconductor Tracker

The SCT comprises over 6 millions silicon micro-strip sensors, of which the strip structure provides at the same time an excellent resolution over a large area and an optimal cost–performance ratio. Four barrel layers of strip sensors are located in the range of 299 mm $< R <$ 514 mm, together with eighteen more disks in the range of 854 mm $< |z| <$ 2720 mm, to give a coverage of $|\eta| < 2.5$. The sensors are grouped into 4088 silicon strip modules, each of which in the barrel layers contains two sets of sensors glued back-to-back at a stereo angle of 40 mrad in between. With one set of strip sensors kept parallel to the beam line and the other one at an angle, the sensors could provide tracking information in the longitudinal direction. The strip sensor has a size of 80 μm $\times$ 120 mm, and it allows a resolution of roughly 23 μm in R–ϕ and 580 μm in z.

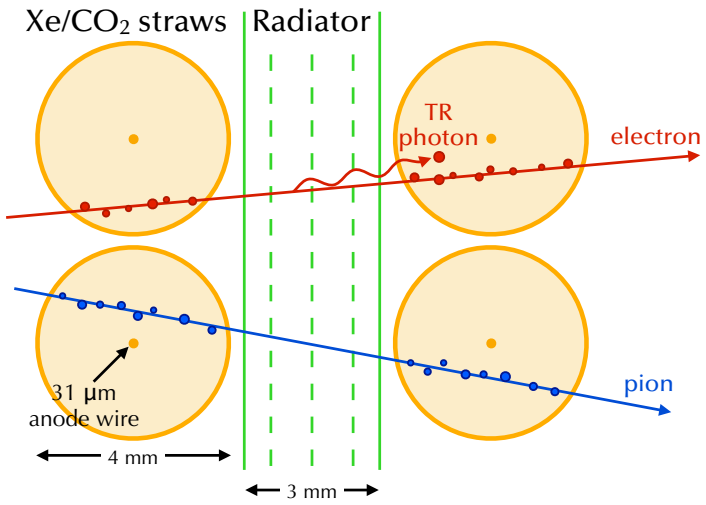

Figure 7.4: An cartoon illustration of the operation principles of the Transition Radiation Tracker.

7.2.3 Transition Radiation Tracker

The TRT is a proportional drift tube tracker that extends the tracking capability of ATLAS up to a radial distance of around one meter over a range of $|\eta| < 2$. The sub-detector consists of 352,256 straw tubes that are filled with a gas mixture of 70% Xe, 27% CO_2 and 3% O_2 in volume[1]. As shown in Figure 7.4, each straw is 4 mm in diameter, with a 31 μm wide gold-plated tungsten anode wire running down the straw center. When a charged particle passes through a straw tube, it ionizes the xenon gas inside. The electrons start to drift towards the wire while the ions drift towards the tube wall due to the 1.5 kV potential applied between the straw tube and the wire. As the electrons accelerate and approach the wire, an avalanche of electrons is induced, resulting in a pulse signal that is amplified by a factor of 20000. The drift time of the electrons gives information about the distance of the track from the wire, leading to an intrinsic resolution of 130 μm per straw. In the barrel region, 144-cm-long straw tubes are aligned in parallel to the beam line in 70 layers, whereas straws in the endcap regions are arranged radially with a length of 37 cm. The former region encompasses the region between 563 mm $< R <$ 1066 mm and $|z| <$ 712 mm, and the latter one occupies the region between 644 mm $< R <$ 1004 mm and 848 mm $< |z| <$ 2710 mm. Thanks to the multiplicity of the straw layers, the transverse momentum resolution of tracks is improved and the number of hits per particle increases by around 35 on average.

In addition to the tracking functionality, a unique feature of the TRT is its ability to identify

[1] Xenon is chosen for its property of good X-ray absorption. The addition of CO_2 and O_2 helps increasing the electron drift velocity, as well as photon quenching

electrons via the detection of transition radiation. The straw tubes made of 60-μm-thick Kapton® film are interleaved with 3-mm-thick mats of polypropylene fibers or foils that serve as radiator material. In a radiator mat, transition radiation x-ray photons are generated when an ultra-relativistic charge particle crosses the boundaries between the radiator material and air gap that have different dielectric constants, leading to larger energy depositions in the straw tubes. Transition radiation will likely occur when the Lorentz factor γ of the charged particle is larger than 1000. Hence, lighter particles like electrons could be distinguished from heavier particles like pions by exploiting the size of the pulse signal. During the end of Run I, several TRT modules developed leakage in inaccessible areas, so Xe-based gas mixture has been replaced by the less expensive argon-based gas mixture for the modules since Run II, even though argon is not very efficient at absorbing transition radiation [139]. A description of the data acquisition system of the TRT is described in more detail in Chapter 9.

7.3 Calorimeters

A calorimeter system is located around the Inner Detector to measure the energy of electrons, photons and hadrons with a coverage up to $|\eta| = 4.9$ for hermeticity. The calorimeters are designed to comprise enough amount of matter such that almost all of the energy of these particles would be absorbed. When any of the particles enters a calorimeter, it would decay into particles of lower energy in a cascade, forming a shower of particles. There are two common classes of calorimeters for the measurement of these showers. One class is called homogeneous calorimeters, which contains a single dense medium that serves as both the absorber and detector. The other class is called sampling calorimeters, which is the one employed in ATLAS. In this kind of calorimeters, layers of passive absorbers, that are used to degrade the energy of the incident particles, are sandwiched with layers of active medium that provides the detectable signal, decoupling the tasks of particle shower containment and energy measurement. A homogeneous calorimeter captures the whole shower and hence gives a better resolution, whereas a sampling calorimeter suffers from sampling fluctuations. However, a sampling calorimeter is less costly, as well as allowing the optimization of segmentation and material choice. The ATLAS calorimeter system consists of two nested sampling calorimeter sub-systems: the electromagnetic (EM) calorimeter on the inside and the hadronic calorimeter on the outside. In addition, a special calorimeter, called the forward calorimeter, is placed near the incident beam to extend the coverage to the high-η region. Figure 7.5 shows a cutaway view of the calorimeter system.

7.3.1 Electromagnetic Calorimeter

The EM calorimeter measures the energy of electrons, positrons and photons. It is composed of a barrel calorimeter and two endcap calorimeters, covering the range of $|\eta| < 1.475$ and $1.4 < |\eta| <$

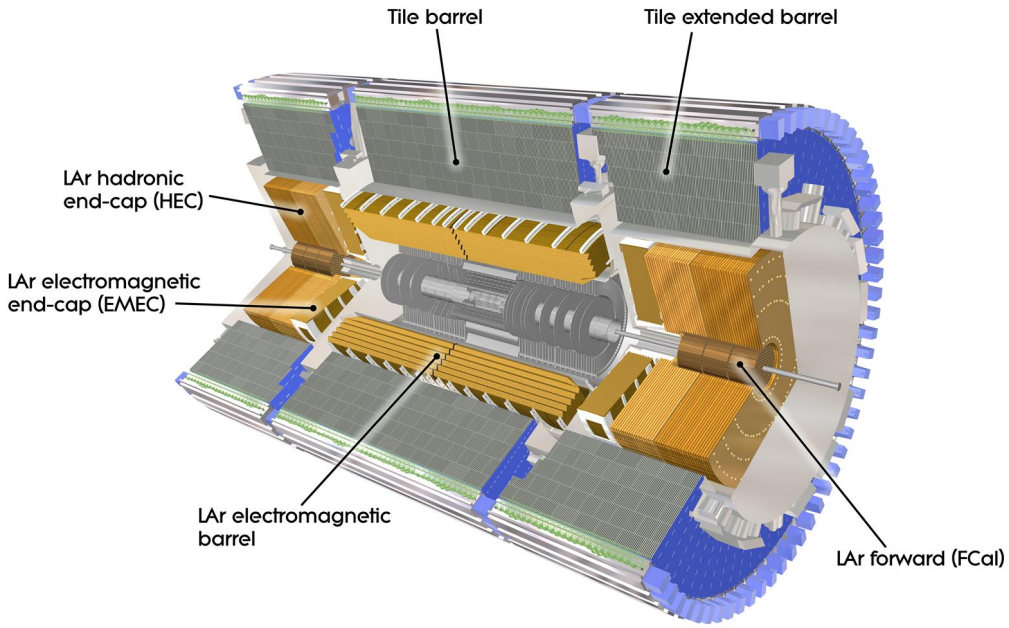

Figure 7.5: Cutaway view of the ATLAS calorimeter system and its sub-systems [140].

3.2 respectively. Both barrel and endcap calorimeters comprise alternating layers of millimeter-thin lead as the absorber and 4-mm-thick honeycomb spacer to contain liquid argon as the active material. As shown in Figure 7.6, the layers are structured in an accordion geometry to provide uniformity without introducing discontinuity in ϕ. As a high-energy electron or positron traverses the calorimeter, it interacts with the lead and emits a photon via bremsstrahlung primarily; the photon then predominantly decays into an electron–positron pair. As the whole process repeats over and over again, an EM shower of electrons, positrons and photons is produced until all of the energy is absorbed. The EM shower ionizes the liquid argon active material on its way, leaving electron–ion pairs to be collected by electrodes with a potential difference applied between them.

The EM calorimeter has three main sampling depths plus one pre-sampler. The innermost pre-sampler layer, covering up to $|\eta| = 1.8$, contains no absorber but only active material to estimate the energy lost by the particle prior to reaching the main calorimeter. The first main layer is finely segmentation in η with a granularity as low as $\Delta\eta = 0.003$, providing the capability to distinguish single-photon signal from boosted neutral pions which mostly decays into nearly collinear photon pairs. The second layer, around 16 radiation lengths[2] (X_0) thick, is the main layer where most of the EM shower is formed and captured. It has a fixed granularity of $\Delta\eta \times \Delta\phi = 0.025 \times 0.025$. The

[2]The distance in a material for which an electron loses $1/e$ of its energy is called the radiation length X_0, corresponding to about $7/9$ of the mean free path of a photon.

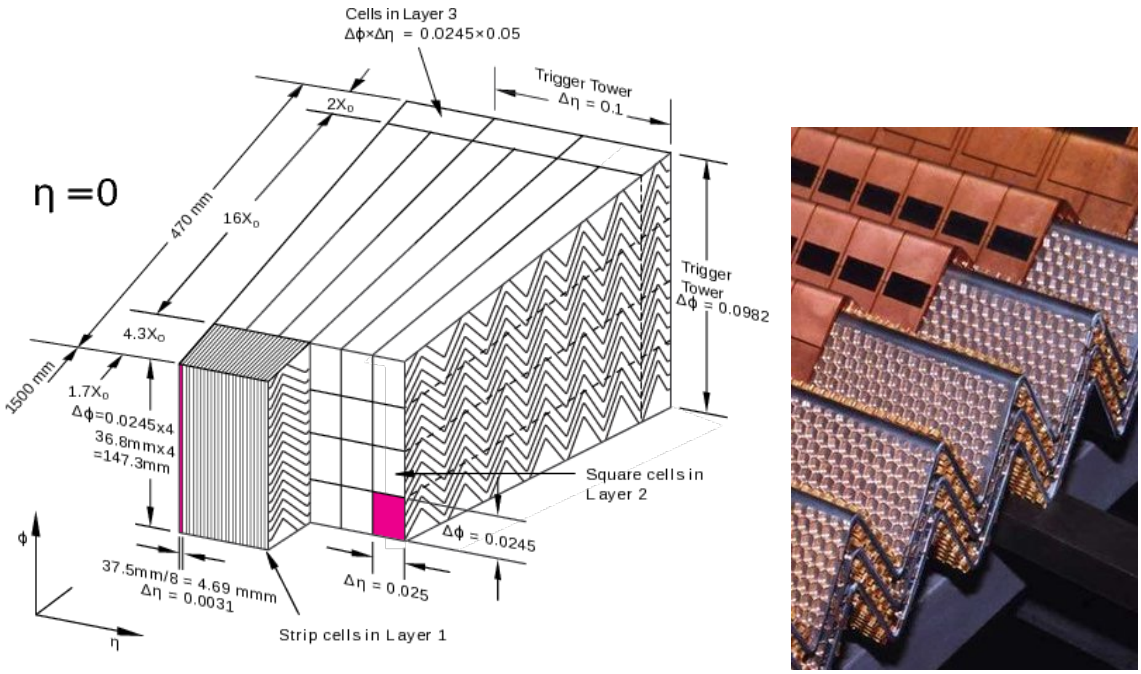

Figure 7.6: Sketch of the accordion geometry in the barrel module for the liquid argon calorimeter (left) [118], and the photography of a partly stacked barrel module showing the accordion-shaped structure (right) [141].

third layer has a coarser granularity of $\Delta\eta \times \Delta\phi = 0.05 \times 0.025$ and a thickness of 2 X_0. It allows corrections for shower leakage behind the EM calorimeter. The whole liquid argon EM calorimeter has a total depth of more than 22 X_0 to ensure excellent containment for EM showers, with a relative energy resolution in the following form of a quadratic sum:

$$\frac{\sigma(E)}{E} = \frac{10\%}{\sqrt{E\,[\text{GeV}]}} \oplus 0.7\%, \tag{7.1}$$

where the first term is a stochastic term depending on intrinsic statistical shower fluctuations and sampling fluctuations, and the second term is a constant that takes into account the inhomogeneous detector response.

7.3.2 Hadronic Calorimeter

The hadronic calorimeter is designed to measure the energy of neutral and charged hadrons. Similar to an EM shower, a hadronic shower is initiated by an incoming high energy particle that cascadingly decays into an exponentially increasing number of particles until all the energies are absorbed. However, the complication of the strong interaction makes the measurement of hadronic showers far more challenging than EM showers. While a hadronic shower deposits part of its energy via

ionization by the charged hadrons in the chain decay, energy deposition is also partially contributed by electromagnetically decaying particles that are generated in the absorption process and initiate EM showers, such as π^0 and η particles. On top of those effects, there is also invisible energy stemming form the interactions of hadrons with nuclei, which has large event–to–event fluctuations. Due to the invisible non-EM contribution and the fluctuating ratio of the strong and electromagnetic interactions, the energy resolution of hadronic showers is significantly worse than EM showers. Moreover, the characteristic interaction length λ for hadronic showers is larger than that for EM showers, so the hadronic calorimeters need to be deeper or denser than the EM calorimeters.

The hadronic calorimeter is composed of two hadronic endcap (HEC) calorimeters and a barrel Tile calorimeter. Each of the HEC calorimeters separated into two disks, together covering the range of $1.5 < |\eta| < 3.2$. The HEC shares similar principle as the EM calorimeter, except different geometries and absorbers. A more conventional flat-plate copper–liquid-argon design is used, with a granularity of $\Delta\eta \times \Delta\phi = 0.1 \times 0.1$ up to $|\eta| = 2.5$ and 0.2×0.2 beyond. The resolution of the HEC is

$$\frac{\sigma(E)}{E} = \frac{50\%}{\sqrt{E\,[\text{GeV}]}} \oplus 3\% \,. \tag{7.2}$$

The Tile calorimeter is arranged in one central barrel covering $|\eta| < 1.0$, and two extended barrels covering $0.8 < |\eta| < 1.7$. It comprises steel plates as absorber and scintillating tiles as active material. The plastic scintillators illuminate when struck by particle showers, and the emitted photons are read out by photomultiplier tubes via wavelength shifting fibers. The Tile calorimeter has three sampling layers of 1.5, 4.1 and 1.8 (1.5, 2.6 and 3.3) λ thick in the (extended) barrel region. The granularity changes from $\Delta\eta \times \Delta\phi = 0.1 \times 0.1$ in the first two layer to $\Delta\eta \times \Delta\phi = 0.2 \times 0.1$ in the third layer. The resolution of the HEC as measured with test beam data is

$$\frac{\sigma(E)}{E} = \frac{56.4\%}{\sqrt{E\,[\text{GeV}]}} \oplus 5.5\% \,. \tag{7.3}$$

7.3.3 Forward Calorimeter

The forward calorimeter is designed to measure forward jets and to improve the reconstruction of missing transverse momentum. It is located between the liquid argon endcap calorimeters and the beam pipe covering the range of $3.1 < |\eta| < 4.9$ to complete the hermeticity of the detector. There are three layers in this calorimeter. The first layer is made of copper and liquid argon just like the hadronic endcap calorimeters, but with very different geometry. A copper absorber matrix is structured to hold copper tubes as the cathodes, one per hollow tube concentrically. In each tube, a copper rod is centered inside as the anode, leaving a very small gap between the rod and the tube wall to be filled with liquid argon. The narrowness of the gap allows fast response to minimize noise from pileup. This layer ensures that EM showers are well-contained and measured. The

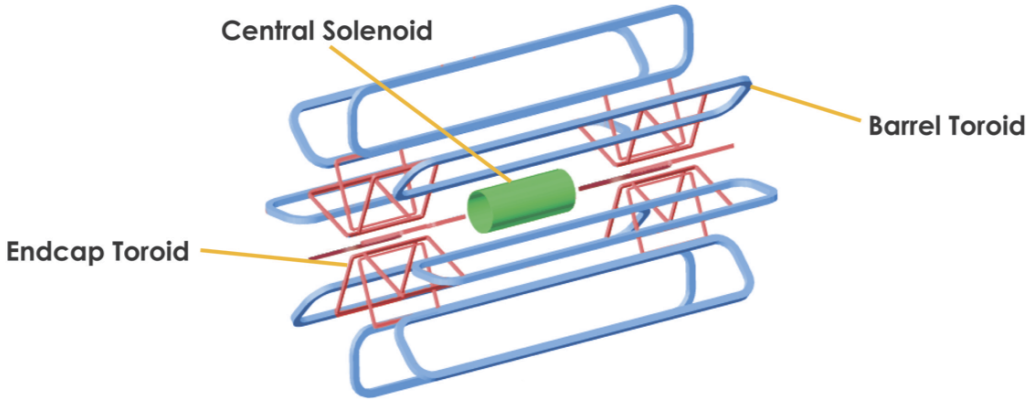

Figure 7.7: A 3-dimensional drawing of the bare windings of the ATLAS magnet system [142].

second and third layers follow the same principle as the first layer, except that tungsten is used as the major absorber instead of copper. These layers estimate the hadronic energy. In addition, a layer of uninstrumented brass is placed at the end of the third layer to prevent punch through to the muon spectrometer. The resolution of the forward calorimeter is

$$\frac{\sigma(E)}{E} = \frac{100\%}{\sqrt{E\,[\mathrm{GeV}]}} \oplus 10\% \,. \tag{7.4}$$

7.4 The Muon Spectrometer

Muons are low-ionizing and thus usually penetrate through the Inner Detector and the calorimeters without losing much energy. The Muon Spectrometer (MS) is the outermost component of ATLAS, which measures the trajectory and provides responsive triggers to muons. It is designed to achieve a momentum resolution up to 10% for a 1 TeV track, or equivalently a sagitta of 500 μm with a precision of 50 μm. In order to accomplish high precision measurement of momentum, a strong magnetic field needs to be applied to bend the highly energetic muons. Such a magnetic field in ATLAS is provided by its unique toroidal magnet system, which consists of a barrel toroid and two endcap toroids as shown in Figure 7.7. The barrel toroid is made of eight rectangular superconducting air-core coils, each encased in vacuum vessel. Similarly, each of the endcap toroids has eight racetrack coils mounted as a single cold mass in a shared vacuum vessel. The toroid magnet system provides a magnetic field of 0.5 T and 1.0 T in the barrel and endcap regions respectively.

The MS consists of four types of sub-detector chambers that utilize slightly different gaseous detector technologies. The chambers are arranged into three cylindrical layers in the barrel region and three planar disks in the endcap region as illustrated in Figure 7.8, covering up to $|\eta| < 2.7$ except a non-instrumented region near $|\eta| = 0$ to reserve space for services of the ID and the calorime-

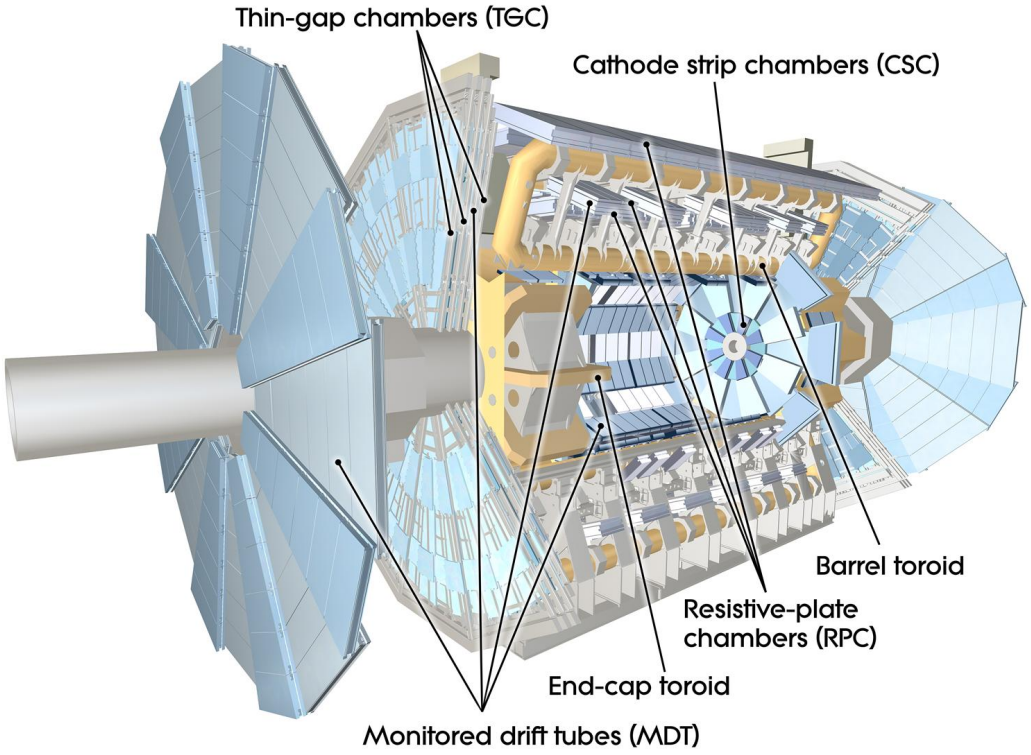

Figure 7.8: Cutaway view of the ATLAS Muon Spectrometer and its sub-systems [143].

ters. Two of the four sub-systems, the Monitored Drift Tube (MDT) chambers and the Cathode Strip Chambers (CSCs), are used to provide high-precision tracking, while the other two chambers, the Resistive Plate Chambers (RPCs) and the Thin Gap Chambers (TGCs), have fast readout system that allows initial trigger decision on muon tracks.

7.4.1 Precision Chambers

The MDT chambers provide most of the tracking in the MS regions. Similar to the TRT, the MDT chambers employ proportional drift tubes for tracking. Each drift tube of 3 cm diameter is coaxial to a 50-μm tungsten–rhenium wire and filled with a gas mixture of Ar–CO_2. In each chamber, drift tubes are closely packed into 6–8 layers, which are divided into two multilayers and mounted on each side of the chamber. Overlapping layers of large and small chambers are used to ensure excellent coverage in the η–ϕ plane as shown in Figure 7.9. To obtain the precise locations of the drift tubes, an optical laser monitoring system is installed to track the alignments and distortions within and among the chambers. The MDT chambers provide a wide coverage of $|\eta| < 2.7$ by situating at the whole three barrel and endcap layers, except the first endcap layer in the range of $2 < |\eta| < 2.7$. Due to a particle flux as high as 200 Hz/cm^2 in this forward region, the CSCs are

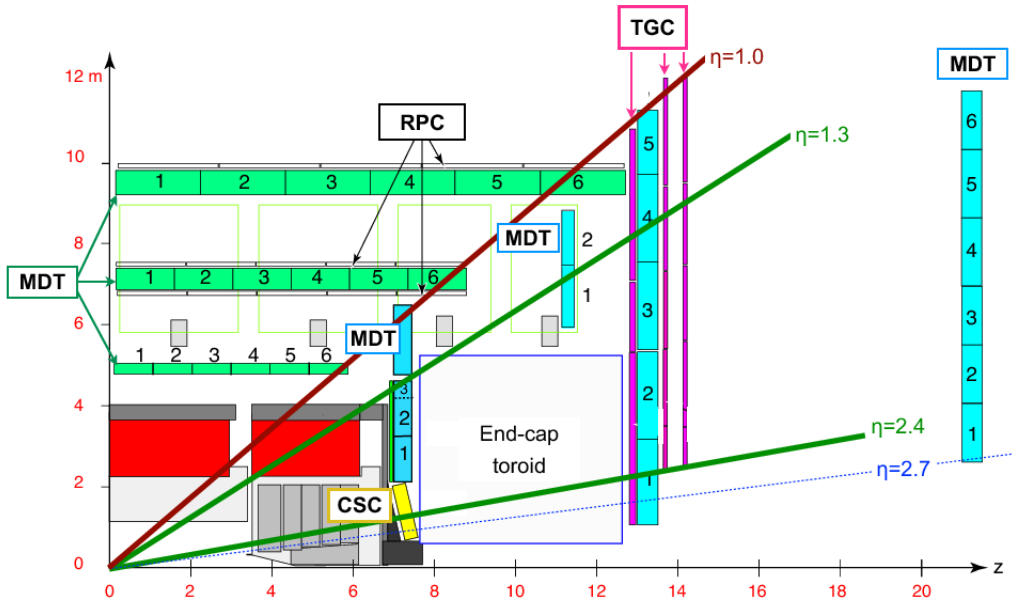

Figure 7.9: A schematic picture of the ATLAS Muon Spectrometer and its sub-systems [144].

deployed to complete the coverage with its higher counting rate capability.

The CSCs are multi-wired proportional chambers, each of which consists of four layers of gas-filled planar gaps with parallel anodes in the middle of the gaps and cathode strip readouts on the interior surfaces of the chamber walls. The 5-mm-thin gap and the high granularity of the orthogonal strips lead to a timing resolution of 7 ns and a position resolution of 40 μm in the bending plane, allowing the CSCs to operate properly in a high flux environment up to 1 kHz/cm^2 without suffering from significant spatial resolution degradations.

7.4.2 Trigger Chambers

The RPCs are used to trigger on muon tracks in the barrel region $|\eta| < 1.05$. In the RPCs, parallel phenolic–melaminic resistive electrode plates are separated by a 2-mm-thin gap filled with a gas mixture of $94.7\%C_2H_2F_4 - 5\%\text{Iso-}C_4H_{10} - 0.3\%SF_6$. A high electric field is applied across the gap to create an avalanche of electrons when traversing charged particles ionize the gas. A signal is then induced on copper readout strips via capacitive coupling and read out by the data acquisition system. Two rectangular layers of gas gaps are sandwiched to form an RPC unit, while the RPC units are partially overlapped in a chamber to eliminate edge effects.

On the other hand, the TGCs provide fast trigger signal in the endcap region $1.05 < |\eta| < 2.4$. Similar to the CSCs, the TGCs work as multi-wired proportional chambers but they have a thinner gap of 2.8 mm that is filled with a highly quenching mixture of 45% n-C_5H_{12} and 55% CO_2. Chamber

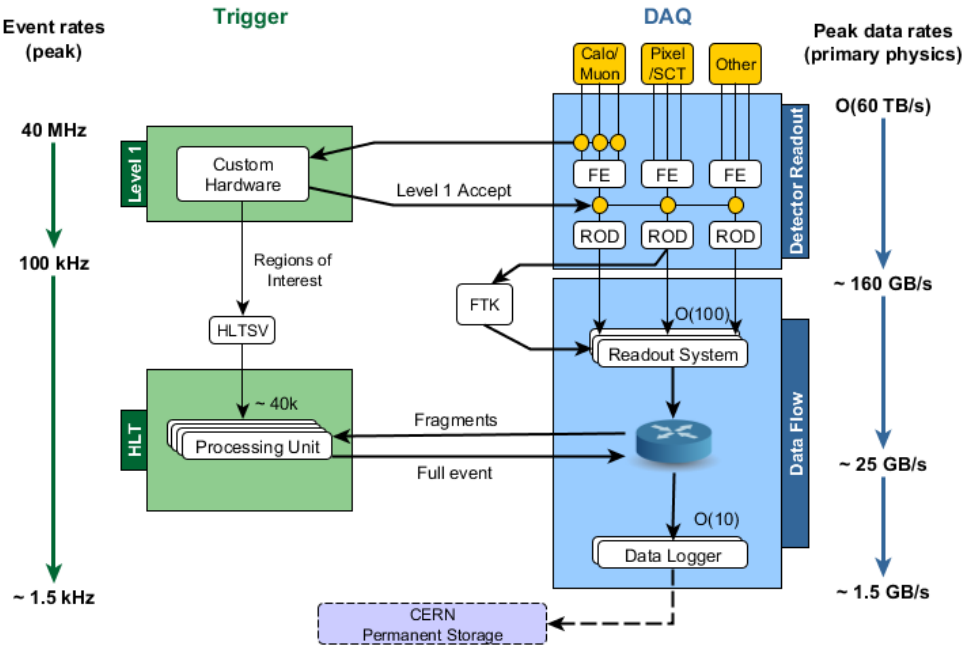

Figure 7.10: Schematic representation of the ATLAS Trigger and Data Acquisition system for Run II [148].

modules are combined in groups of two or three layers to form doublet and triplet modules. One triplet and two doublet modules are used to form the middle endcap disk, and one doublet module for the inner endcap disk.

7.5 Trigger System

The whole ATLAS detector consists of roughly 100 million electronic readout channels, and it typically costs about 1.5 MB to record the compressed information of a single event. Given the 40 MHz bunch crossing rate in Run II, one would need to handle a data stream of 60 TB/s if every bunch crossing is recorded and stored. The enormous amount of the data significantly exceeds the capability of the contemporary data processing and storage system. However, since the cross section for the processes of interest to the ATLAS physics program is orders of magnitude smaller than the inclusive cross section of pp collisions, the vast majority of the collision events could be safely discarded and only interesting collisions are stored for further analysis. The ATLAS infrastructure devoted to this task is known as the Trigger and Data Acquisition (TDAQ) system [145–147] as presented in Figure 7.10.

The ATLAS experiment uses a two-level real-time trigger system to reduce the recording rate down to 1 kHz of events, to stay within the bandwidth of the ATLAS data acquisition (DAQ) system. When the trigger menu contains processes that are far too often triggered on, a prescale factor can be applied to randomly select a predetermined fraction of events that passes a given trigger criteria. The trigger system consists of a hardware-based first-level trigger (L1) and a software-based high-level trigger (HLT). The L1 trigger is implemented on fast custom-built electronics located in the cavern near the detector to minimize latency. It uses coarse-granularity information from the muon chambers and calorimeters to identify Region-of-Interest (RoI) where high transverse momentum muon, electron, photon, jets or large missing transverse momentum is detected. Depending on the findings on the RoI, the Central Trigger Processor (CTP) makes the final decision on whether a trigger should be pulled by sending a *L1 accept* signal to the front-end electronics (FE) and ReadOut Drivers (RODs), requesting them to pass the whole event data downstream to buffers in the ATLAS Central ReadOut System (ROS) [149] for further trigger decision. The CTP is also responsible for preventing the front-end buffers from overflowing by controlling the deadtime between L1 accepts. The L1 trigger reduces the event rate to around 100 kHz within the maximum allowed latency of 2.5 μs. The recorded events are labeled by the CTP with a Run Number for each stable beam production (5–20 hours) and a Luminosity Block Number which is the time unit of luminosity measurement (roughly 1 minute).

Receiving the RoI information from the L1 trigger system, the HLT supervisor (HLTSV) schedules events to the HLT farm of processing units. These processing units perform object reconstruction and calibration using offline-like algorithms, based on fine-granularity calorimeter information, and precision ID and MS measurements from the full-detector event data in the ROS. For efficient HLT trigger decisions, the Fast Tracker (FTK) system is designed as a new track reconstruction system installed during Run II to perform high-speed tracking. If an event is accepted by the HLT, the event data is transferred to on-site storage disks, and then sent to the CERN data center, also known as Tier-0, for complete offline event reconstruction. The HLT trigger system is operated using a large farm of CPUs installed in a room near the cavern, with an average processing time of about 250 ms. It further reduces the event rate to roughly 1.5 kHz. Figure 7.11 shows an example of HLT trigger rates grouped by physics objects in a typical run taken in 2018.

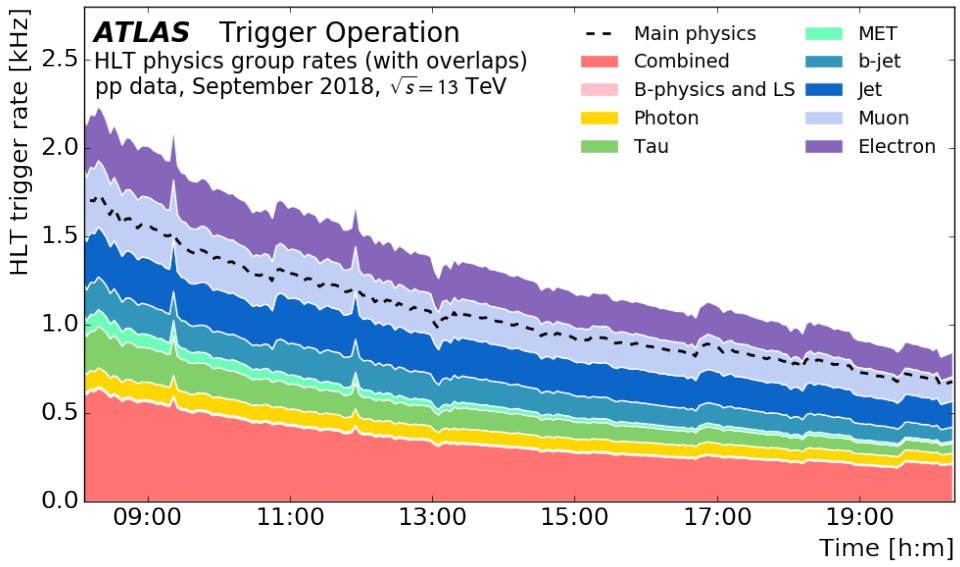

Figure 7.11: HLT rates grouped by physics objects as a function of time in a fill taken in September 2018 with a peak luminosity of $\mathcal{L} = 2.0 \times 10^{34}\text{cm}^{-1}\text{s}^{-1}$ and an average pileup of $\langle\mu\rangle = 56$ [150]. The dashed line shows the HLT main physics stream rate that takes into account the overlap between groups.

Chapter 8

Object Reconstruction

This chapter describes the reconstruction and identification of various physics objects from the tracks and energy measured with the ATLAS detector. As illustrated in Figure 8.1, leptons, photons and hadrons could be distinguished based on the contrasting ways they behave throughout the ATLAS detector. First of all, Section 8.1 gives an overview of track and vertex reconstruction. The signatures in the first analysis (presented in Chapter 11) searching for heavy resonances are photons and hadron jets, of which the reconstructions are described in Section 8.2 and Section 8.4 respectively. For the other analysis (presented in Chapter 12) that searches for leptoquarks, the physics objects of interest in the final states are electrons (Section 8.2), muons (Section 8.3) and hadron jets (Section 8.4). Stable neutral weakly-interacting particles like neutrinos are invisible to the detector, and thus their presence would lead to missing transverse energy. The computation of missing transverse energy is summarized in Section 8.5. Finally, Section 8.6 introduces a list of event cleaning requirements for ensuring high data quality.

8.1 Track and Vertex

A track is a collection of clusters of connected hits in the Inner Detector (see Section 7.2 for the mechanism of the sub-detector), which reconstructs the trajectory of a charged particle, and from the curvature of which the momentum of the charged particle can be determined when given the applied magnetic field. Five parameters are used to describe a track [152]: the transverse impact parameter d_0 and longitudinal impact parameter z_0, which measure the distances from the point of closest approach to the nominal interaction point or primary vertex in the x–y plane and the z-axis respectively; the azimuthal angle ϕ and polar angle θ to represent the initial direction of the momentum at the point of closest approach or primary vertex; and the ratio q/p, defined as the multiplication of the particle charge and the inverse of the momentum, to indicate the curvature radius in the magnetic field.

The main track finding algorithm adopts an inside-out reconstruction [153, 154]. First, it starts

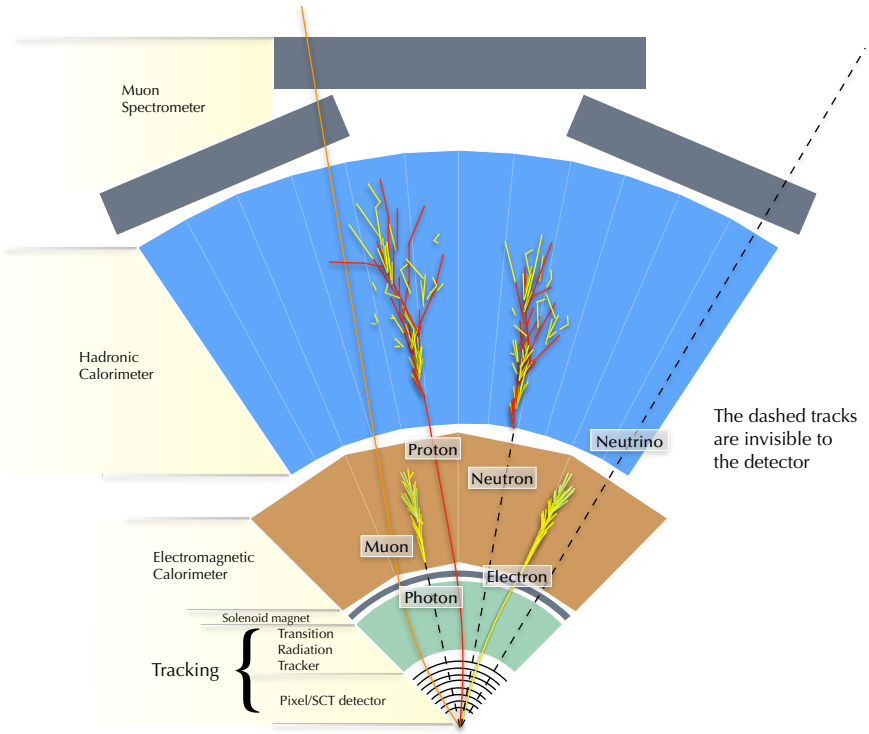

Figure 8.1: A cartoon illustration of how different particles interact with the ATLAS detector, giving rise to their distinctive signatures. Figure adapted from Ref. [151].

from gathering the three-dimensional *space-points* at which silicon detector hits are located. When a charged particle traverse a silicon sensor cell at an angle, or more than one charged particle traverses neighboring cells, signals can be detected in neighboring cells and are grouped together as a cluster. To resolve the merged clusters from close-by particles, a neural network is employed to estimate the multiplicity of particles and the position of the traversing point [155, 156], where the resultant positions are then utilized to form the collection of space-points. Track seeds are constructed from a triplet of space-points, and subsequently, if they pass quality requirements, fed into a Kalman filter [157] to build track candidates by combining with other compatible space-points along the seed path. An ambiguity solver is then called to perform a global χ^2 fit for determining the track parameters, as well as resolving shared space-points. The solver runs recursively on the track candidates in a rank order calculated with a score function that prioritizes good track candidates. The score function rewards tracks that have hits in the Pixel Detector and high number of hits, and penalizes tracks with shared hits or unexpected missing hits along its path. Tracks surviving the ambiguity solver are then extrapolated to the TRT and combined with any associated drift tube hit that leads to improvement in a final track fit. To reconstruct the tracks originating from the secondary vertices of

long-lived particles and photon conversions, a subsidiary outside-in track finder is implemented to extend the reconstructed track segments in the TRT back into the SCT for any compatible hits.

While vertices are the locations where multiple tracks intersect, a primary vertex is defined as the reconstructed position of a pp collision. The primary vertex finding algorithm adopts an iterative fitting-after-finding approach [158, 159]. First, the distribution of the longitudinal impact parameters from all the reconstructed tracks is scanned over to find the mode value. The mode value is then seeded as a vertex candidate to a fitter that uses an adaptive estimator to downweight incompatible tracks. Only compatible tracks are labeled as associated with the fitted vertex, and are removed from the collection of tracks. This procedure is then repeated by finding and fitting another vertex candidate, until no more tracks are left in the collection or no other vertex is found with the remaining tracks. Due to the high luminosity at the LHC in Run 2, each bunch crossing could yield roughly 60 primary vertices; most vertices, however, are from soft QCD interactions. Hence, the vertex with the largest $\sum p_{\mathrm{T}}^2$ of all associated tracks is defined as the hard-scattering vertex, and is used as the reference point for b-jet identification (see Section 8.4.3), whereas the rest of the primary vertices is defined as pileup vertices.

8.2 Photon and Electron

8.2.1 Energy Clustering in Electromagnetic Calorimeter

The reconstructions of electrons and photons rely on the measurement of the energy deposited by showers in the EM calorimeter. A sliding-window algorithm [160] was previously exploited in ATLAS to build energy clusters from calorimeter cells, but a new algorithm using variable-sized topological clusters, called superclusters [161], has been developed later on. The former algorithm is employed in the first analysis of this work, whereas the second analysis uses the latter algorithm. In the sliding-window algorithm, the EM calorimeter is divided into a grid of $N_\eta \times N_\phi = 200 \times 250$ towers of size $\Delta\eta \times \Delta\phi = 0.025 \times 0.025$, corresponding to the granularity of the middle layer of the EM calorimeter. The algorithm scans over the η–ϕ space with a fixed window size of 3×5 towers, in which the energy measured in each layer of the EM calorimeter is summed up. If a local maximum is found, provided that the energy in the window is above 2.5 GeV, then the maximum is considered as a seed position for the cluster, using which to determine the precise cluster direction and energy from a full window size. The full window is of size 3×5 (3×7) towers when identified as unconverted photons (electrons and converted photons) in the barrel region, and always 5×5 towers in the endcap regions. Whilst this algorithm provides excellent reconstruction efficiency of over 97% for electrons with $E_{\mathrm{T}} > 15$ GeV, the supercluster algorithm brings improvements in energy resolution and reconstruction efficiency by accounting for radiative losses due to bremsstrahlung photons or electrons from photon conversions.

The supercluster algorithm begins with EM topoclusters as seed candidates, which are formed by

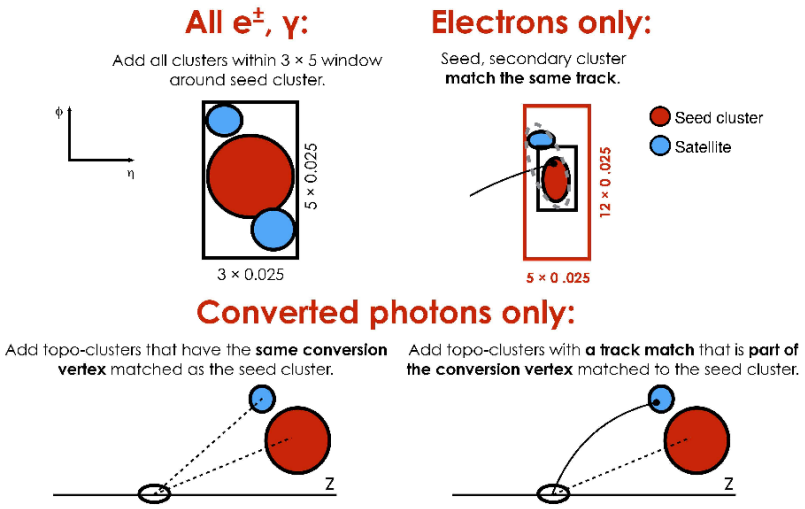

Figure 8.2: Cartoon illustrating the supercluster algorithm for electrons and photons. Figure taken from Ref. [161].

iteratively grouping neighboring cells that have significant signal-to-noise ratio in energy deposits. Figure 8.2 illustrates the key idea of the clustering algorithm. The list of topocluster seeds is looped over in the order of descending E_{T}. To be qualified as a photon supercluster seed, the topocluster must have a minimum transverse energy of 1.5 GeV. Neighboring topoclusters are considered as associated satellite clusters if they are within the window of 3×5 towers around the supercluster seed. For converted photon candidates with only tracks that contain hits in the silicon detectors, a topocluster is also added to the supercluster seed if it has the same conversion vertex, or if its matched track is compatible with the conversion vertex of the supercluster seed. On the other hand, electron superclusters are built independently, such that further classification to photons and electrons is performed afterwards depending on the matching of these energy clusters to tracks and conversion vertexes, as described in Section 8.2.2. For a topocluster to be qualified as an electron supercluster seed, it must be matched to a track containing more than three hits in the silicon detector, and its transverse energy must exceed 1 GeV. Same as a photon supercluster seed, neighboring topoclusters are clustered to the supercluster seed if they fall within the window of 3×5 towers. For electron candidates, a topocluster is also added to the supercluster seed, if it is within the window of 5×12 around the supercluster seed and it shares the same best-matched track as the seed. In this whole process of forming supercluster, any topocluster that has been labeled as a satellite cluster will no longer be used as a seed candidate. At the end of the process, an initial energy calibration and position correction is applied to the photon superclusters and electron superclusters. More details on topological clustering can be found in Ref. [160, 162].

8.2.2 Creation of Photon and Electron Objects

Tracks and conversion vertexes are matched to the energy clusters to reconstruct photon and electron candidates, with a similar manner in the sliding-window and supercluster algorithms. A trivial case would be a candidate being reconstructed only as an electron if the cluster is compatible with a good track but not any good photon conversion vertex, or a case in which the candidate is reconstructed only as an unconverted photon if the cluster is not a good match with any track. Other cases involve some complications to reconstruct converted photons and electrons using tracks that are part of a conversion vertex. There are two types of conversion vertexes, namely double- and single-track conversion vertexes, for both of which an electron hypothesis is tested using information from the TRT to ensure that the tracks are likely electron ones. Double-track conversion vertexes are reconstructed from a pair of oppositely charged tracks, whereas single-track vertexes are individual tracks without hits in the innermost layers of the pixel detector. These double- and single-track vertexes are further categorized based on whether the tracks have silicon hits or not, and labeled as Si- and TRT-tracks respectively. A series of selections is applied to the energy clusters matched to these different kinds of conversion vertexes to identify converted photons and electrons. When a clear decision cannot be made, the object is marked as ambiguous, and reconstructed as both electron and photon, leaving the final classification to each analysis based on their strategy. A complete description of the procedure, as well as the minor difference between the sliding-window and supercluster algorithms, could be found in Ref. [161].

Once the energy clusters are reconstructed as electron and photon objects, the electron and photon energies are calibrated using mostly the same procedure [163]. A simulation-based calibration is performed to restore energy resolution by estimating the impact of upstream material of the calorimeter using a multivariate regression algorithm, which is applied to data and simulation. An equalization of longitudinal energy response among the different layers of the EM calorimeter is applied to the data. Another adjustment for the local uniformities in the calorimeter response is applied to the data, based on measurement studies regarding the ratio of calorimeter energy deposit to track momentum using $Z \to ee$ events. Finally, calibration factors of energy scale and resolution is derived from $Z \to ee$ events and applied universally to electrons and photons. The applicability to low-energy electrons and photons is verified using $J/\Psi \to ee$ and $Z(\to ee)\gamma$ events respectively.

8.2.3 Identification

To further enhance the purity of photon objects and reject non-prompt photons from hadronic jets, two levels of identification criteria, labeled as *Tight* and *Loose* operating points, are defined based on a range of measurements that characterizes shower shapes related to the second EM calorimeter layer and any leakage into the hadronic calorimeter. Additionally, the *Tight* operating point also consider shower shapes in the finely-segmented first layer of the EM calorimeter, as it helps reject highly collimated pairs of photons from $\pi^0 \to \gamma\gamma$ decays. In contrast to the *Loose* one, the *Tight*

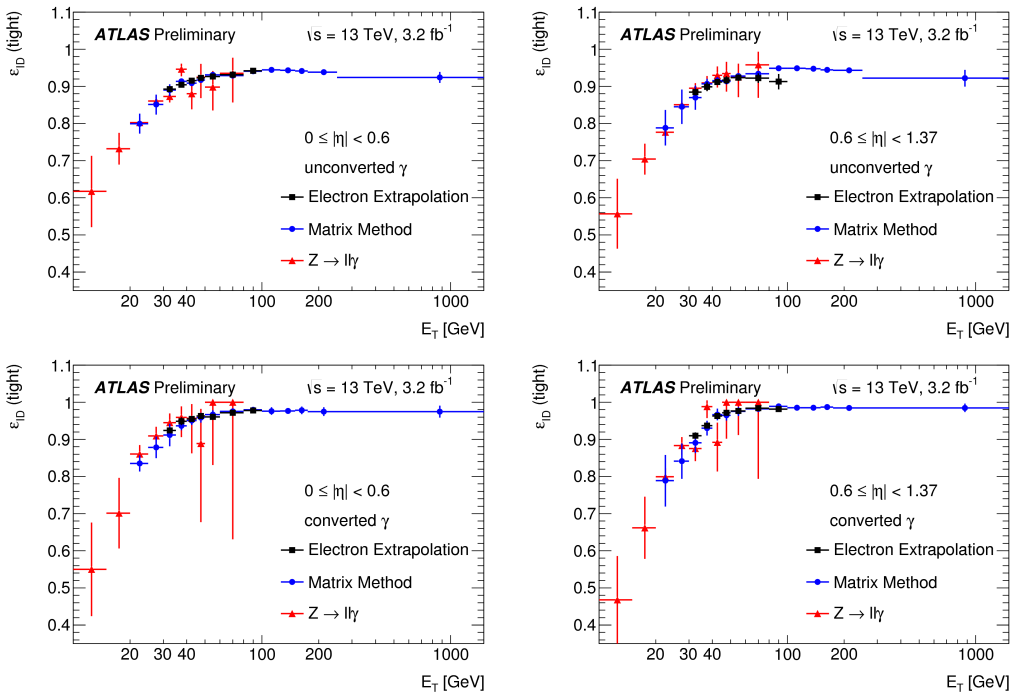

Figure 8.3: The identification efficiency for unconverted and converted photons as a function of E_{T}, measured from radiative Z decays, extrapolation from $Z \to ee$ events, and matrix method. Figures taken from Ref. [164].

operating point is optimized separately for converted and unconverted photons in bins of $|\eta|$ and E_{T}. While the *Loose* operating point is used to trigger on photon objects in this dissertation, the *Tight* one is applied to obtain high-quality photons in the offline analysis. The efficiency of the *Tight* identification operating point in the central region ($|\eta| < 1.37$) is shown in Figure 8.3, as a function of E_{T}.

In a similar fashion, a likelihood-based classifier is designed to identify prompt electrons from three main sources of undesirable backgrounds, including misidentified light hadrons, photon conversions, and non-prompt electrons from heavy flavor decays. In addition to variables that quantify shower shape and hadronic leakage, track-quality and track-cluster matching informations are also included for their separation power. In particular, transition radiation photons in the TRT are used as an indicator to discriminate against hadronic background. Three ATLAS operating points, *Tight*, *Medium* and *Loose*, are optimized in bins of $|\eta|$ and E_{T}. Figure 8.4 shows the data efficiencies of identification measured in $Z \to ee$ events. In this dissertation, *Tight* operating point is selected to guarantee high purity of prompt electrons.

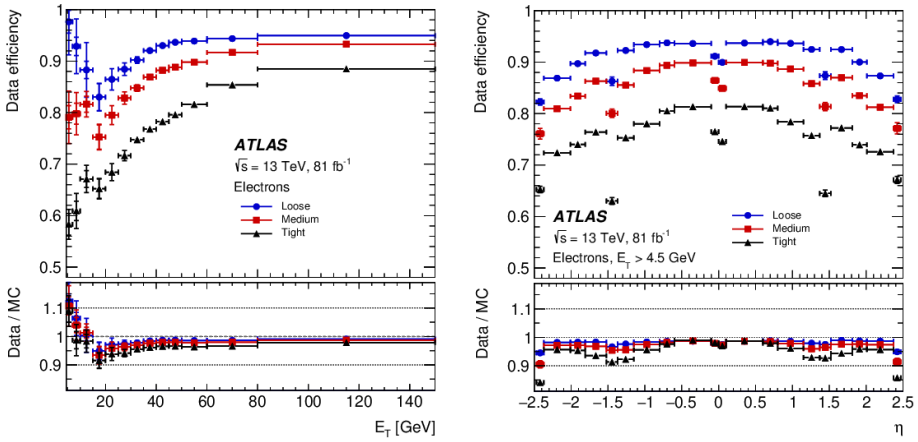

Figure 8.4: The electron identification efficiency measured with $Z \to ee$ events in data. Figures taken from Ref. [161].

8.2.4 Isolation

To suppress fake photons from hadronic backgrounds, photon candidates are required to be isolated from other objects. Calorimeter-based isolation is calculated from the transverse isolation energy $E_{\mathrm{T}}^{\mathrm{cone40}}$, defined as the sum of transverse energies of all topoclusters in the EM and hadronic calorimeters in a cone of $\Delta R = 0.4$ around the direction of the photon momentum, with the reconstructed photon energy deposit removed. Corrections are applied to subtract photon energy that leaks into the isolation cone, as well as to account for contributions from the pileup and underlying event. In this dissertation, photons are required to pass the *TighCaloOnly* operating point such that $E_{\mathrm{T}}^{\mathrm{cone40}} < 0.022\ E_{\mathrm{T}} + 2.45$ GeV. The isolation criteria has a signal efficiency around 98% over the relevant photon E_{T} range.

To maintain a high efficiency of prompt electrons selection while rejecting misidentified electron candidates from hadronic and heavy flavor decays, isolation criteria are also imposed on electron candidates. In the work presented in this dissertation, the definition of calorimeter-based transverse isolation energy employed for electron isolation is slightly different from the photon one. The transverse isolation energy $E_{\mathrm{T}}^{\mathrm{cone20}}$ of electron is computed from the sum of energy within a smaller cone size of $\Delta R = 0.2$ around the electron, but, similarly, the electron energy and pileup contributions are removed. Moreover, a track-based isolation variable $p_{\mathrm{T}}^{\mathrm{varcone20}}$ is calculated from the scalar sum of transverse momenta of $p_{\mathrm{T}} < 1$ GeV tracks, in a variable-sized cone of $\Delta R = \min(10\ \mathrm{GeV}/p_{\mathrm{T}}^{e}, 0.2)$ around the direction of the electron momentum p_{T}^{e}. The *FCLoose* operating point is used in the presented analysis, where the electron candidates are required to have $E_{\mathrm{T}}^{\mathrm{cone20}}/p_{\mathrm{T}}^{e} < 0.20$ and $p_{\mathrm{T}}^{\mathrm{varcone20}}/p_{\mathrm{T}}^{e} < 0.15$.

8.3 Muon

8.3.1 Reconstruction

Muons leave a very clean signature in the ATLAS detector due to their unique minimum ionizing property at the energy scale of the collider. Muon candidates are reconstructed independently with muon tracks in the ID and MS sub-detectors. The reconstruction of muons tracks in the ID is as described above in Section 8.1. In the MS, track segments are first formed in each muon chamber, and then used as seeds, starting from the middle layer, to extend to other layers to form track candidates. In general, a minimum of two segments is required to form a track candidate and segments can be shared by multiple track candidates. A χ^2-based fit is performed to the associated hits with the track candidates to classify whether a candidate is accepted. Four muon reconstruction algorithms are defined to exploit differently information from the sub-detectors [165]:

Standalone muons are muon trajectories solely reconstructed in MS with compatible extrapolation to the hard-scattering vertex, taking into account energy loss in the calorimeter. This recovers muons in the forward region ($2.5 < |\eta| < 2.7$), where the ID is not instrumented.

Combined muons are reconstructed from successful combination of standalone muon tracks and ID tracks. These muon candidates are the main type of reconstructed muons, but limited to the barrel region $|\eta| < 2.5$. This algorithm prevents misidentified non-prompt muons originating from in-flight decays of charged hadrons in the ID, as the momenta measured in the ID and MS are expected to be incompatible.

Segment-tagged muons are reconstructed by extrapolating ID tracks to the MS and matching at least one track segment in the precision chambers.

Calorimeter-tagged muons are reconstructed by matching tracks in the ID with minimum ionizing deposition in the EM calorimeter at the $\eta \approx 0$ region, where muon chambers are partially instrumented.

8.3.2 Identification

To suppress contributions from non-prompt muons that originate from pion and kaon decays, four identification operating points are defined with different level of requirements, namely *Loose*, *Medium*, *Tight* and *High-p_T*. The presented analysis in this work uses the *Medium* and *High-p_T* operating points, where the corresponding efficiencies measured in $Z \to \mu\mu$ events are shown in Figure 8.5.

For the *Medium* operating point, combined muons in the barrel region and standalone muons in forward regions are employed with certain requirements. Combined muon tracks are required to have at least three hits in at least two MDT layers, unless the track falls in the $|\eta| < 0.1$ region, then

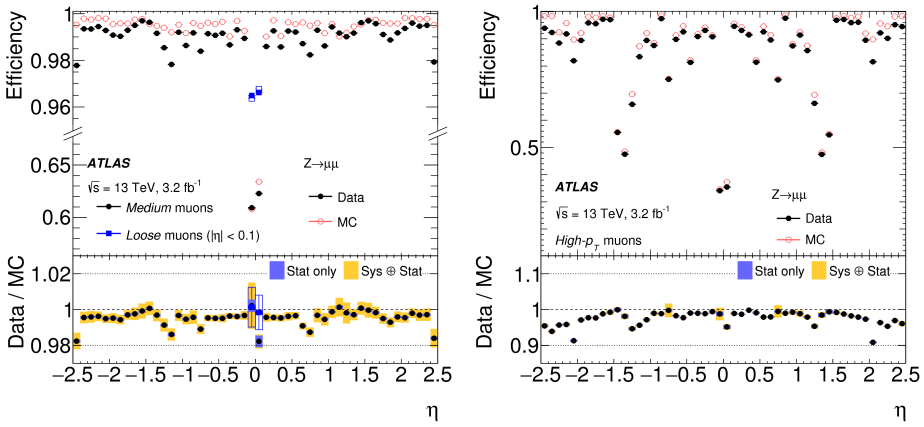

Figure 8.5: The muon identification efficiency measured with $Z \to \mu\mu$ events in data, for the *Medium* (left) and *High-p_T* (right) operating points. Figures taken from Ref. [165].

it must have at least one MDT layer and at most one hole layer. Moreover, the q/p significance is defined as the absolute difference between the charge–momentum ratio measured in the ID and MS over the quadrature sum of their uncertainties to provide identification power against hadrons that decay in flight into muons. A requirement of q/p significance less than 7 is applied to obtain high identification efficiency of prompt muons and non-isolated muons. Standalone muon tracks in the forward region are required to have hits in more than two MDT or CSC layers. The identification efficiency, determined using $t\bar{t}$ Monte Carlo samples, for prompt muons with transverse momentum $20 < p_{\mathrm{T}} < 100$ GeV is roughly constant at the 96% level.

The *High-p_T* identification operating point is designed to improve momentum resolution for high momentum muon tracks above 100 GeV. Combined muon tracks are required to have hits in at least three MDT layers with poorly aligned regions vetoed. Same as the *Medium* operating point, the q/p significance is required to be less than 7σ. Although the reconstruction efficiency is reduced by roughly 20% compared with the *Medium* operating point, the *High-p_T* operating point removes poorly measured high-p_{T} tracks, and thus allows momentum resolution to remain as good as 12-15% for muon momentum of 1 TeV.

Muon momentum is highly sensitive to the internal and relative misalignment of the ID and MS, to any inaccuracy in the description of the magnetic field, and to any miscalculated energy loss by the muons in the materials between the hard-scattering point and MS. High statistics of $J/\Psi \to \mu\mu$ and $Z \to \mu\mu$ events are used to determine the momentum resolution and scale correction, as well as the corresponding systematic uncertainties.

8.3.3 Isolation

Like electrons, there are track-based and calorimeter-based isolation variables to assess how well the muon candidate is spatially separated from other particles. The isolation operating point used in this dissertation is *FCTightTrackOnly_FixedRad*, which depends on two track-based isolation variables, $p_{\mathrm{T}}^{\mathrm{varcone30}}$ and $p_{\mathrm{T}}^{\mathrm{cone20}}$. The former variable $p_{\mathrm{T}}^{\mathrm{varcone30}}$ is calculated from the scalar sum of transverse momenta of $p_{\mathrm{T}} < 1$ GeV tracks in a variable-sized cone of $\Delta R = \min(10\ \mathrm{GeV}/p_{\mathrm{T}}^{\mu}, 0.3)$ around a muon with momentum p_{T}^{μ}. The latter variable $p_{\mathrm{T}}^{\mathrm{cone20}}$ has the same definition, except that a fixed-size cone of $\Delta R = 0.2$ is used instead. For the *FCTightTrackOnly_FixedRad* operating point, the muon candidates are required to have $p_{\mathrm{T}}^{\mathrm{varcone30}}/p_{\mathrm{T}}^{\mu} < 0.06$ for $p_{\mathrm{T}}^{\mu} < 50$ GeV; otherwise, $p_{\mathrm{T}}^{\mathrm{cone20}}/p_{\mathrm{T}}^{\mu} < 0.06$ is required.

8.4 Jet

8.4.1 Reconstruction

Jets are the experimental signatures of quarks and gluons from high-energy collisions. As a direct consequence of color confinement, free quarks and gluons are never directly observed. Instead, when high-energy partons move apart initially, the energy stored in the color field increases and eventually becomes high enough to create new quark–anti-quark pairs by breaking the field. The process continues to generate more quark–anti-quark pairs until the quarks and gluons have sufficiently low energy to cluster into color-neutral hadrons. The hadronization process results in conical showers of hadrons in the directions of the initiating partons.

Unlike electrons and photons, hadronic jets typically have wider shower shapes in the calorimeters and deposit most of their energy in the hadronic calorimeter rather than the EM calorimeter. The topologically connected calorimeter cells with significant energy deposits in the calorimeter are grouped into topoclusters [162]. In the clustering procedure, a topocluster is built by starting from a seed cell with signal-to-noise ratio $|E/\sigma_E| > 4$, iteratively adding neighboring cells with $|E/\sigma_E| > 2$ until neighbors with $2 > |E/\sigma_E| > 0$ remain, and finally including the immediate low-$|E/\sigma_E|$ neighbors.

These topoclusters are then used as jet constituents and fed into a jet reconstruction method commonly used in ATLAS, called the anti-k_t clustering algorithm [166]. It is a sequential recombination algorithm that prioritizes the clustering based on the distance d_{ij} between each pair of jet constituents i and j, and the distance d_{iB} from each constituent i to the beam, defined as:

$$d_{ij} = \min\left(\frac{1}{p_{\mathrm{T},i}^2}, \frac{1}{p_{\mathrm{T},j}^2}\right)\frac{{\Delta R_{ij}}^2}{R^2} \qquad d_{iB} = \frac{1}{p_{\mathrm{T},i}^2}, \tag{8.1}$$

where $\Delta R_{ij} = \sqrt{(\eta_i - \eta_j)^2 + (\phi_i - \phi_j)^2}$ is the distance between the constituents i and j in the η–ϕ

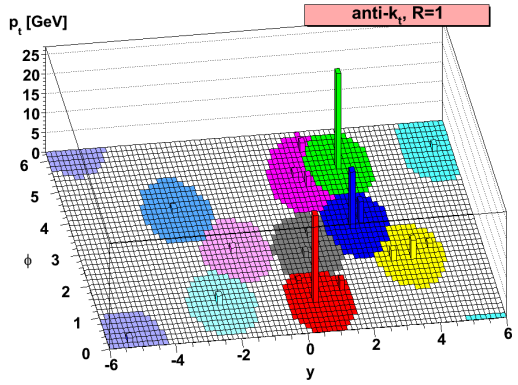

Figure 8.6: Illustration of the anti-k_t clustering algorithm with a radius $R = 1$. Figure taken from Ref. [166].

plane, and R is the free parameter regulating the output jet opening. The minimum distances among all d_{ij} and d_{iB} is identified: if it is a d_{ij} then constituents i and j are combined into a new constituent entity by summing their four-momenta together; if it is a d_{iB} then constituent i is considered as a jet and is removed from the list of constituents. The procedure is repeated until no constituents are left in the list. The FASTJET software package [167] is used to implement the anti-k_t clustering algorithm. In this clustering algorithm, priority is given to jet constituents with higher momentum. Soft particles will tend to cluster with close-by hard particles rather than clustering among themselves due to the term $\min(p_{\mathrm{T},i}^{-2}, p_{\mathrm{T},j}^{-2})$. Also, collinear particles will clustered first because of the factor ${\Delta R_{ij}}^2$. These properties yield infrared- and collinear-safe jet definitions, as well as resilience to changes from background contaminations. Moreover, considering the associated d_{ij} and d_{iB} terms with the hardest jet constituent, d_{ij} would be less than d_{iB} if $\Delta R_{ij} < R$, and favor the clustering of the jet constituent with the closest jet constituent within a distance of R from it. Otherwise, the hardest jet constituent would be output as a reconstructed jet. As shown in Figure 8.6, the resultant jets produced by this algorithm will always be constrained within a radius of R and tend to have a regular circular shape if there is no other hard particle nearby, making them easier to correct for detector-related effects.

In the presented analyses in this work, two types of jets are defined, one with $R = 0.4$ and the other one with $R = 1.0$. These jets are denoted as small-radius (small-R) and large-radius (large-R) jets respectively. The former one is used to identify showers that are initiated by a single parton, whereas the latter one is employed to identify hadronically decaying particles that have transverse momentum much larger than their mass. These boosted particles tend to decay into highly collimated children particles, and are thus likely to be reconstructed as a single jet with large radius. To remove the soft components in a large-R jet that emerge from underlying pileup interactions, a

jet grooming technique called trimming is applied to large-R jets in ATLAS. In the procedure of trimming, the constituents of the large-R jets are reclustered into smaller sub-jets using k_t clustering algorithm [168] with radius $R = 0.2$. If the p_{T} of the sub-jet is less than 5% of the original large-R jet p_{T}, then the sub-jet is removed. The large-R jet kinematics are then recalculated using only the remaining sub-jet constituents, resulting in a stable jet mass distribution under various pileup conditions. To improve the mass resolution of large-R jets, the jet mass is recalculated as a weighted linear combination of the trimmed mass as described above and the track-assisted mass that is defined as $m_{\mathrm{TA}} = m_{\mathrm{track}} \times \frac{p_{\mathrm{T}}^{\mathrm{calo}}}{p_{\mathrm{T}}^{\mathrm{track}}}$, where m_{track} is the invariance mass of the four vector sum of all the associated tracks to the jet, and $p_{\mathrm{T}}^{\mathrm{calo}}$ $\left(p_{\mathrm{T}}^{\mathrm{track}}\right)$ is the transverse momentum of the trimmed jet (of the four vector sum of the associated tracks). The weights depend on the individual resolution of the trimmed mass and the track-assisted mass.

8.4.2 Calibration

After reconstructing jet objects from energy clusters, a calibration procedure is performed to correct for detector effects on the jet energy measurement. Small-R jets are calibrated using a multi-stage procedure [169, 170]. First, the propagation direction of a reconstructed jet is corrected such that the jet traces back to the hard-scattering vertex while keeping the jet energy constant. After correcting the jet orientation, excess jet energy due to in-time and out-of-time pileup is removed by subtracting the average expected energy deposition from pileup contributions over the jet area, followed by a residual correction to remove any remaining pileup dependence as a function of the expected average number of interactions per bunch crossing and the number of primary vertices [171].

Then, the jet energy and pseudorapidity are rescaled to the stable final-state particle level, as well as being corrected for biases originating from transitions in the calorimeter geometry and technology. The calibration is derived, purely based on Monte Carlo simulations, from the ratio of the reconstructed jet energy E^{reco} to the jet energy on particle level E^{truth}, and parameterized as a function of E^{reco} and η. Furthermore, a procedure called the global sequential calibration (GSC) is applied to correct for effects from fluctuations in the jet particle composition and the energy distribution within the jet, using calorimeter, track and muon-segment observables [172].

Finally, an in situ calibration is performed only to data to account for disagreement in the jet energy response between data and MC simulation, due to the imperfect modeling of parton shower formation, detector response, hard scattering and underlying events [173]. The scale factors are determined from the transverse momentum balance between a jet and another well-measured recoiling reference object, typically in di-jet and Z + jets events.

The calibration of large-R jets differs slightly from that of small-R jets, but the principles are the same. One key difference is that the topoclusters used to reconstruct large-R jets are locally calibrated one-by-one via the local cluster weighting (LCW) method to correct for the non-compensating hadronic response of the calorimeters, the signal losses due to the dead material in the

detector or energy deposits below the noise threshold, and the contaminations from pileup processes. Once large-R jets are reconstructed from these rescaled topoclusters using the anti-k_t clustering and grooming algorithms as discussed above, their jet energy and pseudorapidity are calibrated to the particle-level like the small-R jets, based on MC simulation. In addition, the jet invariant mass is also calibrated, because the jet mass could be sensitive to soft contributions over its wide angle. Similarly, an in-situ calibration is performed as a final step to correct for any disagreement between data and MC simulations observed in the jet p_{T}, η and mass spectra.

8.4.3 Jet Tagging

For many physics analyses it could be beneficial to distinguish heavy-flavored quarks and hadronically-decaying bosons from light-flavor quarks and gluons. The identification of jets originating from b-quarks, W bosons, Z bosons and Higgs bosons is of particular relevance for the first analysis. In the second analysis, top tagging techniques based on jet substructure are exploited to separate leptoquark signal from background processes. Each of these jet tagging is discussed below:

b-flavour tagging

Bottom quarks fragment into relatively long-lived B-mesons, which generate jets with unique properties that other light partons do not possess. Because of the long enough lifetime at the order of picoseconds, a B-hadron created in high energy collisions could travel several millimeters away from the primary vertex before decaying, leaving a displaced secondary vertex that could be reconstructed with the high-precision tracking systems. Since B-mesons have much larger mass than the light-flavored ones, it is more likely to have high multiplicities of decay products, for instance an average of 5 charged particles per decay. b-jets also tend to have higher energy than the jets initiated by the other light partons, as B-hadrons carry around 75% of the initial b-quark momentum [174]. Furthermore, most B-hadron decay chains involves a decay to a D-hadron, which would give rise to a tertiary vertex that is further displaced and often close to the B-hadron flight axis. The b-tagging tool employed in this thesis combines the discrimination power of three dedicated taggers, the impact parameter tagging algorithm, the inclusive secondary vertex tagging algorithm, and the JetFitter.

The impact parameter tagging algorithm [175] is based on the measurement of impact parameter, as defined in Section 8.1. While B-hadrons give tracks with significant non-zero impact parameters, most tracks from the primary vertex have a narrow and symmetric impact parameter distribution around zero. The inclusive secondary vertex tagging algorithm [175] reconstructs a secondary vertex from associated tracks with the jet that have high impact parameters, and identifies b-jets based on the secondary vertex decay length. Other observables, like the invariant mass of the tracks associated to the secondary vertex and the fraction of jet energy carried by these tracks, are also considered to increase the discrimination power.

The JetFitter algorithm [176] uses Kalman filter to search for the common axis on which all the primary, secondary and tertiary vertices lie, assuming that the B-hadron decays into a D-hadron. The reconstructed cascade decay topology and the tracks associated to the reconstructed vertices provide discriminating information like the inclusive secondary vertex tagging algorithm.

To exploit the full topology of a b-jet and mitigate the shortcomings of the individual algorithms, the outputs of the algorithms are combined together using a boosted decision tree (BDT) to build a single multivariate discriminant, which is also known as the MV2c algorithm [175, 177]. The balance between c- and light-flavored jet rejections is controlled by tuning the fraction of c- to light-flavored jets in the training sample, and the MV2c10 algorithm chosen for this work corresponds to a 7% c-jet fraction.

***W*/*Z*/Higgs boson tagging**

To distinguish between QCD jets from large-R jets initiated by boosted W/Z/Higgs bosons, spatial proximity of the jet constituents, as well as the invariant mass of the jet, are exploited in boson tagging algorithm. Since the combined mass of a QCD jet is expected to be small, a p_{T}-dependent window cut on the jet mass around the desired boson mass can help discriminate between a boson jet and a QCD jet [178]. The difference in jet substructure is formulated using jet substructure variable $D_2^{(\beta=1)}$, which makes use of the ratios of energy correlations functions that construct a complete representation of the jet by combining the p_{T} and angular separation of all individual, pairs and triplets of jet constituents [179, 180]. Window around the jet mass and upper bound on $D_2^{(\beta=1)}$[1] are tuned to achieve 50% efficiency for jets with p_{T} in the range of 200 GeV to 2000 GeV from decays of a Z or W boson, whereas jets originating from a light-flavored quark or a gluon pass this selection with efficiency between approximately 2.2% and 1.3% in this p_{T} range [181].

In addition, Z boson and Higgs boson have a branching faction of 15% and 58% into the final state of $b\bar{b}$ quark pair [7], so b-tagging techniques could also help identify jets originating from these bosons. The MV2c b-tagging algorithm described above is applied to identify b-flavored track-jets that are reconstructed with radius parameter $R = 0.2$ and matched to the large-R jet of interest by ghost association [171]. The efficiency of the algorithm is 70% when applied to b-jets in simulated $t\bar{t}$ events, and roughly 0.8% for light-flavored jets [175, 182].

Top quark tagging

To identify large-R jets that are likely from the hadronic decay of a top quark, jet substructure information is exploited using the N-subjettiness and the splitting in the jet. The N-subjettiness ratio τ_{32} [183, 184] is used to determine whether a jet has a three-prong or two-

[1] The $D_2^{(\beta=1)}$ maximum cut value varies from 1 to 2.9 for jets with p_{T} in the range of 200 GeV to 2000 GeV.

prong structure. It is defined as the ratio of N-subjettiness variables τ_3 and τ_2, where τ_N describes how well the substructure of a jet resemble N or fewer subjets. Besides, the k_t splitting scale $\sqrt{d_{23}}$ [185, 186] determines the distance between the combined subjets in the second-to-last step of the reclustering with the k_t algorithm, which tends to cluster harder jet constituents last. With the three-portion split reconstructed with the k_t algorithm, one can also construct the minimum pair-wise invariant mass Q_W [187] from the final reclustered k_t subjets to identify the presence of an on-shell W boson in the large-R jet. These three jet substructure variables are employed to provide discriminating power between signal and background in the presented leptoquark analysis.

8.5 Missing Transverse Momentum

Given that the proton bunches circulating in the LHC have approximately zero transverse momentum, the sum of transverse momentum of all the particles in the final state would also have to be zero by conservation of momentum. However, weakly interacting neutral particles like neutrinos would leave the detector undetected, causing an apparent imbalance in the measured momentum in the transverse plane. The missing transverse momentum serves as a proxy for the existence of invisible particles produced in the collisions, and is defined as [188, 189]:

$$\vec{E}^{\text{miss}}_{x(y)} = -\left(\sum_{i\in\text{muons}} \vec{p}^{\,i}_{\text{T}_{x(y)}} + \sum_{i\in\text{electrons}} \vec{p}^{\,i}_{\text{T}_{x(y)}} + \sum_{i\in\text{photons}} \vec{p}^{\,i}_{\text{T}_{x(y)}} + \sum_{i\in\text{jets}} \vec{p}^{\,i}_{\text{T}_{x(y)}} + \sum_{i\in\text{soft term}} \vec{p}^{\,i}_{\text{T}_{x(y)}} \right), \quad (8.2)$$

where each summation term is calculated by the vectorial sum of the momenta of the corresponding physics object, and the soft term accounts for all the tracks that are associated with the hard scattering vertex but do not match any hard physics object. While such a track-based soft term cannot include contribution from soft neutral particles, it is much more robust against pileup effects compared with a calorimeter-based one.

8.6 Data Quality Requirements

To ensure that the data is of good quality for physics analysis, shifters are assigned to monitor the detector in real-time and to assess the quality of the data collected. A *Good Runs List* (GRL) is created to certify the collision events that have stable proton beams and the full ATLAS detector operational. Over the full Run II, ATLAS recorded pp-collision data with an excellent efficiency of over 95%. Only recorded events in the GRL is used for the analyses presented in this dissertation. To ensure that the recorded events are consistent with a pp collision, instead of non-collision events like beam–gas interactions and cosmic rays, there must be a minimum of one reconstructed primary vertex with at least two associated tracks with $p_{\text{T}} > 400$ MeV. Additionally, a set of event cleaning requirements is applied to ensure that the events do not suffer from data corruption in the Tile

calorimeter, noise burst in the liquid-argon calorimeter, nor mis-identified jets stemming from non-pp-collision effects.

Part III

TRT Upgrades and Run II performance

Chapter 9

Transition Radiation Tracker Data Acquisition Upgrades for Run II

In preparation for Run II, the ATLAS detector is upgraded to cope with the increased energy and luminosity of the LHC. The TRT was initially designed to handle 80 kHz L1 trigger rate and at most 50% percentage of straw hits, which is hereafter referred to as occupancy. During Run II data taking, the goal was to trigger on collision events at 100 kHz on L1, in addition to the increase in beam luminosity to double of the initial designed luminosity. The extra detector material installed as the IBL before Run II has also pushed the expected occupancy further. The new level of luminosity corresponds to an average pileup of $\langle\mu\rangle = 60$–70, leading to an occupancy of 75%–85% in the high-z slices of the TRT endcaps. Hence, one of the TRT upgrades is to improve the capability of the readout system to meet the demand from the challenging beam conditions and the higher L1 trigger rate in Run II. The UBC-ATLAS group plays a leading role in the development of the firmware for the TRT RODs, as well as the hardware maintenance of the RODs. This chapter describes the TRT data acquisition system and the modifications in the hardware and firmware of the readout system for the upgrade. Besides, a performance study of the data processing is given in the last section of this chapter.

9.1 A Straw Tubes Detector

As described in Section 7.2.3, the TRT consists of straw tubes in which an avalanche of electrons is induced on the signal wire when a charged particle traverses a straw tube and ionizes the gas atoms filled inside. The electrons collected by the wire are amplified and read out, leading to a pulse signal whose shape depends on the distance of the traverse path from the wire, as well as the active gas properties, the voltage applied to the wire and the magnetic field. While the falling edge of the pulse signal arrives at more or less the same time for all straw tubes after being traversed by a

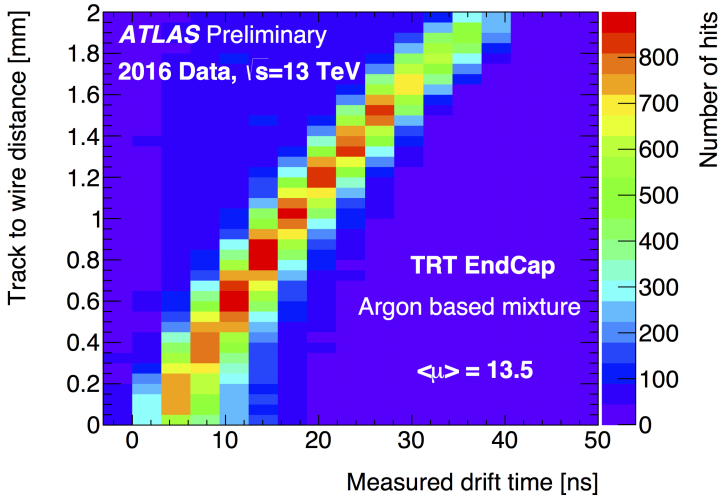

Figure 9.1: The dependency between track-to-wire distance and calibrated drift time for the TRT endcap, as obtained from $\sqrt{s} = 13$ TeV collision data in 2016. Figure taken from Ref. [190]

charged particle, the rising edge gives the arrival time of the first electron in the straw tube. Hence, the closest track-to-wire distance, r, can be inferred from the drift time, t_{drift}, measured from the leading edge at which the signal exceeds a low-level threshold (LT). The LT value is usually set to 200–300 eV. The drift time is calibrated by an offset, t_0, that takes into account the collision time with respect to the TRT readout window, the time-of-flight for the charged particle to travel from the collision point to the straw, and the signal propagation time for the signal to travel along the wire to the readout electronics. Figure 9.1 shows the relationship between the best-fit track-to-wire distance and calibrated drift time for the TRT endcap.

Transition radiation production [191] is a main feature of the TRT for electron identification. Radiators are inserted between straw tubes such that ultra-relativistic particles emit electromagnetic radiation when they travel across the boundary between the radiator material and the air gap. The expected number of emitted photons at the boundary is roughly proportional to the fine structure constant, so the radiator mats are made of many fibers or thin foils spaced by air gaps to maximize the number of medium transitions. The radiation is sizable for emission angle $\theta \lesssim 1/\gamma$, and hence confined to a small cone around the incident particle. The energy radiated per boundary between air and the radiator medium is approximately given by

$$I = \frac{4\pi}{3}\alpha z^2 \gamma \omega_p, \tag{9.1}$$

where α is the fine structure constant, z is the charge of the incident particle, γ is the Lorentz

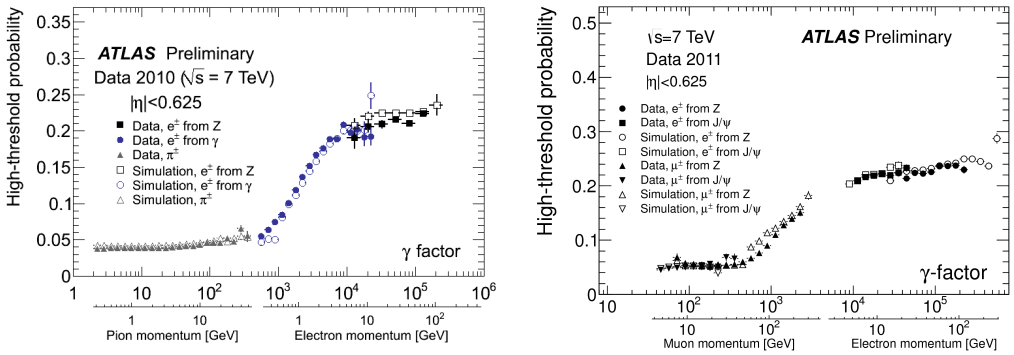

Figure 9.2: The probability of exceeding the high level threshold for electron, pion and muon candidates, as a function of the Lorentz gamma factor, in the TRT barrel. The left plot is evaluated using pions, electrons from photon conversions and electrons from Z boson decays in 2010 data events, taken from Ref. [192]. The right plot is evaluated using electrons and muons from Z boson or J/Ψ decays in 2011 data events, taken from Ref. [193].

factor and ωp is the plasma frequency for the radiator material. The polypropylene radiator in the TRT has a plasma frequency of roughly 20 eV, which is much larger than the plasma frequency of 0.7 eV in air. Since electrons are much lighter and much more likely to be ultra-relativistic than other particles like pions, the emitted transition radiation would have a much higher energy. Thus, a high-level threshold (HT) around 6–7 keV is applied to identify electrons. Figure 9.2 shows the per straw probability of electrons leaving a high-threshold hit as a function of momentum, compared to muons and pions. As the average number of straw hits in the TRT is about 35, the up to 20-25 percent per straw high-threshold probability leads to a high electron identification efficiency.

9.2 TRT Readout System

The chain of TRT readout system [194, 195] can be divided into mainly the on-detector front-end and off-detector back-end electronics as illustrated in Figure 9.3. The former electronics starts with an analog processing integrated circuit, called Amplifier/Shaper/Discriminator/Baseline-Restoration Integrated Circuit (ASDBLR), which amplifies and shapes the signal output from 8 straw tubes with preamplifier, and generates LT and HT signals with discriminator. The LT and HT signals from 2 ASDBLRs are fed into an analog-to-digital conversion circuit, called Digital Time Measurment ReadOut Chip (DTMROC), that digitizes and temporarily stores the data. As shown in the Figure 9.4, the DTMROC has a sampling rate of 320 MHz for the LT signal, yielding 8 bits per straw every 25 ns for time-of-flight information. The HT signal is sampled at 40 MHz, giving one bit for electron identification. If an L1-accept signal is received from the trigger system via the Timing and Trigger Control (TTC) partitions, three successive bunch crossings' worth of data from each straw are stored

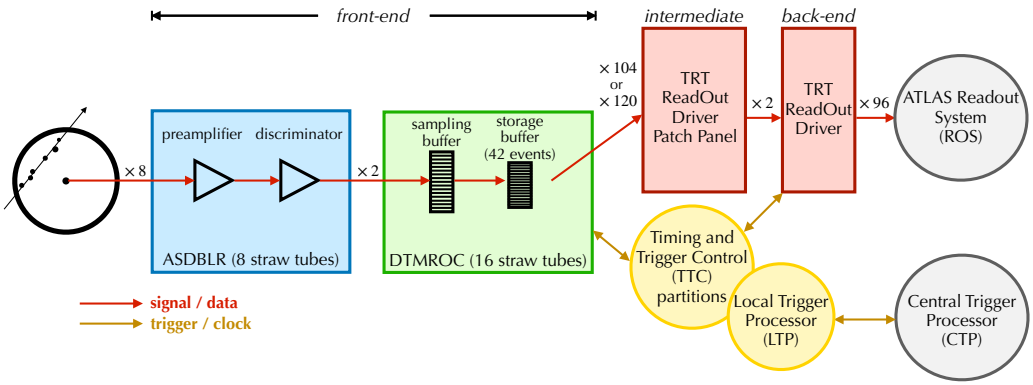

Figure 9.3: The overall schematic representation of the TRT Data Acquisition system. Created based on Ref. [195].

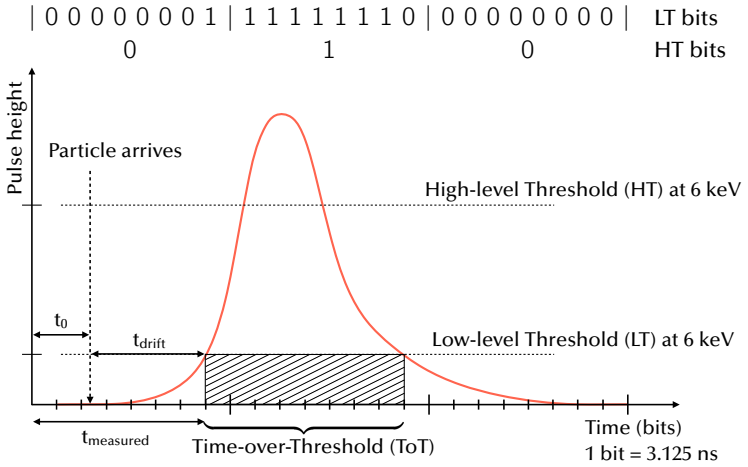

Figure 9.4: A TRT straw pulse sign in the 75 ns readout window, and the response to the low and high level thresholds. Adapted from Ref. [196].

in a buffer, along with a 3-bit preamble and a 9-bit header inserted to represent Level 1 Identifier (L1ID), Bunch Crossing Identifier (BCID) and front-end electronics error information. The buffer can store up to 42 events of data. From the buffer the data is serialized and sent further downstream to the ROD Patch Panels that are located at the MS, and then signals from 120 (104) DTMROCs are sent via optical fibers to the endcap (barrel) ROD for data compression and packing, where the upgrade work presented in this dissertation is contributed to.

The data processing on each ROD integrated circuit can be represented by Figure 9.5. A Xilinx Virtex®-2 field-programmable gate array (FPGA) receives data from the front-end electronics via two patch panels, deserializes the data, and sends each half to two Virtex-4 FPGAs, namely the top

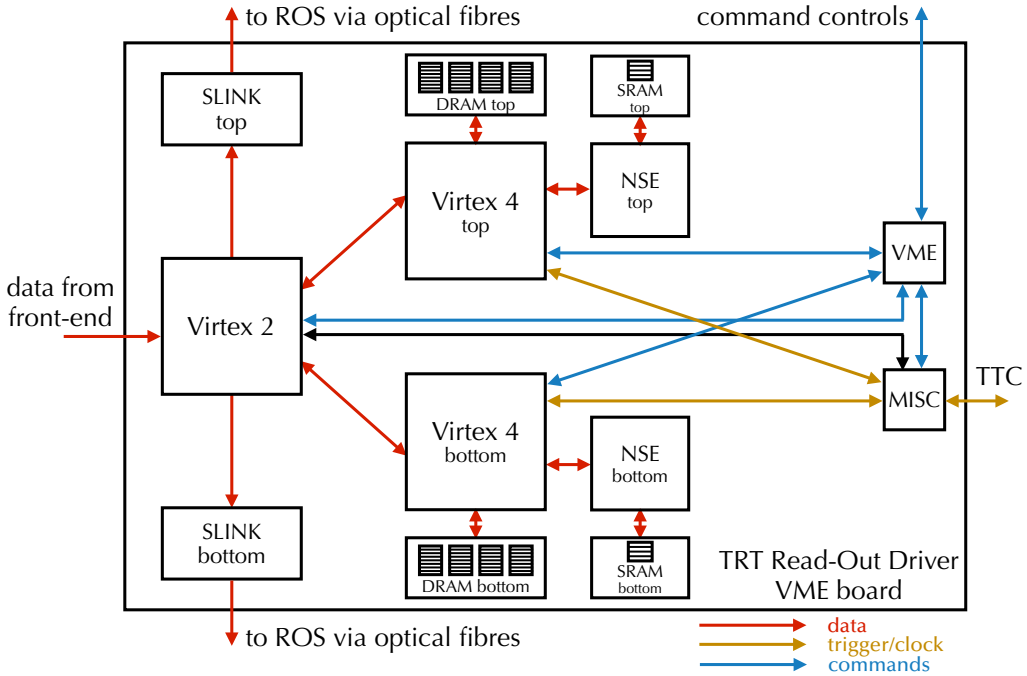

Figure 9.5: The schematic representation of the TRT Readout Driver card. Created based on Ref. [194].

and bottom ROD half. Each Virtex-4 chip checks the consistency of the BCID and L1ID sent by the front-end electronics against those received from the TTC, compresses the incoming data, and formats the data into event fragments with metadata information. Dynamic random-access memory (DRAM) is available on-board to provide storage for buffering, as the compression rate could vary from event to event depending on the data complexity. A data compression scheme is implemented using a Network Search Engine (NSE) application-specific integrated circuit (ASIC) for a high-rate lookup into a compression table which is pre-uploaded to a static random-access memory (SRAM). A Huffman-coding-based compression [197] is employed in the system, where more details are described in the next section. The formatted data for each ROD half is sent from the Virtex-4 chip back to the Virtex-2 chip, and then further downstream to the ROS [149] via the High-speed Optical Link for ATLAS (HOLA) S-LINK interface card [198]. There is a total of 32 ROD (64 ROD halves) for the barrel and 64 ROD (128 ROD halves) for the endcap. Furthermore, a Spartan®-3 FPGA, called the VME chip, is used in each ROD to regulate communication between a single board computer and the other FPGAs on the ROD via a standard VME bus. A second Spartan-3 FPGA, called the MISC chip, handles the communication with the ROD Patch Panels and the TTC, including trigger controls and metadata information.

9.3 Huffman-coding Compression Scheme

The RODs can be operated in no-compression or Huffman-compression mode. In the no-compression mode, each 27-bit straw data is contained in a 32-bit *word* at the least significant bits, while the most significant 5 bits are set to zeros. In other words, each ROD half has at most 1920 straw words in every event data block. In the Huffman-compression mode, a straw word with all zeros, the so-called *zero word*, is compressed as 1_2. If the straw word is a non-zero word, then it is compressed with the Huffman coding scheme.

The Huffman coding [197] is a lossless entropy-based compression algorithm. It is employed in the RODs to compress the 27-bit straw data. While there are, in principle, 2^{27} different possible straw-word patterns, they do not all appear at the same rate. Similar to Morse code, Huffman coding assigns shorter codewords to the more frequent patterns; nevertheless, without the need of any start bit or stop bit, the resulting variable-length codewords are uniquely decodable, as Huffman codewords are constructed from a binary tree. This decodability is a double-edged sword; while data corruption could be instantaneously detected if the data does not match with any codeword, the error will propagate to the rest of the coded sequence of bits. By construction, a Huffman tree is not wasteful and could be proven to be optimal. The expected length of the Huffman code is bounded by

$$H \leq \text{expected length of Huffman code} \leq H + 1\,, \tag{9.2}$$

where H is the information entropy [199] defined as,

$$H = -\sum_{i}^{\text{outcomes}} p_i \log_2 p_i \tag{9.3}$$

for a given probability p_i of outcome i occurring. The entropy essentially represents the exact number of bits needed on average to represent a pattern drawn from a probability distribution for a random variable. Since Huffman coding is optimal to a specific probability distribution of straw-word patterns, the assumption of the probability distribution being the same over the whole detector or under different pileup conditions might be too strong to be realistic. Section 9.5 presents a performance study of the TRT compression scheme during Run II. The compression table for the TRT DAQ system is stored in the SRAMs on the RODs, covering more than 130,000 straw-word patterns. Because the table cannot store the codewords for all possible patterns, if a straw-word pattern is encountered which is not in the table, the 27-bit straw data is processed in an uncompressed format preceded by a 5-bit escape code.

9.4 TRT Data Acquisition Upgrades

When a trigger is received by an DTMROC, the DTMROC packages three bunch crossing worth of data for 16 straws with 3 bits of preamble and 9 bits of header, and sends it serially at a 40 MHz bit

rate. For a 27-bit straw data, This gives 9 $\frac{\text{bits/straw}}{\text{bunch}} \times 3$ bunches $\times$ 16 straws $+$ 3 bits for preamble $+$ 9 bits for metadata $=$ 444 bits per event, so only a maximum of 90 kHz event rate is possible due to a front-end electronics. Fortunately, the drift velocity of electron in the straw tube is about 50 μm/ns, so the maximum time-of-flight for a 2 mm radius is roughly 40 nanosecond. Hence, it is unlikely for the signal pulse to exceed the LT in the last four LT bits. To meet the goal of 100 kHz L1 trigger rate, a reduced readout mode is implemented in the DTMROCs to shorten the 27-bit straw data to 23 bits by dropping these nonessential bits. In addition, the input bandwidth of each ROD half could only handle 160 million words per second. Since each ROD half in the endcap receives a total of 1920 straw words from 120 DTMROCs, the maximum trigger rate is limited to 83 kHz. For this reason, the running rate of the firmware implemented in the Virtex-4 chips has been increased to 200 million words per second in order to keep up with the 100 kHz trigger rate, while meeting the timing closure of the combinational logic circuit in the firmware.

An additional bit masking, called the validity gate, is implemented on the ROD firmware level to impose a programmable time window which determines the validity of a straw-word pattern. In Run II, the validity gate is set to accept a straw word only if an LT hit exists within the time window of 15.625–56.25 ns; otherwise, the whole straw word would be masked to zeros. This suppresses straw-word patterns that originate only from electronic noise or out-of-time pileup, reducing the variety and entropy of the straw-word patterns to be compressed. An average of 97% straw hits from the triggered event remains with this validity gate setting. For similar reason, a bit masking is also applied to the HT bits from the two neighboring bunch crossings, forcing them to be masked to zero at all time.

A limit on the TRT occupancy is the bottleneck in the access speed of the NSE chip which runs at 80 million straw words per second. Given that the data processing rate increases from 160 to 200 million words per second, the maximum TRT occupancy further decreases from 50% to 40%. Moreover, it is a known issue that running the NSE chip at the full rate could drive significant current on the circuitry and cause instability in data processing. To handle occupancy as high as 85%, an in-situ lookup cache feature is developed in the Virtex-4 chips to share the workload of the NSE. Due to the complexity of the Huffman compression table, a Block Random Access Memory is used to store a lookup table that contains at most 4096 straw-word pattern and their corresponding codeword. The codeword for a given straw word is first sought with the lookup cache feature; if it is not found in the shortlisted compression table stored in the in-situ cache memory, then the NSE chip is accessed to retrieve the codeword.

As shown in Figure 9.6, a hash function[1] is used to map the full space of straw-word patterns into 12-bit number as the address of the cache memory space where to store the corresponding codeword. Ideally, one would like to find the perfect hash function that would map the most frequent 4096 patterns to unique addresses to maximize the usage of the cache feature. However, such a hash

[1] Hashing is the transformation of arbitrary-sized data into fixed-length values or keys that represent the original data

function would be, in practice, difficult to find or too complicated to implement on an FPGA. The cyclic redundancy checks (CRCs) algorithm, which is widely used in data transmission to detect errors, is adopted here as the hash function. The algorithm is essentially a polynomial division in binary system, based on the exclusive-or operation. The straw word is treated as the dividend, and the remainder plays the role of the address key for a user-defined divisor as the key generator. Given the quotient and the address key, the straw word is uniquely defined for some key generator. When the ROD firmware is being configured, the codeword and quotient are stored at the generated address key for each straw-word pattern. If two or more straw-word patterns are assigned with the same address, the most frequent one is kept. With an appropriate divisor chosen, the most frequent straw words in the compression table could be cached without collision. During the data processing, the codeword for the straw-word pattern of interest is looked up from the corresponding address, and is ensured to be the matching one by cross-checking the retrieved quotient from the cache memory against the computed one. The CRCs algorithm has an attractive property of randomness in the generation of address keys. Figure 9.7 shows the expected usage of the cache feature for all possible key generators. The highest cache feature usage is achieved at the 44% level when 1001101000111_2 is used as the key generator. The corresponding usage of the cache feature and the NSE chip in bins of codeword length is shown in Figure 9.8. Figure 9.9 shows the dependence of cache-feature–to–NSE usage as a function of average pileup $\langle\mu\rangle$. The compression workload ratio of the cache feature to the NSE chip does not vary much as the average pileup increases and it remains at roughly 12:1. The cache feature has strongly improved the capability of the RODs to cope with any occupancy, assuming that the probability distribution of the straw-word patterns does not vary tremendously in scenarios of different occupancies.

Another limiting factor of the DAQ system is the output bandwidth of the RODs. The data traffic bottleneck per ROD half is the minimum bandwidth along the transmission chain from the Virtex-4 chip to the Virtex-2 chip, to the S-LINK interface card, to the ROS, which had a transmission rate of 60 million, 40 million, and 50 million words per second respectively in the beginning of Run II. Since the input data rate has increased to 200 million words per second for the 100 kHz trigger rate, the compression must be at least five-fold to avoid saturating the output bandwidth. However, the entropy of the straw-word patterns cannot be easily reduced to a low enough quantity to satisfy the compression requirement. Several upgrades are performed in both the ROD firmware and hardware to relieve the stress in the output bandwidth. While the firmware implemented in the Virtex-2 chip has been updated to double the transmission rate to the S-LINK interface card, the S-LINK interface card is also upgraded with a faster oscillator to allow a 25% larger bandwidth. This leads to a final output bandwidth of 60 million words per second, i.e. an increment of 20%, as the bottleneck has now shifted to the transmission bandwidth from the Virtex-4 chip to the Virtex-2 chip.

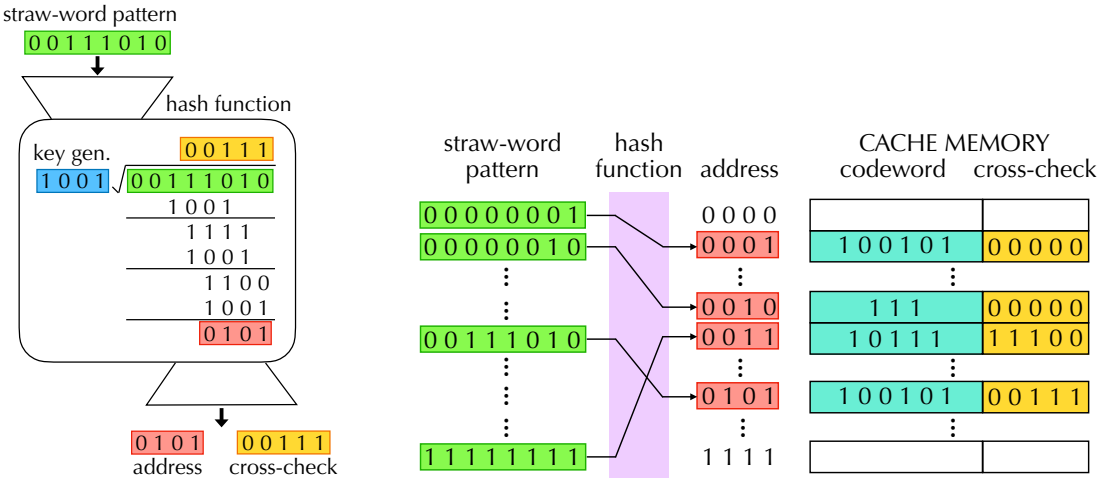

Figure 9.6: The illustration of a simplified cache feature implementation without loss of generality. For demonstration purpose only, 8-bit straw-word patterns and 4-bit address are used in this example.

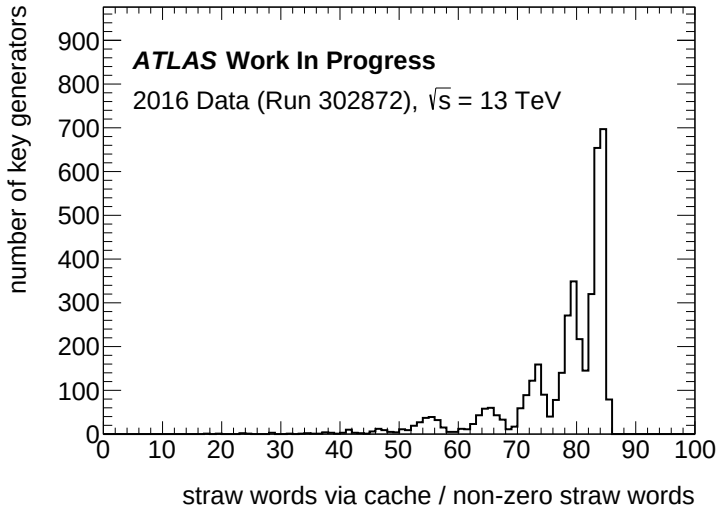

Figure 9.7: The distribution of the percentage of straw words being compressed by the cache feature over the total non-zero straw words for all (2^{12}) possible key generators, as obtained from the compression table built upon $\sqrt{s} = 13$ TeV collision data in 2016.

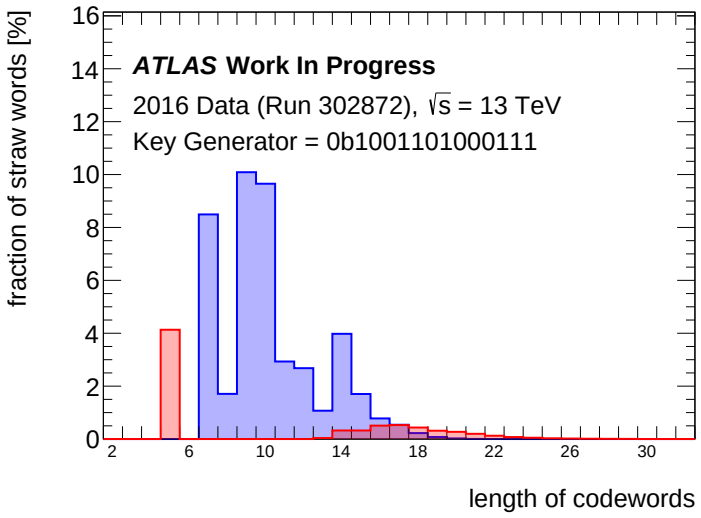

Figure 9.8: The probability of compressing a straw word using the cache feature (blue) and the NSE chip (red), in bins of codeword length, as obtained with the optimal key generator and the compression table built upon $\sqrt{s} = 13$ TeV collision data in 2016. The 4% straw words returned with a 5-bit codeword correspond to the non-zero straw words that are not compressed by the Huffman table, where the 5-bit codeword is the preceding escape code. The two histogram sums up to a total of 50% for this particular dataset that has an occupancy of 50%.

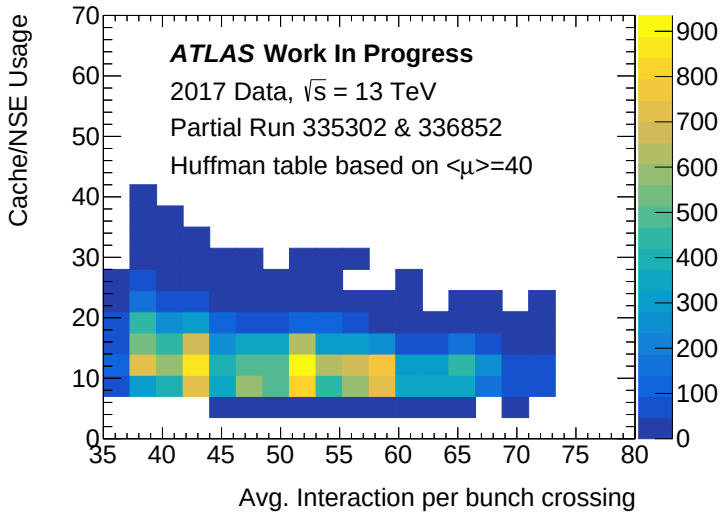

Figure 9.9: The ratio of straw words being processed by the NSE and the cache feature, as a function of average interaction per bunch crossing.

9.5 Compression Performance Study

To assess how well the TRT could cope with high luminosity and pileup, a performance study is performed to estimate the limit of the TRT. The maximum allowed entropy in the data depends on the L1 trigger rate and the 60 million words per second output bandwidth. For a 100 kHz L1 trigger rate, a ROD half can send 600 straw words downstream per event. For each event, part of the bandwidth quota is used to send 20 words for event metadata, data packet size, and end-of-file marker. Another maximum of 60 words are also attached to the formatted data to mark errors related to the front-end electronics and mismatched BCID or L1ID if they exist. Therefore, the allowed data block is left with 520–580 straw words, which is equivalent to a requirement of at most 8.7–9.7 bits per straw data on average after compression.

Data events from a fraction of the $\sqrt{s} = 13$ TeV collision data in Run Number 336852 of Fall 2017 are selected for this study for their representativeness as runs with high-pileup beam conditions; the peak average pileup in a luminosity block is $\langle\mu\rangle = 61.5$. The beams in these runs are produced with the 8b4e scheme (see Section 6.2). The third to sixth bunches of the eight filled bunches are selected to study the high occupancy scenarios. The Huffman table applied in these runs is built upon $\sqrt{s} = 13$ TeV collision data in Run Number 302872 that has a peak average pileup of $\langle\mu\rangle = 40$. The average number of bits per straw in each event is computed and plotted against the TRT occupancy as shown in Figure 9.10. While there is a clear correlation between the average number of bits and the occupancy, the endcap RODs, especially the high-z ones, have a larger data size than the barrel ones as expected from the more forward region. Some of the ROD events in the high-z endcap RODs exceed the limit even with an error block of size zero; however, they do not saturate the output bandwidth on average if the error block is small enough, as the RODs contain large buffers to absorb short-term bandwidth oversubscription. By fitting a quadratic curve to the data points under the constraint of zero words being compressed into 1 bit, the average number of bits can be determined as a function of occupancy. Considering the endcap RODs, the corresponding maximum L1 trigger rate is interpreted as a function of occupancy, as shown in Figure 9.11. The trigger rate limits for the pre-upgrade 40 million words per second output bandwidth are also plotted for comparison. The compression table was updated during Run II with Run Number 339849 to prepare for the coming Run III, as well as the rest of Run II. Figure 9.12 shows the improvement in compression efficiency by updating the Huffman table.

It would be informative to have the predicted occupancy for a given amount of pileup. Since the occupancy of the detector cannot be straightforwardly calculated from the beam luminosity or the expected pileup, the dependence of occupancy on pileup is derived directly from the data using events from a fraction of collision data in Run Number 335302 and 336852. The high-z slices of the TRT endcaps are considered in Figure 9.13 for the extreme situation. The occupancy does not increase by much as the pileup increases. It is estimated that even at an average pileup of $\langle\mu\rangle = 80$, the occupancy only reached 85% and the corresponding maximum trigger rate would be around

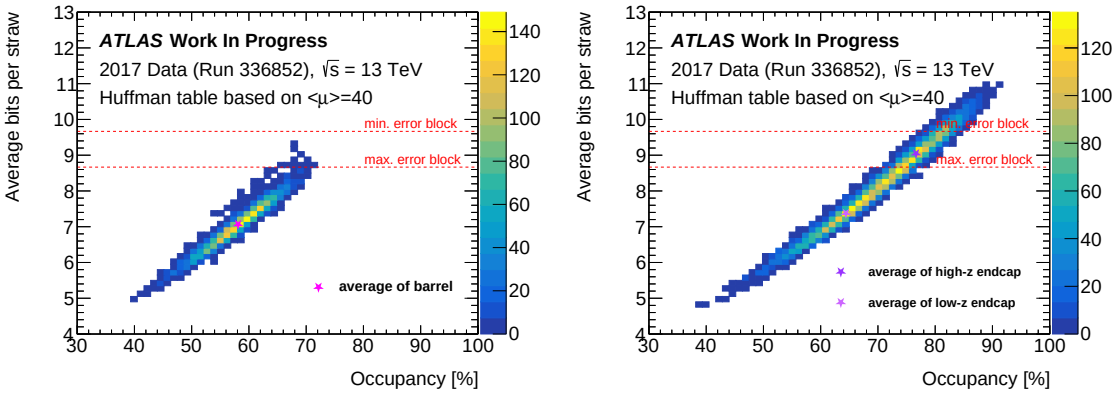

Figure 9.10: The number of average bits per straw as a function of occupancy, for the barrel (left) and endcap (right) RODs using $\sqrt{s} = 13$ TeV collision data in the Luminosity Block 118 of Run Number 336852 in 2017.

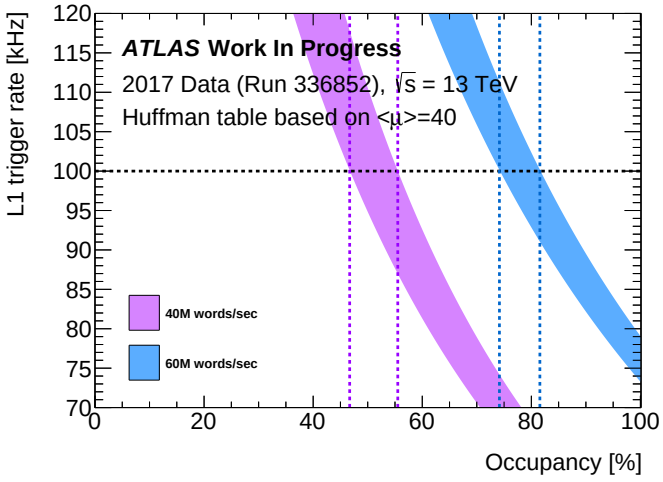

Figure 9.11: The maximum L1 trigger rate as a function of occupancy, for the endcap RODs using $\sqrt{s} = 13$ TeV collision data in the Luminosity Block 118 of Run Number 336852 in 2017. The blue (violet) band represents the range of maximum trigger rate for a given occupancy depending on the size of the error block, for an output bandwidth of 60 (40) million words per second.

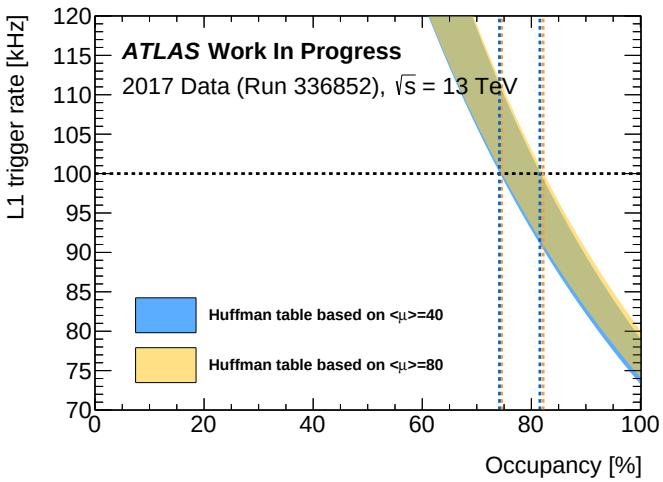

Figure 9.12: The maximum L1 trigger rate as a function of occupancy, for the endcap RODs using $\sqrt{s} = 13$ TeV collision data in the Luminosity Block 118 of Run Number 336852 in 2017. The blue (orange) band represents the range of maximum trigger rate for a given occupancy depending on the size of the error block, for a Huffman table based on collision data with $\langle\mu\rangle = 40$ ($\langle\mu\rangle = 80$).

95 kHz.

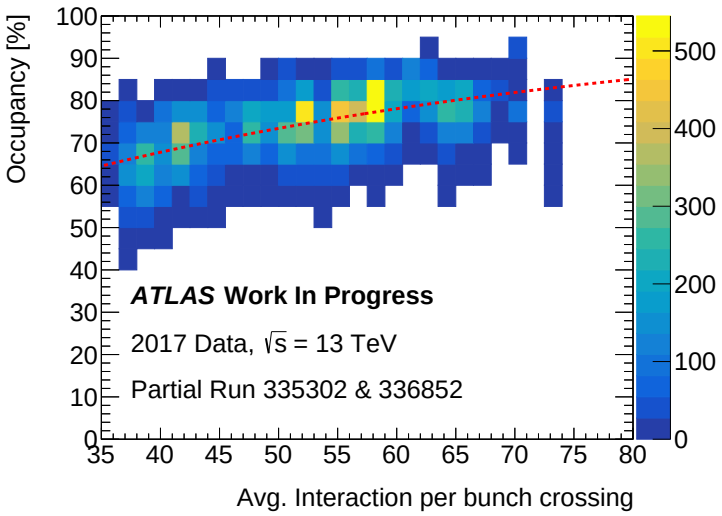

Figure 9.13: The TRT occupancy as a function of average pileup, for the high-z slices of the endcap RODs using $\sqrt{s} = 13$ TeV collision data in the a few representative luminosity blocks of Run Number 335302 and 336852 in 2017.

Part IV

Exotic Search Analyses

Chapter 10

Statistical Analysis Methods

To conclude whether new physics occur in nature, the observed collision data are compared with the background and signal predictions. This chapter describes the inference procedure and statistical techniques commonly used in Chapter 11 and 12 to quantify how consistent the observed data is with the signal hypotheses. Section 10.1 introduces the construction of a likelihood function, on which an inference procedure is based in a modified frequentist fashion as described in Section 10.2. Section 10.3 gives a brief description of the Asimov approximation for the determination of the expected test statistic.

10.1 Likelihood Construction

Let us suppose that $\vartheta = (\mu, \theta)$, with $\mu \in \mathbb{R}^p$ and $\theta \in \mathbb{R}^q$ for some $p, q \in \mathbb{Z}^+$, is the set of unknown parameters that describes a hypothesis, where μ is the parameter(s) of interest and θ is the set of nuisance parameters. In the analyses to be conducted here, as well as many other searches, the parameter of interest is typically the signal cross section σ_{sig} or the signal strength μ_{sig} that represents the scaling factor of the signal model. A signal strength of unity corresponds to the signal-plus-background hypothesis expected from the model, while a zero signal strength corresponds to the SM-background-only hypothesis.

The values of ϑ could be determined from a fit to the observed data x by maximizing a likelihood function that profiles the probability of obtaining the data given some hypothesis. The likelihood function incorporates the specific details of the analysis strategy which could vary slightly from analysis to analysis; nevertheless, it could generally be defined as the product of the measurement

likelihood and an external constraint term, $\rho(\theta)$, for the nuisance parameters:

$$
\begin{aligned}
\mathcal{L}(\mu,\theta) &= P(x|\vartheta) \\
&= \begin{cases}
\prod_{r}^{\text{regions}} \left[\prod_{i}^{N_{\text{bins}}} \text{Pois}\left(n_{r,i}|\lambda(\mu,\theta)\right) \right] \cdot \prod_{k}^{\text{syst}} \rho(\theta_k|\theta_k^0,\sigma_{\theta_k}) & \text{for binned} \\
\prod_{r}^{\text{regions}} \left[\text{Pois}\left(n_r|\lambda(\mu,\theta)\right) \prod_{j}^{\text{events}} f_r(x_j;\theta) \right] \cdot \prod_{k}^{\text{syst}} \rho(\theta_k|\theta_k^0,\sigma_{\theta_k}) & \text{for unbinned}
\end{cases} \\
&= \begin{cases}
\prod_{r}^{\text{regions}} \left[\prod_{i}^{N_{\text{bins}}} \frac{(\mu_{\text{sig}} s_{r,i}+b_{r,i})^{n_{r,i}}}{n_{r,i}!} e^{-(\mu_{\text{sig}} s_{r,i}+b_{r,i})} \right] \cdot \prod_{k}^{\text{syst}} \rho(\theta_k|\theta_k^0,\sigma_{\theta_k}) & \text{for binned} \\
\prod_{r}^{\text{regions}} \left[\frac{(\mu_{\text{sig}} s+b)^{n_r}}{n_r!} e^{-(\mu_{\text{sig}} s+b)} \right. & \\
\qquad \left. \prod_{j}^{\text{events}} \left(\frac{\mu_{\text{sig}} s}{\mu_{\text{sig}} s+b} f_{\text{sig},r}(x_j;\theta) + \frac{b}{\mu_{\text{sig}} s+b} f_{\text{bkg},r}(x_j;\theta) \right) \right] \cdot \prod_{k}^{\text{syst}} \rho(\theta_k|\theta_k^0,\sigma_{\theta_k}) & \text{for unbinned}
\end{cases}
\end{aligned}
\tag{10.1}
$$

In the binned likelihood, the measurement likelihood is defined as the product of Poisson distribution in each bin and each kinematic region, where $n_{r,i}$ is the observed number of events in bin i of region r, $s_{r,i}$ ($b_{r,i}$) is the expected number of signal (background) events which implicitly depends on θ, and θ^0 is the value of nuisance parameters from auxiliary measurements. Similarly, the unbinned measurement likelihood is also based on the Poisson distribution of the total event yield, except that the shape of the distribution is taken into account by the combined probability density function of signal and background. As a separate auxiliary measurement, the $\rho(\theta)$ term is included in the likelihood expression to constraint the nuisance parameters of the systematic uncertainties. Each constraint term is implemented as either a Gaussian or log-normal distribution. For convenience, nuisance parameters are conventionally redefined with central value of zero (or one for the case of normalisation nuisance parameters) and standard deviation of one.

The set of parameters ϑ which maximizes the likelihood function (or, equivalently, minimizes the negative log-likelihood) when all the parameters are being fitted is defined as the unconditional maximum likelihood estimate (MLE) denoted as $\hat{\vartheta}$. If one determines the MLE with part of the parameters fixed to some values, the set of fitted parameters is then referred to as the conditional MLE and is denoted as $\hat{\hat{\vartheta}}$. The mutual relationship between two parameters, θ_i and θ_j, could be studied via the correlation matrix that is defined as:

$$
\text{corr}(\theta_i,\theta_j) = \frac{\text{cov}(\theta_i,\theta_j)}{\sqrt{\text{cov}(\theta_i,\theta_i)\times\text{cov}(\theta_j,\theta_j)}}\,, \tag{10.2}
$$

where the covariance is defined as $\text{cov}(\theta_i,\theta_j) = E[(\hat{\theta}_i-\theta_i)(\hat{\theta}_j-\theta_j)]$. To examine the effect of a maximum likelihood fit on the nuisance parameters, one can look into the change in the fitted mean and standard deviation of the nuisance parameters. If a nuisance parameter has a fitted mean deviated from its initial value, then such a *pull* implies that the data prefers a different value than the

prior. Sometimes the fitted standard deviation could be smaller than the initial value, indicating that the uncertainty has been *constrained* by the data. Besides the changes in the nuisance parameters themselves, it is also beneficial to assess which uncertainty has the largest impact on the determination of μ_{sig}. The impact from each nuisance parameter is individually evaluated by fixing the parameter to its best-fit value $\hat{\theta}$ shifted by its $\pm 1\sigma$ uncertainty and comparing the resultant $\hat{\hat{\mu}}_{\text{sig}}$ value obtained from a re-fit with the nominal best-fit value $\hat{\mu}_{\text{sig}}$. The impacts before and after the best fit are assessed separately to determine the change in impact by setting the pre-fit and post-fit uncertainty of the nuisance parameter, respectively, as the $\pm 1\sigma$ shift. The pre-fit or post-fit impacts of the nuisance parameters on μ_{sig} are then *ranked* to find the most significant uncertainties.

10.2 Profile-likelihood-ratio-based Inference

To determine the underlying model of nature, statistical hypothesis testing is performed to compare various hypotheses against each other. In a hypothesis test, the compatibility of data with a null hypothesis is tested against an alternative hypothesis. One first constructs the sampling distribution of some choice of test statistic, q, under the assumption of the null hypothesis, and then determine whether to reject the null hypothesis or not based on an observed value q_{obs} computed from measurement. The probability of obtaining measured data of equal or greater incompatibility than the observed value under the null hypothesis assumption is called the p-value, i.e. $p_{\text{null}} = \int_{q_{\text{obs}}}^{\infty} f(q_{\text{null}}|H_{\text{null}})dq_{\text{null}}$. It corresponds to the probability of rejecting the null hypothesis when it is true, and it is a custom in the high energy physics community to convert the p-value into an equivalent quantity called significance, defined as $Z = \Phi^{-1}(1-p)$, where Φ is the cumulative distribution of the standard Gaussian distribution.

The test statistic commonly employed at the LHC is defined as:

$$q_\mu = -2\ln\lambda(\mu) = -2\ln\frac{L(\mu,\hat{\hat{\theta}}_\mu)}{L(\hat{\mu},\hat{\theta})}\,, \tag{10.3}$$

where $\lambda(\mu)$ is the likelihood ratio for a fixed value of signal strength μ, and $\hat{\hat{\theta}}_\mu$ is the conditional MLE for the given μ value. Such likelihood-ratio-based test statistics are justified by the Neyman-Pearson lemma which states that the likelihood ratio is the most powerful test for a fixed significance level. This test statistic only depends on μ with the nuisance parameters *profiled* out; however, the nuisance parameters are still being constrained by the auxiliary measurements, resulting in an implicit impact on μ. In a bump hunting search for the discovery of new physics, the relevant test statistic is q_0. Since only positive signal is considered as a legitimate signal, q_0 is forced to be zero if $\hat{\mu} < 0$, assuming that it is in perfect agreement with the $\mu = 0$ hypothesis. The discovery p-value is $p_{\mu=0}$ as defined above, and the criterion for a claim of discovery in the community is usually a significance of 5σ, corresponding to $p = 3\times 10^{-7}$. The reasons for such a high standard

are that the consequence of making such a false claim is huge; underestimating the level of systematic effect could bring significant impact; and the significance might be overestimated due to the look-elsewhere effect. The look-elsewhere effect refers to the problem of claiming overestimated significance due to statistical fluctuations in background when the parameter space, say resonance mass, is scanned and analyzed point by point. The probability of observing an excess in the mass spectrum increases if the discovery hypothesis is tested repeatedly at each mass point over a large range, effectively performing multiple independent experiments. The p-value determined at each fixed mass point is called the local p-value. The more relevant quantity that represents the probability of finding a signal-like excess somewhere in the search range is called the global p-value, which can be calculated by the following approximation [200]:

$$p_{\text{global}} \sim p_{\text{local}} + \langle N_{Z_0} \rangle e^{\frac{Z_0^2 - Z^2}{2}} \tag{10.4}$$

in the case of a one-dimensional scan over the signal mass, where Z_0 is some low-value reference significance, Z is the corresponding significance to the local p-value, and N_{Z_0} is the number of 'upcrossings' at which the significance becomes larger than the reference significance over the scanned mass range. The second term $\langle N_{Z_0} \rangle e^{\frac{Z_0^2 - Z^2}{2}}$ takes into account the probability of obtaining high significance due to random statistical fluctuations.

When the SM is not rejected by the observed data, the CL_s method [201] is employed to determine the signal strength limit, μ_{limit}, above which the signal strength is excluded. A modified p-value is introduced to represent the probability of a hypothesis getting rejected for a test signal strength μ_0:

$$\text{CL}_\text{s}(\mu_0) = \frac{p_{\mu=\mu_0}}{1 - p_{\mu=0}} \,, \tag{10.5}$$

where $p_{\mu=\mu_0}$ is set to one if $\mu_0 < \hat{\mu}$. The CL_s method helps preventing a small signal relative to the background getting excluded due to a downward fluctuation in the observed data, by compensating with the power of the hypothesis test. In the presented analysis, the signal-plus-background hypothesis is excluded at the 95% confidence level if $\text{CL}_\text{s} < 0.05$.

10.3 Median Significance and the Asimov Dataset

One way to obtain the probability distribution $f(q_\mu | H_\mu)$ of the test statistic is by generating pseudo-experiments many times and building a distribution from the test statistic values evaluated using the ensemble of pseudo-experiments. This method, however, is computationally expensive, especially when different μ values are scanned over in the process of an exclusion test. Alternatively, one could approximate the distribution with asymptotic formulae when the sample size is large [202]. Based on Wald's theorem, the estimator $\hat{\mu}$ is approximately distributed as a Gaussian $G(\mu_{\text{true}}, \sigma)$ and the test statistic follows a non-central chi-square distribution with one degree of freedom for a

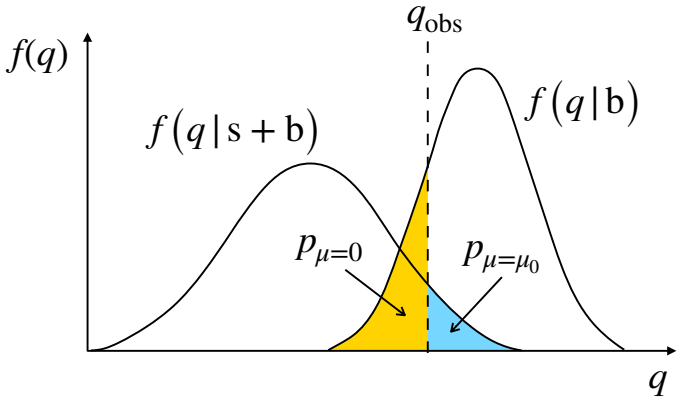

Figure 10.1: A cartoon illustration of the distribution of the test statistic under the background-only and signal-plus-background hypotheses.

single parameter of interest

$$q_\mu \sim \left(\frac{\mu-\hat{\mu}}{\sigma}\right)^2 + \mathcal{O}\left(\frac{1}{\sqrt{N}}\right) , \tag{10.6}$$

where the $\mathcal{O}\left(\frac{1}{\sqrt{N}}\right)$ term is negligible [203]. To estimate the variance of $\hat{\mu}$, the *Asimov* dataset, defined as the pseudo-experiment in which parameters are set equal to their expected values, is considered:

$$\sigma^2 \approx \left.\frac{(\mu-\hat{\mu})^2}{q_{\mu,\text{A}}}\right|_{\hat{\mu}=\mu_{\text{true}},\hat{\theta}=\hat{\hat{\theta}}_{\mu_{\text{true}}}} , \tag{10.7}$$

where μ_{true} is the true value used in the MC simulation and $q_{\mu,\text{A}}$ is the test statistics obtained from the fit to the Asimov dataset. Furthermore, given the test statistic value from the fit to the Asimov dataset, the median discovery and exclusion significance can be calculated by $\text{Median}\left[Z_0\middle|\,\mu_{\text{true}}\right] = \sqrt{q_{0,\text{A}}}$ and $\text{Median}\left[Z_\mu\middle|\,\mu_{\text{true}}=0\right] = \sqrt{q_{\mu,\text{A}}}$ respectively.

Chapter 11

$Z\gamma$ / $W\gamma$ / $H\gamma$ Resonance Search

This chapter describes an analysis that was performed to search for new massive boson resonances, X, with decay modes $X \to W\gamma$, $Z\gamma$ or $H\gamma$, which are predicted by many models of new physics. Examples of such models are technicolor [76] or little Higgs [204] models, as well as models with an extension of the Higgs sector [77] or with extra spatial dimensions [79]. New bosons predicted by these models could decay into final states containing a Z or W boson and a photon. Besides, decays of heavy spin-1 boson to the SM Higgs boson and a photon at one-loop level has been presented as an interesting search channel [80]. A variety of models is considered in the presented analysis to search for spin-0 Higgs-like, spin-1 W- or Z-like, and spin-2 graviton-like bosons.

While a search for heavy resonances can be performed in the leptonic and hadronic decay channels of the Z and W boson with very different strategies, the presented analysis solely focuses on the hadronic decay mode. Being the cleaner channel with lower SM backgrounds, the leptonic channel has a higher sensitivity to resonance masses less than 1 TeV, and thus was the only search channel for $Z\gamma$ and $W\gamma$ resonances with collision data collected at $\sqrt{s} = 7$ and 8 TeV in Run 1 [205, 206]. At larger resonance mass values, where backgrounds are generally small, the hadronic channel has the advantage of high branching fraction at 70%, dominating the sensitivity. A combined search in the leptonic and hadronic decay channels of the $Z\gamma$ resonance was published by ATLAS using 3.2 fb^{-1}of $\sqrt{s} = 13$ TeV data [207], where the hadronic channel enhanced the signal sensitivity in the lower mass region around 1 TeV and extended the search region to high mass around 2.75 TeV. While the leptonic decay channel of $Z\gamma$ resonance searches has been superseded by the analysis published in Ref. [208] using 36.1 fb^{-1}of $\sqrt{s} = 13$ TeV data collected in 2015 and 2016, this presented analysis supersedes the hadronic $Z\gamma$ channel with the same dataset. This analysis also broadens the ATLAS search program by introducing the search for hadronic $W\gamma$ resonances and $H\gamma$ resonances. In the $H\gamma$ search channel, the analysis targets the $H \to b\bar{b}$ decay mode that has a branching fraction of 58%. Figure 11.1 shows examples of lowest-order Feynman diagrams for the targeted processes.

This analysis searches for peaks in the resonance mass $m_{J\gamma}$ spectrum, targeting the high mass

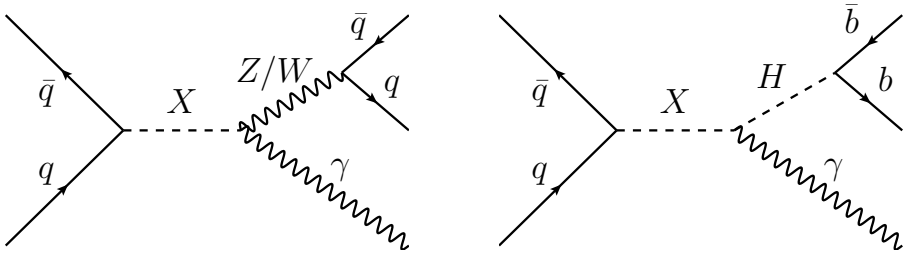

Figure 11.1: Examples of the lowest-order Feynman diagrams contributing to the heavy resonance in the targeted hadronic channel of the $X \to W\gamma$, $Z\gamma$ or $H\gamma$ decay mode.

region between 1.0 and 6.8 TeV, at which the Z, W or Higgs boson in the final state is predominantly boosted and reconstructed as a large-R jet with merged dijet energy clusters. Jet substructure information is used to infer the presence of merged jet topology, and bottom hadron tagging algorithms to identify subjets originating from b-quark fragmentation in the $X \to Z\gamma$ and $X \to H\gamma$ channels.

In this chapter, Section 11.1 summarizes the MC simulation of the studied signal and background processes, as well as the triggers employed for the data selections. Section 11.2 describes the analysis strategy and how events are selected to increase signal sensitivity. The background contributions are estimated with a data-driven method, in which signal and background are modeled using empirical fit function. The signal and background modelings are studied using MC simulations, where a discussion on the choice of functional form used as the models is included in Section 11.3. The statistical framework for the signal extraction procedure is outlined in Section 11.4, and the systematic uncertainties taken into account in Section 11.5. Finally, Section 11.6 presents the interpreted results.

11.1 Data and Simulated Samples

11.1.1 Collision Data

The search is performed with $\sqrt{s} = 13$ TeV pp collisions recorded in 2015 and 2016, corresponding to an integrated luminosity of 36.1 fb^{-1} after applying basic data quality requirements, as described in Section 8.6. Events are selected from the Egamma stream with a single-photon trigger, which requires a photon that possesses transverse energy of 140 GeV and passes the *Loose* photon identification requirement. The trigger is fully efficient with respect to the full analysis selection.

11.1.2 Signal and Background Samples

While the analysis is carried out in a data-driven manner, simulated events for signal and SM background processes are used to optimize the signal sensitivity, determine the signal efficiency, and

evaluate the parameterization of the jet-photon invariant mass spectra in signal and background modeling.

Dedicated MC generators are used to simulate events for the various signal models, in all of which a narrow-width approximation is assumed. Simulated signal events of spin-0 $Z\gamma$ resonances produced via gluon-gluon fusion [209] are generated using POWHEG-BOX [210] with the CT10 [110] PDF set, followed by PYTHIA 8.186 [211] for the parton showering and hadronization with the CTEQ6L1 [212] PDF set and the AZNLO [213] underlying-event tune. The other signal processes, spin-2 $gg/q\bar{q} \to X \to Z\gamma$, spin-1 $q\bar{q} \to X \to W\gamma$ and spin-1 $q\bar{q} \to X \to H\gamma$, are simulated with matrix elements calculated in MADGRAPH5_aMC@NLO v2.3.3 [214] and parton showering performed in PYTHIA 8.186 with the A14 [215] tune and the NNPDF2.3LO [216] PDF set. In these models, the Z (W) boson is transversely (longitudinally) polarized in the $X \to Z\gamma$ ($X \to W\gamma$) decay. To obtain the specific decay modes of interest for this analysis work, the W and Z bosons are forced to decay hadronically, and the Higgs boson is forced to decay into $b\bar{b}$.

The main SM backgrounds, in descending order of importance, are prompt photons in association with hadronic jets (γ+jets), hadronically decaying Z or W bosons produced in association with a photon ($Z/W+\gamma$), and top-quark pair in association with a photon ($t\bar{t}+\gamma$). The productions of γ+jets and $Z/W+\gamma$ processes are simulated using SHERPA 2.1.1 generator [217]. For the dominant γ+jets events, the photon is required to have a minimal transverse energy of 35 GeV, and the matrix elements are calculated at leading order (LO) with up to three or four partons, depending on the photon energy. For the sub-dominant $Z/W+\gamma$ backgrounds, the matrix elements are calculated at LO for up to three additional partons using COMIX [218] and OPENLOOPS [219] matrix element generators. In the production of γ+jets or $Z/W+\gamma$ simulation, events are then merged with the SHERPA parton shower [220] using the ME+PS@LO prescription [221] and the CT10 PDF set. For the generation of $t\bar{t}+\gamma$ process, MADGRAPH5_aMC@NLO v2.3.3 generator interfaced to PYTHIA 8.186 parton-shower model is used, with the A14 underlying-event tune and the NNPDF2.3LO PDF set. For all MC samples, the EVTGEN v1.2.0 program [222] is used to model the properties of the b- and c-hadron decays.

All signal and background events are produced with a full ATLAS detector model based on GEANT 4 [223, 224]. The effect of multiple pp interactions in the same or neighboring bunch crossings is included by overlaying with soft QCD processes modeled with PYTHIA 8.186 using the A3 tune [225] and the MSTW2008LO [112] PDF set. These events are reweighed to match the distribution of the primary pileup vertices as observed in data. A summary of the signal and background processes together with the MC generators, the orders in α_S of cross-section calculations, PDFs, parton-shower models and tunes used is given in Table 11.1.

Background process	Generator	Cross-section normalization	PDF set	Parton showering	Tune
γ+jets	SHERPA 2.1.1	LO	CT10	SHERPA	SHERPA default
$W(\to qq)+\gamma$	SHERPA 2.1.1	LO	CT10	SHERPA	SHERPA default
$Z(\to q\bar{q})+\gamma$	SHERPA 2.1.1	LO	CT10	SHERPA	SHERPA default
$t\bar{t}+\gamma$	MADGRAPH5_aMC@NLO v2.3.3	NLO	NNPDF2.3LO	PYTHIA 8.186	A14
Signal process					
spin-0 $q\bar{q}\to X\to Z\gamma$	POWHEG-BOX	LO	CT10+CTEQ6L1	PYTHIA 8.186	AZNLO
spin-2 $gg\to X\to Z\gamma$	MADGRAPH5_aMC@NLO v2.3.3	NLO	NNPDF2.3LO	PYTHIA 8.186	A14
spin-2 $q\bar{q}\to X\to Z\gamma$	MADGRAPH5_aMC@NLO v2.3.3	NLO	NNPDF2.3LO	PYTHIA 8.186	A14
spin-1 $qq\to X\to W\gamma$	MADGRAPH5_aMC@NLO v2.3.3	NLO	NNPDF2.3LO	PYTHIA 8.186	A14
spin-1 $q\bar{q}\to X\to H\gamma$	MADGRAPH5_aMC@NLO v2.3.3	NLO	NNPDF2.3LO	PYTHIA 8.186	A14

Table 11.1: The event generators and parton shower models used for the simulation of the signal and background processes.

11.2 Event Selections

All photons and large-R jets are required to pass the selection criteria described in Section 8. In order to enhance the purity of the signal in the signal region (SR), events are required to pass the following criteria:

- Events must contain at least one photon candidate with $p_{\mathrm{T}} > 250$ GeV in the barrel calorimeter, $|\eta(\gamma)| < 1.37$.
- Events are required to contain at least one large-R jet candidate with $p_{\mathrm{T}} > 200$ GeV and $|\eta(J)| < 2.0$.
- A large-R jet candidate is vetoed if it overlaps with any photon candidate within $\Delta R < 1.0$.

Since the target range of the heavy resonance is at the TeV level, the photon and large-R jet as the decay products are expected to be highly boosted. While events with a photon reconstructed in the endcap region do not add much to the signal acceptance, they also suffer from high $\gamma+$jets background; therefore only events with a photon in the barrel region are considered. The requirements on the jet η and the overlap removal between the photons and the large-R jets help reducing background from $\gamma+$jets and QCD multijet events. Events passing all of the above selection criteria are considered to be entering the baseline SR. When the event contains more than one photon or more than one large-R jet candidate, only the highest-p_{T} objects are considered for resonance mass $m_{\mathrm{J}\gamma}$ reconstruction and further selections. Due to the different spin hypothesis and production mechanism, the various resonance processes have different angular distributions for the photon-jet final state, and thus have different efficiencies with the baseline selections, as shown in Figure 11.2.

To further optimize the signal sensitivity, the selected baseline events are categorized into four or fewer subclasses, using the large-R jet mass, jet substructure and b-tagging information. Some subclasses target the lower resonance mass region below 3 TeV by applying tighter selections to enhance the purity of signal. As the background contributions fall steeply in the $m_{\mathrm{J}\gamma}$ spectrum, the other subclasses with looser selections are dedicated to increase signal acceptance in the higher $m_{\mathrm{J}\gamma}$

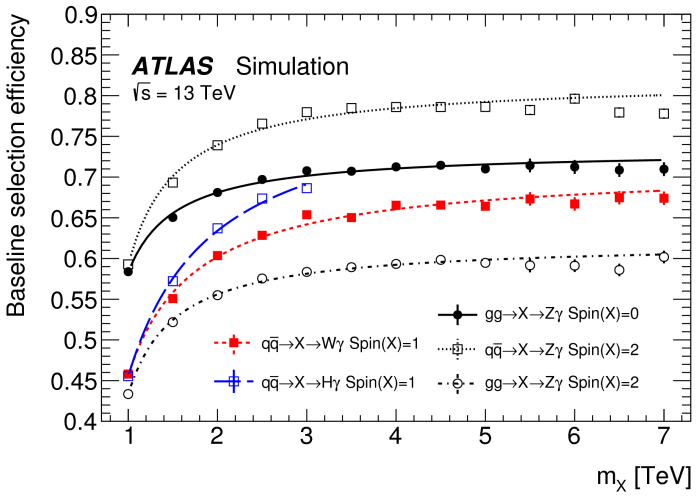

Figure 11.2: Selection efficiencies of the signal events from MC simulations as a function of the resonance mass m_X for the various $X \to W\gamma$, $Z\gamma$ and $H\gamma$ decay mode. The error bars only take into account statistical uncertainties. The lines represent the polynomial fits to the simulated mass points. The line corresponding to the $H\gamma$ resonance terminate at m_X of 3 TeV because the search does not cover the resonance mass region beyond that point. [226]

region. For the $Z\gamma$ channel, four subclasses, namely the BTAG, D2, VMASS and ELSE categories, are used to maximize signal sensitivity. The definitions of these subclasses are outlined in Figure 11.3 and detailed in the next paragraph. The $W\gamma$ channel employs only D2, VMASS and ELSE categories, and the $H\gamma$ channel uses only the BTAG category.

The BTAG category, used in the $Z\gamma$ and $H\gamma$ channels, selects events where the two leading ghost-associated track jets of the large-R jet candidate are b-tagged, providing strong background suppression. A jet mass window cut around the expected boson mass value is also applied to capture the desired boson. The range of the mass window is parameterized as a function of jet p_{T} such that a constant signal efficiency could be maintained across the spectrum. The mass window in the $Z\gamma$ channel varies from 80–106 GeV for jets with p_{T} of 500 GeV to 70–110 GeV for jets with p_{T} of 2.5 TeV. In the $H\gamma$ channel, the mass window range is plainly kept fixed at 93–134 GeV. To reject gluon-initiated jets that can mimic a two-prong substructure by gluon splitting, jets are required to have fewer than 30 associated tracks, n_{trk} [227], that originate from the primary vertex in both $Z\gamma$ and $H\gamma$ channels. The BTAG category starts to lose efficiency significantly at approximately 3 TeV, as shown in Figure 11.4. When the Z or Higgs boson is highly boosted at high resonance masses, the associated track jets become so much more merged together that the detector can no longer effectively reconstruct the fine details of these jet constituents; therefore it cannot identify the b-quark fragmentations efficiently anymore. Figure 11.5 shows the relative efficiencies of the mass window selection and the b-tagging selection separately as a function of the resonance mass,

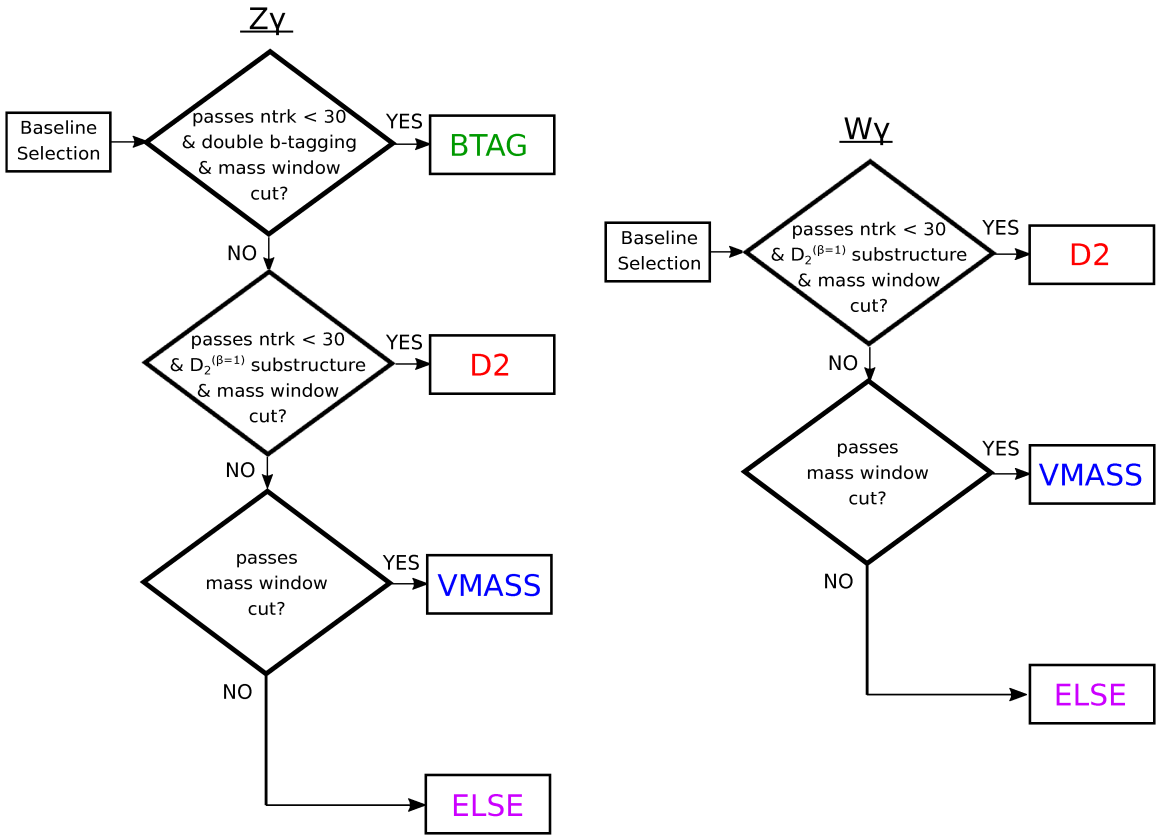

Figure 11.3: Categorization flowcharts of the events in the $Z\gamma$ (left) and $W\gamma$ (right) searches. In the $H\gamma$ search, only the BTAG category is utilized. [226]

with respect to the baseline selection. The relative efficiency of the BTAG category to the baseline selection for a $Z\gamma$ resonance mass of 1 TeV is 3% to 4%, depending on the spin hypothesis and production mechanism, while the efficiency for the background events is 0.02%. For a $H\gamma$ resonance with a mass of 1 TeV and decay mode $H \to b\bar{b}$, the relative efficiency is 25%.

Events rejected by the BTAG category criteria in the $Z\gamma$ channel and events passing the baseline selections in the $W\gamma$ channel are accepted into the D2 category if the large-R jet candidate satisfies the $D_2^{(\beta=1)}$ requirement as described in Section 8.4.3, and a jet mass window cut. The jet mass window cut in the $Z\gamma$ channel stays the same as in the BTAG category. The mass window in the $W\gamma$ channel varies from 71–95 GeV for jets with p_{T} of 500 GeV to 60–100 GeV for jets with p_{T} of 2.5 TeV. For both $Z\gamma$ and $W\gamma$ channels, the $n_{\mathrm{trk}} < 30$ requirement is also applied just as in the BTAG category. The D2 category becomes ineffective beyond 4 TeV, as the $D_2^{(\beta=1)}$ discriminating variable loses its power due to overly merged jet constituents. Relative to the baseline selections, the efficiency of the D2 category in the $m_{\mathrm{J}\gamma}$ range of 1–4 TeV is roughly constant at 20%–25% for a $Z\gamma$ resonance, depending on the spin hypothesis and production mechanism, and 40% for a $W\gamma$ resonance; meanwhile, only a small fraction of background events at 1% (0.5%) enters this category

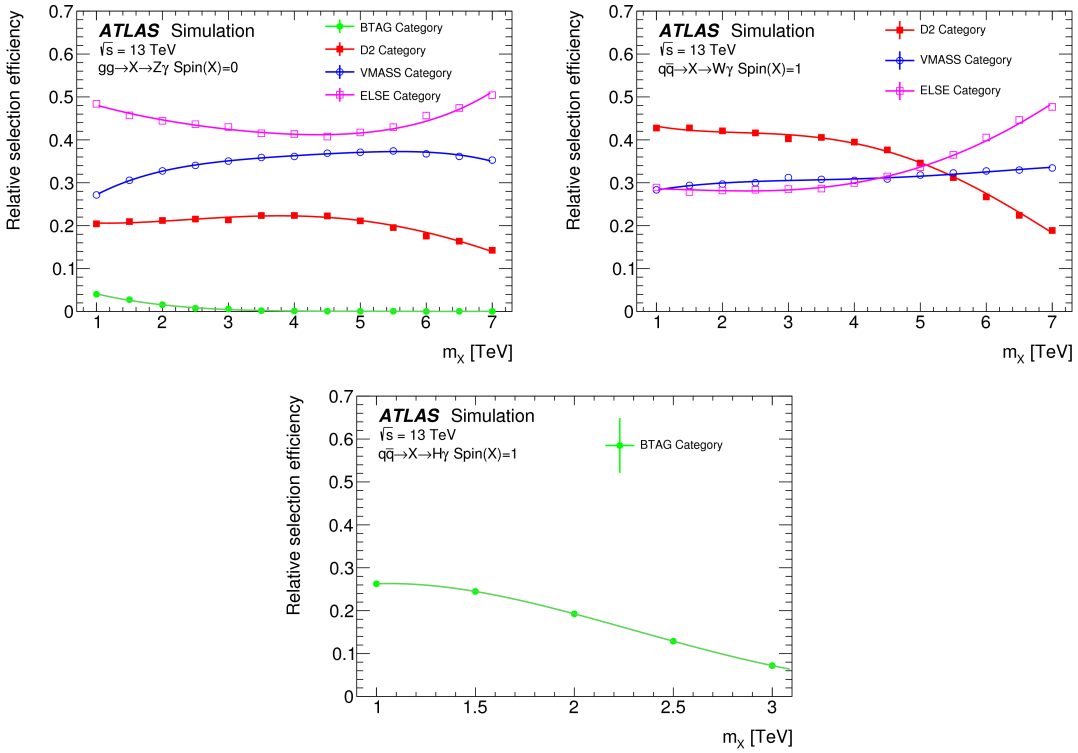

Figure 11.4: Relative efficiencies of the signal events passing the category selections with respect to the baseline selections as a function of the resonance mass m_X for the various $X \to Z\gamma$ (top left), $W\gamma$ (top right) and $H\gamma$ (bottom) decay mode. The error bars only take into account statistical uncertainties, which are found to be negligible. The lines represent the polynomial fits to the simulated mass points. [226]

after passing the baseline selections. The efficiency of D2 category between $Z\gamma$ and $W\gamma$ channels is different because the W boson is longitudinally polarized whereas the Z boson is transversely polarized, resulting in different distribution in the angular separation between the quarks originating from the Z or W boson decays.

Events not entering either of the previous two categories are included in the VMASS category if they only pass the jet mass selection as defined in the D2 category. As the signal efficiency of the BTAG and D2 categories decreases in the higher resonance mass region, the fraction of $Z\gamma$ ($W\gamma$) signal events that enter the VMASS category after passing the baseline selections grows from 25% (28%) at a resonance mass of 1 TeV to 35% (31%) at a resonance mass of 4 TeV. On the other hand, only 9% of the background events enter the VMASS category.

In the end, if an event is not accepted into any of the previous categories, it is then passed to the ELSE category. This category aims at searching for resonances in the very high mass region, where the background contribution is vastly low and thus it is prioritized to maximize signal acceptance.

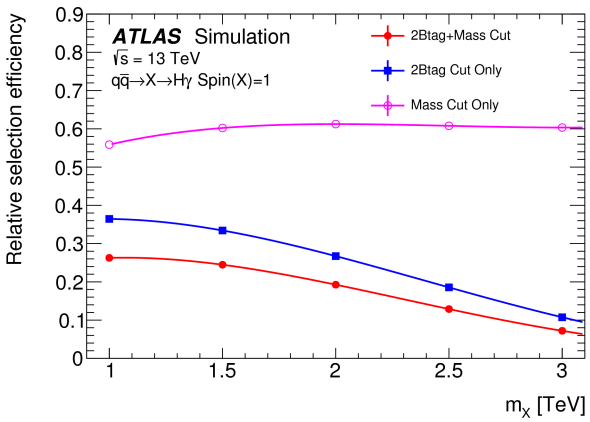

Figure 11.5: Relative efficiencies of the signal events passing the mass window selection (magenta) and b-tagging selection (blue) with respect to the baseline selections as a function of the resonance mass m_X for the various $X \to Z\gamma$ (top left), $W\gamma$ (top right) and $H\gamma$ (bottom) decay mode. The lines represent the polynomial fits to the simulated mass points. [226]

The relative signal efficiency of the ELSE category for the $Z\gamma$ ($W\gamma$) channel increases from 40% (30%) at a resonance mass of 4 TeV to 50% (48%) at a resonance mass of 7 TeV.

11.3 Signal and Background Modeling

Signal and background models are used in a maximum-likelihood fit on the $m_{J\gamma}$ distribution of the selected data events to extract the signal contribution from data. Thus, it is key to have an appropriate model. In this section, a description of the signal and background modeling approach employed in the analysis will be given, while more details on the likelihood fit can be found in Section 11.4.

The function used to describe the data can be written as

$$N_{\text{sig}} \cdot S(m_{J\gamma}) + N_{\text{bkg}} \cdot B(m_{J\gamma}), \tag{11.1}$$

where N_{sig} is the fitted number of signal events, $S(m_{J\gamma})$ is the normalized $m_{J\gamma}$ distribution for a given signal hypothesis, N_{bkg} is the fitted number of background events, and $B(m_{J\gamma})$ is the normalized $m_{J\gamma}$ distribution of the background events. The modeling of the signal peak and the smoothly falling background spectrum in the $m_{J\gamma}$ distribution, i.e. $S(m_{J\gamma})$ and $B(m_{J\gamma})$, are defined as described below.

11.3.1 Signal Modeling

In all of the categories discussed in Section 11.2, the signal shape is modeled by the sum of a Crystal Ball function [228] and a Gaussian function:

$$S(m_{J\gamma}) = f_{\mathcal{C}} \cdot \mathcal{C}(m_{J\gamma}; \mu_{\mathcal{C}}, \sigma_{\mathcal{C}}, \alpha_{\mathcal{C}}, n_{\mathcal{C}}) + (1 - f_{\mathcal{C}}) \cdot \mathcal{G}(m_{J\gamma}; \mu_{\mathcal{G}}, \sigma_{\mathcal{G}}), \tag{11.2}$$

where $f_{\mathcal{C}}$ controls the relative strength of the two distributions, $\mathcal{C}$ is the Crystal Ball function as defined in Equation 11.3, and $\mathcal{G}$ is the Gaussian function with mean $\mu_{\mathcal{G}}$ and standard deviation $\sigma_{\mathcal{G}}$.

$$\begin{aligned} &\mathcal{C}(m_{J\gamma}; \mu_{\mathcal{C}}, \sigma_{\mathcal{C}}, \alpha_{\mathcal{C}}, n_{\mathcal{C}}) \\ =&N_{\mathcal{C}} \cdot \begin{cases} \exp\left(-\frac{(m_{J\gamma}-\mu_{\mathcal{C}})^2}{2\sigma_{\mathcal{C}}^2}\right) & \text{if } \frac{m_{J\gamma}-\mu_{\mathcal{C}}}{\sigma_{\mathcal{C}}} > -\alpha_{\mathcal{C}} \\ \left(\frac{n_{\mathcal{C}}}{\alpha_{\mathcal{C}}}\right)^{n_{\mathcal{C}}} \cdot \exp\left(-\frac{\alpha_{\mathcal{C}}^2}{2}\right) \cdot \left(\frac{n_{\mathcal{C}}}{\alpha_{\mathcal{C}}} - \alpha_{\mathcal{C}} - \frac{m_{J\gamma}-\mu_{\mathcal{C}}}{\sigma_{\mathcal{C}}}\right)^{-n_{\mathcal{C}}} & \text{if } \frac{m_{J\gamma}-\mu_{\mathcal{C}}}{\sigma_{\mathcal{C}}} \leq -\alpha_{\mathcal{C}} \end{cases}, \end{aligned} \tag{11.3}$$

The Crystal Ball function is a fitting function commonly used in high energy physics to model the asymmetric shape in invariant mass reconstructions due to intrinsic detector resolution. It consists of a Gaussian core stitched by a power law tail on one side, with a nice property of being continuously differentiable. The normalization factor $N_{\mathcal{C}}$ depends on the shape parameters, $\mu_{\mathcal{C}}$,$\sigma_{\mathcal{C}}$,$\alpha_{\mathcal{C}}$ and $n_{\mathcal{C}}$, of the function, and does not add any extra degree of freedom to the functional form. The parameters $\mu_{\mathcal{C}}$ and $\sigma_{\mathcal{C}}$ are the mean and the standard deviation of the Gaussian core of the Crystal Ball function, where $\mu_{\mathcal{C}}$, as well as $\mu_{\mathcal{G}}$, is set to the true resonance mass value. $\alpha_{\mathcal{C}}$ represents the position at which the Gaussian part is in junction with the power law tail in terms of the number of standard deviations from $\mu_{\mathcal{C}}$, and is constrained to be between 0 and 4. Together with $\alpha_{\mathcal{C}}$, the parameter $n_{\mathcal{C}}$ controls the decay shape of the exponential tail, and is fixed to 1. While the Crystal Ball function describes the majority of the reconstructed events, the additional Gaussian function $\mathcal{G}$, typically with $\sigma_{\mathcal{G}} > \sigma_{\mathcal{C}}$, improves the modeling of the long tails populated by poorly reconstructed signal events.

To build a signal model for any resonance mass value, the parameters of the signal probability density function (PDF) are parameterized as a function of the resonance mass, based on the fit results using a finite set of simulated samples. For each signal model and category, the parameters are parameterized with polynomials of up to the third degree. Parameterization examples of the parameter $\sigma_{\mathcal{C}}$ are shown in Figure 11.6. For most of the signal models and categories, $\sigma_{\mathcal{C}}$ grows quite linearly by about 15 GeV per 1 TeV increment of resonance mass, starting from about 20 GeV at a resonance mass of 1 TeV. Figure 11.7 shows the comparison among the simulated events, the individually fitted signal model and the parameterized signal model for some representative mass points. Figure 11.8 shows the interpolated signal shapes between the fitted $m_{J\gamma}$ distributions of simulated MC samples for the D2 category of spin-0 $X \to Z\gamma$ and spin-1 $X \to W\gamma$ resonances, and the BTAG category of spin-1 $X \to H\gamma$ resonance.

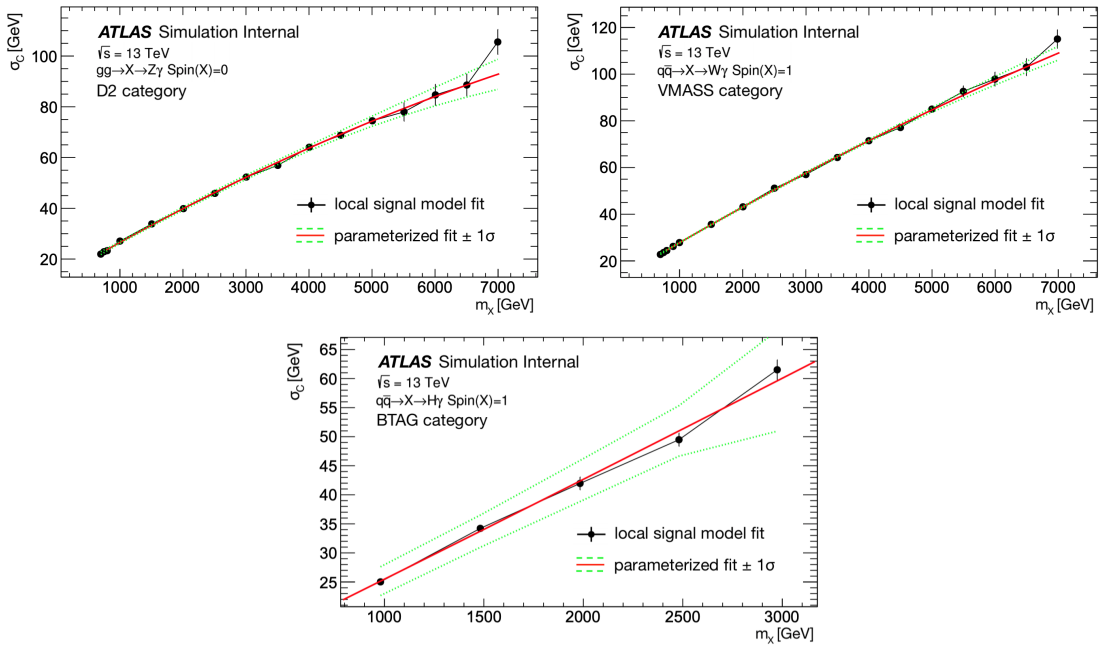

Figure 11.6: The polynomial fit of the fitted σ_C as a function of the resonance mass m_X for several representative categories and channels. The top left plot is for the D2 category of the spin-0 $X \rightarrow Z\gamma$ channel, the top right plot is for the VMASS category of the spin-1 $X \rightarrow W\gamma$ channel $W\gamma$ and the bottom plot is for the BTAG category of the spin-1 $X \rightarrow H\gamma$ channel. Each black dot represents the fitted value at the individual mass points, and the red line represents the fitted polynomial function to the fitted values, where the green line shows the 95% confidence interval of the fit.

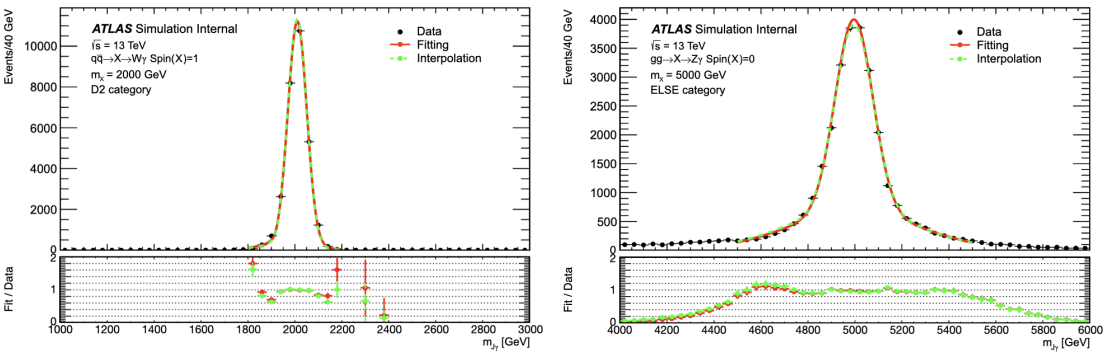

Figure 11.7: The comparison among the simulated events, the individually fitted signal model and the parameterized signal model for a resonance mass of 2000 GeV in the D2 category of the spin-1 $X \rightarrow W\gamma$ channel (left) and a resonance mass of 5000 GeV in the ELSE category of the spin-0 $X \rightarrow Z\gamma$ channel (right).

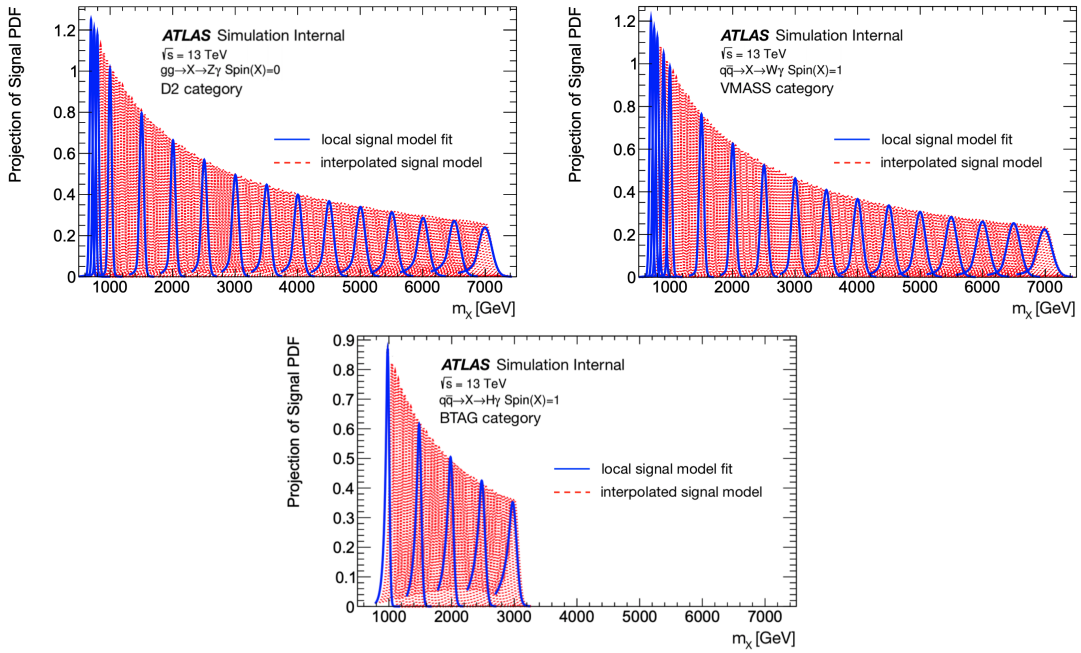

Figure 11.8: The fitted signal probability density function as a function of the resonance mass m_X for several representative categories and channels. The top left plot is for the D2 category of the spin-0 $X \to Z\gamma$ channel, the top right plot is for the VMASS category of the spin-1 $X \to W\gamma$ channel $W\gamma$ and the bottom plot is for the BTAG category of the spin-1 $X \to H\gamma$ channel. The blue line represents the fitted signal model at each simulated sample mass point, and the red line represents the interpolated signal shape from the parameterization of the modeling.

11.3.2 Background Modeling

Simulations in the various channels and categories indicate that the background processes inclusively produce a smoothly falling shape in the $m_{J\gamma}$ distribution. As the continuum background is smooth over a large mass range compared with the narrow resonance decay width, the number of background events underneath the potential signal peak is characterized by an empirical function measured directly from data through a signal-plus-background fit to the observed $m_{J\gamma}$ distribution. The background compositions will be briefly described below, followed by an overview on how the choice of background function is made and how the chosen functional form is tested for its validity.

Background Compositions

The dominant contribution to the predicted background yield is the γ+jets processes, while the production of a Z or W boson in association with a photon contributes secondarily. For events with $m_{J\gamma} > 1$ TeV in the BTAG category of the $Z\gamma$ ($H\gamma$) channels, the contributions from photon production in association with a b-flavored hadron and SM $Z+\gamma$ are 65% and 32% (85% and

13%) respectively. In the D2 category of both the $Z\gamma$ and $W\gamma$ channels, approximately 85% of the contribution is from photon production in association with a light- or c-flavored hadron, and 15% from the SM $Z/W+\gamma$ processes. In other categories, the contributions from γ+jets processes is 95%, and the SM $Z/W+\gamma$ processes are below 5%. The contribution from pair production of top quarks in association with a photon is found to be negligible for all channels and categories. Multijet events could enter the signal regions when one of the jets is misreconstructed as a photon; however, the contribution from such occurrence was estimated to be less than 10% of the events passing the baseline selections and found to be more or less constant with $m_{J\gamma}$ [207]. Therefore, the multijet and $t\bar{t}+\gamma$ production are not considered when the best background functional form is being selected, but they would still be accounted for inclusively in the data-driven background fit.

Choice of Background Modeling Functional Form

The background shape modeling in the $m_{J\gamma}$ distribution is chosen from a family of nested probability density functions similar to the one used in previous searches in dijet final state [229], tested up to five parameters:

$$B(m_{J\gamma};\boldsymbol{p}) = N_B \cdot (1-x)^{p_1} \cdot x^{p_2+p_3\log(x)+p_4\log^2(x)+p_5\log^3(x)}, \tag{11.4}$$

where $\boldsymbol{p} \equiv (p_1, p_2, p_3, p_4, p_5)$ is the vector of shape parameters, N_B is a normalization factor that depends on the shape parameters, and $x \equiv m_{J\gamma}/\sqrt{s}$ is the resonance mass scaled by the center-of-mass energy. The maximum likelihood fit is performed in different $m_{J\gamma}$ range for the various categories: 800–3200 GeV in the BTAG category, 800–7000 GeV in the D2 and VMASS categories, and 2500–7000 GeV in the ELSE category.

The number of parameters should be chosen such that the functional form is complex enough to describe the background spectrum, but not too flexible to unnecessarily accommodate statistical fluctuations or lead to instability in the likelihood fit. Typically categories with high statistics require more degrees of freedom in the fit function to competently describe the experimental features in the spectrum, whereas categories with low statistics could be adequately modeled with fewer parameters as the features are hidden by statistical uncertainties. Four requirements are employed to choose the functional form: (i) the goodness-of-fit assessed by chi-square test is satisfactory, (ii) the bias in the fitted signal due to the choice of the functional form is sufficiently small compared with the statistical uncertainties from the background, (iii) the number of parameters is minimized such that the additional parameter(s) in the more complicated functions does not significantly improve the goodness of fit, and (iv) the complexity of the functional form does not give rise to instability in the likelihood fit.

The bias stemming from the choice of functional form is studied by performing the so-called *spurious signal* test. In this test, the signal-plus-background model is fitted to a background-only

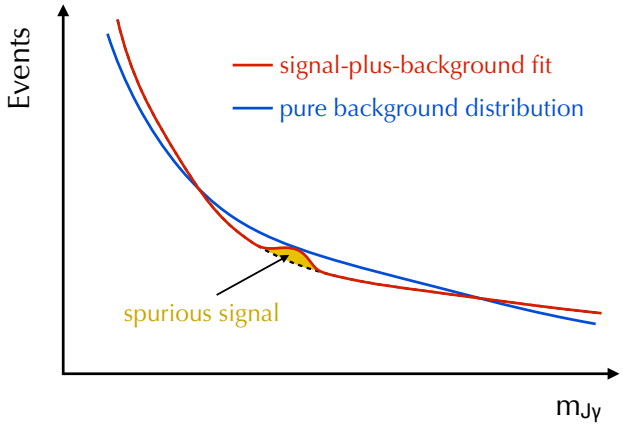

Figure 11.9: A cartoon illustration of how spurious signal could be induced in a signal-plus-background fit when the background functional form does not perfectly model the true background shape.

template based on MC simulation, scaled to the luminosity of the data and assigned with Poisson uncertainty to mimic the expected statistical power of the data. Such a fit aims at determining the number of fake signal events (N_{spur}) induced as a result of the discrepancy between the empirical function and the true background shape, assuming that the simulated sample accurately describes the true distribution. A cartoon illustration of the fit at a mass point is presented in Figure 11.9. The fitted spurious signal is compared with the Poisson error, Δ_{bkg}, on the background yield within 2σ of the signal peak. Furthermore, the background-only template in some categories is simulated with statistically limited samples, which can bring about large statistical fluctuations and thus spurious signal. To estimate the impact of MC statistical power on the spurious signal, the background-only template is fitted again with a signal-plus-background model, except that MC statistical uncertainty is assigned instead of Poisson uncertainty and the background parameters remain fixed as obtained from the previous fit. The uncertainty on the fitted number of signal events is defined as the spurious signal uncertainty, ζ_{spur}, due to the MC statistical power. A functional form is accepted if it satisfies the following spurious signal criteria:

$$N_{\text{spur}} < \begin{cases} 25\%\Delta_{\text{bkg}} + 2\zeta_{\text{spur}} & \text{if } N_{\text{spur}} > 0 \\ 25\%\Delta_{\text{bkg}} - 2\zeta_{\text{spur}} & \text{if } N_{\text{spur}} < 0 \end{cases}, \tag{11.5}$$

Figure 11.10 illustrates the criteria on spurious signal.

To assess the necessity of increasing the number of parameters in the nested functional form, F-test [230] is conducted to determine the minimum number of parameters needed to describe the background distribution. Given two models, 1 and 2, where model 1 is nested within model 2, the

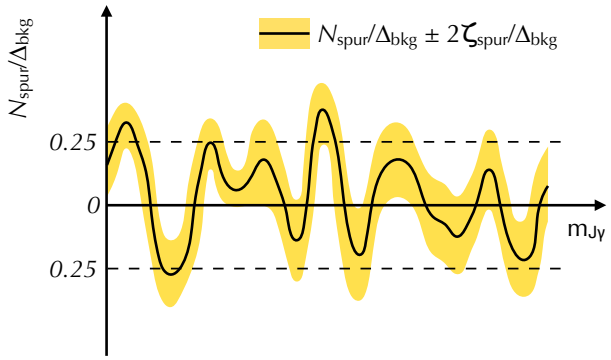

Figure 11.10: A cartoon illustration of the spurious signal requirement.

F-test statistic is defined as:

$$F = \frac{\frac{\sum_i^n \chi^2_{1,i} - \sum_i^n \chi^2_{2,i}}{d_{p_2} - d_{p_1}}}{\frac{\sum_i^n \chi^2_{2,i}}{n - d_{p_1}}}, \tag{11.6}$$

where n is the number of bins that the fit range is divided into, χ^2 is the weighted sum of squared residuals in each bin, and d_p is the number of parameters in the model. F-tests are performed to an ensemble of pseudo-experiments at different luminosities to estimate the trend of the required minimum number of parameters. The functional form, as defined in Equation 11.4, with three parameters ($p_4 = p_5 = 0$) is chosen for the VMASS category, and two parameters ($p_3 = p_4 = p_5 = 0$) for the other categories.

Validation with Pseudo-experiments

The search is kept *blinded* until the design of the analysis is finalized, with the aim of eliminating biases from the analysts' expectations. To evaluate how robust the background modeling will be on the real data, especially in the tail region of the continuum background where the data events are poorly populated, the chosen functional form is tested with pseudo-experiments before unblinding. For each channel and category, an ensemble of pseudo-datasets is generated based on the $m_{J\gamma}$ distribution of the expected background, with the total background yield of each pseudo-dataset randomly sampled from the expected Poisson distribution, and fitted with the selected functional form. Figure 11.11 shows some examples of the background fit to a pseudo-experiment for the D2 category of the $Z\gamma$ channel, the VMASS category of the $W\gamma$ channel, and the BTAG category of the $H\gamma$ channel. In general, the background fit and the MC expectation show reasonably good agreement in the tail region even when there is no event in the pseudo-dataset to fit with.

Additionally, *signal injection* tests are performed with the pseudo-experiments, in which a signal

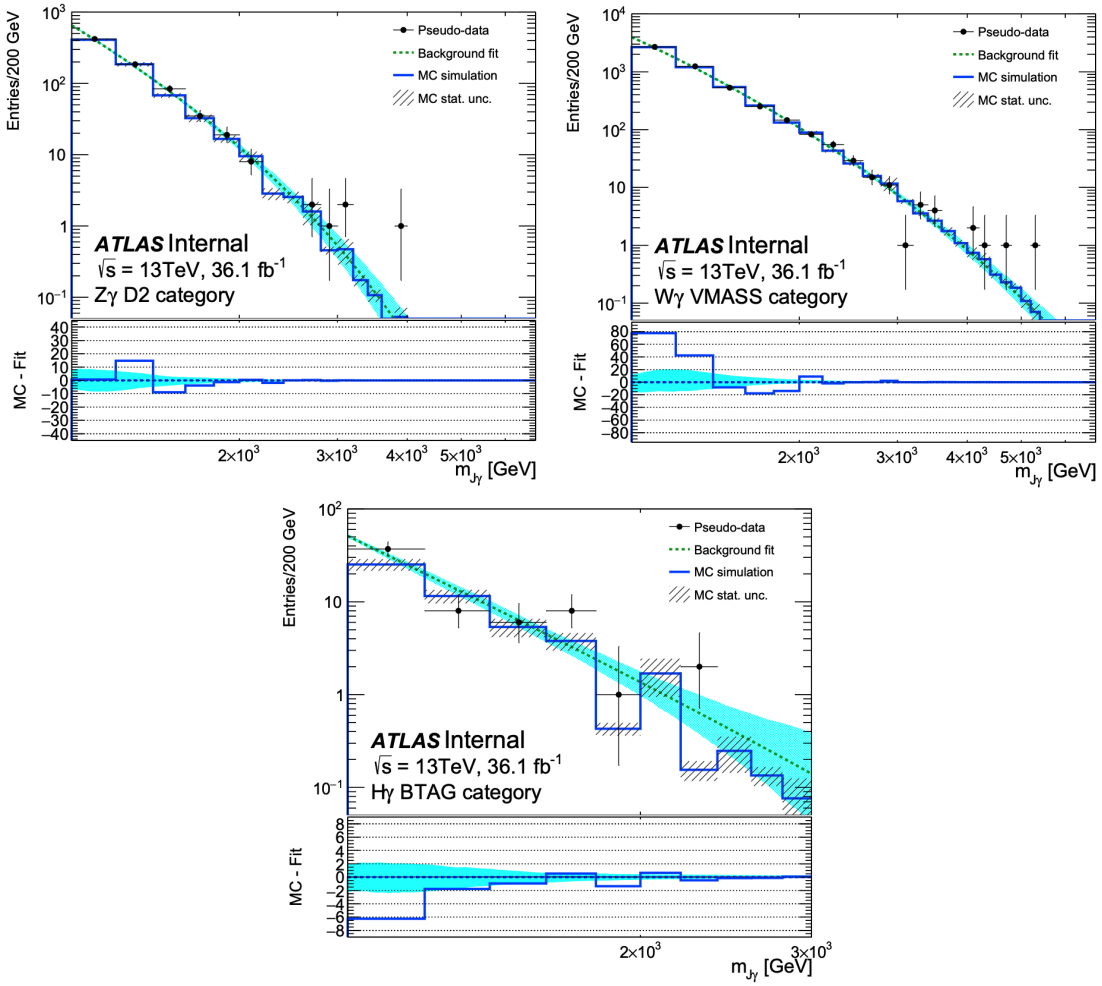

Figure 11.11: The background-only fit to an example of pseudo-experiments for several representative categories and channels. The top left plot is for the D2 category of the spin-0 $X \rightarrow Z\gamma$ channel, the top right plot is for the VMASS category of the spin-1 $X \rightarrow W\gamma$ channel and the bottom plot is for the BTAG category of the spin-1 $X \rightarrow H\gamma$ channel. The blue line represents the expected background yield based on simulation, the hatched band is the statistical uncertainty of the MC simulation, the black dots shows the distribution of a generated pseudo-experiment, the dashed line shows the background-only fit to the pseudo-experiment, and the cyan band is the 1σ uncertainty around the background fit.

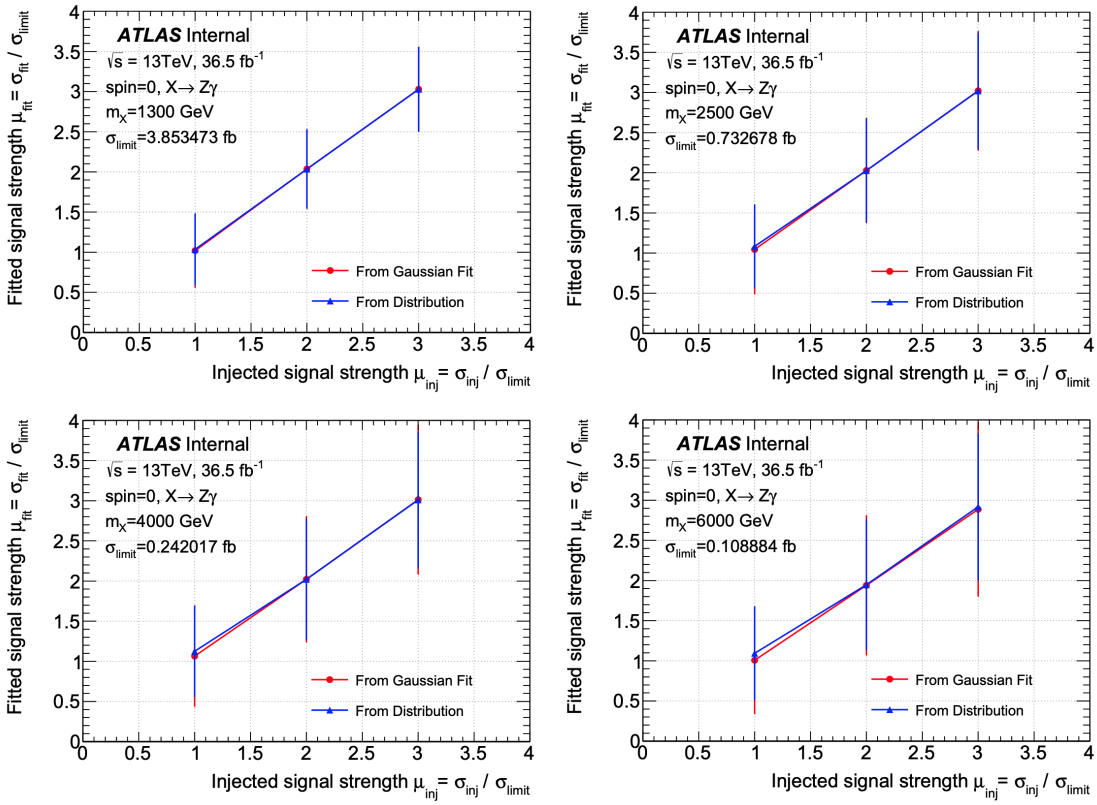

Figure 11.12: The comparison between the injected and fitted signal strength in signal injection test for spin-0 $X \rightarrow Z\gamma$ channel. The top left, top right, bottom left and bottom right plots show the test results for an injected signal of resonance mass at 1300, 2500, 4000 and 6000 GeV respectively. The blue dots represent the mean of extracted signal strengths, and the red dots represent the mean of the fitted signal strength distribution.

process is included in the pseudo-datasets and fitted with a signal-plus-background model. The test is performed for each signal hypothesis at various signal strength and resonance mass values. Ideally, the extracted signal strength from the ensemble of pseudo-datasets will be distributed as a Gaussian random variable with a mean value equal to the injected signal strength. As an example, Figure 11.12 shows the signal injection test results at a few representative resonance mass values in the spin-0 $X \rightarrow Z\gamma$ channel. The fitted and injected signal strength were observed to match well within uncertainty at large.

11.4 Statistical Analysis

A profile-likelihood-ratio test method, as introduced in Chapter 10, is employed in the analysis to search for a localized excess over a smoothly falling background in the $m_{J\gamma}$ spectrum. The parameter

of interest in the analysis is the signal cross section times the branching fraction of the resonance decaying into $Z\gamma$ or $W\gamma$ ($H\gamma$) with subsequent hadronic ($b\bar{b}$) decays of the boson, $\sigma\mathcal{B}_{\text{had}}$. The likelihood function is defined in an unbinned fashion, as the following:

$$\mathcal{L} = \prod_{c}^{\text{categories}} \left[\frac{N_c(\sigma\mathcal{B}_{\text{had}};\, \boldsymbol{p}_c, \theta_c)^{n_c}}{n_c!} e^{-N_c(\sigma\mathcal{B}_{\text{had}},\, \boldsymbol{p}_c, \theta_c)} \prod_{j}^{\text{events}} f_{\text{tot},c}(m_{\text{J}\gamma,j}; \sigma\mathcal{B}_{\text{had}},\, \boldsymbol{p}_c, \theta_c, m_X) \right] \prod_{k}^{\text{syst}} \rho(\theta_k)\ , \tag{11.7}$$

where c represents the event category, j is the event index, n_c (N_c) is the observed (expected) total number of events in category c, $f_{\text{tot},c}$ is the signal-plus-background probability density function in the $m_{\text{J}\gamma}$ spectrum, and $\rho(\theta_k)$ is the constraint term for the nuisance parameters. The expected total number of events in a category c is the sum of the fitted number of background events, $N_{\text{bkg},c}$, the hypothesized number of signal events, $N_{\text{sig},c}$, and the fitted number of spurious signal $N_{\text{spur},c}$. The combined probability density function $f_{\text{tot},c}$ is defined as a function of resonance mass $m_{\text{J}\gamma}$, and it depends on the parameter of interest $\sigma\mathcal{B}_{\text{had}}$, the parameters of the background modeling function $\boldsymbol{p}_c$, the nuisance parameters for systematic uncertainties θ_c, and the hypothetical resonance mass m_X. The function can be written as:

$$\begin{aligned} f_{\text{tot},c}(m_{\text{J}\gamma,j}; \sigma\mathcal{B}_{\text{had}},\, \boldsymbol{p}_c, \theta_c, m_X) = & \frac{1}{N_c(\sigma\mathcal{B}_{\text{had}}, \theta_c)} \Big[N_{\text{bkg},c} B_j(m_{\text{J}\gamma,j}; \boldsymbol{p}, \theta^{\text{shape}}_{\text{bkg},c}) \\ & + \Big(N_{\text{sig},c}(\sigma\mathcal{B}_{\text{had}}; \theta^{\text{yield}}_{\text{sig},c}, m_X) + N_{\text{spur},c}(\theta_{\text{spur},c}, m_X) \Big) \cdot S_c(m_{\text{J}\gamma,j}; \theta^{\text{shape}}_{\text{sig},c}) \Big]\ , \end{aligned} \tag{11.8}$$

where $\theta^{\text{shape}}_{\text{bkg},c}$, $\theta^{\text{shape}}_{\text{sig},c}$, $\theta^{\text{yield}}_{\text{sig},c}$, and $\theta_{\text{spur},c}$ are the nuisance parameters associated with the systematic uncertainties related to the background and signal modeling of the resonance mass distribution, the signal yield, and the spurious signal respectively. These nuisance parameters are a subset of the whole nuisance parameter set θ. The chosen functional form for the background, $B_j(m_{\text{J}\gamma,j}; \boldsymbol{p}, \theta^{\text{shape}}_{\text{bkg},c})$, and signal, $S_c(m_{\text{J}\gamma,j}; \theta^{\text{shape}}_{\text{sig},c})$, are defined in Section 11.3. All the categories are fitted simultaneously to extract the MLE of $\sigma\mathcal{B}_{\text{had}}$ in each of the $Z\gamma$, $W\gamma$ and $H\gamma$ channels separately.

Local p-values are computed, considering a particular value of m_X at a time, to determine how likely the observed data is incompatible with the background-only hypothesis. Thereafter, global p-values are deduced approximately by penalizing the local p-value based on the effective search trial counts for the $m_{\text{J}\gamma}$ range examined. The modified frequentist (CL_s) method with asymptotic approximation is used to set upper limits on $\sigma\mathcal{B}_{\text{had}}$ at 95% confidence level, which are subsequently translated into limits on the signal cross section multiplied by the branching fraction of the resonance with any decay of the $Z/W/H$ bosons, $\sigma\mathcal{B}$, by taking into account the branching fraction of $Z \to q\bar{q}$ (69.91%) and $W \to q\bar{q}$ (67.41%) as measured in [7], as well as the theoretical branching fraction of $H \to b\bar{b}$ (58.24%) [231]. The p-value and exclusion limit calculations are repeatedly performed in the range of 1 TeV to 6.8 TeV with a step size of 20 GeV to guarantee finer resolution than

the detector resolution in the $m_{J\gamma}$ spectrum. Along the whole search range, the various categories are considered over different ranges: 1 TeV $< m_X <$ 3 TeV for the BTAG category, 1 TeV $< m_X <$ 6.8 TeV for the D2 and VMASS categories, and 3 TeV $< m_X <$ 6.8 TeV for the ELSE category. To assess the validity of the asymptotic approximation for the whole probed $m_{J\gamma}$ spectrum, cross-checks with sampling distributions generated using pseudo-experiments are also performed. The approximation is found to deliver good agreement with the sampling approach at the lower m_X regime, but lead to limits that are slightly stronger than those obtained with pseudo-experiments, up to 30% for large m_X values due to small event yield. The fit results are presented in Section 11.6.

11.5 Systematic Uncertainties

This section gives an overview of the systematic uncertainties in the signal modeling and background estimation, and their impact on the normalization and shape of the $m_{J\gamma}$ distribution. The systematic uncertainties considered in this analysis can be classified into experimental and theoretical ones. Sources of experimental uncertainties include uncertainties on the measured integrated luminosity, uncertainties associated with the background modeling technique, and uncertainties related to the detection, reconstruction, and identification of photons and jets. Theoretical uncertainties are taken into account for the simulation effects on the signal process only, since the background yields are derived from data.

Detector-related and theoretical uncertainties could affect both the signal shape and efficiency. The impact of the uncertainties for resonance masses from 1 TeV to 7 TeV in steps of 500 GeV is evaluated by determining the relative change in the expected position of the signal peak, the core width σ_C of the signal peak and the relative change in signal efficiency. The relative changes in the signal shape and efficiency are then parameterized as a function of m_X with third degree polynomial regression, and incorporated into the likelihood as discussed in Section 11.4.

11.5.1 Experimental Uncertainties

Luminosity

Accurate luminosity measurements are fundamental for any physics measurement or new physics search. The integrated luminosity uncertainty in the combined 2015 and 2016 data, obtained using the LUCID-2 Cherenkov detector [232], is 2.1%. The uncertainty is derived from the calibrations of the luminosity measurements performed in August 2015 and May 2016, using the measured beam widths from beam-separation scans in the horizontal and vertical direction, the average number of inelastic pp collisions in colliding bunches, and the number of protons in the colliding bunches. Details about the methodology can be found in Ref. [233]. This systematic uncertainty is applied to the signal yield only.

Uncertainty in Background Estimation

Since an ad hoc parameterized functional form is used to model the background from data and it does not necessarily describe the true form as from first principles, there is a potential bias in the estimated signal event yield if the background is mis-modeled. Such bias is estimated as the number of extracted signal events in a signal-plus-background fit on background-only simulated events, and is referred to as the spurious signal as discussed in Section 11.3.2. The absolute number of spurious signal is parameterized as a function of m_X using an exponential function, and incorporated into the likelihood to account for the systematic uncertainty in background estimation. The impact on the uncertainty by mis-modeling of the background composition in the simulation has been studied by varying the fraction of subdominant $W/Z+$jets and $\gamma+b/c$ jet backgrounds by 50%. The change in spurious signal estimation is found to be negligible. The impact of the spurious signal uncertainty on the exclusion limits is discussed in Section 11.6.2.

Detector-related Uncertainties

- **Photon**: The uncertainties of photon energy scale and resolution mostly affect the signal peak shape. The uncertainty on the p_{T} scale shifts the signal peak position, while the uncertainty on the p_{T} resolution affects the width of the signal peak. These uncertainties are evaluated in calibrations using $Z \to ee$ data events, as discussed in Section 8.2.2. The uncertainty associated with the photon energy scale contributes to a shift of 0.5% in the signal peak position, and the photon energy resolution affects the signal mass resolution by 1% in the low-mass region to 3% in the high-mass region. Besides, other sources of photon-related uncertainty stem from the measurements of identification, isolation and trigger efficiency, which are evaluated using $Z \to ee\gamma$, $Z \to ee$ and inclusive photon data events. The photon identification, isolation and trigger systematic uncertainties affect mainly the signal yield, and introduce an uncertainty of less than 1.5%, 0.5%, and 0.1% in the signal efficiency respectively.

- **Large-R jet**: Similar to the photon energy scale and resolution, the uncertainties of jet energy scale and resolution have an impact primarily on the signal peak position and width respectively. The uncertainties on the scale and resolution of jet mass and the jet substructure variable $D_2^{(\beta=1)}$ affect mostly the signal normalization and efficiency as they are utilized in the event selection criteria. The jet energy, jet mass and $D_2^{(\beta=1)}$ scale uncertainties are evaluated using the ratio of the calorimeter-based to the track-based measurements in observed and simulated dijet events, which takes into account uncertainties associated with the track reconstruction efficiency, the impact parameter resolution, the impact of high pile-up environment on the track reconstruction, the rate for fake tracks and the sagitta biases. The other resolution uncertainties are estimated by applying additional smearing on the jet energy, jet mass or $D_2^{(\beta=1)}$ variable, according to the corresponding uncertainties in resolution measure-

ments. The uncertainty associated with the jet energy scale contributes to a shift of 1–3% in the signal peak position, while the jet energy resolution impacts the signal peak resolution by 5% in the low-mass region to 15% in the high-mass region. The jet energy uncertainties also contribute to a 2–6% uncertainty in the signal efficiency. The jet mass and $D_2^{(\beta=1)}$ uncertainties are found to introduce an uncertainty of 3–6% and less than 1% in the signal efficiency, respectively.

- **Number of primary-vertex-originated tracks associated with the jet**: The uncertainty on the number of charged tracks originating from the primary vertex and associated with the untrimmed jet can affect the signal selection efficiency. The mismodeling of the n_{trk} is estimated by comparing the data with MC simulation in enriched W/Z+jets regions. The systematic uncertainty in the efficiency of the $n_{\text{trk}} < 30$ requirement per tagged large-R jet is found to be about 6% [227].

- **Heavy-flavour jet identification**: The uncertainty of b-tagging on track jets is evaluated from the measurement of correction factors that account for the difference between simulation and data. The correction factors for light-, c- and b-jets are measured separately as a function of the jet p_{T} and η. The three correction factors have multiple sources of uncertainty; these uncertainties are simplified to form a uncorrelated set of uncertainties that are treated independently, with five uncertainties for light-jets, four for c-jets and three for b-jets. The uncertainty for b-tagged track-jets ranges between 2% and 8% for track-jets with $p_{\text{T}} < 250$ GeV. For track-jets with $p_{\text{T}} > 250$ GeV, the uncertainty in the b-tagging efficiency is extrapolated using simulation, and is estimated to be 9% for track-jets with $p_{\text{T}} > 400$ GeV. The b-tagging efficiency uncertainty results in an impact of 10–20% on the signal efficiency.

- **Pileup modeling**: A pile-up reweighting procedure is applied to reweight the simulated samples such that the distribution of the number of interactions per bunch crossing matches the measured one for the relevant data-taking periods. The associated uncertainty is used to estimate the uncertainty of pileup modeling. The pileup modeling systematic uncertainty contributes to a 1–2% impact on the signal efficiency.

11.5.2 Theoretical Uncertainties

Parton Distribution Function

The uncertainty of PDF modeling is estimated for the signal samples by comparing the nominal PDF with the 50 variations in the NNPDF error set to take into account sources of uncertainties from experimental measurement error and from theoretical approximations. These variations are orthogonalized such that each variation could be considered independently as a source of uncertainty, and

Table 11.2: Effect of systematic uncertainties on the signal normalization and efficiency, the position of the signal peak, and the core width of the signal peak $\sigma_{\mathcal{C}}$. The last two rows show the theoretical uncertainty effects on the signal acceptances.

	Impact on normalization and efficiency [%]
Luminosity	2.1
Jet energy scale	2 – 6
Photon identification and isolation	0.5 – 1.5
Flavor tagging	10 – 20
n_{trk} associated with the jet	6
Jet mass resolution	3 – 6
$D_2^{(\beta=1)}$ scale and resolution	< 1
Pile-up modeling	1 – 2
	Impact on signal peak position [%]
Jet energy and mass scale	1 – 3
Photon energy scale	<0.5
	Impact on signal peak resolution [%]
Jet energy resolution	5(m_X <2.5 TeV) – 15 (m_X ≥2.5 TeV)
Photon energy resolution	1 – 3
	Impact on acceptance [%]
PDF	2 – 12
Parton Shower	2

are thus called *eigen-variations*. The uncertainty of the PDF variations on the acceptance is computed as the standard deviation of the changes in acceptance with the alternative PDFs [234]. The uncertainty on the acceptance for the signal processes produced via gluon–gluon fusion is found to vary from 12% in the low-mass region to 2% in the high-mass region, and for signal processes produced via $q\bar{q}$ annihilation the uncertainty varies from 5% to 2%.

Parton Showering

Uncertainty of parton shower modeling is estimated for the signal samples, by comparing the nominal PYTHIA A14 tunes with 5 eigen-variations that takes into account the effects from underlying event, jet structure, and extra jet productions. The uncertainty of parton shower modeling on the acceptance is computed as the standard deviation of the changes in acceptance for the alternative parton shower models, and is found to be roughly 2%.

Table 11.2 summarizes the major effects of the systematic uncertainties from the various sources on the signal yield and signal shape parameters.

11.6 Results

11.6.1 Unblinded Signal Region Fit

A simultaneous unbinned fit to the $m_{J\gamma}$ distribution in the various categories is performed separately for each search channel, as described in Section 11.4. The global background-only fit results are shown in Figure 11.13, 11.14, and 11.15, in which the comparison between the data and background-only fit is separately plotted for each category per channel, along with a few representative hypothetical signal curves overlaid on top of the background fit. All statistical and systematic uncertainties are considered in the fit. The total numbers of data events passing the baseline selection and each category of the search channels are shown in Table 11.3. The event with the highest $m_{J\gamma}$ at a value of 6.3 TeV has a large-R jet of mass 63 GeV, and is found in the ELSE (VMASS) category of the $Z\gamma$ ($W\gamma$) search.

Selection	Event yield in category ($m_{J\gamma} > 1$ TeV)				
	Baseline	BTAG	D2	VMASS	ELSE
$Z\gamma$ search	60,237	25	784	5,569	53,859
$W\gamma$ search	60,237	N/A	661	5,216	54,360
$H\gamma$ search	60,237	59	N/A	N/A	N/A

Table 11.3: Event yields after passing the baseline selection for each category in the $Z\gamma$, $W\gamma$, and the $H\gamma$ searches. Only events with $m_{J\gamma} > 1$ TeV are considered.

11.6.2 Dominant Sources of Uncertainty

The influence of each nuisance parameter on the fit result, as well as the pull on the nuisance parameters by the fit, is evaluated as described in Section 10.1. The 30 nuisance parameters with the most impact on the parameter of interest $\sigma\mathcal{B}_{\text{had}}$ are shown in Figure 11.16, 11.17 and 11.18. While the sensitivity of the analysis is primarily determined by the statistical power of the data, the dominant source of systematic uncertainties is related to the effect of spurious-signal uncertainty. The impact of the spurious-signal uncertainty on the cross section limit varies from 20% at $m_X =$ 1 TeV to 1% at $m_X = 6.8$ TeV. Another large systematic uncertainty in the $H\gamma$ channel comes from the heavy-flavor jet identification efficiency, which has an impact of 13–20% on the limit depending on m_X. This source of systematic uncertainty has little importance in the $Z\gamma$ channel when BTAG category is combined with other categories in a global fit.

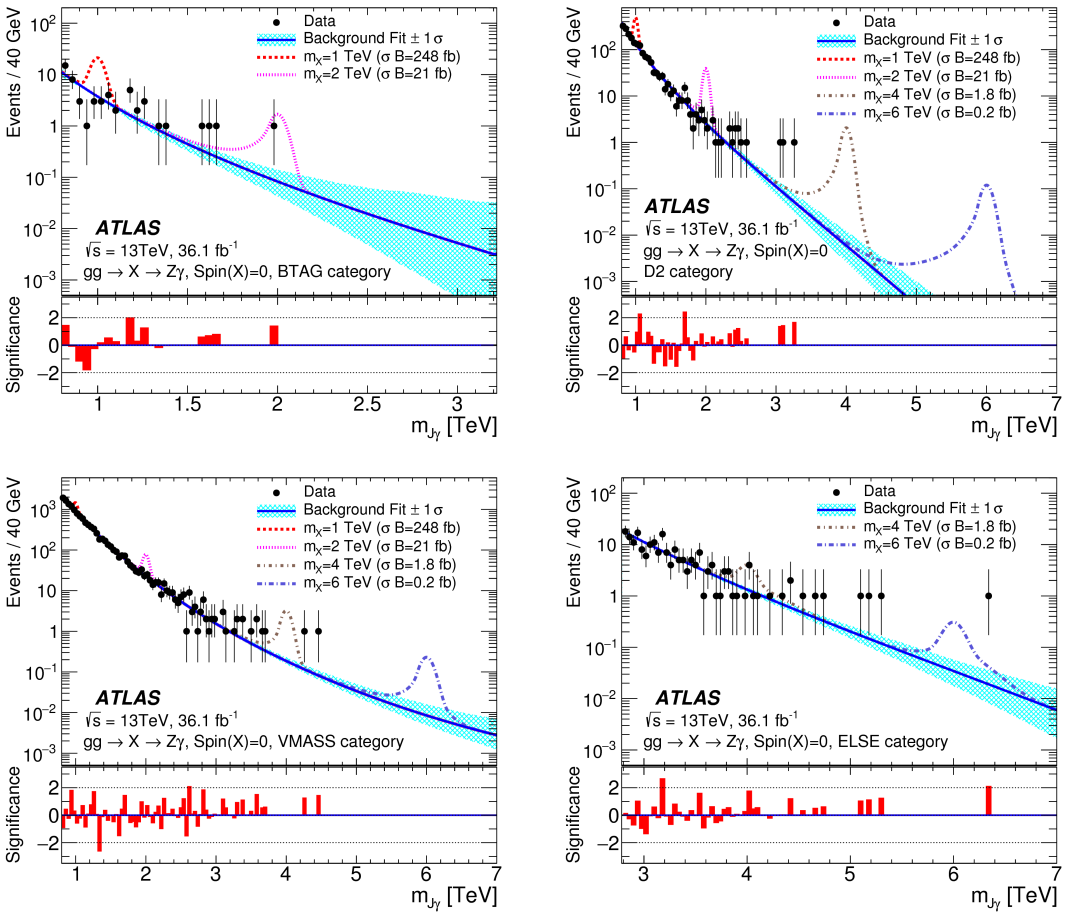

Figure 11.13: The background-only fit to data for the $X \rightarrow Z\gamma$ channels, where the top left plot shows the BTAG category, the top right plot shows the D2 category, the bottom left plot shows the VMASS category, and the bottom right plot shows the ELSE category. The black dots are the data, the blue line is the background-only fit to the data, the cyan hatched band is the background modeling uncertainty. The spin-0 $X \rightarrow Z\gamma$ signal distributions for various resonance mass hypothesis are overlaid for reference, where the cross section is at the exclusion limit level multiplied by factors of 20 for m_X =1 TeV, 10 for m_X =2 TeV, 5 for m_X =4 TeV, and 1 for m_X =6 TeV. [226]

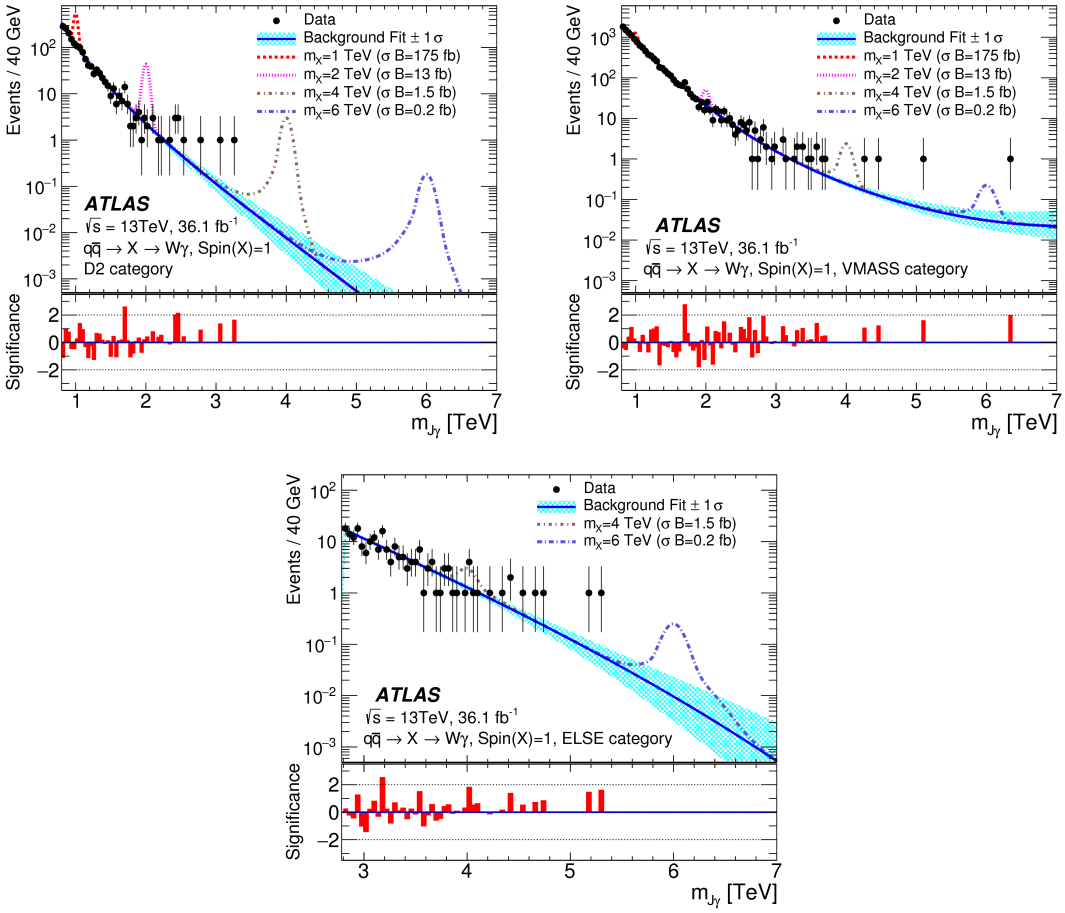

Figure 11.14: The global background-only fit to the data in the spin-1 $X \rightarrow W\gamma$ channel, where the top left plot shows the D2 category, the top right plot shows the VMASS category, and the bottom plot shows the ELSE category. The black dots are the data, the blue line is the background-only fit to the data, the cyan hatched band is the background modeling uncertainty. The signal distributions for various resonance mass hypothesis are overlaid for reference, where the cross section is at the exclusion limit level multiplied by factors of 20 for m_X =1 TeV, 10 for m_X =2 TeV, 5 for m_X =4 TeV, and 1 for m_X =6 TeV. [226]

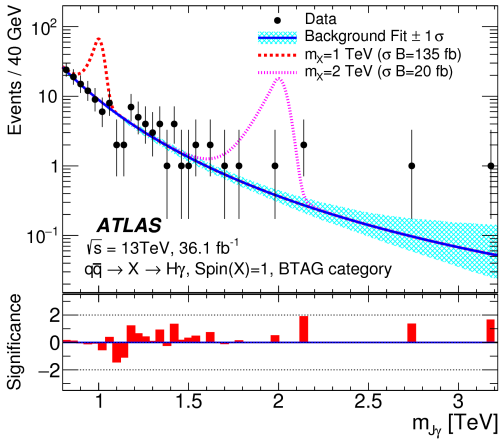

Figure 11.15: The background-only fit to data for the BTAG category of the spin-1 $X \rightarrow H\gamma$ channel. The black dots are the data, the blue line is the background-only fit to the data, the cyan hatched band is the background modeling uncertainty. The signal distributions for various resonance mass hypothesis are overlaid for reference, where the cross section is at the exclusion limit level multiplied by factors of 20 for m_X =1 TeV, 10 for m_X =2 TeV, 5 for m_X =4 TeV, and 1 for m_X =6 TeV. [226]

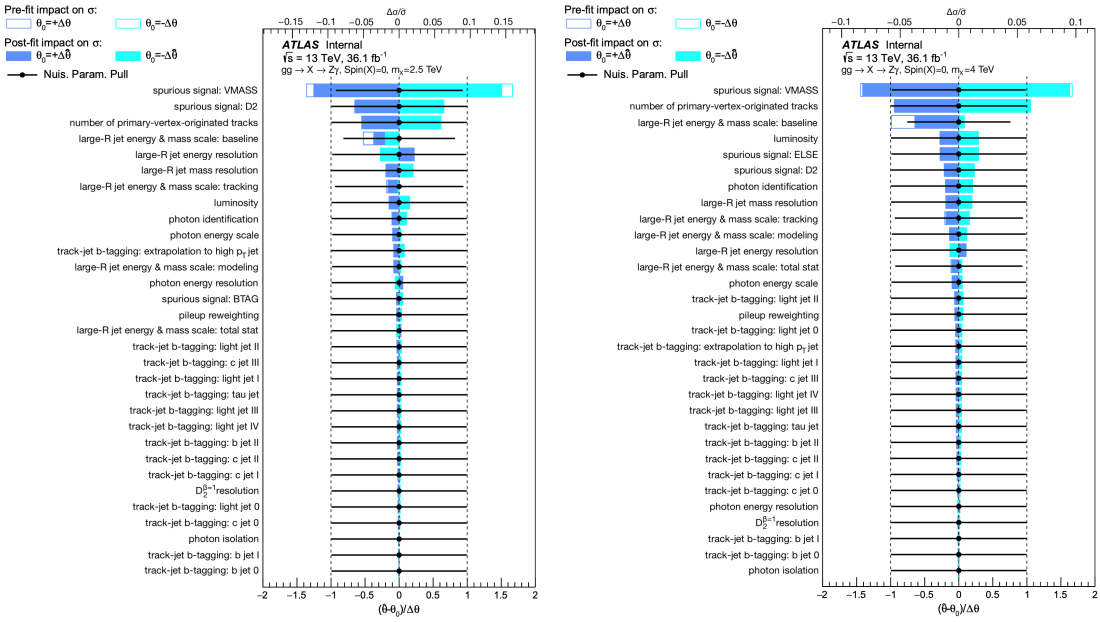

Figure 11.16: Ranking of nuisance parameters based on the impact on the best-fit $\hat{\sigma}$ value, for two representative signal mass points, 2.5 TeV (left) and 4 TeV (right), in the spin-0 $X \rightarrow Z\gamma$ channel. The open areas correspond to the pre-fit upward and downward variations, and the solid areas correspond to the post-fit ones. The dots represent the corresponding pulls for the nuisance parameters. Only the top 30 ranked nuisance parameters are shown.

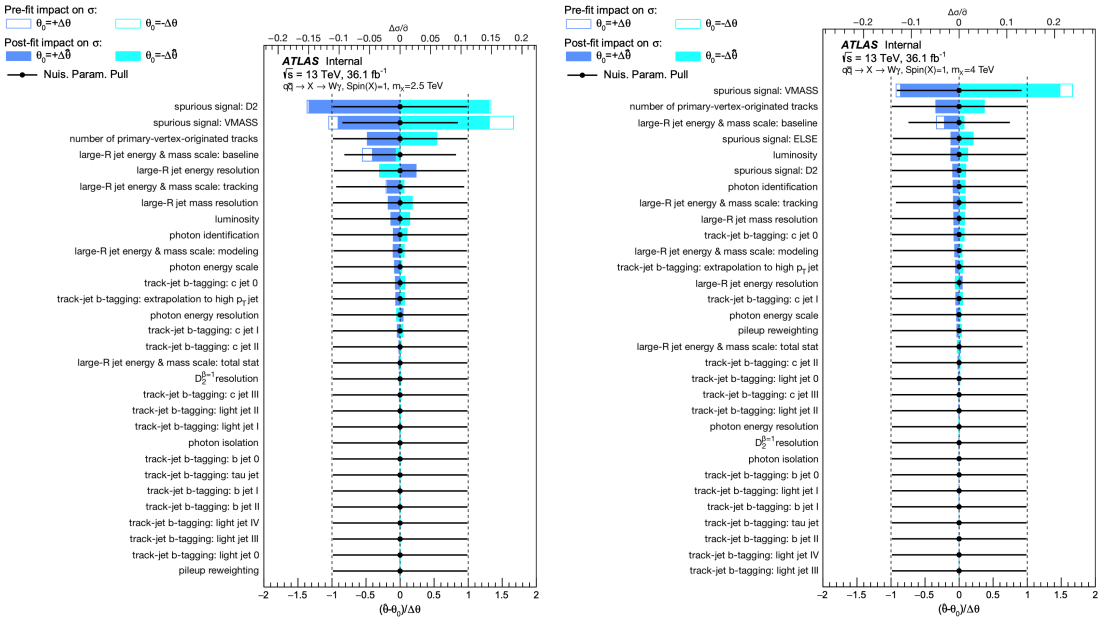

Figure 11.17: Ranking of nuisance parameters based on the impact on the best-fit $\hat{\sigma}$ value, for two representative signal mass points, 2.5 TeV (left) and 4 TeV (right), in the spin-1 $X \to W\gamma$ channel. The open areas correspond to the pre-fit upward and downward variations, and the solid areas correspond to the post-fit ones. The dots represent the corresponding pulls for the nuisance parameters. Only the top 30 ranked nuisance parameters are shown.

11.6.3 Statistical Interpretation

No statistically significant excess with respect to the SM prediction is observed in all of the search channels. The largest deviation from the background-only hypothesis is found in the $W\gamma$ search at $m_{J\gamma} = 2.5$ TeV, corresponding to a local significance of 2.7σ and a global significance of less than 1σ.

Since no significant excess is found, limits are set on the resonance production cross section $\sigma\mathcal{B}$ for the various spin and production hypothesis. At 95% confidence level, upper limits are placed on the cross section as a function of m_X under the narrow-width approximation. As shown in Figure 11.19 and 11.20, the $\sigma\mathcal{B}$ limits on $Z\gamma$ and $W\gamma$ production range from 10 fb for a resonance mass of 1 TeV to 0.1 fb for a resonance mass of 6.8 TeV. The limit setting on $W\gamma$ productions serves as the first ATLAS search results scrutinizing the hadronic W boson decays. Figure 11.21 shows the $\sigma\mathcal{B}$ limits on $H\gamma$ production, which range over $[4,10]$ fb for $m_X \in [1,3]$ TeV, with the lowest limit around the resonance mass of 1.9 TeV. The expected cross section limit rises for $m_X > 2$ TeV because of the drop in b-tagging efficiency for the high-momentum jets. This analysis is the first search for heavy resonances decaying into a Higgs boson and a photon.

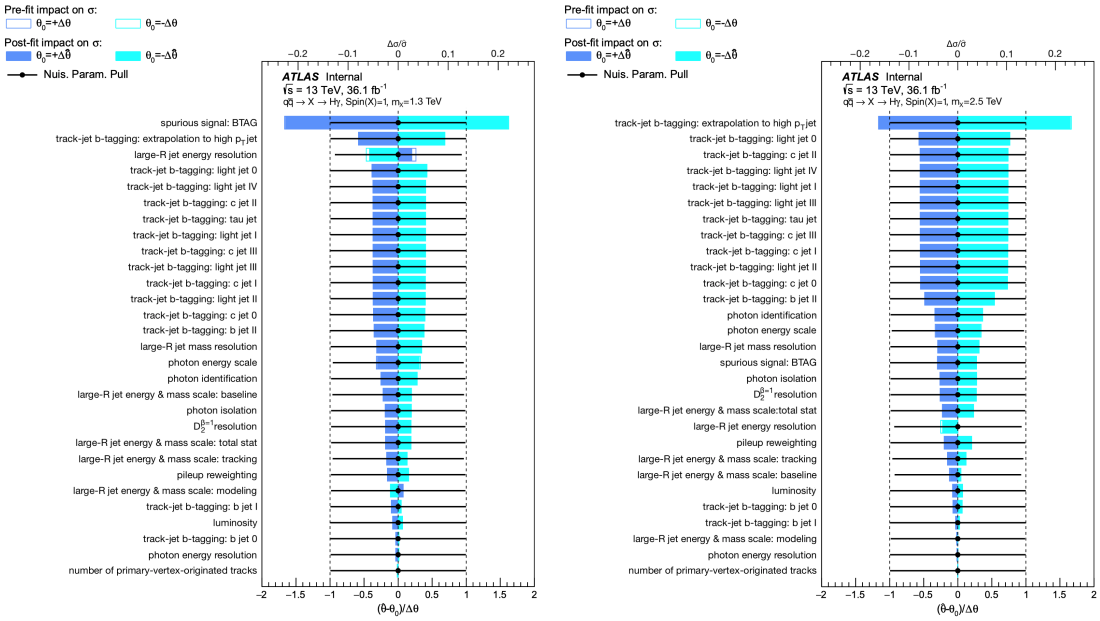

Figure 11.18: Ranking of nuisance parameters based on the impact on the best-fit $\hat{\sigma}$ value, for two representative signal mass points, 1.3 TeV (left) and 2.5 TeV (right), in the spin-1 $X \rightarrow H\gamma$ channel. The open areas correspond to the pre-fit upward and downward variations, and the solid areas correspond to the post-fit ones. The dots represent the corresponding pulls for the nuisance parameters. Only the top 30 ranked nuisance parameters are shown.

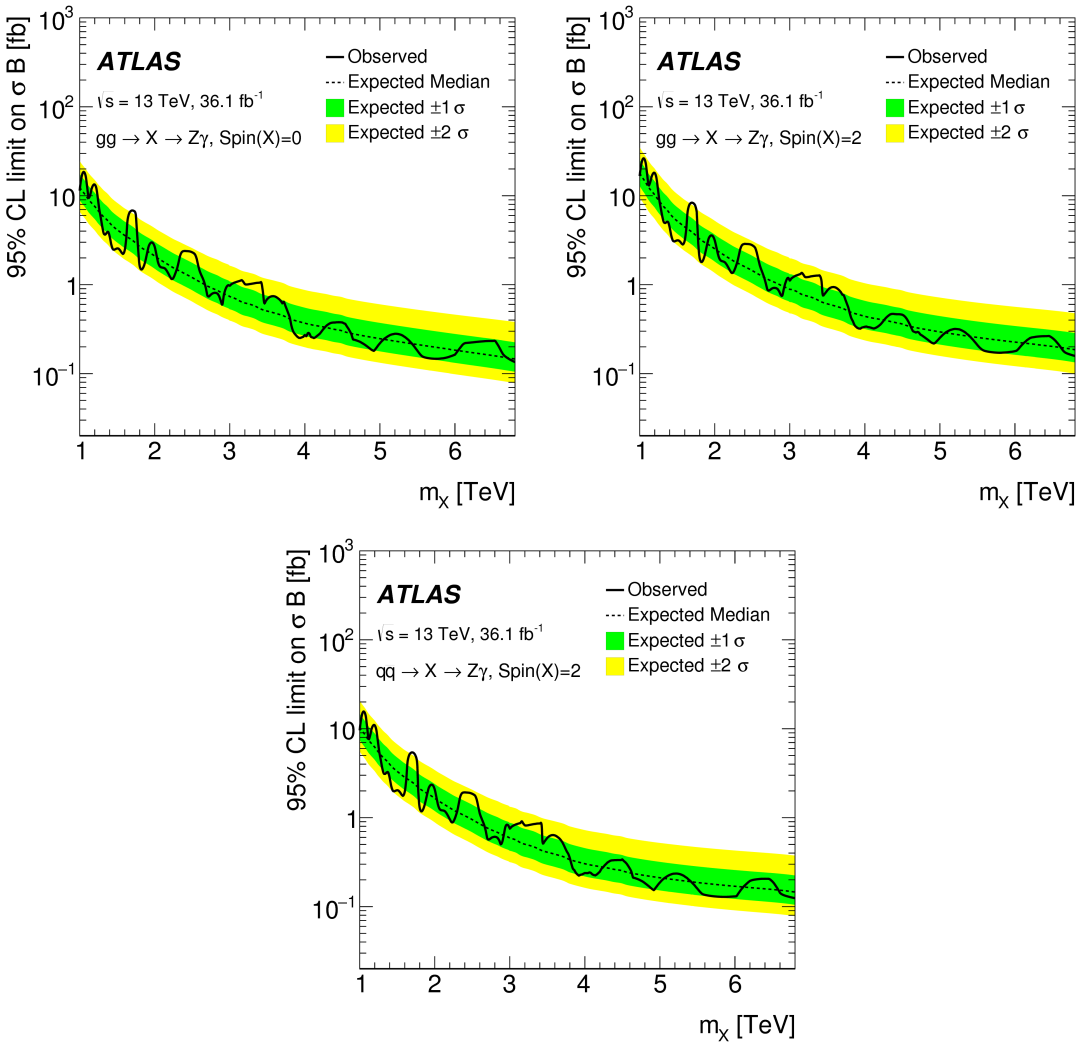

Figure 11.19: Upper limits at 95% CL on $\sigma\mathcal{B}$ as a function of resonance mass m_X for the $X \to Z\gamma$ channel. The top left plot is for the spin-0 $X \to Z\gamma$ production via gluon–gluon fusion, the top right plot is for the spin-2 $X \to Z\gamma$ production via gluon–gluon fusion, and the bottom plot is for the spin-2 $X \to Z\gamma$ production via quark–antiquark annihilation. Observed limits are shown as a black solid line and expected limits as a black dashed line. The green and yellow shaded bands correspond to ± 1 and ± 2 standard deviations, respectively, around the expected limit. [226]

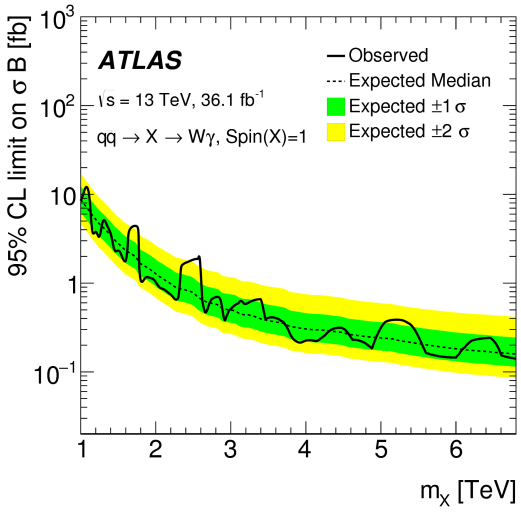

Figure 11.20: Upper limits at 95% CL on $\sigma\mathcal{B}$ as a function of resonance mass m_X for the spin-1 $X \rightarrow W\gamma$ channel. Observed limits are shown as a black solid line and expected limits as a black dashed line. The green and yellow shaded bands correspond to ± 1 and ± 2 standard deviations, respectively, around the expected limit. [226]

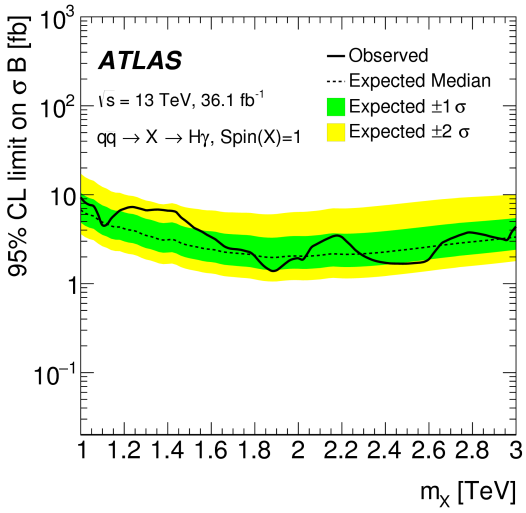

Figure 11.21: Upper limits at 95% CL on $\sigma\mathcal{B}$ as a function of resonance mass m_X for the spin-1 $X \rightarrow H\gamma$ channel. Observed limits are shown as a black solid line and expected limits as a black dashed line. The green and yellow shaded bands correspond to ± 1 and ± 2 standard deviations, respectively, around the expected limit. [226]

Chapter 12

Leptoquark Search

This chapter presents the second analysis in this dissertation, which searches for scalar LQ pair productions. As discussed in Section 4.2, LQs are hypothetical color-triplet bosons that couple to both leptons and quarks. It is predicted by many GUT models and motivated by observed anomalies in B-physics and muon anomalous magnetic dipole moment measurements. While previous LQ searches up until early Run II only target LQs that couple to the same generation of leptons and quarks, this analysis serves as one of the leading efforts in the extension of the ATLAS LQ search program to cover various cross-generational LQ models. For the first time top-philic cross-generational LQs are searched for in ATLAS. A summary of other previous LQ searches in ATLAS and CMS can be found in Section 4.2.2.

This analysis focuses on pair productions of LQs, each decaying into a top quark and an electron, or a top quark and a muon. The search considers the fully hadronic top-quark final state, which takes up 46% of the branching fraction of the $t\bar{t}$ decay modes. The hadronic $t\bar{t}$ channel usually suffers from higher QCD background, but the hadronic channel in this case takes advantage of a clean signal of isolated charged leptons to trigger on. Furthermore, LQs at the TeV scale are of particular interest to explain the observed anomalies. The resultant hadronic decay products of top quarks originating from TeV-scale LQs tend to be contained within a single large-R jet. Therefore, the analysis targets the boosted regime, in which the signatures of the final state would consist of two opposite-sign same-flavor charged leptons and two large-R jets. Simultaneous couplings of LQs to the first- and second-generation leptons are constrained by rare lepton-flavor-violating decay measurements as discussed in Section 4.2.3, and thus not considered here. Section 12.1 summarizes the simulation of LQ signals and relevant SM backgrounds, and the triggers used to record data. Section 12.2 gives an overview of the analysis strategy, including how the sensitivity of the search to LQ signals is optimized using a multivariate discriminator based on boosted decision trees (BDTs). The dominant backgrounds come from $t\bar{t}$ and $Z+$jets processes, where their normalization is derived from dedicated control region (CR) in a data-driven way. An excess of events over the SM backgrounds is

sought using the distribution of the BDT output score, with a binned maximum likelihood method as described in Section 12.3. Systematic uncertainties taken in account are described in Section 12.4, and the interpreted results are presented in Section 12.5.

12.1 Data and Simulated Samples

12.1.1 Collision Data

This analysis is performed with $\sqrt{s} = 13$ TeV pp collisions recorded in the full Run II during 2015–2018, corresponding to an integrated luminosity of 139 fb^{-1} after applying the basic data quality requirements like the other presented analysis. Events are selected from the Egamma and Muon streams using a collection of single-lepton triggers as listed in Table 12.1. For the single-electron triggers, events are recorded if it contains an electron that has p_{T} higher than 26 GeV (24 GeV in 2015) and satisfies isolation requirements, or p_{T} higher than 60 GeV regardless of the isolation quality [235]. For the single-muon triggers, events are recorded if it has an isolated muon with $p_{\mathrm{T}} > 26$ GeV (20 GeV in 2015) or any muon with $p_{\mathrm{T}} > 50$ GeV [236].

Decay channel	Data period	Trigger
electron	2015	HLT_e24_lhmedium_L1EM20VH HLT_e60_lhmedium
	2016-2018	HLT_e26_lhtight_nod0_ivarloose HLT_e60_lhmedium_nod0
muon	2015	HLT_mu20_iloose_L1MU15 HLT_mu50
	2016-2018	HLT_mu26_ivarmedium HLT_mu50

Table 12.1: A summary of lepton triggers used for the leptoquark analysis.

12.1.2 Signal and Background Samples

To study the characteristics of the signal and background processes, MC samples are generated using different event generators depending on the event process. All signal and background samples are then passed to the GEANT 4-based detector simulation [223, 224] to model the detector response. To model the effect of pileup collisions, each generated signal and background event is overlaid by underlying low p_{T} multi-jet events simulated using PYTHIA 8.186 [211] with the A3 tune [225] and the NNPDF2.3LO PDF set [216]. These simulated signal and background samples are then reweighted to describe the pileup distribution as observed in the data. In all MC samples, except the ones generated using SHERPA, the EVTGEN v1.6.0 (EVTGEN v1.2.0 for $t\bar{t}+Z$ events) program is

used to simulate the properties of the bottom and charm hadron decays.

Samples for the signal process of scalar leptoquark pair production are generated at NLO [237] using MADGRAPH5_aMC@NLO v2.6.0 generator [214] with the NNPDF3.0 NLO PDF set [115]. The decay of the top quarks is simulated using the MADSPIN decay modeling program [238] which takes into account spin correlations. The processes of parton shower, fragmentation and underlying events are modeled using PYTHIA 8.230 [239] with the A14 tune [215] and the NNPDF2.3LO PDF set. The LQ simulations are produced with LQ masses between 900 GeV and 2000 GeV, in steps of 100 GeV, with additional mass points 1350, 1450 and 1550 GeV for finer steps around the expected sensitivity limit. The coupling $\lambda_{\mathrm{LQ}\to\ell t}$ is set to $\sqrt{4\pi\alpha}$ [240] such that the intrinsic LQ decay width is less than 0.2% of its mass and thus the LQ is considered to decay promptly. In addition, the model parameter β is set to 1 such that all leptoquarks decay into a top quark and an electron or muon rather than a bottom quark and a neutrino. The top quarks in the final state are forced to decay hadronically in the simulated samples.

The simulation process of the two dominant SM backgrounds, $t\bar{t}$ and $Z+$jets, and the other minor backgrounds considered is summarized in Table 12.2. The productions of $t\bar{t}$ and single-top processes in the Wt- and s-channel are performed using POWHEG-BOX v2 generator [210] with the NNPDF3.0 NLO PDF set. The t-channel single-top events are simulated using POWHEG-BOX v1 generator with the NNPDF3.0 NLO PDF set. The productions of all the $t\bar{t}$ and single-top processes are interfaced to PYTHIA 8.230 parton-shower model with the A14 underlying-event tune and the NNPDF2.3LO PDF set. The top quark mass is set to 172.5 GeV, and the h_{damp} parameter, which effectively controls the high-p_{T} radiation, is set to 1.5 times of the top quark mass [241]. The cross sections of $t\bar{t}$ and single-top processes are normalized to NNLO in perturbative QCD as calculated with the Top++2.0 program, including soft-gluon resummation to next-to-next-to-leading-log (NNLL) accuracy [242–250].

For generation of the $t\bar{t}+Z$ events, MADGRAPH5_aMC@NLO v2.3.3 generator at NLO interfaced to PYTHIA 8.212 parton-shower model is used with the A14 underlying-event tune and the NNPDF2.3LO PDF set. The productions of W or Z bosons in association with jets, and semi-leptonic on-shell diboson process, are simulated using SHERPA 2.2.1 generator [217] with the NNPDF3.0 PDF set. For $Z+$jets and $W+$jets (diboson) events, matrix elements are calculated in perturbative QCD for up to two (one) partons at NLO and up to four (three) partons at LO using the COMIX [218] and OPENLOOPS [219] matrix element generators. In all cases of $Z+$jets, $W+$jets and diboson processes, events are then merged with the SHERPA parton shower algorithm [220] using the ME+PS@LO prescription [221].

12.2 Analysis Strategy

This presented analysis targets the cross-generational leptoquarks that decay into a top quark and an electron or a top quark and a muon, where both top quarks decay hadronically. It is optimized

Background process	Generator	Cross-section normalization	PDF set	Parton showering	Tune
$t\bar{t}$	POWHEG-BOX v2	NNLO+NNLL	NNPDF 3.0	PYTHIA 8.230	A14
s- and Wt-channel single-top	POWHEG-BOX v2	NNLO+NNLL	NNPDF 3.0	PYTHIA 8.230	A14
t-channel single-top	POWHEG-BOX v1	NNLO+NNLL	NNPDF 3.0	PYTHIA 8.230	A14
$t\bar{t}+Z$	MADGRAPH5_aMC@NLO v2.3.3	NLO	NNPDF 3.0	PYTHIA 8.212	A14
Z+jets	SHERPA 2.2.1	NNLO	NNPDF 3.0	SHERPA	SHERPA default
W+jets	SHERPA 2.2.1	NNLO	NNPDF 3.0	SHERPA	SHERPA default
Semi-leptonic diboson	SHERPA 2.2.1	NLO	NNPDF 3.0	SHERPA	SHERPA default
Signal process					
LQ$\rightarrow te$	MADGRAPH5_aMC@NLO v2.6.0	NLO	NNPDF3.0	PYTHIA 8.230	A14
LQ$\rightarrow t\mu$	MADGRAPH5_aMC@NLO v2.6.0	NLO	NNPDF3.0	PYTHIA 8.230	A14

Table 12.2: The event generators and parton shower models used for the simulation of the signal and background processes.

for LQ masses larger than 1 TeV, at which the decay products of each resultant top quark tend to be contained within a single high-p_{T} large-R jet. Hence, the targeted final state contains a pair of same-flavor opposite-sign leptons and a pair of large-R jets. A BDT approach, based on kinematic and jet substructure discriminating variables, is employed to classify events as originating from signal or background processes in the signal region. Dedicated control regions are constructed to control the normalization of the dominant backgrounds: $t\bar{t}$ and Z+jets production. The extraction of signal strength is obtained via a simultaneous likelihood fit to the BDT discriminant distribution and the control region yields. This section outlines the selection criteria for the signal and control regions, and the construction of the BDT classifier.

12.2.1 Event Selections

In order to reduce the reducible SM backgrounds and keep as many signal events as possible, a set of loose selection criteria are applied to define the signal region. Events entering the signal region are then further classified using a BDT approach, as described in Section 12.2.2. In the signal region, events are required to have exactly two opposite-sign, same-flavor isolated leptons with p_{T} above 100 GeV. The presence of the two leptons makes a distinctive signature against SM QCD background. To guarantee the best muon resolution and the removal of poorly measured muon tracks in the high-p_{T} regime, the muon candidates are required to pass the *High-p_T* muon identification criteria, unless the leading muon's p_{T} is less than 800 GeV then the *Medium* muon identification selection is applied. Since 60–80% of the signal events are expected to have two or more large-R jets in the range of LQ masses of 1000–1900 GeV, an additional requirement of at least two large-R jets with $p_{\mathrm{T}} > 200$ GeV and $|\eta| < 2.0$ is applied. Since high-p_{T} electrons could deposit significant amount of energy in the calorimeter, they could be reconstructed as large-R jets. To avoid double counting the electrons as large-R jets, electron energy is removed from any overlapping large-R jets before applying the jet requirements. This results in 20% better signal efficiency compared with rejecting large-R jets that overlap with a reconstructed electron. A final requirement of the signal region is a cut on the invariant mass of the lepton pair $m_{\ell\ell} > 120$ GeV, which reduces background contributions

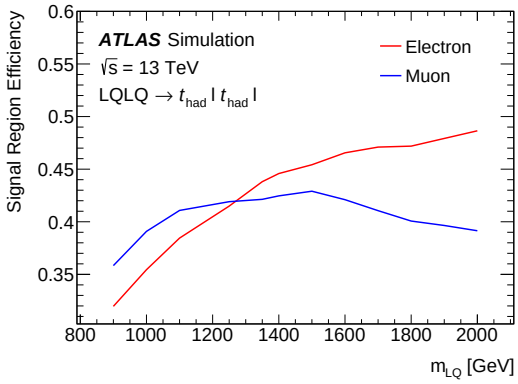

Figure 12.1: Signal acceptance times efficiency to pass the SR selection criteria as a function of LQ mass for the electron (red) and muon (blue) channel. [97]

from Z bosons or other low-mass resonances. Given that $\beta = 1$ and the top quarks in the final state both decay hadronically, the acceptance times efficiency of the SR selection for LQ masses in the range of 900–2000 GeV varies between 32% and 49% in the electron channel, and between 36% and 43% in the muon channel, as shown in Figure 12.1.

After passing the SR selections, the dominant backgrounds are from the $t\bar{t}$ and Z + jets processes. Dedicated control regions are defined to derive the normalizations of these background processes from the data. For the $t\bar{t}$-enriched CR, the selection criteria are the same as the SR, except that a single-electron trigger or a single-muon trigger must be satisfied and the events must contain exactly one opposite-sign electron–muon pair. The Z + jets-enriched CR is kept orthogonal to the SR by selecting events in a dilepton invariant mass window $70 < m_{\ell\ell} < 110$ GeV around the Z boson mass peak. A summary of the event selections for the signal and control regions is given in Table 12.3. At first, only data in the CRs are considered as part of a blinded fit configuration. After verifying that there is good agreement between the observed data and the normalized background predictions, an intermediate step of partial unblinding is taken to validate the agreement at the background-like end of the BDT discriminant distribution in the SR. Once a satisfactory agreement is verified, a final unblinded fit is performed in the complete SR and CRs. The purity of $t\bar{t}$ and Z + jets background is above 91% and 87% in the respective CR with signal contamination below 0.4% to avoid prematurely unblinding the analysis. In the partial unblinding step, the signal–to–background ratio in the unblinded phase space of the SR is ensured to be less than 0.005.

Table 12.3: Summary of event selections applied in the signal and control regions. Leptons and large-R jets are, respectively, denoted by ℓ and J.

	$t\bar{t}$ CR	Z+jets CR	SR
Leptons	$p_{\mathrm{T}}^{\ell} > 100$ GeV, $\lvert\eta_e\rvert < 2.47$, $\lvert\eta_\mu\rvert < 2.5$		
	$N_\ell = 2$; opposite-sign		
Large-R jets	$p_{\mathrm{T}}^{\mathrm{J}} > 200$ GeV, $\lvert\eta_{\mathrm{J}}\rvert < 2.0$, $m_{\mathrm{J}} > 50$ GeV		
	$N_{\mathrm{J}} \geq 2$		
Dilepton invariant mass	$m_{\ell\ell} > 120$ GeV	70 GeV $< m_{\ell\ell} <$ 110 GeV	$m_{\ell\ell} > 120$ GeV
Lepton flavor	$e\mu$	ee or $\mu\mu$	

12.2.2 Parameterized BDT Approach

BDT Algorithm

To maximize the sensitivity to the signal process, a BDT approach is chosen to classify the signal from the $t\bar{t}$ and Z+jets background processes in the signal region, using the XGBOOST framework [251] as the back end for mathematical computations. XGBOOST is a powerful machine learning tool based on gradient boosting decision tree algorithm, in which an ensemble of weak decision trees is combined to obtain a strong classifier. The implemented algorithm in this analysis is restricted to contain at most 1000 trees with a maximal tree depth of 3 layers, while early stopping is enabled if no further improvement in the classification is obtained after 10 iterations of tree building. To avoid overtraining the classifier, nested cross validation [252] is performed to obtain an unbiased evaluation of the classifier performance. An output score is produced by the classifier to represent the predicted probability of the event being a signal, and is used as the final discriminant to separate LQ signal events from the SM backgrounds.

Discriminating Variables

To differentiate LQ signal from the SM background events, a natural basis of kinematic observables are constructed, utilizing Lorentz symmetry to reduce unnecessary duplication of observables, in the rest frames of intermediate particle states, conditioned on the hypotheses of the LQ pair, dileptonic $t\bar{t}$ or Z+jets decay processes. A technique called Recursive Jigsaw Reconstruction [253] is applied to analyze the event topologies of these hypotheses, resolving the kinematic and combinatoric ambiguities associated with the invisible and indistinguishable particles in the event reconstruction. Decay trees as shown in Fig 12.2 describe how the different intermediate states decay to the final state particles in an event based on the various hypotheses. The details of the event reconstruction process for each hypothesis are described below:

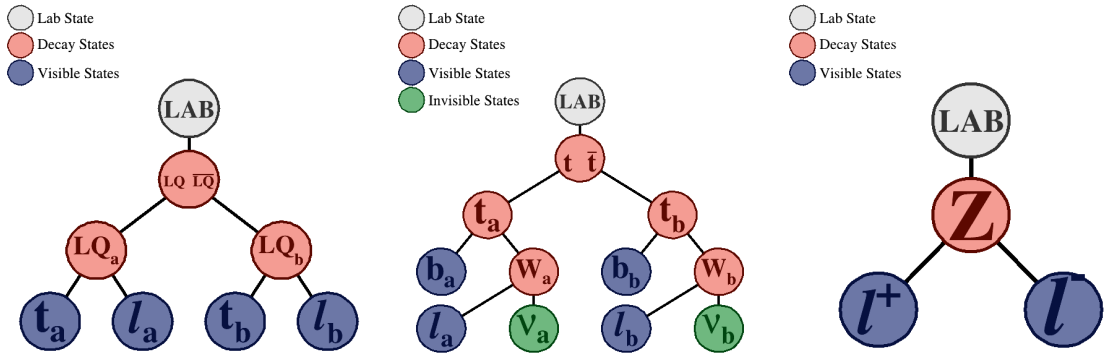

Figure 12.2: The decay trees of LQ pair, dileptonic $t\bar{t}$ and Z + jets hypotheses.

LQ hypothesis is based on the two charged lepton candidates and the two leading large-R jets as the top quark candidates, forming the final state particles in LQ pair productions. The combinatoric ambiguity in the pairing of large-R jets and leptons to reconstruct the LQ candidates is resolved by minimizing the mass difference between the two LQ candidates.

Dileptonic $t\bar{t}$ hypothesis is based on the assumption that the two b-quarks in the final state are reconstructed as small-R jets, along with two leptons. The measured $E_{\mathrm{T}}^{\mathrm{miss}}$ is interpreted as the transverse momentum of the invisible di-neutrino system. The 'min ΔM_{top}' approach in Ref. [253] is adopted to resolve the combinatoric ambiguity of the b–ℓ pairing and the kinematic ambiguity associated with the invisible neutrinos. It was shown that in this approach the observables from the two hemispheres are largely decoupled, as well as being estimated accurately with respect to their true values. The procedure can be described in four steps:

1. Resolve the combinatoric ambiguity by choosing the b–ℓ pairing that minimizes $m_{\mathrm{a}}^2 + m_{\mathrm{b}}^2$, where m_{a} and m_{b} are the masses of the b–ℓ pairs.
2. Choose the mass of the invisible system such that $m_{\nu\nu} = 2\left|\vec{p}^{\,\ell\ell}_{\ell_{\mathrm{a/b}}}\right|$ and $m_{\nu_{\mathrm{a/b}}} = 0$.
3. Choose the longitudinal momentum of the invisible system in the lab frame such that the pseudorapidity of the invisible system is equal to that of the visible system containing two jets and two charged leptons, i.e. $\eta_{\nu\nu} = \eta_{b\ell b\ell}$.
4. Resolve the kinematic ambiguity by specifying the four vector of each neutrino such that $|m_{t_{\mathrm{a}}} - m_{t_{\mathrm{b}}}|$ is minimized.

Leptonic Z hypothesis is based on two charged leptons, where no kinematic nor combinatoric ambiguity needs to be resolved. Straightforward reconstruction of the Z boson is obtained from the dilepton system.

Once the kinematics of the intermediate particles are reconstructed, the invariant masses and the momentum of the intermediate particles evaluated in the parent particle's rest frame are used as

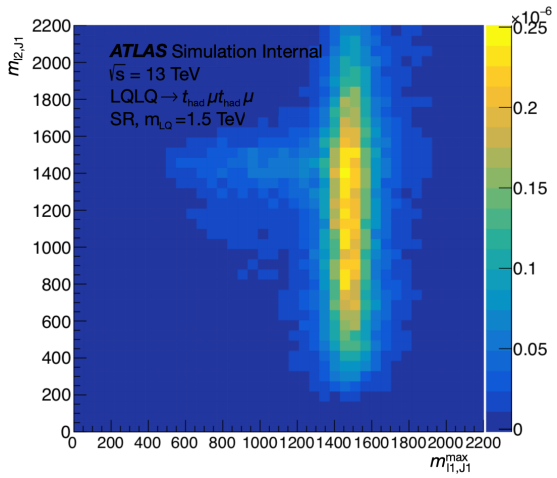

Figure 12.3: The distribution of the higher reconstructed LQ mass $m^{\text{max}}_{\ell 1,\text{J1}}$ against the invariant mass of the lepton–jet pair with alternative pairing $m_{\ell 2,\text{J1}}$ in the signal region of muon channel for a LQ signal of $m_{\text{LQ}} = 1.5$ TeV.

discriminating variables. To form a complete basis of observables, one would also use the decay angles that are insensitive to mass splittings; however, these observables are not considered in the presented analysis in order to minimize the dependence of the search on the spin nature of LQ. As the combinatoric ambiguity might not be resolved to the true pairing occasionally, invariant masses sensitive to the choice of pairing are created with a copy that has the alternative pairing. For instance, Figure 12.3 shows the 2D distribution of $m^{\text{max}}_{\ell 1,\text{J1}}$ against $m_{\ell 2,\text{J1}}$ with the LQ hypothesis in the muon channel for a LQ signal with $m_{\text{LQ}} = 1500$ GeV, where $m^{\text{max}}_{\ell 1,\text{J1}}$ is the higher reconstructed LQ mass with the lepton–jet pair labeled as $\ell 1$ and J1, and $m_{\ell 2,\text{J1}}$ is the invariant mass of the lepton–jet pair using $\ell 2$ and J1. The LQ mass is well reconstructed around the expected value for most of the LQ signal events except the ones in the tail region. By intentionally swapping the pairing, these misreconstructed events could also be restored with invariant mass closer to the expected value.

To provide additional separation power, variables related to the visible and invisible event activity, defined in the lab frame, are also used as input variables to the classifier. These variables include the scalar p_{T} sum of the two leptons L_{T}, the scalar p_{T} sum of the two leading large-R jets H_{T}, the scalar p_{T} sum of the two leptons and two large-R jets S_{T}, the missing transverse momentum $E^{\text{miss}}_{\text{T}}$, and the significance of missing transverse momentum defined as $E^{\text{miss}}_{\text{T}}/\sqrt{H_{\text{T}}}$. Lastly, jet substructure information is exploited to identify large-R jets that are likely to have originated from the hadronic decay of a top quark, using the N-subjettiness ratio τ_{32} [183, 184], the splitting measure $\sqrt{d_{23}}$ [185, 186] and the Q_W variables [187][1]. The description of these variables can be found in

[1]Since the kinematics of large-R jets are modified by subtracting the energy of any electron overlapping with the large-R jet, the substructure variables are no longer compatible and thus not used in the electron channel

Section 8.4.3. A complete list of input variables to the classifier is provided in Table 12.4.

To ensure that the MC simulation is reasonably well-modeled such that no bias from mis-modeling is introduced to the training, the background expectation from simulation is compared with the data in the CRs. In general, the input variables and BDT output scores are found to be in good agreement between the data and MC prediction. As an example, Figure 12.4 shows the distributions of the dilepton invariant mass in the $Z+$jets CR of the electron and muon channel. Figure 12.5 shows the reconstructed W mass based on a dileptonic $t\bar{t}$ hypothesis in the $t\bar{t}$ CR of the electron and muon channel.

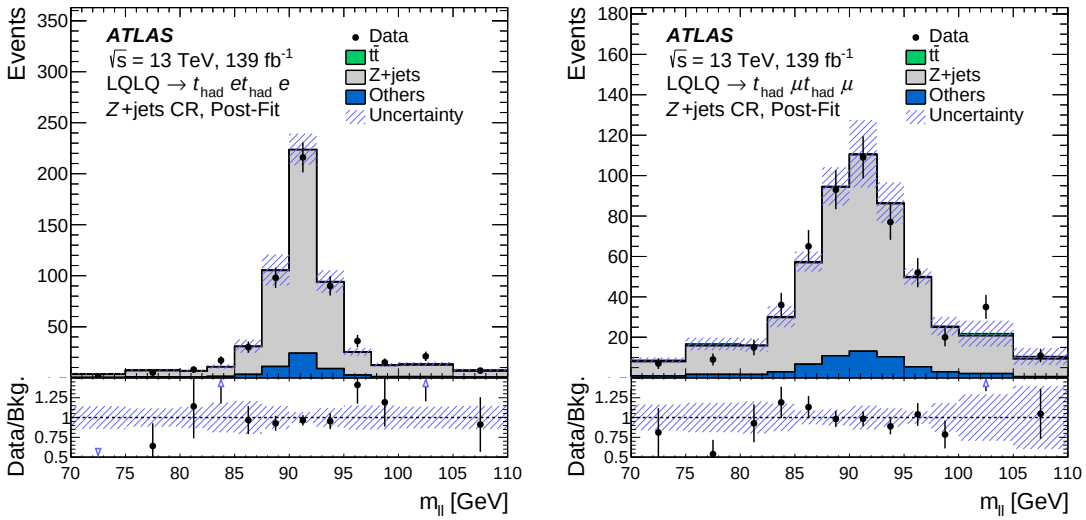

Figure 12.4: The distributions of dilepton invariant mass $m_{\ell\ell}$ in the $Z+$jets CR after the simultaneous background-only fit of the electron (left) and muon (right) channel. The bottom panels show the ratio of data to expected background. The hatched band represents the total uncertainty. [97]

Table 12.4: The discriminating variables used in the signal–background discrimination training can be classified into five different groups. The first three groups include kinematic variables that are physics-based rather than detector-based, conditioned on different physics process hypotheses: LQ, dileptonic $t\bar{t}$ and leptonic Z decay hypothesis. These physics-based kinematic variables include the invariant masses and the momenta of intermediate and final-state particles in their parent's rest frame. In the dileptonic $t\bar{t}$ decay hypothesis, the combinatoric ambiguity in the small-R-jet–lepton pairing is resolved using the 'min ΔM_{top} approach' of the recursive jigsaw reconstruction technique [253]. The reconstructed hemisphere of the decay process associated with the leading (subleading) lepton is labeled with 1 (2). The fourth group of variables is detector-based and defined in the lab frame. These variables are related to the event-level activity of visible objects or missing transverse momentum. The last group of variables is used to identify the three-prong jet structure of hadronic top-quark decays and is used only in the muon channel.

Input variables		
LQ hypothesis	m_{LQLQ}	Invariant mass of LQ pair system, reconstructed from two leptons and two large-R jets
	$m^{\text{max}}_{\ell 1,\text{J1}}$	The higher mass of the two LQ candidates, with the lepton–jet pair labeled as $\ell 1$ and J1.
	$m^{\text{min}}_{\ell 2,\text{J2}}$	The lower mass of the two LQ candidates, with the lepton–jet pair labeled as $\ell 2$ and J2.
	$m_{\ell 2,\text{J1}}$	Invariant mass of lepton–jet pair $\ell 2$ and J1
	$m_{\ell 1,\text{J2}}$	Invariant mass of lepton–jet pair $\ell 1$ and J2
	m_{J1}	Invariant mass of large-R jet J1
	m_{J2}	Invariant mass of large-R jet J2
	$E^{\text{LQ}}_{\ell 1}$	Energy of lepton $\ell 1$ in its LQ parent's rest frame
	$E^{\text{LQ}}_{\ell 2}$	Energy of lepton $\ell 2$ in its LQ parent's rest frame
	E^{LQ}_{t1}	Energy of large-R jet J1 in its LQ parent's rest frame
	E^{LQ}_{t2}	Energy of large-R jet J2 in its LQ parent's rest frame
Dilepton $t\bar{t}$ hypothesis	m_{tt}	Invariant mass of $t\bar{t}$ system, reconstructed from two leptons, two resolved jets and $E_{\text{T}}^{\text{miss}}$
	$m_{t1'}$	Invariant mass of top quark $t1'$, reconstructed from W boson $W1'$ and b-quark $b1'$
	$m_{t2'}$	Invariant mass of top quark $t2'$, reconstructed from W boson $W2'$ and b-quark $b2'$
	$m_{t1',\text{ swapped}}$	Invariant mass of top quark $t1'$, with its b-quark child $b1'$ swapped with that of top quark $t2'$
	$m_{t2',\text{ swapped}}$	Invariant mass of top quark $t2'$, with its b-quark child $b2'$ swapped with that of top quark $t1'$
	$m_{W1'}$	Invariant mass of W boson $W1'$, reconstructed from the leading lepton $\ell 1'$ and $E_{\text{T}}^{\text{miss}}$
	$m_{W2'}$	Invariant mass of W boson $W2'$, reconstructed from the subleading lepton $\ell 2'$ and $E_{\text{T}}^{\text{miss}}$
	$E^{t}_{b1'}$	Energy of small-R jet j1 as b-quark candidate $b1'$ in its top quark parent ($t1'$) rest frame
	$E^{t}_{b2'}$	Energy of small-R jet j2 as b-quark candidate $b2'$ in its top quark parent ($t2'$) rest frame
	$E^{W}_{\ell 1'}$	Energy of the leading lepton $\ell 1'$ in its W boson parent ($W1'$) rest frame
	$E^{W}_{\ell 2'}$	Energy of the subleading lepton $\ell 2'$ in its W boson parent ($W2'$) rest frame
$Z \to \ell\ell$ hypothesis	$m_{\ell\ell}$	Invariant mass of the dilepton system
	$p^{\text{lab}}_{\text{T},\ell\ell}$	Transverse momentum of the dilepton system in the lab frame
Detector-based	L_{T}	Scalar p_{T} sum of the two leptons
	H_{T}	Scalar p_{T} sum of the two leading large-R jets
	S_{T}	Scalar p_{T} sum of the two leptons and the two leading large-R jets
	$E_{\text{T}}^{\text{miss}}$	Missing transverse momentum
	$E_{\text{T}}^{\text{miss}}$ sig.	Missing transverse momentum significance, defined as $E_{\text{T}}^{\text{miss}}/\sqrt{H_{\text{T}}}$
Jet substructure	sd_{23}	k_t splitting scale for the 2nd and 3rd subjet, defined as $\text{sd}_{23} = \min(p_{\text{T},2}, p_{\text{T},3}) \times \Delta R_{23}$
	τ_{32}^{WTA}	The ratio of τ_3 to τ_2, where N-subjettiness variable τ_N is defined as $\tau_N = \frac{1}{d_0}\sum_{i\in\text{jet constituents}} p_{\text{T},i} \times \min(\delta R_{1i}, ..., \delta R_{Ni})$ with $d_0 = \sum_{i\in\text{jet constituents}} p_{\text{T},i} \times R$, where R is the radius parameter of the jet, and δR_{ji} is the distance between the subjet j and the constituent i. WTA denotes the winner-take-all (WTA) recombination scheme [**wta**] used in subjet reconstruction.
	Q_{w}	The minimum invariant mass of the two subjets in the second-to-last reclustering step of the k_t algorithm, applied to a large-R jet
MVA parameterization	$m_{\text{LQ, hypo}}$	Set to the test mass point at which the model is utilized. In the training phase, this parameter is set to the corresponding LQ mass for the signal samples, and a uniformly distributed random value from the training set of LQ mass points for the background samples.

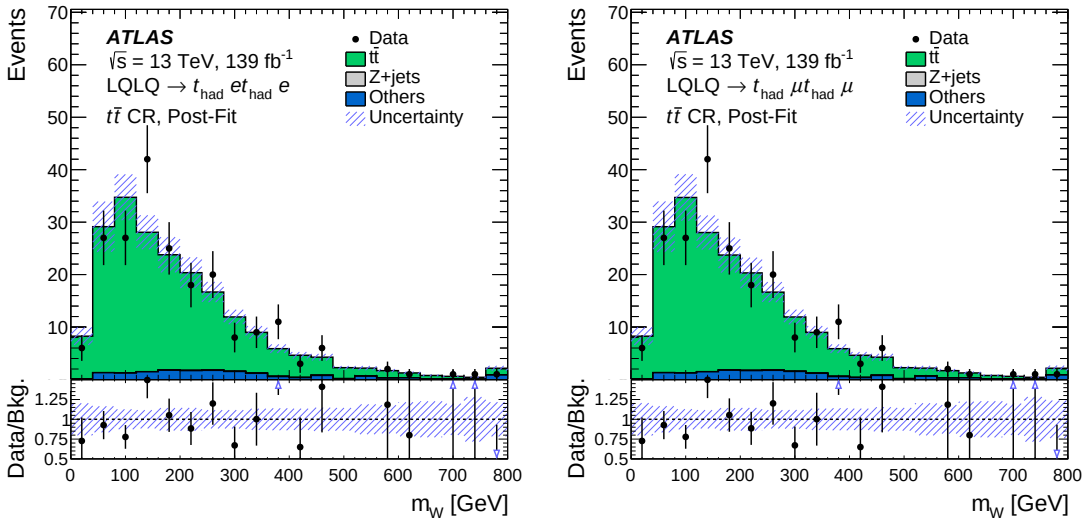

Figure 12.5: The distributions of the reconstructed W mass associated with the leading lepton assuming a dileptonic hypothesis in the $t\bar{t}$ CR after the simultaneous background-only fit of the electron (left) and muon (right) channel. The bottom panels show the ratio of data to expected background. The hatched band represents the total uncertainty. [97]

Parameterized Machine Learning

As the characteristics of the LQ signal vary with m_{LQ}, the theoretical LQ mass $m_{\mathrm{LQ,\,hypo}}$ is also included as part of the inputs to the BDT classifier, following the approach presented in Ref. [254]. During the training phase, $m_{\mathrm{LQ,\,hypo}}$ is set to the corresponding true m_{LQ} value for the signal events, and is uniformly selected from the training set of the LQ mass points for the SM background events. This way when the classifier is used in practice, it will produce a conditional BDT output score that depends on the choice of the input parameter $m_{\mathrm{LQ,\,hypo}}$. As a result, the sensitivity to the signal process could be optimized over a wide range of LQ mass using only one BDT classifier even for mass values where it has not been given training samples. The parameterized BDT is trained with signal events simulated for m_{LQ} values from 900 GeV to 1900 GeV, with a 200 GeV step size. The modeling of the BDT distribution of the two major backgrounds is validated using the events in the $Z+$jets and $t\bar{t}$ CRs, as shown in Figure 12.6 and 12.7 for a few representative mass points.

The binning of the BDT discriminant in the SR is optimized to maximize the signal sensitivity while ensuring a minimum of three background events in the highest BDT bin. The final choice of binning is three bins, which hereafter are referred to as the low, mid and high BDT SR. Figure 12.8 shows the relative efficiency of the signal events to be categorized in the high BDT SR with respect to the inclusive SR efficiency. Of the signal events which enter the signal region, over 94% fall into the high BDT SR while only 1% and 8% of the $t\bar{t}$ and $Z+$jets background do so, respectively. To validate the usefulness of the parameterization, the method is compared with two alternatives,

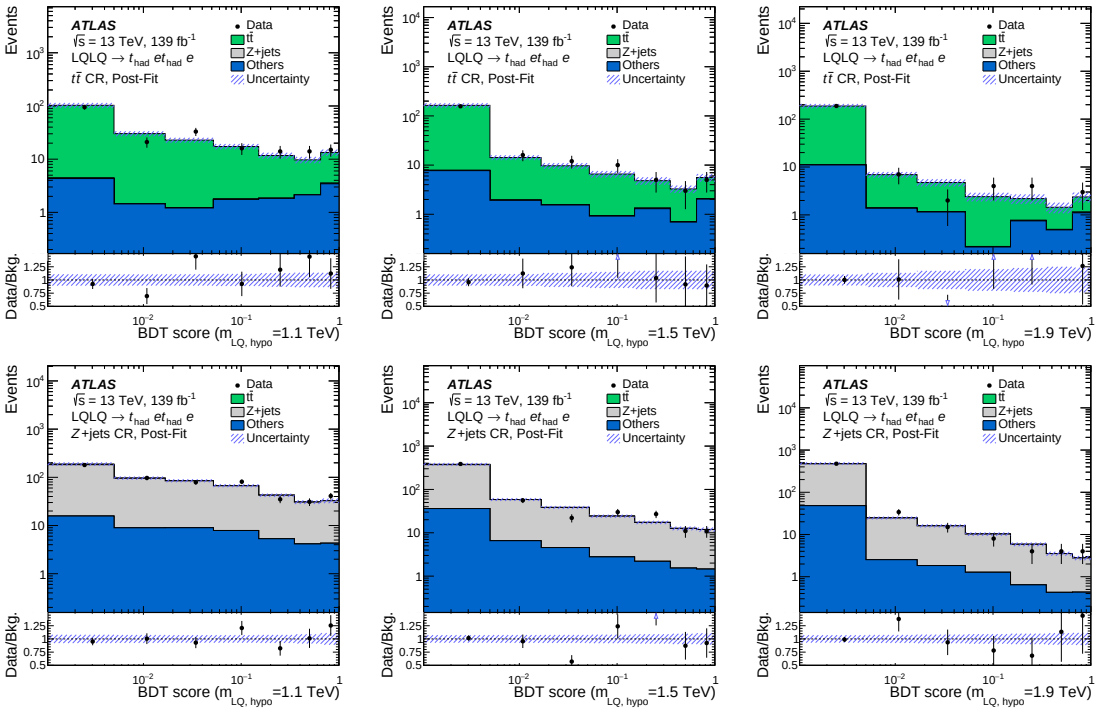

Figure 12.6: The distributions of the BDT output score in the $t\bar{t}$ (top row) and the Z+jets (bottom row) for LQ masses of 1.1 TeV (left), 1.5 TeV (middle) and 1.9 TeV (right) in the electron channel after the simultaneous background-only fit of the CRs. The bottom panels show the ratio of data to expected background. The hatched band represents the total uncertainty. [97]

in one of which individual BDT classifiers are trained at one particular m_{LQ} value and used for all other values, and in another of which a single BDT classifier is trained using an unlabeled mixture of signal samples and used for all mass values. As illustrated in Figure 12.9, the performance of the former method gives the best performance based on the area-under-the-curve (AUC) metric at the corresponding targeted mass involved in the training, but the performance degrades as the mass value gets further away from the trained one. While the latter method does not perform as well as the former one that uses designated classifier for each mass value, it uses only one classifier to provide reasonable discriminating power generally over the mass range. A balance between maximizing the signal sensitivity and minimizing the number of distinct classifiers is struck by using the parameterized method, allowing simpler implementation without any appreciable loss of performance.

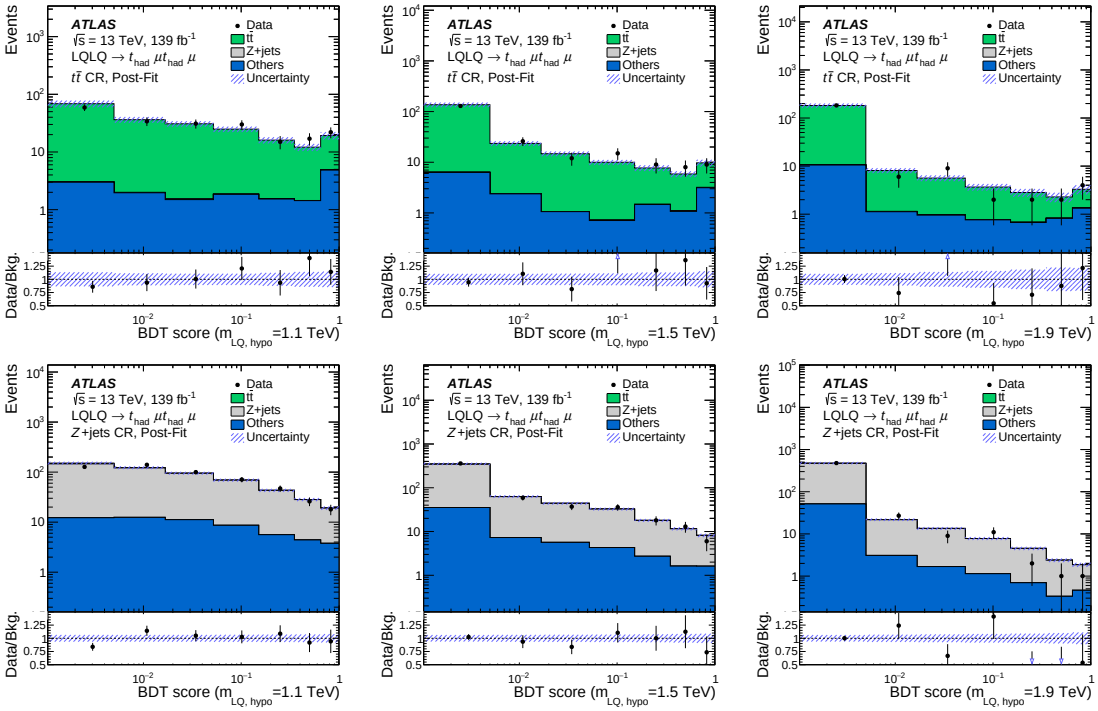

Figure 12.7: The distributions of the BDT output score in the $t\bar{t}$ (top row) and the $Z+$jets (bottom row) for LQ masses of 1.1 TeV (left), 1.5 TeV (middle) and 1.9 TeV (right) in the muon channel after the simultaneous background-only fit of the CRs. The bottom panels show the ratio of data to expected background. The hatched band represents the total uncertainty. [97]

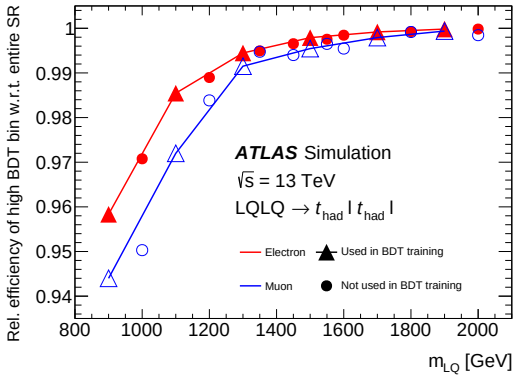

Figure 12.8: The relative efficiency for signal events to be categorized in the high BDT signal region with respect to the signal region efficiency as a function of LQ mass for the electron (red) and muon (blue) channel. The triangle data points are the LQ mass points used in the BDT training, with straight lines connected in between. The circle data points are the mass points that are not involved in the training. [97]

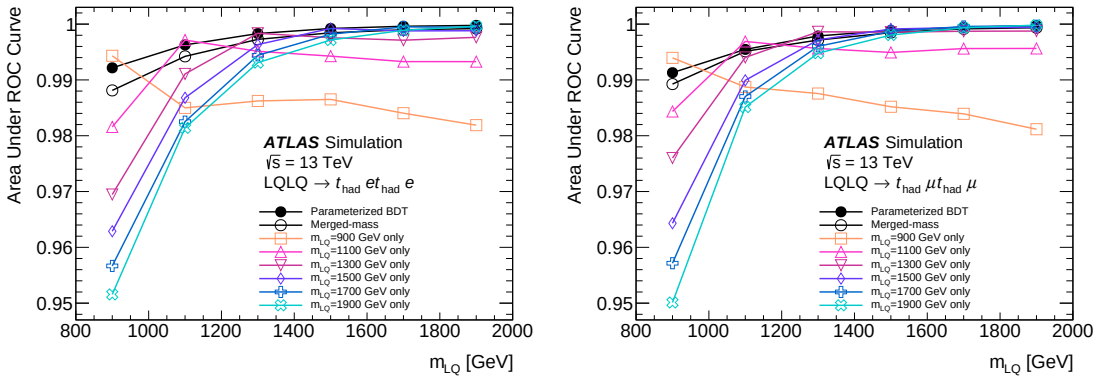

Figure 12.9: Comparison of the performances in the signal–background discrimination for the parameterized BDT (solid dot) which learns the classification as a function of LQ mass, a single BDT trained with an unlabeled mixture of all samples together (open circle), and dedicated BDTs trained with the sample of a specific mass point (coloured), evaluated based on the area under the curve (AUC) metric. The left and right plots are for electron and muon channel respectively. As expected, the parameterized BDT scores higher than the single BDT trained with unlabeled samples, and slightly lower than the dedicated BDTs. [97]

12.3 Statistical Analysis

The BDT discriminant distribution in the SR and the expected yields in the $t\bar{t}$ and $Z+$jets CRs are combined in a simultaneous fit to test for the existence of leptoquark pair productions, separately in the electron and muon channel. The parameter of interest is defined as the signal strength μ; however, results are converted into the corresponding cross section for straightforward interpretation. The statistical analysis is based on a binned likelihood function constructed as a product of the Poisson distribution over each bin of all regions, along with constraint terms on nuisance parameters to encode the effect of the statistical and systematic uncertainties on the signal and background expectations. The systematics are either shared among bins affecting the *normalization* of a process, or treated bin-by-bin with no correlation for *shape* effects. Gaussian or log-normal distributions are employed to model the distribution of the nuisance parameters. The form of likelihood is defined in Equation 10.1. The normalizations of the dominant backgrounds, the $t\bar{t}$ and $Z+$jets processes, are constrained by auxiliary measurements performed in the dedicated control regions. Two nuisance parameters, $k_{t\bar{t}}$ and $k_{Z+\text{jets}}$, are introduced to represent the normalization factors of the $t\bar{t}$ and $Z+$jets processes respectively.

In the same manner as the other presented analysis, the local p-values are computed to examine the compatibility of the data and the background-only hypothesis. If no significant discrepancy is observed, the CL_s approach with the asymptotic approximation is used to set upper limits on the signal strength μ at 95% confidence level. The p-value and exclusion limit calculations are

performed, assuming $\beta = 1.0$ with fully hadronic top decays, for LQ mass values from 900 GeV to 2000 GeV at a 100 GeV step size in general and a finer 50 GeV step size around the expected LQ mass exclusion limit.

Cross-checks with sampling distributions generated using pseudo-experiments were performed to test the validity of the asymptotic approximation for the probed leptoquark mass range. The signal cross-section limits derived with the asymptotic formulae are found to be underestimated by as much as 10% for both channels, leading to an impact of less than 5 GeV on the exclusion mass limits.

12.4 Systematic Uncertainties

This section describes the sources of experimental and theoretical systematic uncertainties taken into account. The experimental systematic uncertainties correspond to systematic errors originating from the apparatus used to collect the data, including uncertainties related to luminosity measurement, object reconstruction (jets, electrons, muons, missing transverse energy, etc.), triggering and pileup effects. The theoretical uncertainties stem from the modeling of hard scattering, fragmentation, hadronization and additional radiation in the simulated samples. Statistical uncertainties on the signal and background predictions originating from the finite number of simulated events are also taken into account in the fit via the inclusion of a nuisance parameter in each bin. The systematic uncertainty from each source is incorporated into the profile-likelihood fit via a Gaussian-distributed or log-normal nuisance parameter as mentioned in Section 12.3.

12.4.1 Experimental Uncertainties

Luminosity

The calibration of the luminosity scale is derived with the LUCID-2 detector [232] following the same methodology for the primary luminosity measurements as described in the previously presented analysis (Section 11.5) [233]. The uncertainty in the integrated luminosity in the combined 2015–2018 data is estimated to be 1.7%.

Detector-related Uncertainties

- **Lepton**: For both electrons and muons, uncertainties on the energy scale and resolution are assessed using the reconstructed distribution of Z peak with $Z \to \ell\ell$ events, as discussed in Section 8.2 and 8.3. The muon resolution uncertainty is evaluated separately between the Inner Detector and Muon Spectrometer, while additional uncertainties are applied on muons to account for an observed charge-dependent sagitta bias. Besides, uncertainties of reconstruction, identification, isolation and trigger efficiency are derived from comparisons between the

data and MC using the tag-and-probe method [165]. Due to the impact of possible misalignment between layers of the MS, as well as between the MS and the ID, conservative systematic uncertainties are included to account for the consequent degradation in muon momentum resolution.

- **Jet**: The uncertainties on the scale and resolution of jet mass and energy are measured using several in situ calibrations, including η-intercalibration with dijet events, $Z+$jets balance, $\gamma+$jets balance and multi-jet balance, which takes into account the effects related to pileup, flavor composition, flavor response, and punch-through jets. The uncertainty associated with the jet vertex tagger is evaluated exploiting the tag-and-probe method with $Z(\rightarrow \mu\mu) +$ jets events. Additional uncertainties are included to account for the impacts on jet energy scale due to the analysis-specific removal of electron energy from the large-R jets.

- **Missing transverse momentum**: The uncertainties regarding the scale and resolution of the missing transverse momentum are evaluated by assessing the systematic uncertainty originating from the soft underlying events via the soft term in the missing transverse momentum calculations. The uncertainties are calculated from the data–to–MC comparisons using events with $Z \rightarrow \mu\mu$ final states without jets.

- **Pileup**: In the same manner as the previously presented analysis, a pileup reweighting procedure is applied to correct for the difference in the distribution of the number of interactions per bunch crossing between the data and MC simulation such that pileup-dependent physics observables are better modeled in the simulated events.

12.4.2 Theoretical Uncertainties

Cross-section Uncertainties

Theoretical cross section uncertainties are applied to the simulated signal and background samples. The uncertainty for LQ pair production takes into account PDF, α_S and scale uncertainties in the approximate NNLO + NNLL calculation of the cross section. The PDF and α_S uncertainties are estimated from the PDF4LHC15 error set [255]. The effect of uncertainties in the renormalization and factorization scales is estimated by varying the scales by a factor of two about the central value. The overall uncertainty increases from 10% at 1 TeV to 25% at 2 TeV. This cross-section uncertainty is not included in the profile-likelihood fit, but only represented as the uncertainty band around the theoretical cross-section line in the final results (see Figure 12.12). The uncertainties for $W+$jets and diboson production are conservatively assumed to be 50% [256, 257]. For single top quark and $t\bar{t}\,V$ production, the uncertainties are taken as 7% [258, 259] and 30% [260], respectively.

The normalizations of $t\bar{t}$ and $Z+$jets processes are determined from the data via the normalization parameters.

Generator Modeling Uncertainties

Modeling uncertainties are estimated for the signal as well as $Z+$jets, $t\bar{t}$ and single-top-quark backgrounds, by comparing the nominal simulated samples with alternative generator modeling. The alternative systematic samples are normalized to the same cross section as the nominal samples, to consider only the impact of alternative modeling on the shape and acceptance.

For the LQ signal, alternative systematic samples are compared with the nominal sample to account for uncertainties in the QCD running coupling, the PDF and the radiation modeling. The QCD running coupling uncertainty is evaluated by considering the variations with the same nominal PDF but two different α_S value 0.118 ± 0.001. The uncertainties due to the choice of PDF are estimated with the PDF4LHC15 error set, which includes 100 eigen-variations of the nominal PDF, and two alternative PDFs, MMHT and CT14. To estimate the uncertainty of additional radiation modeling, renormalization and factorization scales are independently varied up and down by a factor of two. The maximum shift within the envelope of the variations is taken as the estimate of the scale uncertainty. The uncertainty of initial-state gluon radiation is also estimated by comparing with simulated samples generated with enhanced or reduced initial-state radiation.

For the $Z+$jets background, three sources of modeling uncertainties related to the radiation scales, choice of PDF and α_S estimates are considered. In the same manner as the LQ signal, these uncertainties are evaluated by comparing with alternative samples of variations in the renormalization and factorization scales, the PDF choice, and the up- and down-variation of α_S.

For the $t\bar{t}$ background, four sources of modeling uncertainties related to the hard scatter generation, parton showering, additional radiation and PDF are considered. The uncertainty of the matrix-element calculation is evaluated by comparing two different MC generators, MADGRAPH5_aMC@NLO and POWHEG-BOX, both interfaced to PYTHIA for parton showering and hadronization. To estimate the uncertainty of the fragmentation and hadronization model, two different parton shower algorithms, PYTHIA and HERWIG, are compared while keeping the same matrix-element generation provided by POWHEG-BOX. The uncertainty of the amount of additional initial- and final-state gluon radiation are assessed by comparing simulated samples generated with enhanced or reduced initial-state radiation, double h_{damp} parameter, and variations of the radiation scales. Like the LQ signal and $Z+$jets background, the uncertainty on the choice of PDF is estimated with the PDF4LHC15 error set.

In this analysis, the single-top-quark background comes mainly from the Wt-channel and is a minor background. The modeling uncertainty of the single-top-quark background is evaluated the same way as the $t\bar{t}$ background, except that an additional systematic uncertainty is considered to account for the uncertainty stemming from the interference between Wt-channel single-top resonant

production and double resonant $t\bar{t}$ production. Different treatments could be employed to factorize out the $t\bar{t}$ contribution from the matrix-element calculation, one of which is the diagram removal (DR) method that removes the interference between Wt and $t\bar{t}$ production by not considering the Feynman diagrams of double resonant $t\bar{t}$ process. Another method is the diagram subtraction (DS) method, which removes the $t\bar{t}$ contribution by introducing an arbitrary subtraction term to cancel out the resonant top quark pole and to keep the interference contribution. The relative difference between the two methods is taken as a systematic uncertainty.

12.4.3 Systematic Handling

Pruning

To reduce the computation time of the profile likelihood fit and to avoid numerical instabilities, the nuisance parameters associated to the systematic uncertainties are removed, or so-called *pruned*, if they do not change the results considerably. If an uncertainty leads to an impact on the normalization by more than 3% or a shape variation by more than 3% between neighboring bins, the relevant nuisance parameter is included in the likelihood fit. While roughly 60% of nuisance parameters are pruned completely for all signal and control regions, the effect of pruning on the exclusion mass limits is found to be less than 1 GeV.

Smoothing

To prevent misleadingly enlarged constraints on nuisance parameters due to statistical fluctuations, a smoothing procedure is commonly applied in ATLAS analyses. Since this analysis is quite simple, with only three bins in the SR, smoothing is not applied.

Symmetrization

To simplify the statistical analysis, all uncertainties except the normalization uncertainties are symmetrized. For systematic uncertainties with one-sided variation, the variation in the alternative setup is taken as the $+1\sigma$ and -1σ effect. For uncertainties with both up and down variations, the 'average' of the up and down variations is calculated bin by bin as the $\pm 1\sigma$ effect.

12.5 Results

12.5.1 Unblinded Fit Results

Figure 12.10 and Table 12.5 summarize the estimates of each background source and the unblinded observed data event yield in the signal and control regions after a global background-only fit, in which statistical and systematic uncertainties are considered. Both the figure and table correspond to

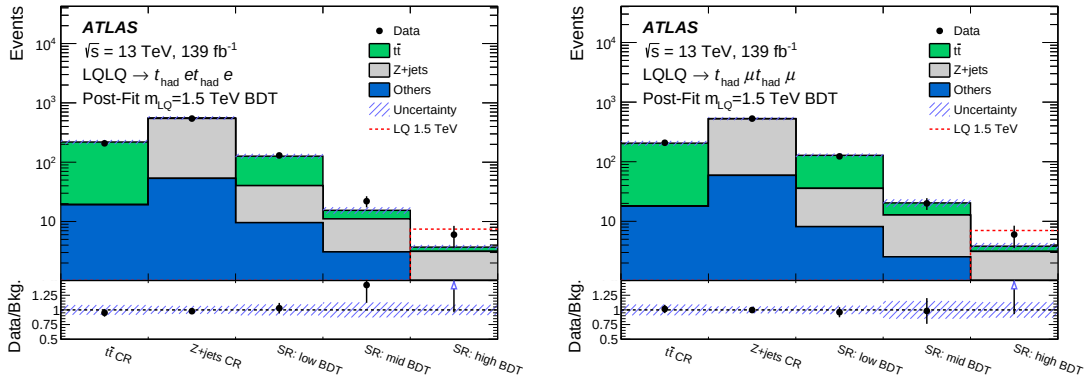

Figure 12.10: Fit results (background-only) for the binned BDT output score distribution in the signal region of the electron (left) and muon (right) channel, and the overall number of events in the $t\bar{t}$ and $Z+$jets control regions. The lower panel shows the ratio of data to the fitted background yields. The band represents the systematic uncertainty after the maximum-likelihood fit. [97]

the SR binning for a representative LQ mass of 1500 GeV, and the expected signal event yield for the same LQ mass is shown alongside for reference. Due to the correlations between the fit parameters, the uncertainty of the total event yield shown in the table is not identical to the sum in quadrature of each component. The nuisance parameters associated to the normalization of the $t\bar{t}$ and $Z+$jets predictions are pulled due to the constraint from the dedicated control regions. In the electron (muon) channel, the ratio of the $t\bar{t}$ post-fit yield to the pre-fit yield is $0.90 \pm 0.25 (0.84 \pm 0.24)$. The ratio of the $Z+$jets post-fit yield to the pre-fit yield is $0.95 \pm 0.20 (0.87 \pm 0.10)$.

12.5.2 Dominant Sources of Uncertainty

The sensitivity of the analysis is primarily limited by the statistical uncertainty of the data. The impact of each nuisance parameter on the best-fit signal strength, as well as the pull on the nuisance parameters, is assessed like the previously presented analysis. The impact from top 20 ranked nuisance parameters are shown in Figure 12.11. Generally, none of the nuisance parameters is significantly constrained by the data. Including all systematic uncertainties weakens the expected exclusion mass limits by only around 10 GeV, and for a LQ mass of 1.5 TeV the cross-section limit is weakened by less than 7% in both the electron and muon channel.

12.5.3 Statistical Interpretation

In neither of the electron and muon channels do we observe significant excess of events above the background-only expectation within the search range of 900–2000 GeV, indicating that there is no evidence of LQ pair production decaying into top quarks and charged leptons (electrons or muons). The highest local significance of 1.2 (1.3) standard deviations is observed for a leptoquark mass of

Table 12.5: Event yields in the signal and control regions before and after the background-only fit to data in the electron and muon channel. The quoted uncertainties include statistical and systematic uncertainties; for the $t\bar{t}$ and Z+jets backgrounds no cross-section uncertainty is included since it is a free parameter of the fit. The contributions from single top, $t\bar{t}V$, diboson and W+jets production are included in the 'Others' category. In the post-fit case, the uncertainties in the individual background components can be larger than the uncertainty in the sum of the backgrounds, due to the correlations between the fit parameters. Both signal models correspond to $m_{\mathrm{LQ}} = 1500$ GeV assuming 100% branching ratio into a hadronically decaying top quark and a charged lepton.

Electron Channel					
	$t\bar{t}$ CR	Z+jets CR	SR: low BDT	SR: mid BDT	SR: high BDT
Sample	Pre-fit				
$t\bar{t}$	222 ± 58	9.6 ± 7.8	90 ± 30	4.3 ± 1.9	0.6 ± 0.3
Z+jets	0.3 ± 0.1	520 ± 100	32.7 ± 5.9	8.2 ± 1.8	2.9 ± 0.8
Others	16.1 ± 5.3	55 ± 18	6.7 ± 3.6	2.1 ± 1.1	0.3 ± 0.1
Total background	238 ± 60	590 ± 110	130 ± 36	14.6 ± 3.4	3.7 ± 0.9
Signal (m_{LQ} = 1500 GeV)	< 0.001	0.006 ± 0.002	< 0.001	0.015 ± 0.004	7.4 ± 1.6
	Post-fit				
$t\bar{t}$	200 ± 19	10.3 ± 5.3	86 ± 10	4.4 ± 1.0	0.6 ± 0.1
Z+jets	0.22 ± 0.04	493 ± 43	30.7 ± 2.9	8.0 ± 0.9	2.8 ± 0.3
Others	19.1 ± 5.7	53 ± 19	9.6 ± 5.2	3.1 ± 1.6	0.3 ± 0.1
Total background	219 ± 18	556 ± 38	126 ± 12	15.4 ± 2.0	3.7 ± 0.3
Data	208	544	130	22	6

Muon Channel					
	$t\bar{t}$ CR	Z+jets CR	SR: low BDT	SR: mid BDT	SR: high BDT
Sample	Pre-fit				
$t\bar{t}$	222 ± 58	8.9 ± 6.9	112 ± 23	8.3 ± 5.0	0.8 ± 0.5
Z+jets	0.3 ± 0.1	532 ± 45	31.7 ± 2.8	11.7 ± 1.3	2.9 ± 0.3
Others	16.1 ± 6.9	59 ± 19	7.6 ± 4.1	2.2 ± 1.7	0.6 ± 0.4
Total background	238 ± 60	600 ± 53	152 ± 24	22.2 ± 6.2	4.2 ± 1.0
Signal (m_{LQ} = 1500 GeV)	< 0.001	0.013 ± 0.003	< 0.001	0.031 ± 0.007	7.0 ± 1.4
	Post-fit				
$t\bar{t}$	187 ± 19	7.9 ± 4.1	92.2 ± 9.3	7.6 ± 2.9	0.7 ± 0.3
Z+jets	0.22 ± 0.03	463 ± 36	27.6 ± 2.2	10.2 ± 1.0	2.5 ± 0.3
Others	17.9 ± 7.5	59 ± 18	8.1 ± 4.1	2.5 ± 1.8	0.6 ± 0.5
Total background	205 ± 19	530 ± 32	127.9 ± 9.3	20.4 ± 3.1	3.8 ± 0.5
Data	208	529	123	20	6

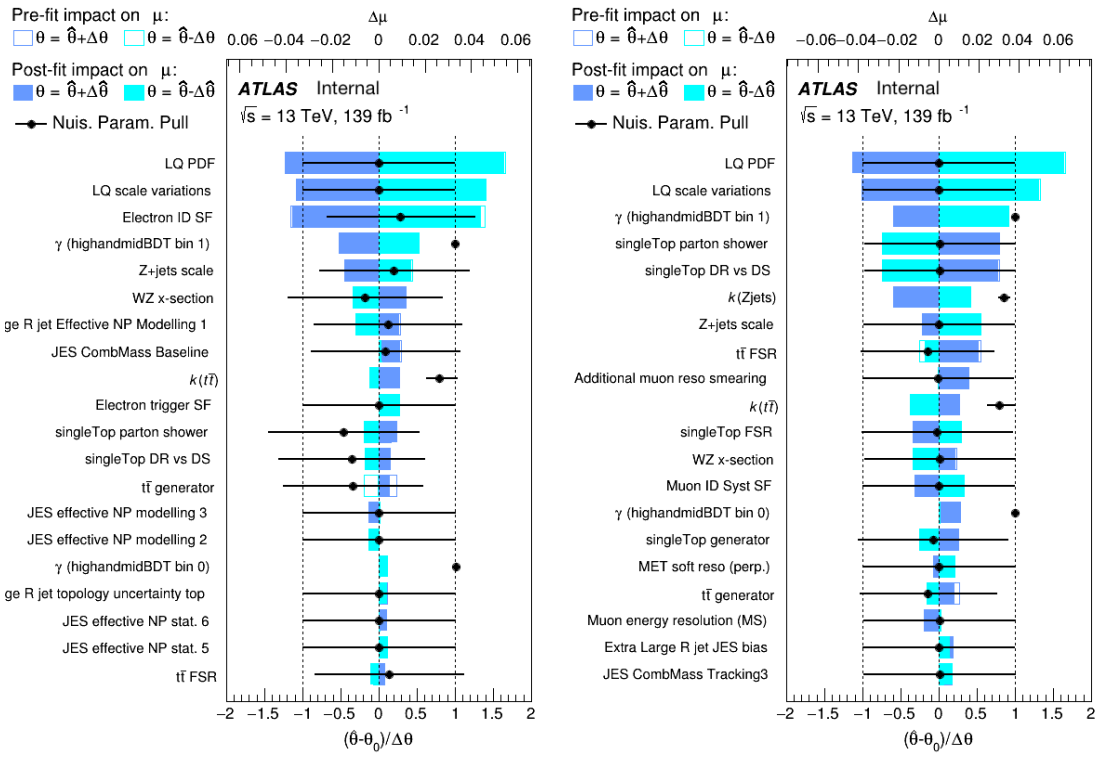

Figure 12.11: Ranking of nuisance parameters based on the impact on the best-fit $\hat{\mu}$ value, for a representative signal mass of 1.5 TeV, in the electron (left) and muon (right) channel. The open areas correspond to the pre-fit upward and downward variations, and the solid areas correspond to the post-fit ones. The dots represent the corresponding pulls for the nuisance parameters. The MC statistical components per bin, γ, and the background normalization parameters, k, have priors at 1, while all other nuisance parameters have priors at 0. Only the top 20 ranked nuisance parameters are shown.

1450 (1600) GeV in the electron (muon) channel.

As no excess is found, exclusion limit setting at the 95% confidence level is performed on leptoquark pair production in $\beta = 1$ scenario, as presented in Figure 12.12. Since the BDT classifier is parameterized to provide excellent discriminating power over the whole m_{LQ} search range, the signal sensitivity that mostly comes from the high BDT SR exhibits a weak dependence on the leptoquark mass, resulting in a flat cross-section limit over the search range. The upper cross-section limits are compared with the central value of the theoretical NNLO + NNLL prediction of the signal cross section to determine a lower mass limit on m_{LQ}. The observed (expected) lower limit on m_{LQ} are found to be 1480 (1560) GeV and 1470 (1540) GeV for the electron and muon channel respectively.

Exclusion contours may also be determined in the $\mathcal{B}$–m_{LQ} plane in terms of the lower mass limits at different branching ratios of a leptoquark decaying into a charged lepton and a top quark.

Assume that there is zero acceptance for LQ decays involving neutrinos, the mass limit is computed by scaling the theoretical cross section by the branching ratio squared, and scanning over various values of $\mathcal{B}$ in step size of 0.1. The presented results, as shown in Figure 12.13, establish the first ATLAS search for leptoquarks with top-philic cross-generational couplings.

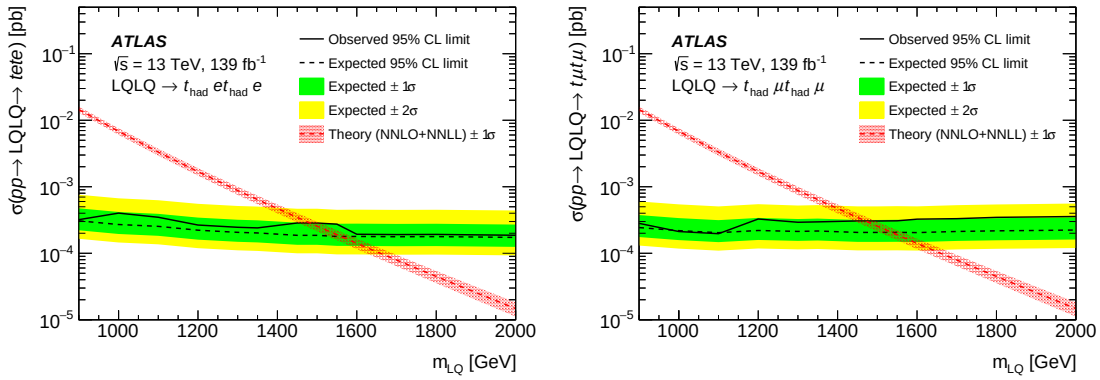

Figure 12.12: Upper limits at 95% CL on the cross section of LQ pair production as a function of LQ mass, assuming a branching ratio $\mathcal{B}(\mathrm{LQ} \to t\ell^{\pm}) = 1$, for the electron (left) and muon (right) channel. Observed limits are shown as a black solid line and expected limits as a black dashed line. The green and yellow shaded bands correspond to ± 1 and ± 2 standard deviations, respectively, around the expected limit. The red curve and band show the nominal theoretical prediction and its ± 1 standard deviation uncertainty. [97]

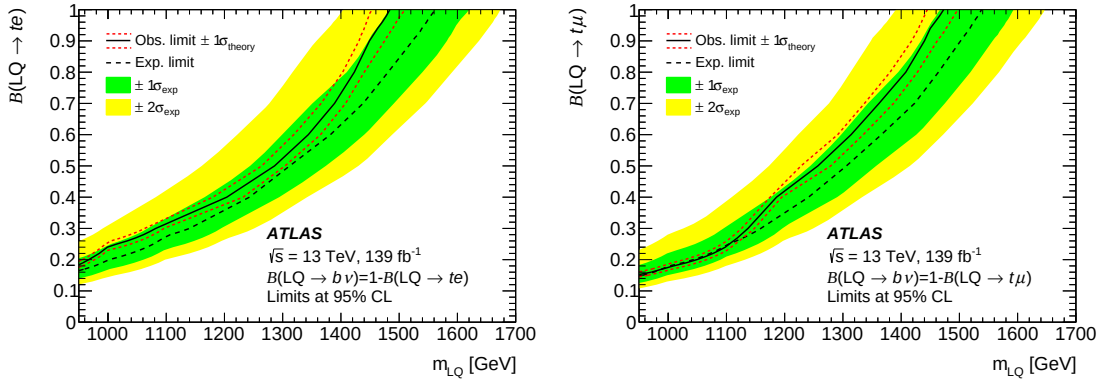

Figure 12.13: Lower exclusion limits on the leptoquark mass for scalar leptoquark pair production as a function of the branching ratio into a top quark and an electron (left) or a muon (right) at 95% CL. The observed nominal limits are indicated by a black solid curve, with the surrounding red dotted lines obtained by varying the signal cross section by uncertainties from PDFs, renormalization and factorization scales, and the strong coupling constant α_S. Expected limits are indicated with a black dashed curve, with the yellow and green bands indicating the ± 1 standard deviation and ± 2 standard deviation excursions due to experimental and modeling uncertainties. [97]

Chapter 13

Conclusions and Outlook

This dissertation has presented the upgrade of the Transition Radiation Tracker data acquisition system for the higher trigger rate and higher luminosity conditions in LHC Run II. Several developments were made in the firmware and hardware of the off-detector readout system to achieve larger bandwidth and more efficient compression beyond the original design. The maximum trigger rate that the readout system can handle has increased by $\sim 20\%$, and the maximum occupancy has increased by $\sim 30\%$ at 100 kHz trigger rate. These improvements allowed the TRT to handle average pileup as high as $\langle\mu\rangle = 60$–70 during Run II.

For Run III, the targeted mean pileup will be around 60. The data should still be within the bandwidth of the TRT DAQ system, as the occupancy would be increasing much more slowly even if the pileup increases further. There were suggestions to implement a surjective mapping of straw-word patterns to reduce their variations and thus lowering the entropy; however, such mapping would not be very effective in reducing the data volume due to the logarithmic behavior of entropy. One potential solution to further improve the compression efficiency is to remove the constraint of having zero words hard-codedly compressed as a single bit, which is a constraint originated from the historical implementation of decoding in the offline software. While it is true that the zero words would always be compressed as one bit way back when the occupancy was less than 50%, this is no longer always the case in Run II as we have reached occupancy way beyond 50%. In fact, if the occupancy is larger than 66%, the optimal Huffman encoding would always compress a zero word into a codeword with at least two bits, no matter how the frequency of the other straw-word patterns is distributed. Since zero word is still the most frequent straw-word pattern, properly optimizing the Huffman encoding and compressing the zero words could bring appreciable improvement, unlike the other proposed surjective mapping solution.

Two searches for new massive bosons were also presented in this dissertation. In the first search presented in Chapter 11, heavy resonances decaying into a hadronic $Z/W/H$ boson and a photon were sought for in the boosted regime. The large-R-jet–photon system was explored for potential

new s-channel resonances using data-driven background modeling techniques. Results were interpreted on the partial Run II dataset with an integrated luminosity of 36.1 fb^{-1} of proton–proton collisions collected at $\sqrt{s} = 13$ TeV with the ATLAS detector. No excess of signal events was observed in any search channel. Exclusion limits were set on the resonance production cross section times the branching fraction of the resonance with any decay of the $Z/W/H$ bosons down to 0.1–10 fb for resonance masses between 1 and 6.8 TeV. The $X \to W\gamma$ search was the first hadronic channel of its kind conducted on ATLAS, while the $X \to H\gamma$ resonance was considered for the first time. Figure 13.1 compares the results between the presented hadronic channel of $X \to Z\gamma$ resonance search with the leptonic channel published in Ref. [208], where both channels explore the same dataset. The leptonic channel exploits Z boson decays to electron pairs or muon pairs. The hadronic channel is found to be compatible with the leptonic channel at around 1.5 TeV.

One future direction to improve the analysis is the tagging of the hadronic decays of $Z/W/H$ bosons. A novel large-R jet reconstruction method has been developed to create a new kind of jets for the high momentum domain, called Track-CaloCluster jets [261]. The jet substructure resolution is greatly improved by taking advantage of the superior angular resolution of the tracking detector, while the jet energy measurements rely on the better energy resolution of the calorimeter at high momentum. The use of Track-CaloCluster jets can directly improve the efficiency of boson tagging that applies cuts on jet substructure variables like $D_2^{(\beta=1)}$, leading to an increase in sensitivity. Another direction of exploration is the background modeling methodology. While the background functional form used in the presented analysis has demonstrated its usefulness in describing falling background spectrum in multiple high energy physics analyses, the choice of functional form is a bit ad hoc. One interesting idea is to perform background modeling with a regression technique that is widely used in machine learning industries, called Gaussian Processes [262]. It has the advantage of being non-parametric, so assumption on the functional form is no longer needed.

In the second search presented in Chapter 12, pair productions of scalar leptoquarks decaying into first- or second-generation leptons and fully hadronic top quarks were sought for. A parameterized BDT classifier was developed to distinguish between the signal and background events. Results were interpreted on the full Run II dataset with an integrated luminosity of 139 fb^{-1} of proton–proton collisions. No evidence of leptoquarks was found in both of the electron and muon channel. Exclusion limits were set on the leptoquark masses up to 1.48 TeV and 1.47 TeV in the electron and muon channel respectively. This analysis was the first ATLAS publication searching for top-philic cross-generational leptoquarks. Figure 13.2 shows how other relevant ATLAS searches could exclude the LQ model at the various branching fraction of leptoquarks decaying into a top-quark–charged-lepton pair or a bottom-quark–neutrino pair.

The presented leptoquark analysis focuses on the fully hadronic decay channel of the top-quark pair; it would be interesting to investigate how much sensitivity could be added by including the semi-leptonic channel which has roughly the same branching fraction. Moreover, the presented

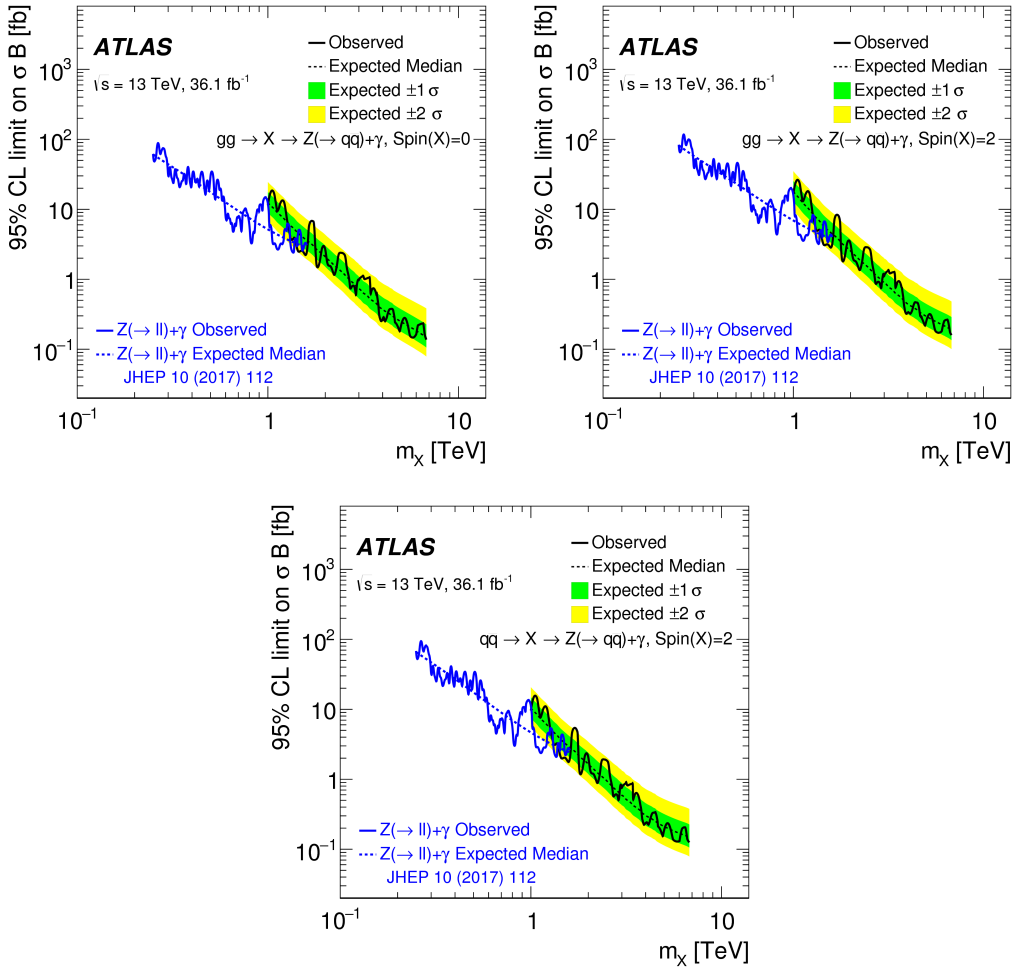

Figure 13.1: Comparison of upper exclusion limits at 95% CL on $\sigma\mathcal{B}$ as a function of resonance mass m_X between the leptonic and hadronic channel of the $X \to Z\gamma$ decay mode. The top left plot is for the spin-0 $X \to Z\gamma$ production via gluon–gluon fusion, the top right plot is for the spin-2 $X \to Z\gamma$ production via gluon–gluon fusion, and the bottom plot is for the spin-2 $X \to Z\gamma$ production via quark–antiquark annihilation. Limit results from the hadronic channel are shown with black lines, and leptonic channel with blue lines. [226]

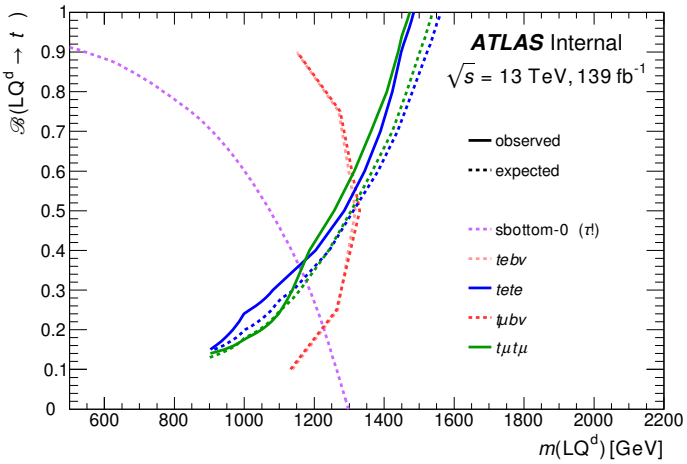

Figure 13.2: Overlays of the exclusion contours for leptoquarks decaying into a top-quark–charged-lepton pair or a bottom-quark–neutrino pair from various relevant analyses. The blue and green lines are the exclusion limits of the presented leptoquark analysis, the red and orange lines are the exclusion limits of an analysis targeting the $\mathcal{B} = 0.5$ final state, and the purple line is the exclusion limit that targets the $b\nu b\nu$ final state.

analysis is likely sensitive to vector leptoquark models, although the recast of these experimental results could not be conducted within my graduation timescale. It was shown in Ref. [84] that the kinematics of scalar and vector leptoquarks are quite similar, and thus they should share more or less the same efficiency. In addition, it was suggested in Ref. [263] that requiring at least one hadronically decaying boosted top quark could capture both the single and pair productions of top-philic leptoquarks. It might be beneficial to categorize events into a signal region with at least two large-R jets, and another signal region with exactly one large-R jet. Besides being sensitive to the single productions, the latter signal region could possibly improve signal sensitivity to pair production around $m_{\mathrm{LQ}} = 1$ TeV, where each top quark is marginally boosted enough to be contained within a large-R jet.

Even though no new particles have been found in the presented analyses and other searches, there remains a window in which physics beyond the SM might be discovered. New phenomena could be revealed with future data of up to 350 fb^{-1} from the third run of the LHC, or at the high-luminosity LHC that is designed to provide five times the luminosity the LHC provides and aimed to record around 3000 fb^{-1} of collision data. The continuation of the search program of the ATLAS collaboration will contribute to the advancement of our understanding of the nature, whether new physics will be discovered or more stringent constraints will be placed on physics beyond the Standard Model.

Bibliography

[1] S. Glashow, *Partial-symmetries of weak interactions*, Nucl. Phys. **22** (1961) 579 (cit. on pp. 4, 7, 8).

[2] S. Weinberg, *A Model of Leptons*, Phys. Rev. Lett. **19** (1967) 1264 (cit. on pp. 4, 7, 8).

[3] A. Salam, *Weak and electromagnetic interactions*, Conf. Proc. C **680519** (1968) 367 (cit. on pp. 4, 7, 8).

[4] D. Griffiths, *Introduction to Elementary Particles*, Wiley, 2008, ISBN: 978-3-527-40601-2 (cit. on p. 4).

[5] ATLAS Collaboration, *Observation of a new particle in the search for the Standard Model Higgs boson with the ATLAS detector at the LHC*, Phys. Lett. B **716** (2012) 1, arXiv: 1207.7214 [hep-ex] (cit. on pp. 4, 7).

[6] CMS Collaboration, *Observation of a new boson at a mass of 125 GeV with the CMS experiment at the LHC*, Phys. Lett. B **716** (2012) 30, arXiv: 1207.7235 [hep-ex] (cit. on pp. 4, 7).

[7] Particle Data Group, *Review of Particle Physics*, PTEP **2020** (2020) 083C01 (cit. on pp. 5, 6, 14, 18, 32, 71, 111).

[8] A. Loureiro et al., *On The Upper Bound of Neutrino Masses from Combined Cosmological Observations and Particle Physics Experiments*, Phys. Rev. Lett. **123** (2019) 081301, arXiv: 1811.02578 [astro-ph.CO] (cit. on p. 5).

[9] D. Galbraith and C. Burgard, *The Standard Model Infographic*, [Online; visited on November 13, 2020], URL: https://cds.cern.ch/record/1473657 (cit. on p. 5).

[10] C.-N. Yang and R. L. Mills, *Conservation of Isotopic Spin and Isotopic Gauge Invariance*, Phys. Rev. **96** (1954) 191, ed. by J.-P. Hsu and D. Fine (cit. on p. 7).

[11] C. Wu, E. Ambler, R. Hayward, D. Hoppes, and R. Hudson, *Experimental Test of Parity Conservation in Beta Decay*, Phys. Rev. **105** (1957) 1413 (cit. on p. 8).

[12] M. Goldhaber, L. Grodzins, and A. Sunyar, *Helicity of Neutrinos*, Phys. Rev. **109** (1958) 1015 (cit. on p. 8).

[13] R. Feynman and M. Gell-Mann, *Theory of the Fermi Interaction*, Phys. Rev. **109** (1958) 193, ed. by L. Brown (cit. on p. 8).

[14] E. Sudarshan and R. Marshak, *Chirality Invariance and the Universal Fermi Interaction*, Phys. Rev. **109** (1958) 1860 (cit. on p. 8).

[15] F. Hasert et al., *Search for elastic muon-neutrino electron scattering*, Phys. Lett. B **46** (1973) 121 (cit. on p. 8).

[16] T. Nakano and K. Nishijima, *Charge Independence for V-particles*, Prog. Theor. Phys. **10** (1953) 581 (cit. on p. 8).

[17] M. Gell-Mann, *The interpretation of the new particles as displaced charge multiplets*, Nuovo Cim. **4** (1956) 848 (cit. on p. 8).

[18] F. Englert and R. Brout, *Broken Symmetry and the Mass of Gauge Vector Mesons*, Phys. Rev. Lett. **13** (1964) 321, ed. by J. Taylor (cit. on p. 9).

[19] P. W. Higgs, *Broken Symmetries and the Masses of Gauge Bosons*, Phys. Rev. Lett. **13** (1964) 508, ed. by J. Taylor (cit. on p. 9).

[20] P. W. Higgs, *Spontaneous Symmetry Breakdown without Massless Bosons*, Phys. Rev. **145** (1966) 1156 (cit. on p. 9).

[21] G. Guralnik, C. Hagen, and T. Kibble, *Global Conservation Laws and Massless Particles*, Phys. Rev. Lett. **13** (1964) 585, ed. by J. Taylor (cit. on p. 9).

[22] N. Cabibbo, *Unitary Symmetry and Leptonic Decays*, Phys. Rev. Lett. **10** (1963) 531 (cit. on p. 12).

[23] M. Kobayashi and T. Maskawa, *CP-Violation in the Renormalizable Theory of Weak Interaction*, Prog. Theor. Phys. **49** (1973) 652 (cit. on p. 12).

[24] ATLAS Collaboration, *Observation of Higgs boson production in association with a top quark pair at the LHC with the ATLAS detector*, Phys. Lett. B **784** (2018) 173, arXiv: 1806.00425 [hep-ex] (cit. on p. 15).

[25] CMS Collaboration, *Observation of $t\bar{t}H$ Production*, Phys. Rev. Lett. **120** (2018) 231801, arXiv: 1804.02610 [hep-ex] (cit. on p. 15).

[26] ATLAS Collaboration, *Summary plots from the ATLAS Standard Model physics group*, [Online; visited on November 13, 2020], URL: https://atlas.web.cern.ch/Atlas/GROUPS/PHYSICS/CombinedSummaryPlots/SM/ (cit. on p. 16).

[27] R. Blumenhagen, D. Lüst, and S. Theisen, *Basic Concepts of String Theory*, Theoretical and Mathematical Physics, Springer, 2013, ISBN: 978-3-642-29496-9 (cit. on p. 16).

[28] A. Ashtekar and J. Lewandowski, *Background independent quantum gravity: a status report*, Class. Quant. Grav. **21** (2004) R53, arXiv: gr-qc/0404018 (cit. on p. 16).

[29] C. Rovelli, *Spin Foams*, PoS **QGQGS 2011** (2013) 003 (cit. on p. 16).

[30] S. Dodelson, *Modern Cosmology*, Academic Press, 2003, ISBN: 978-0-12-219141-1 (cit. on p. 16).

[31] D. Fixsen et al., *The Cosmic Microwave Background Spectrum from the Full COBE FIRAS Data Set*, Astrophys. J. **473** (1996) 576, arXiv: astro-ph/9605054 (cit. on p. 17).

[32] D. Baumann, "INFLATION", *Theoretical Advanced Study Institute in Elementary Particle Physics: Physics of the Large and the Small*, 2011 523, arXiv: 0907.5424 [hep-th] (cit. on p. 17).

[33] A. Linde, *A new inflationary universe scenario: A possible solution of the horizon, flatness, homogeneity, isotropy and primordial monopole problems*, Physics Letters B **108** (1982) 389, ISSN: 0370-2693, URL: https://www.sciencedirect.com/science/article/pii/0370269382912199 (cit. on p. 17).

[34] COBE Collaboration, *The COBE Mission: Its Design and Performance Two Years after Launch*, Astrophys. J. **397** (1992) 420 (cit. on p. 17).

[35] WMAP Collaboration, *The Microwave Anisotropy Probe (MAP) mission*, Astrophys. J. **583** (2003) 1, arXiv: astro-ph/0301158 (cit. on p. 17).

[36] Planck Collaboration, *Planck 2018 results. I. Overview and the cosmological legacy of Planck*, Astron. Astrophys. **641** (2020) A1, arXiv: 1807.06205 [astro-ph.CO] (cit. on p. 17).

[37] Planck Collaboration, *Planck 2018 results. VI. Cosmological parameters*, Astron. Astrophys. **641** (2020) A6, arXiv: 1807.06209 [astro-ph.CO] (cit. on p. 17).

[38] A. Riotto, "Theories of Baryogenesis", *ICTP Summer School in High-Energy Physics and Cosmology*, 1998 326, arXiv: hep-ph/9807454 (cit. on p. 18).

[39] A. D. Sakharov, *Violation ofCPin variance,Casymmetry, and baryon asymmetry of the universe*, Soviet Physics Uspekhi **34** (1991) 392, URL: https://doi.org/10.1070/pu1991v034n05abeh002497 (cit. on p. 18).

[40] C. Baker et al., *Improved Experimental Limit on the Electric Dipole Moment of the Neutron*, Phys. Rev. Lett. **97** (2006) 131801, arXiv: hep-ex/0602020 (cit. on p. 18).

[41] M. Gonzalez-Garcia and M. Maltoni, *Phenomenology with massive neutrinos*, Phys. Rept. **460** (2008) 1, arXiv: 0704.1800 [hep-ph] (cit. on p. 18).

[42] P. Minkowski, $\mu \to e\gamma$ *at a Rate of One Out of* 10^9 *Muon Decays?*, Phys. Lett. B **67** (1977) 421 (cit. on p. 18).

[43] T. Yanagida, *Horizontal gauge symmetry and masses of neutrinos*, Conf. Proc. C **7902131** (1979) 95, ed. by O. Sawada and A. Sugamoto (cit. on p. 18).

[44] S. L. Glashow, *The Future of Elementary Particle Physics*, NATO Sci. Ser. B **61** (1980) 687 (cit. on p. 18).

[45] M. Gell-Mann, P. Ramond, and R. Slansky, *Complex Spinors and Unified Theories*, Conf. Proc. C **790927** (1979) 315, arXiv: 1306.4669 [hep-th] (cit. on p. 18).

[46] R. N. Mohapatra and G. Senjanovic, *Neutrino Masses and Mixings in Gauge Models with Spontaneous Parity Violation*, Phys. Rev. D **23** (1981) 165 (cit. on p. 18).

[47] S. L. Glashow, J. Iliopoulos, and L. Maiani, *Weak Interactions with Lepton-Hadron Symmetry*, Phys. Rev. D **2** (7 1970) 1285, URL: https://link.aps.org/doi/10.1103/PhysRevD.2.1285 (cit. on p. 20).

[48] LHCb Collaboration, *Test of lepton universality in beauty-quark decays*, (2021), arXiv: 2103.11769 [hep-ex] (cit. on p. 20).

[49] LHCb Collaboration, *Search for Lepton-Universality Violation in* $B^+ \to K^+\ell^+\ell^-$ *Decays*, Phys. Rev. Lett. **122** (2019) 191801, arXiv: 1903.09252 [hep-ex] (cit. on p. 20).

[50] Belle Collaboration, *Test of lepton-flavor universality in $B \to K^* \ell^+ \ell^-$ decays at Belle*, (2019), arXiv: 1904.02440 [hep-ex] (cit. on p. 20).

[51] LHCb Collaboration, *Test of lepton universality with $B^0 \to K^{*0} \ell^+ \ell^-$ decays*, JHEP **08** (2017) 055, arXiv: 1705.05802 [hep-ex] (cit. on p. 20).

[52] LHCb Collaboration, *Measurement of CP-Averaged Observables in the $B^0 \to K^{*0} \mu^+ \mu^-$ Decay*, Phys. Rev. Lett. **125** (1 2020) 011802, URL: https://link.aps.org/doi/10.1103/PhysRevLett.125.011802 (cit. on p. 20).

[53] J. Aebischer et al., *B-decay discrepancies after Moriond 2019*, Eur. Phys. J. C **80** (2020) 252, arXiv: 1903.10434 [hep-ph] (cit. on pp. 20, 21).

[54] Belle Collaboration, *Measurement of $\mathcal{R}(D)$ and $\mathcal{R}(D^*)$ with a semileptonic tagging method*, (2019), arXiv: 1904.08794 [hep-ex] (cit. on p. 20).

[55] BABAR Collaboration, *Measurement of an excess of $\overline{B} \to D^{(*)} \tau^- \overline{\nu}_\tau$ decays and implications for charged Higgs bosons*, Phys. Rev. D **88** (2013) 072012, arXiv: 1303.0571 [hep-ex] (cit. on p. 21).

[56] Belle Collaboration, *Measurement of the branching ratio of $\overline{B} \to D^{(*)} \tau^- \overline{\nu}_\tau$ relative to $\overline{B} \to D^{(*)} \ell^- \overline{\nu}_\ell$ decays with hadronic tagging at Belle*, Phys. Rev. D **92** (2015) 072014, arXiv: 1507.03233 [hep-ex] (cit. on p. 21).

[57] LHCb Collaboration, *Measurement of the Ratio of Branching Fractions $\mathcal{B}(\overline{B}^0 \to D^{*+} \tau^- \overline{\nu}_\tau) / \mathcal{B}(\overline{B}^0 \to D^{*+} \mu^- \overline{\nu}_\mu)$*, Phys. Rev. Lett. **115** (2015) 111803, [Erratum: Phys.Rev.Lett. 115, 159901 (2015)], arXiv: 1506.08614 [hep-ex] (cit. on p. 21).

[58] Belle Collaboration, *Measurement of the τ lepton polarization and $R(D^*)$ in the decay $\overline{B} \to D^* \tau^- \overline{\nu}_\tau$ with one-prong hadronic τ decays at Belle*, Phys. Rev. D **97** (2018) 012004, arXiv: 1709.00129 [hep-ex] (cit. on p. 21).

[59] LHCb Collaboration, *Test of lepton flavor universality by the measurement of the $B^0 \to D^{*-} \tau^+ \nu_\tau$ branching fraction using three-prong τ decays*, Phys. Rev. D **97** (2018) 072013, arXiv: 1711.02505 [hep-ex] (cit. on p. 21).

[60] Y. S. Amhis et al., *Averages of b-hadron, c-hadron, and τ-lepton properties as of 2018*, (2019), updated results and plots available at https://hflav.web.cern.ch/, arXiv: 1909.12524 [hep-ex] (cit. on p. 21).

[61] Muon g-2 Collaboration, *Final report of the E821 muon anomalous magnetic moment measurement at BNL*, Phys. Rev. D **73** (2006) 072003, arXiv: hep-ex/0602035 (cit. on p. 21).

[62] Muon g-2 Collaboration, *Measurement of the Positive Muon Anomalous Magnetic Moment to 0.46 ppm*, Phys. Rev. Lett. **126** (14 2021) 141801, URL: https://link.aps.org/doi/10.1103/PhysRevLett.126.141801 (cit. on p. 21).

[63] T. Aoyama et al., *The anomalous magnetic moment of the muon in the Standard Model*, Phys. Rept. **887** (2020) 1, arXiv: 2006.04822 [hep-ph] (cit. on p. 21).

[64] S. P. Martin, *A Supersymmetry Primer*, Adv. Ser. Direct. High Energy Phys. **18** (1998) 1, arXiv: hep-ph/9709356 (cit. on p. 23).

[65] B. Bellazzini, C. Petersson, and R. Torre, *Photophilic Higgs boson from sgoldstino mixing*, Phys. Rev. D **86** (2012) 033016, arXiv: 1207.0803 [hep-ph] (cit. on p. 24).

[66] E. Dudas, C. Petersson, and P. Tziveloglou, *Low scale supersymmetry breaking and its LHC signatures*, Nucl. Phys. B **870** (2013) 353, arXiv: 1211.5609 [hep-ph] (cit. on p. 24).

[67] C. T. Hill and E. H. Simmons, *Strong dynamics and electroweak symmetry breaking*, Phys. Rept. **381** (2003) 235, [Erratum: Phys.Rept. 390, 553–554 (2004)], arXiv: hep-ph/0203079 (cit. on p. 24).

[68] D. B. Kaplan and H. Georgi, *SU(2) × U(1) breaking by vacuum misalignment*, Phys. Lett. B **136** (1984) 183 (cit. on p. 24).

[69] T. Kaluza, *Zum Unitätsproblem der Physik*, Int. J. Mod. Phys. D **27** (2018) 1870001, arXiv: 1803.08616 [physics.hist-ph] (cit. on p. 24).

[70] O. Klein, *Quantum Theory and Five-Dimensional Theory of Relativity. (In German and English)*, Z. Phys. **37** (1926) 895, ed. by J. Taylor (cit. on p. 24).

[71] T. Appelquist, A. Chodos, and P. Freund, eds., *MODERN KALUZA-KLEIN THEORIES*, 1987 (cit. on p. 24).

[72] N. Arkani-Hamed, S. Dimopoulos, and G. Dvali, *The hierarchy problem and new dimensions at a millimeter*, Phys. Lett. B **429** (1998) 263, arXiv: hep-ph/9803315 (cit. on p. 24).

[73] I. Antoniadis, N. Arkani-Hamed, S. Dimopoulos, and G. Dvali, *New dimensions at a millimeter to a fermi and superstrings at a TeV*, Phys. Lett. B **436** (1998) 257, arXiv: hep-ph/9804398 (cit. on p. 24).

[74] N. Arkani-Hamed, S. Dimopoulos, and G. Dvali, *Phenomenology, astrophysics, and cosmology of theories with submillimeter dimensions and TeV scale quantum gravity*, Phys. Rev. D **59** (1999) 086004, arXiv: hep-ph/9807344 (cit. on p. 24).

[75] L. Randall and R. Sundrum, *Large Mass Hierarchy from a Small Extra Dimension*, Phys. Rev. Lett. **83** (1999) 3370, arXiv: hep-ph/9905221 (cit. on p. 24).

[76] E. Eichten and K. Lane, *Low-scale technicolor at the Tevatron and LHC*, Phys. Lett. B **669** (2008) 235, arXiv: 0706.2339 [hep-ph] (cit. on pp. 25, 95).

[77] I. Low, J. Lykken, and G. Shaughnessy, *Singlet scalars as Higgs boson imposters at the Large Hadron Collider*, Phys. Rev. D **84** (2011) 035027, arXiv: 1105.4587 [hep-ph] (cit. on pp. 25, 95).

[78] A. Freitas and P. Schwaller, *Multi-photon signals from composite models at LHC*, JHEP **01** (2011) 022, arXiv: 1010.2528 [hep-ph] (cit. on p. 25).

[79] B. C. Allanach, J. P. Skittrall, and K. Sridhar, *Z boson decay to photon plus Kaluza-Klein graviton in large extra dimensions*, JHEP **11** (2007) 089, arXiv: 0705.1953 [hep-ph] (cit. on pp. 25, 95).

[80] B. A. Dobrescu, P. J. Fox, and J. Kearney, *Higgs–photon resonances*, Eur. Phys. J. C **77** (2017) 704, arXiv: 1705.08433 [hep-ph] (cit. on pp. 25, 95).

[81] H. Georgi and S. Glashow, *Unity of All Elementary-Particle Forces*, Phys. Rev. Lett. **32** (1974) 438 (cit. on p. 25).

[82] J. C. Pati and A. Salam, *Lepton number as the fourth "color"*, Phys. Rev. D **10** (1974) 275, [Erratum: Phys.Rev.D 11, 703–703 (1975)] (cit. on p. 25).

[83] M. J. Baker, J. Fuentes-Martín, G. Isidori, and M. König, *High-p_T signatures in vector–leptoquark models*, Eur. Phys. J. C **79** (2019) 334, arXiv: 1901.10480 [hep-ph] (cit. on p. 27).

[84] B. Diaz, M. Schmaltz, and Y.-M. Zhong, *The leptoquark hunter's guide: pair production*, JHEP **10** (2017) 097, arXiv: 1706.05033 [hep-ph] (cit. on pp. 27, 29, 150).

[85] M. Schmaltz and Y.-M. Zhong, *The leptoquark Hunter's guide: large coupling*, JHEP **01** (2019) 132, arXiv: 1810.10017 [hep-ph] (cit. on p. 29).

[86] CMS Collaboration, *Search for single production of scalar leptoquarks in proton–proton collisions at $\sqrt{s} = 8\,TeV$*, Phys. Rev. D **93** (2016) 032005, arXiv: 1509.03750 [hep-ex] (cit. on pp. 28, 30).

[87] CMS Collaboration, *Search for third-generation scalar leptoquarks decaying to a top quark and a τ lepton at $\sqrt{s} = 13\,TeV$*, Eur. Phys. J. C **78** (2018) 707, arXiv: 1803.02864 [hep-ex] (cit. on pp. 28, 30).

[88] CMS Collaboration, *Search for a singly produced third-generation scalar leptoquark decaying to a τ lepton and a bottom quark in proton–proton collisions at $\sqrt{s} = 13\,TeV$*, JHEP **07** (2018) 115, arXiv: 1806.03472 [hep-ex] (cit. on pp. 28, 30).

[89] CMS Collaboration, *Search for pair production of second-generation leptoquarks at $\sqrt{s} = 13\,TeV$*, Phys. Rev. D **99** (2019) 032014, arXiv: 1808.05082 [hep-ex] (cit. on pp. 28, 30).

[90] CMS Collaboration, *Search for Leptoquarks Coupled to Third-Generation Quarks in Proton–Proton Collisions at $\sqrt{s} = 13\,TeV$*, Phys. Rev. Lett. **121** (2018) 241802, arXiv: 1809.05558 [hep-ex] (cit. on pp. 28–30).

[91] CMS Collaboration, *Search for heavy neutrinos and third-generation leptoquarks in hadronic states of two τ leptons and two jets in proton–proton collisions at $\sqrt{s} = 13\,TeV$*, JHEP **03** (2019) 170, arXiv: 1811.00806 [hep-ex] (cit. on pp. 28, 30).

[92] CMS Collaboration, *Search for pair production of first-generation scalar leptoquarks at $\sqrt{s} = 13\,TeV$*, Phys. Rev. D **99** (2019) 052002, arXiv: 1811.01197 [hep-ex] (cit. on pp. 28, 30).

[93] ATLAS Collaboration, *Searches for third-generation scalar leptoquarks in $\sqrt{s} = 13\,TeV$ pp collisions with the ATLAS detector*, JHEP **06** (2019) 144, arXiv: 1902.08103 [hep-ex] (cit. on pp. 28, 30).

[94] CMS Collaboration, *Searches for physics beyond the standard model with the M_{T2} variable in hadronic final states with and without disappearing tracks in proton–proton collisions at $\sqrt{s} = 13\,TeV$*, Eur. Phys. J. C **80** (2020) 3, arXiv: 1909.03460 [hep-ex] (cit. on pp. 28, 30).

[95] ATLAS Collaboration, *Search for a scalar partner of the top quark in the all-hadronic $t\bar{t}$ plus missing transverse momentum final state at $\sqrt{s} = 13$ TeV with the ATLAS detector*, Eur. Phys. J. C **80** (2020) 737, arXiv: 2004.14060 [hep-ex] (cit. on pp. 28, 30).

[96] ATLAS Collaboration, *Search for pairs of scalar leptoquarks decaying into quarks and electrons or muons in $\sqrt{s}$ = 13 TeV pp collisions with the ATLAS detector*, JHEP **10** (2020) 112, arXiv: 2006.05872 [hep-ex] (cit. on pp. 28, 30).

[97] ATLAS Collaboration, *Search for pair production of scalar leptoquarks decaying into first- or second-generation leptons and top quarks in proton-proton collisions at $\sqrt{s}$ = 13 TeV with the ATLAS detector*, (2020), arXiv: 2010.02098 [hep-ex] (cit. on pp. 28, 30, 128, 132, 134–137, 142, 145, 146).

[98] ATLAS Collaboration, *Search for pair production of third-generation scalar leptoquarks decaying into a top quark and a tau-lepton in pp collisions at $\sqrt{s}$ = 13 TeV with the ATLAS detector*, ATLAS-CONF-2020-029 (2020), URL: https://cds.cern.ch/record/2725735 (cit. on pp. 28, 30).

[99] CMS Collaboration, *Search for singly and pair-produced leptoquarks coupling to third-generation fermions in proton-proton collisions at $\sqrt{s} = 13$ TeV*, (2020), arXiv: 2012.04178 [hep-ex] (cit. on p. 30).

[100] V. Takhistov, "Review of Nucleon Decay Searches at Super-Kamiokande", *51st Rencontres de Moriond on EW Interactions and Unified Theories*, 2016 437, arXiv: 1605.03235 [hep-ex] (cit. on p. 29).

[101] I. Doršner, S. Fajfer, A. Greljo, J. Kamenik, and N. Košnik, *Physics of leptoquarks in precision experiments and at particle colliders*, Phys. Rept. **641** (2016) 1, arXiv: 1603.04993 [hep-ph] (cit. on p. 29).

[102] R. Mandal and A. Pich, *Constraints on scalar leptoquarks from lepton and kaon physics*, JHEP **12** (2019) 089, arXiv: 1908.11155 [hep-ph] (cit. on p. 29).

[103] MEG Collaboration, *Search for the lepton flavour violating decay $\mu^+ \to e^+\gamma$ with the full dataset of the MEG experiment*, Eur. Phys. J. C **76** (2016) 434, arXiv: 1605.05081 [hep-ex] (cit. on p. 29).

[104] G. Hiller, D. Loose, and I. Nišandžić, *Flavorful leptoquarks at hadron colliders*, Phys. Rev. D **97** (2018) 075004, arXiv: 1801.09399 [hep-ph] (cit. on p. 29).

[105] J. E. Camargo-Molina, A. Celis, and D. A. Faroughy, *Anomalies in bottom from new physics in top*, Phys. Lett. B **784** (2018) 284, arXiv: 1805.04917 [hep-ph] (cit. on p. 31).

[106] V. Gribov and L. Lipatov, *Deep inelastic ep scattering in perturbation theory*, Sov. J. Nucl. Phys. **15** (1972) 438 (cit. on p. 32).

[107] Y. L. Dokshitzer, *Calculation of the Structure Functions for Deep Inelastic Scattering and e+ e- Annihilation by Perturbation Theory in Quantum Chromodynamics.*, Sov. Phys. JETP **46** (1977) 641 (cit. on p. 32).

[108] G. Altarelli and G. Parisi, *Asymptotic freedom in parton language*, Nucl. Phys. B **126** (1977) 298 (cit. on p. 32).

[109] P. M. Nadolsky et al., *Implications of CTEQ global analysis for collider observation*, Phys. Rev. D **78** (2008) 013004, arXiv: 0802.0007 [hep-ph] (cit. on p. 32).

[110] H.-L. Lai et al., *New parton distributions for collider physics*, Phys. Rev. D **82** (2010) 074024, arXiv: 1007.2241 [hep-ph] (cit. on pp. 32, 97).

[111] S. Dulat et al., *New parton distribution functions from a global analysis of quantum chromodynamics*, Phys. Rev. D **93** (2016) 033006, arXiv: 1506.07443 [hep-ph] (cit. on p. 32).

[112] A. D. Martin, W. J. Stirling, R. S. Thorne, and G. Watt, *Parton distributions for the LHC*, Eur. Phys. J. C **63** (2009) 189, arXiv: 0901.0002 [hep-ph] (cit. on pp. 33, 97).

[113] L. Harland-Lang, A. Martin, P. Motylinski, and R. Thorne, *Parton distributions in the LHC era: MMHT 2014 PDFs*, Eur. Phys. J. C **75** (2015) 204, arXiv: 1412.3989 [hep-ph] (cit. on p. 33).

[114] NNPDF Collaboration, *A first unbiased global NLO determination of parton distributions and their uncertainties*, Nucl. Phys. B **838** (2010) 136, arXiv: 1002.4407 [hep-ph] (cit. on p. 33).

[115] NNPDF Collaboration, *Parton distributions for the LHC run II*, JHEP **04** (2015) 040, arXiv: 1410.8849 [hep-ph] (cit. on pp. 33, 126).

[116] J. C. Collins and D. E. Soper, *The Theorems of Perturbative QCD*, Ann. Rev. Nucl. Part. Sci. **37** (1987) 383 (cit. on p. 33).

[117] *LHC Design Report Vol.1: The LHC Main Ring*, (2004), ed. by O. S. Bruning et al. (cit. on p. 36).

[118] ATLAS Collaboration, *The ATLAS Experiment at the CERN Large Hadron Collider*, JINST **3** (2008) S08003 (cit. on pp. 36, 43, 50).

[119] CMS Collaboration, *The CMS experiment at the CERN LHC*, JINST **3** (2008) S08004 (cit. on p. 36).

[120] ALICE Collaboration, *The ALICE experiment at the CERN LHC*, JINST **3** (2008) S08002 (cit. on p. 36).

[121] LHCb Collaboration, *The LHCb Detector at the LHC*, JINST **3** (2008) S08005 (cit. on p. 36).

[122] LHCf Collaboration, *The LHCf detector at the CERN Large Hadron Collider*, JINST **3** (2008) S08006 (cit. on p. 36).

[123] TOTEM Collaboration, *The TOTEM experiment at the CERN Large Hadron Collider*, JINST **3** (2008) S08007 (cit. on p. 36).

[124] MoEDAL Collaboration, *The MoEDAL experiment at the LHC: status and results*, J. Phys. Conf. Ser. **873** (2017) 012010, ed. by B. Grzadkowski, J. Kalinowski, and M. Krawczyk, arXiv: 1703.07141 [hep-ex] (cit. on p. 36).

[125] FASER Collaboration, *FASER: ForwArd Search ExpeRiment at the LHC*, (2019), arXiv: 1901.04468 [hep-ex] (cit. on p. 36).

[126] C. De Melis, *The CERN accelerator complex. Complexe des accélérateurs du CERN*, (2016), General Photo, URL: https://cds.cern.ch/record/2119882 (cit. on p. 37).

[127] R. Bailey and P. Collier, *Standard Filling Schemes for Various LHC Operation Modes*, tech. rep. LHC-PROJECT-NOTE-323, CERN, 2003, URL: https://cds.cern.ch/record/691782 (cit. on p. 38).

[128] H. Damerau, A. Findlay, S. Gilardoni, and S. Hancock, "RF Manipulations for Higher Brightness LHC-type Beams", *4th International Particle Accelerator Conference*, 2013 WEPEA044 (cit. on p. 38).

[129] H. Bartosik and G. Rumolo, "Beams from the injectors", *7th Evian Workshop on LHC beam operation*, CERN, 2017 233 (cit. on p. 38).

[130] S. Dubourg, T. Argyropoulos, and G. Trad, eds., *Proceedings, 8th Evian Workshop on LHC beam operation: Evian Les Bains, France, December 12-14, 2017*, CERN, 2019 (cit. on p. 38).

[131] W. Herr and B. Muratori, "Concept of luminosity", *CERN Accelerator School and DESY Zeuthen: Accelerator Physics*, 2003 361 (cit. on p. 39).

[132] ATLAS Collaboration, *Results and plots of ATLAS luminosity measurements in Run 2*, [Online; visited on November 29, 2020], URL: https://twiki.cern.ch/twiki/bin/view/AtlasPublic/LuminosityPublicResultsRun2 (cit. on pp. 41, 42).

[133] S. Dubourg, M. Schaumann, and D. Walsh, eds., *Proceedings of the 2019 Evian Workshop on LHC Beam Operations*, 2019 (cit. on p. 40).

[134] J. Pequenao, "Computer generated image of the whole ATLAS detector", 2008, URL: https://cds.cern.ch/record/1095924 (cit. on p. 44).

[135] J. Pequenao, "Computer generated image of the ATLAS inner detector", 2008, URL: https://cds.cern.ch/record/1095926 (cit. on p. 45).

[136] ATLAS Collaboration, *Study of the material of the ATLAS inner detector for Run 2 of the LHC*, JINST **12** (2017) P12009, arXiv: 1707.02826 [hep-ex] (cit. on p. 46).

[137] ATLAS Collaboration, *ATLAS Insertable B-Layer: Technical Design Report*, ATLAS-TDR-19; CERN-LHCC-2010-013, 2010, URL: https://cds.cern.ch/record/1291633 (cit. on p. 46).

[138] B. Abbott et al., *Production and integration of the ATLAS Insertable B-Layer*, JINST **13** (2018) T05008, arXiv: 1803.00844 [physics.ins-det] (cit. on p. 46).

[139] ATLAS Collaboration, *Performance of the ATLAS Transition Radiation Tracker in Run 1 of the LHC: tracker properties*, JINST **12** (2017) P05002, arXiv: 1702.06473 [hep-ex] (cit. on p. 48).

[140] J. Pequenao, "Computer Generated image of the ATLAS calorimeter", 2008, URL: https://cds.cern.ch/record/1095927 (cit. on p. 49).

[141] "ATLAS electromagnetic calorimeter layer", 1993, URL: https://cds.cern.ch/record/39737 (cit. on p. 50).

[142] *ATLAS magnet system : Technical Design Report*, (1997) (cit. on p. 52).

[143] J. Pequenao, "Computer generated image of the ATLAS Muons subsystem", 2008, URL: https://cds.cern.ch/record/1095929 (cit. on p. 53).

[144] ATLAS Collaboration, *Performance of the ATLAS muon trigger in pp collisions at* $\sqrt{s} = 8\,TeV$, Eur. Phys. J. C **75** (2015) 120, arXiv: 1408.3179 [hep-ex] (cit. on p. 54).

[145] ATLAS Collaboration, *The ATLAS Data Acquisition and High Level Trigger system*, JINST **11** (2016) P06008 (cit. on p. 55).

[146] ATLAS Collaboration, *Performance of the ATLAS trigger system in 2015*, Eur. Phys. J. C **77** (2017) 317, arXiv: 1611.09661 [hep-ex] (cit. on p. 55).

[147] ATLAS Collaboration, *Trigger Menu in 2017*, ATL-DAQ-PUB-2018-002, 2018, URL: https://cds.cern.ch/record/2625986 (cit. on p. 55).

[148] ATLAS Collaboration, *Plots and diagrams of ATLAS Trigger and Data Acquisition system*, [Online; visited on November 29, 2020], URL: https://twiki.cern.ch/twiki/bin/view/AtlasPublic/ApprovedPlotsDAQ (cit. on p. 55).

[149] G. Crone et al., *The ATLAS ReadOut System—Performance with first data and perspective for the future*, Nucl. Instrum. Meth. A **623** (2010) 534, ed. by H. Iwasaki, T. K. Komatsubara, and Y. Sugimoto (cit. on pp. 56, 79).

[150] ATLAS Collaboration, *ATLAS Trigger Operation Public Results*, [Online; visited on November 29, 2020], URL: https://twiki.cern.ch/twiki/bin/view/AtlasPublic/TriggerOperationPublicResults (cit. on p. 57).

[151] J. Pequenao and P. Schaffner, "How ATLAS detects particles: diagram of particle paths in the detector", 2013, URL: https://cds.cern.ch/record/1505342 (cit. on p. 59).

[152] F. Akesson et al., *ATLAS tracking event data model*, tech. rep., 2006 (cit. on p. 58).

[153] ATLAS Collaboration, *Performance of the ATLAS track reconstruction algorithms in dense environments in LHC Run 2*, Eur. Phys. J. C **77** (2017) 673, arXiv: 1704.07983 [hep-ex] (cit. on p. 58).

[154] T. Cornelissen et al., *The new ATLAS track reconstruction (NEWT)*, J. Phys. Conf. Ser. **119** (2008) 032014, ed. by R. Sobie, R. Tafirout, and J. Thomson (cit. on p. 58).

[155] ATLAS Collaboration, *Training and validation of the ATLAS pixel clustering neural networks*, tech. rep., 2018 (cit. on p. 59).

[156] ATLAS Collaboration, *A neural network clustering algorithm for the ATLAS silicon pixel detector*, JINST **9** (2014) P09009, arXiv: 1406.7690 [hep-ex] (cit. on p. 59).

[157] R. Fruhwirth, *Application of Kalman filtering to track and vertex fitting*, Nucl. Instrum. Meth. A **262** (1987) 444 (cit. on p. 59).

[158] ATLAS Collaboration, *Reconstruction of primary vertices at the ATLAS experiment in Run 1 proton–proton collisions at the LHC*, Eur. Phys. J. C **77** (2017) 332, arXiv: 1611.10235 [hep-ex] (cit. on p. 60).

[159] G. Borissov et al., *ATLAS strategy for primary vertex reconstruction during Run-2 of the LHC*, tech. rep. 7, 2015 072041 (cit. on p. 60).

[160] W. Lampl et al., *Calorimeter Clustering Algorithms: Description and Performance*, ATL-LARG-PUB-2008-002, 2008, URL: https://cds.cern.ch/record/1099735 (cit. on pp. 60, 61).

[161] ATLAS Collaboration, *Electron and photon performance measurements with the ATLAS detector using the 2015–2017 LHC proton–proton collision data*, JINST **14** (2019) P12006, arXiv: 1908.00005 [hep-ex] (cit. on pp. 60–62, 64).

[162] ATLAS Collaboration, *Topological cell clustering in the ATLAS calorimeters and its performance in LHC Run 1*, Eur. Phys. J. C **77** (2017) 490, arXiv: 1603.02934 [hep-ex] (cit. on pp. 61, 67).

[163] ATLAS Collaboration, *Electron and photon energy calibration with the ATLAS detector using 2015–2016 LHC proton–proton collision data*, JINST **14** (2019) P03017, arXiv: 1812.03848 [hep-ex] (cit. on p. 62).

[164] ATLAS Collaboration, *Photon identification in 2015 ATLAS data*, ATL-PHYS-PUB-2016-014, 2016, URL: https://cds.cern.ch/record/2203125 (cit. on p. 63).

[165] ATLAS Collaboration, *Muon reconstruction performance of the ATLAS detector in proton–proton collision data at* $\sqrt{s} = 13\,TeV$, Eur. Phys. J. C **76** (2016) 292, arXiv: 1603.05598 [hep-ex] (cit. on pp. 65, 66, 139).

[166] M. Cacciari, G. P. Salam, and G. Soyez, *The anti-k_t jet clustering algorithm*, JHEP **04** (2008) 063, arXiv: 0802.1189 [hep-ph] (cit. on pp. 67, 68).

[167] M. Cacciari, G. P. Salam, and G. Soyez, *FastJet user manual*, Eur. Phys. J. C **72** (2012) 1896, arXiv: 1111.6097 [hep-ph] (cit. on p. 68).

[168] S. D. Ellis and D. E. Soper, *Successive combination jet algorithm for hadron collisions*, Phys. Rev. D **48** (1993) 3160, arXiv: hep-ph/9305266 (cit. on p. 69).

[169] ATLAS Collaboration, *Jet Calibration and Systematic Uncertainties for Jets Reconstructed in the ATLAS Detector at* $\sqrt{s} = 13\ TeV$, ATL-PHYS-PUB-2015-015, 2015, URL: https://cds.cern.ch/record/2037613 (cit. on p. 69).

[170] ATLAS Collaboration, *Monte Carlo Calibration and Combination of In-situ Measurements of Jet Energy Scale, Jet Energy Resolution and Jet Mass in ATLAS*, ATLAS-CONF-2015-037, 2015, URL: https://cds.cern.ch/record/2044941 (cit. on p. 69).

[171] M. Cacciari and G. P. Salam, *Pileup subtraction using jet areas*, Phys. Lett. B **659** (2008) 119, arXiv: 0707.1378 [hep-ph] (cit. on pp. 69, 71).

[172] ATLAS Collaboration, *Jet energy scale measurements and their systematic uncertainties in proton–proton collisions at* $\sqrt{s} = 13\,TeV$ *with the ATLAS detector*, Phys. Rev. D **96** (2017) 072002, arXiv: 1703.09665 [hep-ex] (cit. on p. 69).

[173] ATLAS Collaboration, *Jet energy measurement and its systematic uncertainty in proton–proton collisions at* $\sqrt{s} = 7\,TeV$ *with the ATLAS detector*, Eur. Phys. J. C **75** (2015) 17, arXiv: 1406.0076 [hep-ex] (cit. on p. 69).

[174] ALEPH Collaboration, *Study of the fragmentation of b quarks into B mesons at the Z peak*, Phys. Lett. B **512** (2001) 30, arXiv: hep-ex/0106051 (cit. on p. 70).

[175] ATLAS Collaboration, *Performance of b-jet identification in the ATLAS experiment*, JINST **11** (2016) P04008, arXiv: 1512.01094 [hep-ex] (cit. on pp. 70, 71).

[176] ATLAS Collaboration, *Topological b-hadron decay reconstruction and identification of b-jets with the JetFitter package in the ATLAS experiment at the LHC*, ATL-PHYS-PUB-2018-025, 2018, URL: https://cds.cern.ch/record/2645405 (cit. on p. 71).

[177] ATLAS Collaboration, *Measurements of b-jet tagging efficiency with the ATLAS detector using* $t\bar{t}$ *events at* $\sqrt{s} = 13\,TeV$, JHEP **08** (2018) 089, arXiv: 1805.01845 [hep-ex] (cit. on p. 71).

[178] ATLAS Collaboration, *Jet mass reconstruction with the ATLAS Detector in early Run 2 data*, ATLAS-CONF-2016-035, 2016, URL: https://cds.cern.ch/record/2200211 (cit. on p. 71).

[179] A. J. Larkoski, G. P. Salam, and J. Thaler, *Energy correlation functions for jet substructure*, JHEP **06** (2013) 108, arXiv: 1305.0007 [hep-ph] (cit. on p. 71).

[180] A. J. Larkoski, I. Moult, and D. Neill, *Power counting to better jet observables*, JHEP **12** (2014) 009, arXiv: 1409.6298 [hep-ph] (cit. on p. 71).

[181] ATLAS Collaboration, *Identification of Boosted, Hadronically-Decaying W and Z Bosons in $\sqrt{s} = 13$ TeV Monte Carlo Simulations for ATLAS*, ATL-PHYS-PUB-2015-033, 2015, URL: https://cds.cern.ch/record/2041461 (cit. on p. 71).

[182] ATLAS Collaboration, *Optimisation of the ATLAS b-tagging performance for the 2016 LHC Run*, ATL-PHYS-PUB-2016-012, 2016, URL: https://cds.cern.ch/record/2160731 (cit. on p. 71).

[183] J. Thaler and K. Van Tilburg, *Identifying boosted objects with N-subjettiness*, JHEP **03** (2011) 015, arXiv: 1011.2268 [hep-ph] (cit. on pp. 71, 131).

[184] J. Thaler and K. Van Tilburg, *Maximizing boosted top identification by minimizing N-subjettiness*, JHEP **02** (2012) 093, arXiv: 1108.2701 [hep-ph] (cit. on pp. 71, 131).

[185] J. Butterworth, B. Cox, and J. R. Forshaw, *WW scattering at the CERN LHC*, Phys. Rev. D **65** (2002) 096014, arXiv: hep-ph/0201098 (cit. on pp. 72, 131).

[186] ATLAS Collaboration, *Performance of boosted top quark identification in 2012 ATLAS data*, ATLAS-CONF-2013-084, 2013, URL: https://cds.cern.ch/record/1571040 (cit. on pp. 72, 131).

[187] J. Thaler and L.-T. Wang, *Strategies to identify boosted tops*, JHEP **07** (2008) 092, arXiv: 0806.0023 [hep-ph] (cit. on pp. 72, 131).

[188] ATLAS Collaboration, *E_T^{miss} performance in the ATLAS detector using 2015–2016 LHC pp collisions*, ATLAS-CONF-2018-023, 2018, URL: https://cds.cern.ch/record/2625233 (cit. on p. 72).

[189] ATLAS Collaboration, *Performance of missing transverse momentum reconstruction with the ATLAS detector using proton–proton collisions at $\sqrt{s} = 13$ TeV*, Eur. Phys. J. C **78** (2018) 903, arXiv: 1802.08168 [hep-ex] (cit. on p. 72).

[190] ATLAS Collaboration, *TRT performance results from 13 TeV collision data (2015/2016)*, [Online; visited on November 13, 2020], URL: https://atlas.web.cern.ch/Atlas/GROUPS/PHYSICS/PLOTS/TRT-2016-001/ (cit. on p. 76).

[191] J. D. Jackson, *Classical Electrodynamics*, Wiley, 1998, ISBN: 978-0-471-30932-1 (cit. on p. 76).

[192] ATLAS Collaboration, *Particle Identification Performance of the ATLAS Transition Radiation Tracker*, ATLAS-CONF-2011-128, 2011, URL: https://cds.cern.ch/record/1383793 (cit. on p. 77).

[193] ATLAS Collaboration, *Basic ATLAS TRT performance studies of Run 1*, ATL-INDET-PUB-2014-001, 2014, URL: https://cds.cern.ch/record/1669603 (cit. on p. 77).

[194] ATLAS Collaboration, *The ATLAS TRT electronics*, JINST **3** (2008) P06007 (cit. on pp. 77, 79).

[195] A. Bingul, *The ATLAS TRT and its performance at LHC*, J. Phys. Conf. Ser. **347** (2012) 012025, ed. by S. A. Cetin, P. Jenni, V. E. Ozcan, and V. N. Senoguz (cit. on pp. 77, 78).

[196] S. Mehlhase and T. C. Petersen, *A probability based approach to PID in the TRT detector of ATLAS*, tech. rep. ATL-COM-INDET-2006-017, CERN, 2006, URL: https://cds.cern.ch/record/988085 (cit. on p. 78).

[197] D. A. Huffman, *A Method for the Construction of Minimum-Redundancy Codes*, Proceedings of the IRE **40** (1952) 1098 (cit. on pp. 79, 80).

[198] H. C. van der Bij, R. A. McLaren, O. Boyle, and G. Rubin, *S-LINK, a data link interface specification for the LHC era*, IEEE Transactions on Nuclear Science **44** (1997) 398 (cit. on p. 79).

[199] C. E. Shannon, *A mathematical theory of communication*, The Bell System Technical Journal **27** (1948) 379 (cit. on p. 80).

[200] E. Gross and O. Vitells, *Trial factors for the look elsewhere effect in high energy physics*, Eur. Phys. J. C **70** (2010) 525, arXiv: 1005.1891 [physics.data-an] (cit. on p. 93).

[201] A. L. Read, *Presentation of search results: the CL_S technique*, J. Phys. G **28** (2002) 2693 (cit. on p. 93).

[202] G. Cowan, K. Cranmer, E. Gross, and O. Vitells, *Asymptotic formulae for likelihood-based tests of new physics*, Eur. Phys. J. C **71** (2011) 1554, arXiv: 1007.1727 [physics.data-an] (cit. on p. 93), Erratum: Eur. Phys. J. C **73** (2013) 2501.

[203] A. Wald, *Tests of Statistical Hypotheses Concerning Several Parameters When the Number of Observations is Large*, Transactions of the American Mathematical Society **54** (1943) 426, ISSN: 00029947, URL: http://www.jstor.org/stable/1990256 (cit. on p. 94).

[204] N. Arkani-Hamed, A. G. Cohen, and H. Georgi, *Electroweak symmetry breaking from dimensional deconstruction*, Phys. Lett. B **513** (2001) 232, arXiv: hep-ph/0105239 (cit. on p. 95).

[205] ATLAS Collaboration, *Measurements of $W\gamma$ and $Z\gamma$ production in pp collisions at $\sqrt{s} = 7$ TeV with the ATLAS detector at the LHC*, Phys. Rev. D **87** (2013) 112003, arXiv: 1302.1283 [hep-ex] (cit. on p. 95), Erratum: Phys. Rev. D **91** (2015) 119901.

[206] ATLAS Collaboration, *Search for new resonances in $W\gamma$ and $Z\gamma$ Final States in pp Collisions at $\sqrt{s} = 8$ TeV with the ATLAS Detector*, Phys. Lett. B **738** (2014) 428, arXiv: 1407.8150 [hep-ex] (cit. on p. 95).

[207] ATLAS Collaboration, *Search for heavy resonances decaying to a Z boson and a photon in pp collisions at $\sqrt{s} = 13$ TeV with the ATLAS detector*, Phys. Lett. B **764** (2017) 11, arXiv: 1607.06363 [hep-ex] (cit. on pp. 95, 106).

[208] ATLAS Collaboration, *Searches for the $Z\gamma$ decay mode of the Higgs boson and for new high-mass resonances in pp collisions at $\sqrt{s} = 13$ TeV with the ATLAS detector*, JHEP **10** (2017) 112, arXiv: 1708.00212 [hep-ex] (cit. on pp. 95, 148).

[209] E. Bagnaschi, G. Degrassi, P. Slavich, and A. Vicini, *Higgs production via gluon fusion in the POWHEG approach in the SM and in the MSSM*, JHEP **02** (2012) 088, arXiv: 1111.2854 [hep-ph] (cit. on p. 97).

[210] S. Alioli, P. Nason, C. Oleari, and E. Re, *A general framework for implementing NLO calculations in shower Monte Carlo programs: the POWHEG BOX*, JHEP **06** (2010) 043, arXiv: 1002.2581 [hep-ph] (cit. on pp. 97, 126).

[211] T. Sjöstrand, S. Mrenna, and P. Skands, *A brief introduction to PYTHIA 8.1*, Comput. Phys. Commun. **178** (2008) 852, arXiv: 0710.3820 [hep-ph] (cit. on pp. 97, 125).

[212] J. Pumplin et al., *New Generation of Parton Distributions with Uncertainties from Global QCD Analysis*, JHEP **07** (2002) 012, arXiv: hep-ph/0201195 (cit. on p. 97).

[213] ATLAS Collaboration, *Measurement of the Z/γ^* boson transverse momentum distribution in pp collisions at $\sqrt{s} = 7$ TeV with the ATLAS detector*, JHEP **09** (2014) 145, arXiv: 1406.3660 [hep-ex] (cit. on p. 97).

[214] J. Alwall et al., *The automated computation of tree-level and next-to-leading order differential cross sections, and their matching to parton shower simulations*, JHEP **07** (2014) 079, arXiv: 1405.0301 [hep-ph] (cit. on pp. 97, 126).

[215] ATLAS Collaboration, *ATLAS Pythia 8 tunes to 7 TeV data*, ATL-PHYS-PUB-2014-021, 2014, URL: https://cds.cern.ch/record/1966419 (cit. on pp. 97, 126).

[216] R. D. Ball et al., *Parton distributions with LHC data*, Nucl. Phys. B **867** (2013) 244, arXiv: 1207.1303 [hep-ph] (cit. on pp. 97, 125).

[217] T. Gleisberg et al., *Event generation with SHERPA 1.1*, JHEP **02** (2009) 007, arXiv: 0811.4622 [hep-ph] (cit. on pp. 97, 126).

[218] T. Gleisberg and S. Höche, *Comix, a new matrix element generator*, JHEP **12** (2008) 039, arXiv: 0808.3674 [hep-ph] (cit. on pp. 97, 126).

[219] F. Cascioli, P. Maierhöfer, and S. Pozzorini, *Scattering Amplitudes with Open Loops*, Phys. Rev. Lett. **108** (2012) 111601, arXiv: 1111.5206 [hep-ph] (cit. on pp. 97, 126).

[220] S. Schumann and F. Krauss, *A parton shower algorithm based on Catani–Seymour dipole factorisation*, JHEP **03** (2008) 038, arXiv: 0709.1027 [hep-ph] (cit. on pp. 97, 126).

[221] S. Höche, F. Krauss, S. Schumann, and F. Siegert, *QCD matrix elements and truncated showers*, JHEP **05** (2009) 053, arXiv: 0903.1219 [hep-ph] (cit. on pp. 97, 126).

[222] D. J. Lange, *The EvtGen particle decay simulation package*, Nucl. Instrum. Meth. A **462** (2001) 152 (cit. on p. 97).

[223] ATLAS Collaboration, *The ATLAS Simulation Infrastructure*, Eur. Phys. J. C **70** (2010) 823, arXiv: 1005.4568 [physics.ins-det] (cit. on pp. 97, 125).

[224] S. Agostinelli et al., GEANT4 – *a simulation toolkit*, Nucl. Instrum. Meth. A **506** (2003) 250 (cit. on pp. 97, 125).

[225] ATLAS Collaboration, *The Pythia 8 A3 tune description of ATLAS minimum bias and inelastic measurements incorporating the Donnachie–Landshoff diffractive model*, ATL-PHYS-PUB-2016-017, 2016, URL: https://cds.cern.ch/record/2206965 (cit. on pp. 97, 125).

[226] ATLAS Collaboration, *Search for heavy resonances decaying to a photon and a hadronically decaying $Z/W/H$ boson in pp collisions at $\sqrt{s} = 13$ TeV with the ATLAS detector*, Phys. Rev. D **98** (2018) 032015, arXiv: 1805.01908 [hep-ex] (cit. on pp. 99–102, 117–119, 122, 123, 149).

[227] ATLAS Collaboration, *Search for diboson resonances with boson-tagged jets in pp collisions at $\sqrt{s} = 13$ TeV with the ATLAS detector*, Phys. Lett. B **777** (2018) 91, arXiv: 1708.04445 [hep-ex] (cit. on pp. 99, 114).

[228] M. Oreglia, "A Study of the Reactions $\psi' \to \gamma\gamma\psi$", PhD thesis, 1980 (cit. on p. 103).

[229] ATLAS Collaboration, *Search for new phenomena in dijet mass and angular distributions from pp collisions at $\sqrt{s} = 13$ TeV with the ATLAS detector*, Phys. Lett. B **754** (2016) 302, arXiv: 1512.01530 [hep-ex] (cit. on p. 106).

[230] P. Gregory, *Bayesian Logical Data Analysis for the Physical Sciences: A Comparative Approach with Mathematica® Support*, Cambridge University Press, 2005 (cit. on p. 107).

[231] LHC Higgs Cross Section Working Group, *Handbook of LHC Higgs Cross Sections: 4. Deciphering the Nature of the Higgs Sector*, (2016), arXiv: 1610.07922 [hep-ph] (cit. on p. 111).

[232] Avoni, G. and others, *The new LUCID-2 detector for luminosity measurement and monitoring in ATLAS*, JINST **13** (2018) P07017 (cit. on pp. 112, 138).

[233] ATLAS Collaboration, *Luminosity determination in pp collisions at $\sqrt{s} = 8$ TeV using the ATLAS detector at the LHC*, Eur. Phys. J. C **76** (2016) 653, arXiv: 1608.03953 [hep-ex] (cit. on pp. 112, 138).

[234] A. Buckley et al., *LHAPDF6: parton density access in the LHC precision era*, Eur. Phys. J. C **75** (2015) 132, arXiv: 1412.7420 [hep-ph] (cit. on p. 115).

[235] ATLAS Collaboration, *Performance of electron and photon triggers in ATLAS during LHC Run 2*, Eur. Phys. J. C **80** (2020) 47, arXiv: 1909.00761 [hep-ex] (cit. on p. 125).

[236] ATLAS Collaboration, *Performance of the ATLAS muon triggers in Run 2*, JINST **15** (2020) P09015, arXiv: 2004.13447 [hep-ex] (cit. on p. 125).

[237] T. Mandal, S. Mitra, and S. Seth, *Pair production of scalar leptoquarks at the LHC to NLO parton shower accuracy*, Phys. Rev. D **93** (2016) 035018, arXiv: 1506.07369 [hep-ph] (cit. on p. 126).

[238] P. Artoisenet, R. Frederix, O. Mattelaer, and R. Rietkerk, *Automatic spin-entangled decays of heavy resonances in Monte Carlo simulations*, JHEP **03** (2013) 015, arXiv: 1212.3460 [hep-ph] (cit. on p. 126).

[239] T. Sjöstrand et al., *An introduction to PYTHIA 8.2*, Comput. Phys. Commun. **191** (2015) 159, arXiv: 1410.3012 [hep-ph] (cit. on p. 126).

[240] A. Belyaev, C. Leroy, R. Mehdiyev, and A. Pukhov, *Leptoquark single and pair production at LHC with CalcHEP/CompHEP in the complete model*, JHEP **09** (2005) 005, arXiv: hep-ph/0502067 (cit. on p. 126).

[241] ATLAS Collaboration, *Studies on top-quark Monte Carlo modelling for Top2016*, ATL-PHYS-PUB-2016-020, 2016, URL: https://cds.cern.ch/record/2216168 (cit. on p. 126).

[242] M. Czakon and A. Mitov, *Top++: A program for the calculation of the top-pair cross-section at hadron colliders*, Comput. Phys. Commun. **185** (2014) 2930, arXiv: 1112.5675 [hep-ph] (cit. on p. 126).

[243] M. Cacciari, M. Czakon, M. Mangano, A. Mitov, and P. Nason, *Top-pair production at hadron colliders with next-to-next-to-leading logarithmic soft-gluon resummation*, Phys. Lett. B **710** (2012) 612, arXiv: 1111.5869 [hep-ph] (cit. on p. 126).

[244] P. Bärnreuther, M. Czakon, and A. Mitov, *Percent-Level-Precision Physics at the Tevatron: Next-to-Next-to-Leading Order QCD Corrections to $q\bar{q} \to t\bar{t} + X$*, Phys. Rev. Lett. **109** (2012) 132001, arXiv: 1204.5201 [hep-ph] (cit. on p. 126).

[245] M. Czakon and A. Mitov, *NNLO corrections to top-pair production at hadron colliders: the all-fermionic scattering channels*, JHEP **12** (2012) 054, arXiv: 1207.0236 [hep-ph] (cit. on p. 126).

[246] M. Czakon and A. Mitov, *NNLO corrections to top pair production at hadron colliders: the quark-gluon reaction*, JHEP **01** (2013) 080, arXiv: 1210.6832 [hep-ph] (cit. on p. 126).

[247] M. Czakon, P. Fiedler, and A. Mitov, *Total Top-Quark Pair-Production Cross Section at Hadron Colliders Through $O(\alpha_S^4)$*, Phys. Rev. Lett. **110** (2013) 252004, arXiv: 1303.6254 [hep-ph] (cit. on p. 126).

[248] N. Kidonakis, *Next-to-next-to-leading-order collinear and soft gluon corrections for t-channel single top quark production*, Phys. Rev. D **83** (2011) 091503, arXiv: 1103.2792 [hep-ph] (cit. on p. 126).

[249] N. Kidonakis, *Two-loop soft anomalous dimensions for single top quark associated production with a W^- or H^-*, Phys. Rev. D **82** (2010) 054018, arXiv: 1005.4451 [hep-ph] (cit. on p. 126).

[250] N. Kidonakis, *Next-to-next-to-leading logarithm resummation for s-channel single top quark production*, Phys. Rev. D **81** (2010) 054028, arXiv: 1001.5034 [hep-ph] (cit. on p. 126).

[251] T. Chen and C. Guestrin, *XGBoost: A Scalable Tree Boosting System*, (2016), arXiv: 1603.02754 (cit. on p. 129).

[252] M. Stone, *Cross-Validatory Choice and Assessment of Statistical Predictions*, J. Roy. Stat. Soc. B **36** (1974) 111 (cit. on p. 129).

[253] P. Jackson and C. Rogan, *Recursive jigsaw reconstruction: HEP event analysis in the presence of kinematic and combinatoric ambiguities*, Phys. Rev. D **96** (2017) 112007, arXiv: 1705.10733 [hep-ph] (cit. on pp. 129, 130, 133).

[254] P. Baldi, K. Cranmer, T. Faucett, P. Sadowski, and D. Whiteson, *Parameterized neural networks for high-energy physics*, Eur. Phys. J. C **76** (2016) 235, arXiv: 1601.07913 [hep-ex] (cit. on p. 134).

[255] J. Butterworth et al., *PDF4LHC recommendations for LHC Run II*, J. Phys. G **43** (2016) 023001, arXiv: 1510.03865 [hep-ph] (cit. on p. 139).

[256] K. Melnikov and F. Petriello, *Electroweak gauge boson production at hadron colliders through $\mathcal{O}(\alpha_s^2)$*, Phys. Rev. D **74** (2006) 114017, arXiv: hep-ph/0609070 (cit. on p. 139).

[257] ATLAS Collaboration, *Multi-boson simulation for* 13 *TeV ATLAS analyses*, ATL-PHYS-PUB-2016-002, 2016, URL: https://cds.cern.ch/record/2119986 (cit. on p. 139).

[258] M. Aliev et al., *HATHOR – HAdronic Top and Heavy quarks crOss section calculatoR*, Comput. Phys. Commun. **182** (2011) 1034, arXiv: 1007.1327 [hep-ph] (cit. on p. 139).

[259] P. Kant et al., HATHOR *for single top-quark production: Updated predictions and uncertainty estimates for single top-quark production in hadronic collisions*, Comput. Phys. Commun. **191** (2015) 74, arXiv: 1406.4403 [hep-ph] (cit. on p. 139).

[260] ATLAS Collaboration, *Modelling of the $t\bar{t}H$ and $t\bar{t}V$ $(V = W, Z)$ processes for $\sqrt{s} = 13$ TeV ATLAS analyses*, ATL-PHYS-PUB-2016-005, 2016, URL: https://cds.cern.ch/record/2120826 (cit. on p. 139).

[261] ATLAS Collaboration, *Improving jet substructure performance in ATLAS using Track-CaloClusters*, ATL-PHYS-PUB-2017-015, 2017, URL: https://cds.cern.ch/record/2275636 (cit. on p. 148).

[262] C. Rasmussen and C. Williams, *Gaussian Processes for Machine Learning*, Adaptive Computation and Machine Learning, MIT Press, 2006 248 (cit. on p. 148).

[263] K. Chandak, T. Mandal, and S. Mitra, *Hunting for scalar leptoquarks with boosted tops and light leptons*, Phys. Rev. D **100** (2019) 075019, arXiv: 1907.11194 [hep-ph] (cit. on p. 150).